Cuprous Oxide Photoelectrodes for Photoelectrochemical Water Splitting towards Unassisted Solar Hydrogen Production.

Thèse N° 7340

Linfeng PAN

2019

EPFL
ÉCOLE POLYTECHNIQUE
FÉDÉRALE DE LAUSANNE

.

Au milieu de l'hiver,

j'ai découvert en moi un invincible été.

- Albert Camus

Abstract

The solutions to problems could be the sources of new problems. The rapid development since the Industrial Revolution has granted people higher living standards with upgraded sanitary conditions. As results of that, world population was soaring in the last 50 years. Even though the population growth is not prominent in developed areas, resource consumption could still rise due to the demand for better living conditions. Energy, the driving power for development, is massively required at an unprecedented rate owing to stable economic growth recently. The strong dependence on fossil fuel has not only caused geographical tension, but also is changing the ecology and global weather at a worrying speed.

Renewable energy was believed to be both the future choice of energy source and remedies to environmental problems today. However, most renewable sources were indirect solar energy, which share the problems of low energy density, intermittence and limited transportation. One of the promising methods is to convert and store the solar energy in solar fuels such as hydrogen. Solar fuels have comparable energy density to fossil fuels and can be consumed in a similar way based on the existing infrastructure. The existing solar water splitting devices can be ascribed into 3 categories, namely photovoltaic-powered electrolysis, photoelectrochemical water splitting, and photocatalysis. Among which, photoelectrochemical water splitting holds the potential of being low cost and high efficiency simultaneously.

This thesis was focused on the development of Cu_2O photocathodes in several aspects towards standalone solar water splitting devices. Cu_2O, a p-type semiconductor, has been studied as the photoabsorber in photovoltaic applications since last century. It's oxide nature and abundance render it attractive in the solar water splitting field as it could be easily fabricated with desired structure at low cost. The suitable band gap of Cu_2O and semiconductor property has made it an excellent photocathode material candidate. However, as the degradation reaction potentials of Cu_2O are straddled by the conduction and valence band of the material, it could degrade easily in contact with electrolyte under illumination. The best solution is to apply protection layers against the electrolyte while use effective junctions to separate the photo-generated charges, which could both enhance the performance and avoid self-degradation.

With delicate band energy level alignment, Cu_2O/Ga_2O_3 p-n junction was formed to facilitate the electron transport towards the surface of the electrode. As the minority carrier in Cu_2O, electrons are considered as the main limiting factor for the photoelectrode. In the first part of the thesis, the band energy levels were measured with detailed characterizations. By integrating the data and illustrating the band diagram, I show the origin of the enhanced performance. Similar electron transport engineering was done in the case of Cu_2S. Both photoelectrodes exhibit outstanding photoelectrochemical performance.

Echoing the last part, the next part of research was focused on the hole transport side. Though Au has many advantages applied as the hole ohmic contact, its scarcity and unselective conduction leave considerable space for further development. CuSCN was electrodeposited and used as the hole transport material for Cu_2O photocathodes for the first time. Through careful measurement, the band tail-assisted hole transport was revealed between the Cu_2O and CuSCN. Due to the excellent electronic properties of solution processed CuSCN, planar Cu_2O photocathodes exhibit greatly enhanced fill factor.

In the third part, I describe the study of the Cu_2O photoabsorber itself. Firstly, the nanowire Cu_2O decoupled the light absorption and electron transport paths. As a result, electrons only have to travel the radius of the wire to reach the catalysts while holes, which have longer diffusion length, still can be efficiently collected at the back contact. In the meantime, light absorption was improved as the nanowire jungle could harvest scattering light as well. Then, high-quality single-crystal Cu_2O films with three orientations are successfully fabricated. Their anisotropic photoelectrochemical behaviors imply the anisotropic optical and electronic properties. As the single-crystal films show well-established material characteristics, they provide exceptional platform for fundamental spectroscopic and material studies.

Finally, to show the advances made on the Cu_2O photocathodes, early attempts of building dual-absorber tandems are described. Both PEC-PEC and PEC-PV tandems based on Cu_2O photocathodes are demonstrated delivering record solar-to-hydrogen efficiencies. Discussions on future improvement of such tandems are presented at the end according to the experience gained during device construction.

Keywords

Solar energy; Photoelectrochemical water splitting; Cu_2O photocathodes; Heterojunction; ALD; Tandem devices.

Résumé

Le développement rapide qui résultat de la révolution industrielle a permis d'améliorer la qualité de vie et l'espérance de vie de l'humanité. Une conséquence directe de cette modernisation fut la forte croissance de la population mondiale au cours des 50 ans dernières années. Une forte augmentation de la population induit inéluctablement une augmentation des ressources telles que l'énergie. La dépendance de la société actuelle aux énergies fossiles a causé de fortes perturbations politico-économiques.

Les énergies renouvelables se sont présentées comme étant les candidats les plus prometteurs pour remplacer les énergies fossiles et remédier aux problèmes actuels. Cependant, la majorité des sources d'énergie renouvelable dérivée de la conversion indirecte de l'énergie solaire, souffre de problèmes tels qu'une limitation en termes de densité énergétique et un fonctionnement intermittent. La solution la plus prometteuse serait donc de stocker l'énergie contenue dans le soleil sous forme de molécule de dihydrogène. Cette nouvelle forme de réserve d'énergie appelée carburants solaires, partagent certaines caractéristiques communes avec les carburants fossiles : une densité énergétique comparable et un system de transport et de consommation similaire à celui utilisé pour les carburants fossiles. Il existe trois types de systèmes capables de convertir l'eau en dihydrogène en utilisait l'énergie solaire : l'électrolyse assistée par le photovoltaïque, les cellules photo catalytiques et les cellules photo électrochimiques. Ces dernières se présentent comme était les candidats les plus prometteurs en termes de rendement mais aussi de coût de production.

Cette thèse présente le développement de photocathodes à base d'oxyde de Cuivre(I)(Cu_2O) dans le but d'obtenir des cellules photo électrochimiques opérationnelles. L'oxyde de cuivre (I) est un semi-conducteur de type p, utilisé comme photo absorbeur dans le domaine photovoltaïque pendant environs un siècle. Il est naturellement très abondant ce qui le rend intéressent pour la fabrication de cellules photo électrochimiques peu onéreuses. Le band gap du Cu_2O ainsi que ses propriétés semi conductrices en fait un candidat idéal en tant que matériel pour la fabrication de photocathodes. Cependant, la stabilité du Cu_2O est relativement faible dans l'électrolytes utilisé durant les conditions d'illumination. Pour remédier à ce problème, une couche ou plusieurs couches de protection peut être déposée sur la surface du matériel pour le protéger de l'électrolyte. Il est toutefois important de s'assurer que l'interface entre l'oxyde de Cuivre(I) et la

couche de protection assure une séparation efficace des charges pour garantir un fonctionnement optimal de la cellule.

De ce fait une jonction p-n entre Cu_2O et Ga_2O_3 a été créée pour garantir un transport d'électron performant à la surface de l'électrode. Dans un premier temps, les niveaux d'énergie de ce matériel ont été mesurées et caractérisés en détails dans le but de déterminer le diagramme de bandes, ce qui m'a permis d'identifier l'origine de l'amélioration des performances. La même stratégie a été appliquée pour des photocathodes à base de Cu_2S. Dans les deux cas, les performances des cellules photo-électrochimiques ont drastiquement été améliorées.

Dans la partie suivante, les efforts ont été concentré autour de la partie conductrice de trous. Malgré les avantages des électrodes à base d'or, plusieurs éléments peuvent être améliorés et notamment la sélectivité de l'électrode. Du CuSCN a été électro-déposé et utilisé comme coucher conductrice de trous sur des photocathodes à base d'oxyde de cuivre(I) pour la première fois. Le band tail de l'interface entre les deux matériaux a été déterminée avec soins et grâce aux excellentes propriétés électroniques du CuSCN, les électrodes planaires de Cu_2O ont montré un fill factor nettement amélioré. Dans la troisième partie, je décris l'optimisation du Cu_2O. Dans un premier temps, il a été observé que les nano filaments de Cu_2O permettent de découpler le transport de charges et l'absorption de la lumière. De ce fait, les électrons sont les seuls à diffuser à travers la section de ces nano filaments tandis que les trous peuvent être récupéré au back contact de manière efficace. De plus, la structure en filament a aussi permis d'améliorer l'absorption de la lumière. Ensuite, des cristaux uniques de Cu_2O de haute qualité possédant 3 orientations différentes ont été fabriqués. L'anisotropie photo électrochimique de ces cristaux a démontré d'intrinsèque comportements électroniques et optiques eux aussi fortement dépendant de l'orientation de ces cristaux.

La dernière partie présente les essais préliminaires dans la fabrication d'absorbeur tandems tels que les PEC-PEC ou les PEC-PV. Dans les deux cas, les photocathodes à base de Cu_2O ont présenté de performances record en termes de conversion énergie solaire sous forme de dihydrogène.

Mots-clés

Energie solaire; Fractionnement photoélectrochimique de l'eau; Photocathodes de Cu_2O; Hétérojonction; ALD; Appareils en tandem.

Contents

1 Introduction

1.1 Energy challenges

Enabled by improved sanitary conditions and rising science and technology, the world has experienced rapid growth in population since the second half of the twentieth century.[1] This trend could last in the next 30 years and the world population will reach 9 billion (Figure 1.1). Along with the population explosion comes the soaring living standards in many regions, which in turn prolonged the life expectancy. The technologies previously owned only by pioneering countries during Industrial Revolutions are now shared by almost all. However, most technologies are not aiming to save resources, but to consume in a faster way to sustain the development. Challenges are made, as the consumption seems to be leading the global ecology to the verge of collapse while more energy is necessary to sustain rapid development.
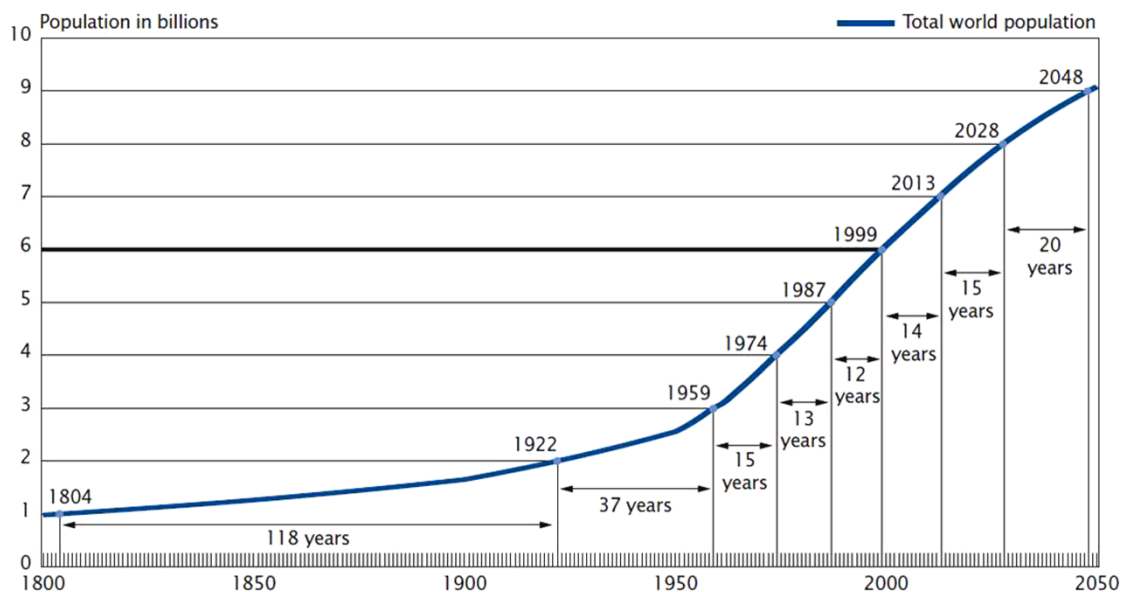
Figure 1.1 | Total world population.[1]

Energy is at the heart of development. It provides food and heat, and support human communication and development. The world total primary energy supply has increased from 5523 Mtoe in 1971 to 13761 Mtoe in 2016.[2] Even though two oil crises occurred in 1973 and 1979, more than 80% of the total primary energy supply was still supported by

fossil fuels, i.e. oil, coal and nature gas (Figure 1.2a). According to the International Energy Agency (IEA), global energy consumption in 2018 increased nearly twice the average growth since 2010 while the energy consumption could increase by 50% till 2050. If the shares of various energies do not change significantly, equal proportion of growth in fossil fuel production is in demand. However, according to the IEA, oil production should only realize an average annual gain of 0.5%.[2,3]
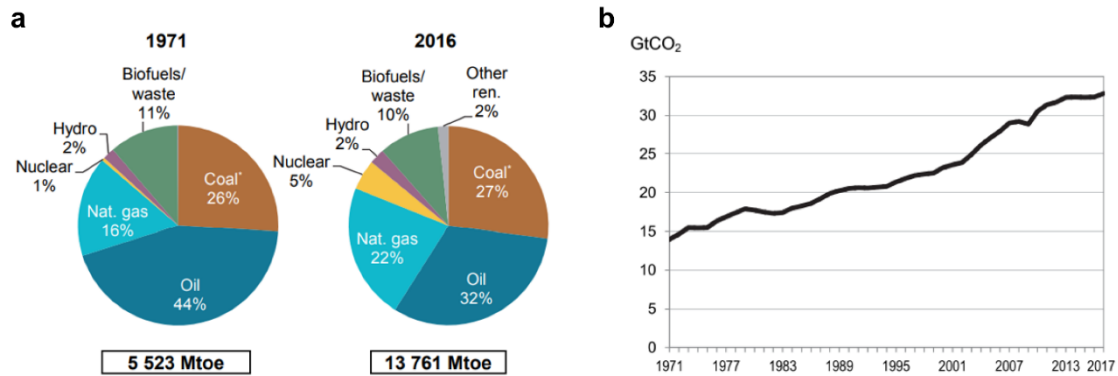
Figure 1.2 | a, Total primary energy supply by fuel in 1971 and 2016.[2] b, Global CO_2 emission trend from fuel combustion.[3]

As the consequences of burning fossil fuels, a range of environmental problems including climate change hit the world. Many factors, however, contribute to the increase of temperature, such as volcanic eruptions, astronomic variations, solar activities and trapped solar energy in Earth. The last one is related to atmospheric greenhouse gas concentration, which is directly related to human activities, also known as "anthropogenic forcing".[4] Small groups of experts still question the accuracy of the applied climate models. Nevertheless, the vast majority of scientists, as well as numerous national science academies, accept the anthropogenic impact on recent climate warming.[4,5] Greenhouse gases are playing important roles for the existence of lives on Earth, but exponentially increasing greenhouse gas concentration in the atmosphere could profoundly affect human societies and natural environment. In 2016, global CO_2 emission reached 32.31 Gt, which is around 140% of emission in 2000 (Figure 1.2b). As a result of robust global economy and high energy consumption, CO_2 emission increased to 33.1 Gt and hit a new record in 2018.

Challenges are presented as it is of human needs to develop, which could lead to an increase of 35% in energy demand in the next 20 years, while in the same period, CO_2 emission needs to be reduced by 35% to 450 ppm. A transformation to sustainable and efficient energy consumption should happen in both developed and new economies.

1.2 Solar energy

1.2.1 Source of solar energy

During the Industrial Revolution, fossil fuels replaced wood as the primary energy resources. They are formed through complex and extremely slow processes under anoxic conditions.[6] If one looks at the energy aspect, they are chemically stored solar energy via photosynthesis dating back to the Carboniferous time. Yet, solar energy not only indirectly provides the fossil fuels, it also directly fuels almost all kinds of renewable energies, such as hydropower, wind energy, biomass, photovoltaic, solar thermal energy.[7]

The sun, with a radiant emittance of 2.846×10^{26} W in total, is a nuclear reactor at a mean distance of 1.5×10^{11} m from the Earth.[8] 90 % of its energy is generated in a spherical region with a radius which is 23% of the Sun's. Energy is released in a fusion reaction where four protons fuse into one helium nucleus at approximately 10^7 K. The opaque and strongly ionized outer surface, namely the photosphere, has an effective black-body temperature of $\sim$ 6000 K and solar energy is radiated through heat and light into the universe. It can be calculated from the following equation:

$$E = \varepsilon \sigma T_s^4$$

where ε is the emissivity of the Sun's surface and σ is the Stefan-Boltzmann constant. At the average Earth-Sun distance, the Sun is not strictly a point source, therefore sunlight rays are not truly parallel but with a cone angle of 0.529°.[9] The total solar energy reaching our outer atmosphere amounts to 175000 TW. Assuming that the usable fraction of 1 % and hypothetical conversion efficiency of 10 %, there will still be more than enough energy provided to the world. If solar energy was used in the direct way, the gap between huge energy demand in the future and current energy supply could be filled while keeping the environmental impact to its minimum.

1.2.1 Solar spectrum

If both the inhomogeneous temperature and altitude distribution on the Sun's surface was neglected to make the approximation, the solar radiation spectrum can be found by regarding the Sun as a thermal-equilibrium source with black body temperature of 6000K. According to the Plank's radiation law, the magnitude of radiation at temperature T as a function of wavelength λ in µm is:

$$E_{\lambda b} = \frac{C_1}{\lambda^5 \left[e^{\frac{C_2}{\lambda T}} - 1 \right]}$$

where $E_{\lambda b}$ is the energy emitted per unit area per unit time per unit wavelength interval at λ, C_1 = 3.742×10^8 W μm^4 m^{-2} and C_2 = 14387.9 μm K.[7,8]
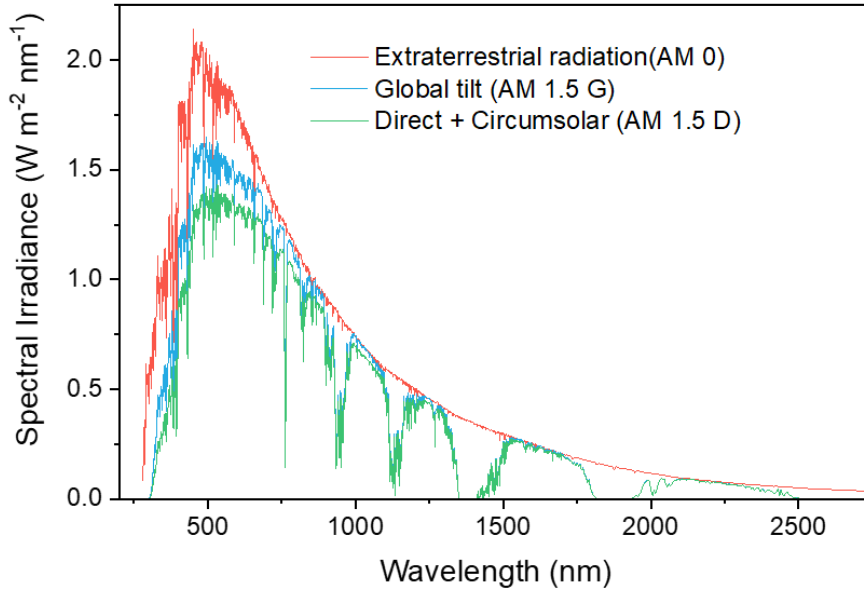
Figure 1.3 | Solar spectral irradiance (ASTM G-173-03, International standard ISO 9845-1, 1992)

However, the terrestrial solar radiation spectrum has a series of different features comparing to the extraterrestrial spectrum as the radiation must pass through the atmosphere (Figure 1.3). Scattering and absorption could happen which changes the overall power and spectral content. In addition, local variations, such as humidity, clouds and pollution, along with latitude and seasonal change will also contribute. The air mass (AM) concept was introduced, as the solar radiation has a certain direction. The amount of attenuation is greatly dependent on the distance that radiation pass through. The air mass is defined in the following equation:

$$\text{Air mass} = \frac{path\ length\ in\ the\ atmosphere}{vertical\ atmosphere\ depth} = \frac{1}{\cos \theta_z}$$

where θ_z is the zenith angle (the angle between sunlight rays and a vertical line to the horizontal plane).[8] In this definition, the extraterrestrial spectrum has an AM of 0 and if the Sun is directly overhead (perpendicular to the earth surface), the AM is 1. Two special spectra named AM 1.5 G and AM 1.5 D should be mentioned. These two spectra are commonly used in solar energy related research as standards. G stands for global and the

AM 1.5 G spectrum includes both direct and diffuse solar radiation. D stands for direct and the AM 1.5 D includes direct radiation only. The global spectrum has around 10% higher intensity than the direct spectrum. For the sake of convenience, the intensity of the standard AM 1.5 G was normalized from 970 W m^{-2} to 1000 W m^{-2}.

1.3 Solar fuels

Solar energy is one of the major solutions to future energy demand. However, its performance can vary significantly within a very short period. Apart from alternation of day and night, the intensity of solar radiation could change drastically due to meteorological conditions and pollution. This feature is shared by other renewable energies such as wind power.[10] Another disadvantage of solar energy is that the radiation power density is too small which is 1000 W m^{-2} according to the AM 1.5 G spectrum. A very large area is needed to power, for instance, a car to run at highway speed. To smooth the fluctuation and provide reliable energy supply to the world, solar energy must be stored.

It is viable to harness and store solar energy in many ways. In nature, this process is known as photosynthesis. It takes place inside a plant and synthesizes hydrocarbons using CO_2 and water. From the energy perspective, solar energy was converted into chemical energy and stored to power future organisms' activities. Fuels are unrivalled in terms of energy density and could be economically consumed base on existing infrastructure. However, the natural way is inefficient and the usage could release the fixed CO_2 back to the atmosphere again. One of the promising ways to harvest the solar energy and store them in various types of desired fuels is to mimic the natural photosynthesis.

1.4 Photoelectrochemical water splitting: Fundamentals*

1.4.1 Introduction to photoelectrochemical water splitting

Artificial photosynthesis promises to become a sustainable way to harvest solar energy

and store it in chemical fuels by means of photoelectrochemical (PEC) synthesis. Although it is intriguing to shift the fossil-fuel based economy to a renewable carbon-neutral one, which will, in the meantime, alleviate environmental problems, there is still a long way to go before it rivals traditional energy sources. Existing solar water splitting devices can be sorted into three categories, photovoltaic-powered electrolysis (PVE), PEC water splitting, and photocatalysis (PC). PEC and PC systems hold the potential to further cut down the cost of devices due to the simple structure where photoabsorbers and catalysts are closely integrated. PC is expected to be the least expensive approach; however, additional cost and concerns rise in subsequent explosive gas separation. At the heart of all devices, semiconductor photoabsorbers should be efficient, robust and cheap to satisfy the strict requirements on the market.

Photoelectrochemical water splitting has evolved from simple configurations, which demonstrate the application of basic concepts to sophisticated devices that offers meaningful solar fuel production efficiencies. Generally, four steps are involved in a complete solar water splitting process. The first two, related to photons, are light absorption and photoexcitation, while the last two, associated with photogenerated charges, are charge separation and surface reaction. Regardless of the complicated structure of the cells, at least one of the electrodes is a semiconductor, which functions as the photo-absorber that can convert photons into electron-hole pairs to power the whole system. Thereafter, junctions, which partake gradient electrochemical potentials, vectorially separate electrons and holes. Due to the difficulties to enumerate all kinds of devices, we choose to explain the underlying principles based on the fundamental differences in various junctions.

1.4.2 Semiconductor junctions for charge separation

The most straightforward device features a semiconductor-electrolyte junction (SEJ). When a semiconductor is in contact with electrolyte, charges will flow across the semiconductor-electrolyte interface due to possible Fermi energy mismatch between the two sides of the interface. When equilibrium is reached, a region near the surface of the semiconductor that is distinct from the bulk is formed, which is known as the space-charge region. Accordingly, an electrical double layer, known as the Helmholtz layer, is formed in electrolyte. In the case of a p-type semiconductor that owns suitable bandgap for water splitting, electrons will flow into the solid and cause hole depletion (the majority carriers). As a result, the semiconductor has an n-type surface region, which in

combination with the p-type bulk, forms an inversion layer near the interface. On the band diagram that shows electron energy levels, downward bending takes place for both conduction band (CB) edge and valence band (VB) edge that are close to the interface. When the semiconductor is illuminated, photons with energies greater than the bandgap will excite electrons from the VB into the CB and leave holes in the valence bands. In the non-equilibrium condition (under illumination), split quasi-Fermi levels of electrons ($E_{F, n}$) and holes ($E_{F, p}$) are used to indicate the built-in voltage which is known as the open-circuit voltage (V_{OC}). Electrons and holes tend to recombine, however, those in the space-charge region can be separated efficiently due to the anisotropic electric field. Therefore, electrons will flow towards the electrolyte to reduce water. Holes are collected at the back via an ohmic contact and will oxidize water at the wired counter electrode (anode).

Figure 1.4 | Schematic diagrams with inbuilt energy diagrams showing electrons and holes flowing directions under illumination, where E_F n is the electron quasi-Fermi level, $E_{F, p}$ is the hole quasi-Fermi level, E_C shows the energy level of conduction band, E_V shows the energy level of valence band, e^- denotes electrons, h^+ denotes holes and hv denotes photons. Here cases of photocathodes are chosen to represent different configurations: a, single-electrode (also called: "half-cell"), b, photocathode-photoanode tandem and c, monolithic PEC tandem (artificial leaf). All configurations feature semiconductor-electrolyte junctions for charge separation.

We illustrated the electronic energy levels and electrochemistry in the devices taking p-type semiconductors as an example (Figure 1.4a). Analogous circumstances can be reasoned for n-type materials. The configuration using one semiconductor and one counter electrode is referred to the "half-cell" configuration. This basic arrangement is commonly used to study a specific semiconductor or to carry out quantum efficiency measurements. To achieve overall water splitting with the half-cell configuration, the only bandgap has to straddle the water reduction and oxidation potentials, where a minimum band gap of 2 eV is necessary to generate enough photovoltage to overcome catalytic

overpotentials and thermodynamic potentials for water splitting. Most oxides own large bandgaps that are more than 3 eV, like TiO_2 (3.0-3.2 eV) and ZnO (3.2-3.3 eV), but their band edges can be too close to water reduction potential, leaving insufficient potential to drive the reaction. Another major problem with large bandgap semiconductors is that they can only absorb ultraviolet (UV) part of solar light, while the power of UV light only takes up around 4% of global solar power at sea level.[11] All factors are keeping the practical solar-to-hydrogen efficiencies (η_{STH}) of this model below 1%. External bias is often applied to solve the dilemma that it's almost insurmountable to provide large photovoltage and harvest a significant portion of sunlight at the same time with one photoabsorber.

Despite the difficulty, new materials are continuously discovered through the half-cell configuration, which also support the construction of the second configuration as illustrated in Figure 1.4b. This tandem is constructed with parallel positioned p-type photocathodes and n-type photoanodes that are wired together. Both photoelectrodes are separating charges with SEJs. As semiconductors are capable of transmitting photons with energy smaller than their bandgaps, if all layers of the front absorber are transparent, the rear semiconductor can still harvest the penetrated part of light with longer wavelengths. Therefore, the semiconductor with a larger bandgap should be used as the front absorber and the one with smaller bandgap will be used as the rear one to follow the logic. Though two photoabsorbers must share the sunlight, which will result in a lower current density, their photovoltages will be added up. With this configuration, unassisted PEC water splitting is possible. One should note that since the two semiconductors are wired with series connection, their current densities have to match. A simple way to predict the operating current density is to overlay the working current density curve of the front transparent photoelectrode and the current density curve of the rear photoelectrode acquired with the front one as a mask, and find the crossing point. A variation of this structure features a monolithic electrode that has two photoelectrodes integrated back-to-back, as shown in Figure 1.4c. This architecture, known as the "artificial leaf", has been considered more economic because it is easy to fabricate due to its simple structure. The interlayer plays the role of electron-hole recombination layer, as well as the backbone of the whole device. In all cases, catalysts are often incorporated onto the semiconductor surface to improve the charge-injection kinetics.

The second category highlights a buried solid-state junction (SSJ). Apart from Schottky junctions, the most well studied SSJs are p-n junctions which form the core of most
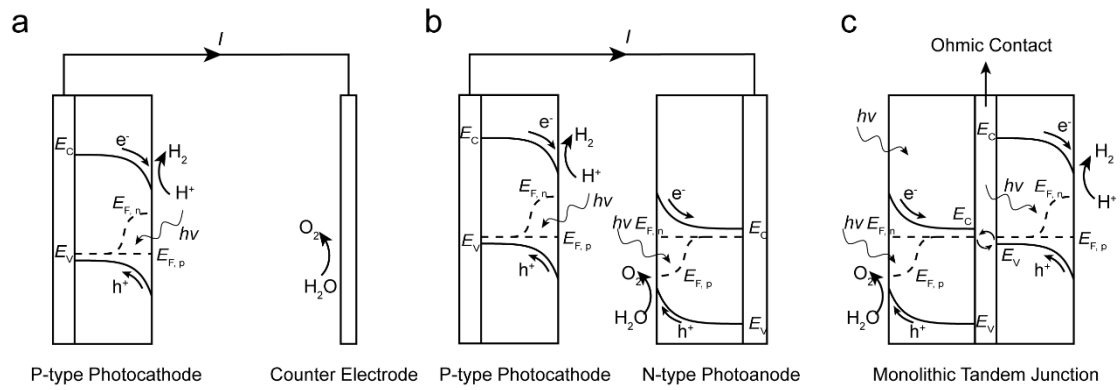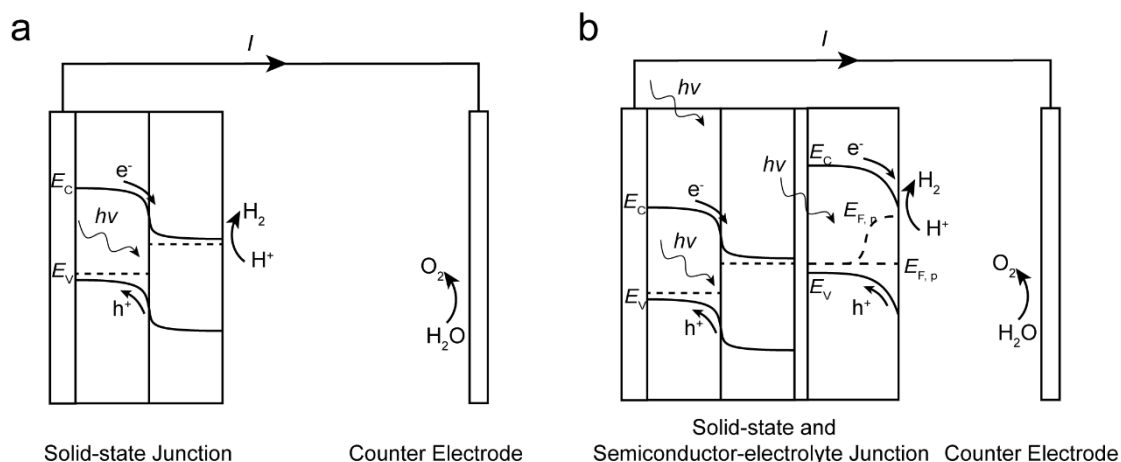
Figure 1.5 | Schematic diagrams with inbuilt energy diagrams showing electrons and holes flowing directions under illumination, where $E_{F, n}$ is the electron quasi-Fermi level, $E_{F, p}$ is the hole quasi-Fermi level, E_C shows the energy level of conduction band, E_V shows the energy level of valence band, e^- denotes electrons, h^+ denotes holes and $h\nu$ denotes photons. Here cases of photocathodes are chosen to represent different configurations: a, buried p-n junction and b, PEC-PV tandem. All configurations feature at least one solid-state junction to separate charges.

photovoltaic cells. When a p-type semiconductor and a n-type semiconductor are joined, holes from the p-type one will diffuse into the n-type part. Similar transport happens for electrons along the other direction. A built-in electric field is formed by left charged dopants that are fixed in the crystal lattice. The equilibrium is reached when drift current which is caused by built-in electric field equals to diffusion current (net current is zero). Band bending happens near the interface due to the electron energy change as a function of position caused by the electric field as shown in Figure 1.5a. When the junction is illuminated, photo-excited electrons and holes will be efficiently separated towards n-type semiconductor and p-type semiconductor, respectively. Different from a SEJ, dissimilar behaviors may happen when semiconductor is immersed in different electrolytes. SSJ provides V_{OC} solely depending on Fermi level differences between the two solid semiconductors, so a SSJ can be considered as an external bias powered by solar energy.

The simplest configuration that consists single SSJ is illustrated in Figure 1.5a. In principle, this structure has very little difference to a PVE system. The major differences are whether catalysts are integrated on the semiconductor and whether semiconductor is immersed in the electrolyte. Variants of such configuration that have more tandem junctions connected in series are either positioned "side-by-side", parallel, or monolithic. The advantage of such arrangement is higher efficiency and better flexibility of floating

photovoltage compared to the SEJ. To collect the advantage of both junctions, an SEJ can be integrated to an SSJ as shown in Figure 1.5b, which is known as the PV-PEC configuration. Additional voltage is provided by the PV to bias the photoelectrode for unassisted solar water splitting. This configuration harvest both the high-efficiency of a PV cell and the great stability of wide-bandgap semiconductor, such as oxides. In this design, a recombination layer is required as the interlayer in the monolithic tandem junction devices.

1.4.3 Solar-to-fuel conversion efficiencies

The key factor that makes the difference between fundamental research and a thriving technology that can be considered as one of the solutions against energy problems is efficiency. To assess the solar-to-fuel conversion efficiency of devices, various metrics are created.

The most common technique is to measure the photocurrent density, j_{ph}, of the photoelectrodes during the potential scanning in a certain potential window. Usually, a potentiostat is used to record the j_{ph} as a function of applied potential (E) with the configuration of Figure 1.4a. In the j_{ph}-E plot, one can find information of onset potential, E_{on}, and plateau current density j_{max}. If certain calculation is applied, the applied-bias photon-to-current efficiency (ABPE) can be obtained with the following equation:

$$\eta_{\mathrm{ABPE}} = \frac{j_{ph}(V_{redox} - V_{app})}{P_{in}}$$

where V_{redox} is the redox potential for water oxidation (+1.23 V versus reversible hydrogen electrode, RHE); V_{app} is the voltage betwwen the working electrode and counter electrode, and P_{in} is the incident light power. In this measurement, the real chemical product is not directly measured, so there's possibility that the recorded current density consists corrosion current and/or redox current of other species in the electrolyte or on the electrodes. The effective way to distinguish that is to measure the Faradaic efficiency (η_F) with the equation as follows:

$$\eta_F = \frac{n_{H2} \times 2 \times F}{Q_{WE}}$$

The n_{H2} is the total amount of hydrogen usually measured by gas chromatography; Q_{WE} is the total charge passed through the working electrode; F is the Faraday constant; Theoretically, the faradaic efficiency should be 100% if all photoexcited electrons and

holes are used to split water. In practice, during the stability test (with chronoamperometry technique), delay or fluctuation may happen due to the formation of bubbles, accumulation in cell headspace or bubble desorption.

Another commonly used metric is the incident photon-to-current efficiency (η_{IPCE}). Still using the configuration in Figure 1.4a, the incident monochromatic light wavelength is varied while fixing the applied potential and recording the current density. η_{IPCE} is calculated as follows:

$$\eta_{\mathrm{IPCE}} = \frac{\frac{j_{ph}}{e} \times \frac{hc}{\lambda}}{P_{in}}$$

where j_{ph} is the photocurrent density at specific incident beam wavelength; e is the charge of an electron; h is the Planck constant; c is the speed of light; P_{in} is the power of incident light with particular wavelength. Despite the influence of applied potential, this metric shows the conversion efficiency dependent on incident photon energy. One can expect the onset wavelength is closely related to the bandgap of a semiconductor, and matching between photocurrent density of the applied potential and integrated wavelength dependent current density. Similar to IPCE, absorbed photon-to-current conversion efficiency (η_{APCE}) is defined as the photon-to-current conversion efficiency based on absorbed light. So η_{APCE} equals to η_{IPCE} divided by the fraction of absorbed incident light.

The last important metric is the solar-to-hydrogen efficiency (η_{STH}) defined as total energy stored over input solar energy. This is relatively true conversion efficiency that usually can not be measured with the half-cell configuration. If a bias is used, the bias input should be excluded when calculating the total energy stored. In most cases, this efficiency is given for unassisted systems which can be obtained by comparing Gibbs free energy of generated hydrogen to solar energy illuminated on the testing area. While the more frequently used variant equation is as follows:

$$\eta_{STH} = \frac{1.23\,V \times j_{ph}}{P_{in}}$$

where 1.23 V corresponds to the Gibbs free energy of the reaction; j_{ph} is the photocurrent density of the whole system; P_{in} is the power of incident light.

1.5 Photoelectrochemical water splitting: Oxide semiconductors[†]

Due to their excellent chemical and electronic properties, metal oxide materials are playing important roles at the beginning of this research area.[12–14] Most of them have excellent chemical stability to endure long-term PEC operation in electrolyte that probably contains acids or alkalis. The high availability and simple fabricating methods have lowered both their cost and difficulty of nano-structuring. As the economic technique for solar water splitting should not be based on the most efficient devices that cost over the odds, developing inexpensive materials that exhibit high performance is more viable for PEC technology to meet the market.

Metal oxides with d^0 band own large bandgap, because their VB is dominated by O $2p$ levels, which makes the valence band relatively lower. Although their large bandgap is limiting the absorption coverage of the solar spectrum, which make them impossible to beat the efficiencies delivered by photovoltaic materials, such as III-V semiconductors and Si,[15–17] their stability grants them the ability to protect other materials from corrosion. Another strategy making oxide semiconductors bandgaps narrower is to dope or create inter-gap defect levels. Finding new oxide materials, such as transition metal oxides that consist of d^n metals are also attractive. It is worth mentioning that much more options are with ternary or even quaternary metal oxides, where more than 200,000 candidates exist.[18] Once the material composition is determined, surface engineering, nano-structuring, junction design and catalyst integration could further enhance light absorption, charge transfer and charge injection. Detailed examples will be explained in the following section.

1.5.1 Oxide photocathodes

Among p-type binary oxide semiconductors, Cu_2O is the most promising semiconductor for solar water splitting. The p-type property is resulted from Cu vacancies.[19] Its valence band is formed by hybridization of Cu $3d$ and O $2p$ bands. At the top of the VB, states are

derived from fully occupied Cu $3d^{10}$, which leads to high mobility.[20] With a direct bandgap of around 2.0 eV, its CB and VB are well straddling the hydrogen evolution and oxygen evolution potentials, resulting in a theoretical current density of 14.7 mA cm^{-2} based on AM 1.5 G solar spectrum.[21] However, the redox potentials of Cu^{I} to Cu^{II} and Cu^{I} to Cu^{0} lie between the CB and VB, so when Cu_2O is illuminated and in contact with H_2O, photo-excited electrons and holes are prone to corrode itself instead of splitting water. Various works are carried out trying to regulate its crystal phases and structures via different preparation methods to achieve better stability, but none of them achieved satisfying results.[22]
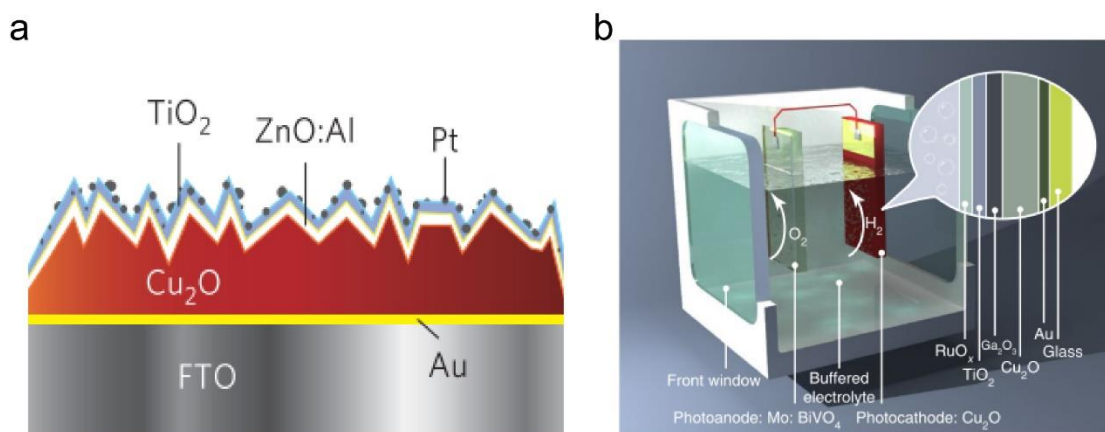
Figure 1.6 | a, Schematic representation of the photocathode structure. b, Illustration of the unbiased all-oxide tandem solar water split, consisting Cu_2O as the photocathode and Mo-doped $BiVO_4$ as the photoanode. Reproduced by permission from Springer Nature (Copyright 2018, Springer Nature).[21,25]

Seminal work was done by Paracchino et al, who deposited aluminum doped zinc oxide (AZO) and titanium oxide (TiO_2) with atomic layer deposition (ALD), as shown in Figure 1.6a.[21] As an important transparent conductive oxide (TCO), AZO functions as the electron transporting layer which helps to efficiently separate the photo-generated charges and reduces photo-degradation. In the meantime, the TiO_2 protection layer insulates the Cu_2O from electrolyte. The two main problems for Cu_2O degradation were greatly alleviated, resulting in a 7.6 mA cm^{-2} at 0 V vs. RHE under simulated AM 1.5 G sunlight. 20 minutes of stable operation was attained with gas quantification. Since most previous Cu_2O photocathodes are not protected, this stands as the first case where the current is almost purely provided by photocurrent. Later works focusing on improving the stability of the system replaced the Pt catalyst and the TiO_2 protection layer. RuO$_x$ was used as a substitute of Pt to improve the adhesion of catalyst on electrode surface.[23] With better attachment and uniform coating on the TiO_2 layer, more than 25 hours of stable operation was

achieved in pH 5 electrolyte. Earth-abundant catalysts such as NiMo,[24,25] MoS_2[26] and $FeNiO_x$[27] are also applied on Cu_2O photocathodes to cut down the cost. Mayer et al. replaced ALD TiO_2 with ALD SnO_x, where 57 hours of sustained photoelectrochemical water splitting was obtained, maintaining 90% of its initial photocurrent.[28] Carbon was coated on Cu_2O photocathodes with facile solution process and subsequent carbonization without co-catalyst, which resulted in similar stability with ALD layers protected electrodes. [29]

The electron diffusion length of solution-processed Cu_2O is estimated to be less than 100 nm.[30] In terms of efficient electron injection to the catalysts while maximizing the harvest of photons, nanowire is an eminent option.[25,29,31] The electrons only have to travel the radius of the wire, in the meantime, as holes have relatively longer diffusion length, they can still be efficiently collected along the wire at the back contact. Besides, the photons have better opportunities to be absorbed in the nanowire forest, which harvests both reflected and scattered light. Additionally, catalyst working loading per area is reduced due to larger actual area, which can be interpreted to more active catalyst if area is normalized. Another improvement was first demonstrated during the development of Cu_2O photovoltaic cells.[32] Gallium oxide layer was applied on Cu_2O to buffer the electron conduction which greatly enhanced the photovoltage. By integrating the gallium oxide, the Cu_2O radial junction was formed giving around 10 mA cm^{-2} current density at 0 V vs. RHE, which represents the best-performing oxide photocathodes.[25] Conformal NiMo catalyst was coated with underpotential electrodeposition which allows the operation of the electrode in alkaline electrolyte for 8 hours. Finally, an unassisted all-oxide tandem was built with $Mo:BiVO_4$ photoanode which delivers ~3% η_{STH}, as shown in Figure 1.6b.
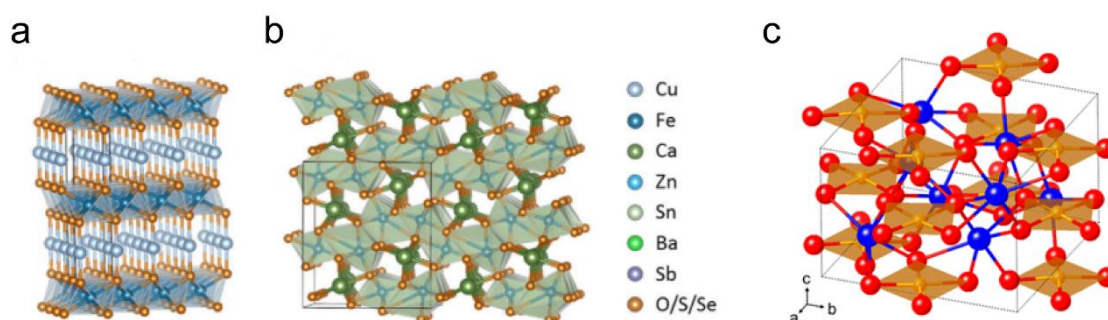

Figure 1.7 | Crystal structures of a, $CuFeO_2$, b, $CaFe_2O_4$ c, $CuBi_2O_4$, where Bi, Cu and O atoms are represented by blue, orange and red sphere, respectively. Reproduced with permission (Copyright 2018, Wiley-VCH).[130] Reproduced with permission (Copyright 2018, American Chemical Society).[45]

Copper-based delafossites constitute one big variety of photocathode materials, such as $CuFeO_2$,[33–36] $CuRhO_2$,[37] $CuCrO_2$,[38] $CuAlO_2$[39] and $CuGaO_2$,[40] and they are exhibiting good stability as photocathode materials. Among them, $CuFeO_2$ is interesting as it's made of cheap and abundant elements on earth. It's crystal structure features Cu^{+1} cations forming layers between face-sharing FeO_6 octahedra units (Figure 1.7a).[18] It has relatively small bandgap of 1.5 eV, which has favorable conduction band for water reduction. A simple sol-gel process could form a pure and high-quality film giving sacrificial photocurrent onset at 0.9 V and density of 1.5 mA cm^{-2} at 0.35 V vs. RHE.[33] By hybrid microwave annealing post-treatment, Lee's group enhanced the performance by 4 times compared to conventional thermal annealing, which gives doubled photocurrent density.[41] Moon's group prepared $CuFeO_2$ coated microsphere photocathodes.[42] With precise control over the dimension of microsphere, the novel photonic crystal structure is able to amplify the light absorption thus the photocurrent. Later, they further improved the photocathode by building a homocentric heterojunction with $CuAlO_2$ where 9-fold photocurrent enhancement was achieved.[43] With the assist of time-resolved microwave conductivity (TRMC), extreme ultraviolet (XUV) and optical spectroscopy, the dynamics of electrons and holes are explained, showing that reducing the surface recombination could further enhance the performance.

With a high-throughput screening system, $CuBi_2O_4$ was found to be a new material with high visible-light responsiveness.[44,45] $CuBi_2O_4$ is a p-type semiconductor with bandgap of 1.6-1.8 eV which corresponds to a maximum theoretical j_{ph} of 20 mA cm^{-2}. Its crystal structure is formed by stacks of $[CuO_4]$ that are connected to Bi (Figure 1.7c). Cu vacancies are the origin of its p-type nature.[18] Though its mobility is relatively low of 10^{-3} cm^2 V^{-1} s^{-1}, the flatband potential is at about 1.26-1.29 V vs. RHE, which is quite positive compared to that of other p-type photocathodes.[45] After finding the high photoactivity of $CuBi_2O_4$ in 2007, various methods are explored to synthesize it such as electrodeposition,[46–48] low-temperature crystal growth,[49] hydrothermal reactions[50] and spray pyrolysis.[51] Lei et al. fabricated $CuBi_2O_4$ on gold coated FTO, which enhanced the crystal quality and reduced the resistance, thus achieved a photocurrent density of -1.2 mA cm^{-2} at 0.1 V vs. RHE.[48] Choi et al. doped $CuBi_2O_4$ with Ag via a two-step electrodeposition which increased the hole concentration thus the hole transport.[52] A stable photocurrent density of 1.3 mA cm^{-2} at 0.6 V vs. RHE was maintained for 2 hours using H_2O_2 as the electron scavenger. While the accumulated electrons at the electrode surface during the water reduction without electron scavenger renders less stable performance. Krol et al. did a thorough study on

$CuBi_2O_4$ and determined the key opto-electronic parameters.[45] They found that the limiting factors for $CuBi_2O_4$ photocathodes are poor light absorption, short charge diffusion length and weak charge injection at the electrode surface. Strategies such as using a nanostructured scaffold and protection layer could benefit the conductivity and stability respectively. Later they fabricated a uniform $CuBi_2O_4$ film showing the current benchmark photocurrent density of 2.0 mA cm^{-2} at 0.6 V vs. RHE under AM 1.5 G illumination.[51] The unassisted water splitting tandem device with configuration in Figure 1.4b was assembled with TiO_2 photoanode in Chu's group.[53]

The spinel ferrites with general formula of AB_2O_4, where A and B are of +2 and +3 respectively, represent an emerging class of ternary oxide photoelectrode materials (Figure 1.7b). Among them, $CaFe_2O_4$ is one of the most studied p-type semiconductors. Its relatively narrow bandgap of 1.9 eV enables the absorption of most part of the visible light. As the CB and VB are straddling the hydrogen evolution and oxygen evolution potentials, it is considered one of the most promising photocathode materials.[54] The pioneering work was done by Matsumoto et al. who characterized the electronic properties and used $CaFe_2O_4$ for PEC water splitting in 1987.[55] Though it's not showing satisfying performance due to strong bulk recombination, this thorough work revealed most important semiconductor parameters of $CaFe_2O_4$ as an strong candidate of photocathode material. Their following work improved the photoactivity of $CaFe_2O_4$ by doping it with Na^+ and Mg^{2+} to improve the conductivity and explained the degradation mechanism.[56] Later doping of Au, CuO and Ag was attempted.[57] Among them, carrier mobility of the semiconductor was improved by Ag doping due to relaxed distorted crystal lattice, resulting in a 23-time photocurrent enhancement. Ida et al. fabricated an oriented $CaFe_2O_4$ via a solution process.[54] Furthermore, an unassisted tandem cell was built in their group with a TiO_2 photoanode showing the potential of this photocathode material. A detailed theoretical and experimental electrochemical impedance spectroscopic study was done on $CaFe_2O_4$ pointing out that the bulk recombination is dominating.[58] Establishing a solid-state junction for efficient charge separation could further improve charge transfer therefore the performance.

Other copper-based materials such as vanadates,[59] niobates,[60,61] and tantalates[62,63] are also attracting a lot of interest due to suitable band energies and good stability.[64]

1.5.2   Oxide photoanodes

As the main characters of the old photocatalysis and photoelectrochemical water splitting

field, the wide bandgap metal oxides have provided researchers an important and accessible platform for studying preparation methods, devices and photoelectrochemical properties of semiconductors. The most studied ones are TiO_2,[65-69] ZnO,[70,71] $SrTiO_3$[72] and Ta_2O_5[73], which own bandgaps between 3.0 eV and 3.9 eV. In the case of TiO_2, due to the large band gap, the theoretical η_{STH} is ~1% according to Shockley-Queisser limit (Figure 1.8a).[74,75] Researchers have improved its efficiency considerably via nano-structures which offers the advantages of better light absorption and efficient charge injection. The most famous ones are nanotubes and nanowires.[65-68,70,71,76] In the meantime, the electronic properties are not favorable. In the case of TiO_2, the diffusion length is found to be ~10 nm, which is about 1000-fold worse than most PV materials.[74] Despite their unfavorable bandgaps and poor electronic properties, their excellent stability, easy synthetic methods and low cost have granted them indispensable roles such as protection layers,[21] electron conductors[77] and scaffold.[77]

Due to its great abundance and proper bandgap, hematite with diverse chemical structures and properties are synthesized. Its 2.1 eV bandgap along with extraordinary chemical stability attracted a lot of attention. Sharing the common advantage of stable binary oxide, hematite has been readily synthesized via various methods including ballistic deposition,[78,79] atmospheric pressure chemical vapor deposition (APCVD),[80-82] solution processes,[83] thermal annealing,[84,85] atomic layer deposition,[86,87] and hydrothermal reactions.[88] However, like TiO_2, hematite also shows disadvantages such as low electric conductivity, short carrier diffusion length (2-20 nm) and poor oxygen evolution catalytic activity.[89] Most of the efforts are made to nanostructure hematite photoanodes. The film prepared by APCVD resulted in a highly developed dendritic film with roughness factor of 21.[80] The photocurrent density is around 2.2 mA cm^{-2} at 1.23 V vs. RHE, which created a benchmark for hematite photoanodes. By optimizing the depositing angle of reactive ballistic deposition, porous nanocolumnar hematite film was obtained.[78] Though with relatively lower performance, mesoporous hematite photoanode is obtained by simple solution-based colloidal methods.[83] All of the methods are capable of the precisely composition control, thus creating an opportunity for doping.[79,90-92] The PEC performance of hematite photoanodes can be enhanced by increasing donor density. While it is widely accepted that increasing majority carrier concentration leads to improved charge transport, there is a balance between extrinsic donor density and trap concentration. Therefore, researchers applied surface passivation as an effective approach to reduce surface traps thus suppressing surface recombination.[90,93] Similarly,

facilitating the charge injection with oxygen evolution catalysts could also deplete the separated charges quickly.[94,95] A delicate integration of above mentioned strategies pushed the photocurrent density of hematite over 3 mA cm^{-2} at 1.23 V vs. RHE under AM 1.5 G spectrum illumination (Figure 1.8b).[82]
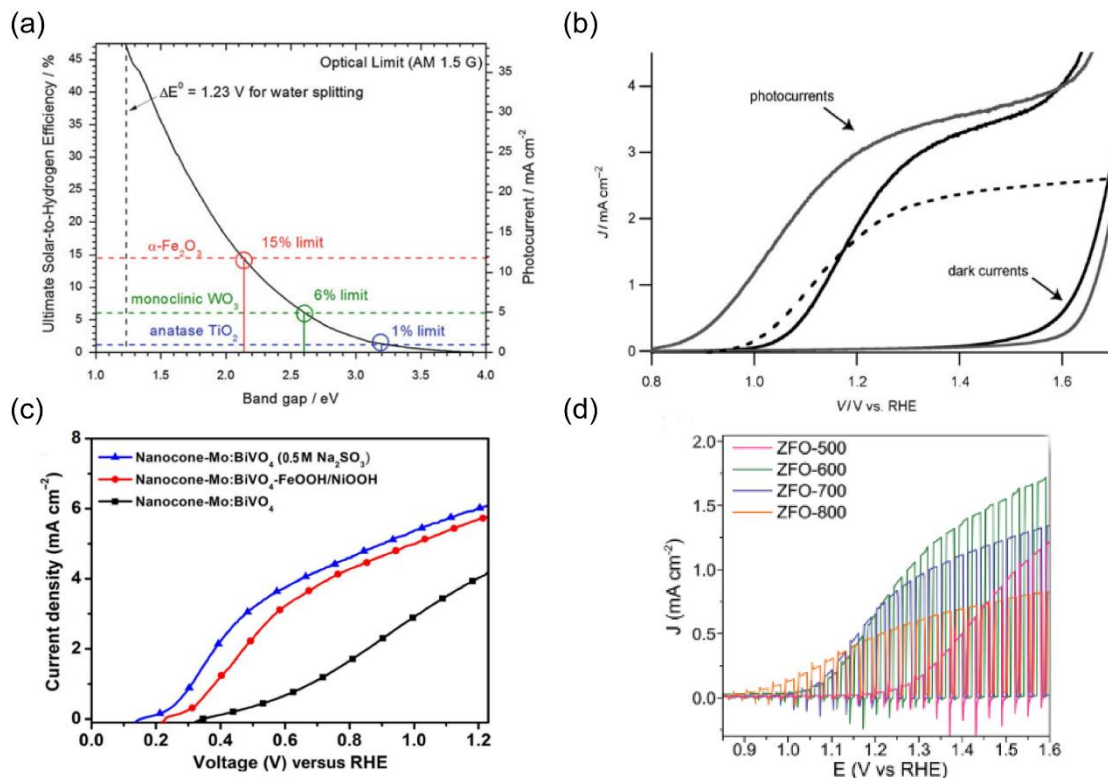
Figure 1.8 | a, Theoretical maximum solar-to-hydrogen conversion efficiency (left axis) and photocurrent density (right axis) as a function of semiconductor bandgap. The theoretical maximum η_{STH} efficiencies only considers the first thermodynamic principle of energy conservation and is analogous to the ultimate efficiency of a p-n junction solar cell by Schockley and Queisser. Reproduced with permission (Copyright 2018, Springer Nature).[75] b, PEC performance of the unmodified hematite photoanode (solid black trace), and the same anode that was functionalized with IrO$_2$ nanoparticles (solid gray trace). Reproduced with permission (Copyright 2018, Wiley-VCH).[82] c, j-V curves of the nanocore Mo:BiVO$_4$ film measured in phosphate buffer solution containing 0.5 M Na$_2$SO$_3$ and the nanocone Mo:BiVO$_4$/Fe(Ni)OOH film measured in phosphate buffer solution. Reproduced with permission (Copyright 2018, Springer Nature).[131] (d) Linear scanning j-V curves of ZFO photoanode in 1 M NaOH under intermittent 1 sun illumination (100 mW cm^{-2}). Reproduced with permission (Copyright 2018, Wiley-VCH).[132]

Since the first work on n-type BiVO$_4$ by Kudo et al.,[96] there are more than 300 publications on using BiVO$_4$ for photocatalysis and photoelectrochemical water splitting.[18,64] Among the 3 polymorphs of it, the most active phase is clinobisvanate with monoclinic

structure.[97] $BiVO_4$ has a direct bandgap of 2.3-2.5 eV, which is absorbing most of the visible light spectrum to 530 nm. The conduction band of $BiVO_4$, which is formed by overlapping Bi $6p$ and V $3d$-O $2p$ bands, is very close to the hydrogen evolution potential, but it's a good photoanode for water oxidation. Like most of the oxide photoelectrodes, $BiVO_4$ is suffering from its poor charge transport properties. To efficiently utilize photo-generated charges, nanostructured $BiVO_4$ was fabricate to shorten the necessary diffusion length. Mullins et al. synthesized nanostructured $BiVO_4$ by reactive ballistic deposition.[98] They found that with larger glancing incident angle, the photoactivity varies because of surface structures and morphology. Through a seed-mediated solution growth, ordered arrays of pyramid-shaped $BiVO_4$ was achieved.[99] Another strategy for solving the charge transport problem is to dope $BiVO_4$. Typical effective donors are Mo^{6+} or W^{6+} which are replacing the V^{5+} to increase electronic conductivity.[100–102] Another similar way is to create more defects in $BiVO_4$ with hydrogen treatment.[103] Li's group applied hydrogen treatment, which increses the donor density, and achieved 3.5 mA cm^{-2} photocurrent density at ~1.2 V vs. RHE. Either by building a gradient dopant concentration in the out-of-plane direction, i.e. a distributed n^+-n homojunction,[103] or by fabricating a type II heterojunction to assist charge separation,[104] the performance has been greatly enhanced.[105–107] Another limiting factor for $BiVO_4$ PEC performance is the slow oxygen evolution kinetics. To address the issue, co-catalysts such as $NiFeO_x$,[108] CoO_x[109] and CoP[101] are used to improve charge injection. However, despite the initial intention, the roles of the catalysts have led to an ongoing debate. Similar to the discussion on hematite, the catalyst accelerate the oxygen evolution reaction and also functions to passivate surface traps.[110,111] Moreover, the competition between water oxidation and charge recombination complicates the discussion. Nevertheless, the great advance of $BiVO_4$ photoanode has prompted several PV-PEC tandems which gives exciting η_{STH} values.[106,112,113] With the best-performing $BiVO_4$ photoanode which delivers ~5.82 mA cm^{-2} photocurrent density at 1.23 V vs. RHE, a tandem with perovskite solar cell delivers 6.2% η_{STH} efficiency (Figure 1.8c).

As an n-type spinel ferrite counterpart of $CaFe_2O_4$, $ZnFe_2O_4$ has been studied as composite component before being used independently as photoanode materials.[114–116] It has a bandgap of 1.9-2.1 eV, which corresponds to a maximum theoretical photocurrent density of ~14.5 mA cm^{-2}. Though it generally exhibits more cathodic onset compared to hematite, preparation methods are limited due to the high crystalizing temperature. Wijayantha et al. obtained nanostructured $ZnFe_2O_4$ thin film via aerosol-assisted chemical vapor deposition (AACVD).[117] Lee's group prepared $ZnFe_2O_4$ nanorods by a simple solution

method.[118] A demonstration of sequential atomic layer deposition and following annealing allow uniform coating of zinc ferrite on a macroporous scaffold.[119] However their photocurrent densities are below 1 mA cm^{-2}. Post-treatment has been applied to enhance the performance. Lee et al. have found that a thermal treatment in hydrogen environment or vacuum can boost the photoactivity up to 20 times.[118] By hybrid microwave annealing at 550 ^{o}C, they converted ZnO-coated FeOOH nanorods to $ZnFe_2O_4$, and the photocurrent density was improved by 15 times.[120] Doping was also applied in Zou's group via spray pyrolysis.[121] Because of the enhanced carrier concentration as well as the carrier transport, the photocurrent of Ti^{4+} doped $ZnFe_2O_4$ photoanode was 8.75 times higher compared to that of the pure $ZnFe_2O_4$ photoanode. Sivula's group found the link between degree of cation disorder and PEC performance. By adjusting the forming temperature which has significant impact on crystal structure, they obtained a benchmark photocurrent density of 1.0 mA cm^{-2} at 1.23 V vs. RHE with nickel-iron oxide facilitating the OER performance (Figure 1.8d).

1.6 Methods

1.6.1 Solar simulator

Most photoelectrochemical tests consist of devices such as solar simulators, PEC testing cells and potentiostat. As one of the most important lab devices, solar simulators require careful maintenance and rigorous calibrations. Only by following a careful calibrating protocol, can a researcher gain reproducible results which become legal references.
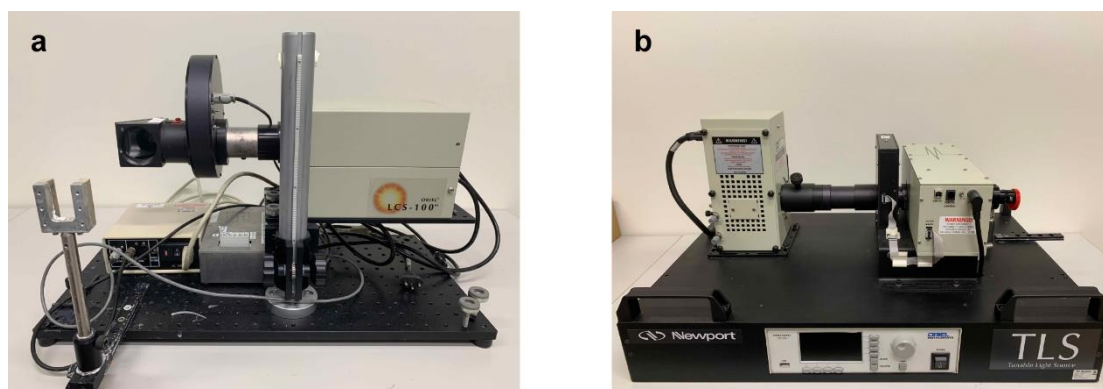

Figure 1.9 | a, Photo of Newport LCS-100 small area solar simulator mounted on an optical breadboard. b, Photo of Newport TLS-300XU monochromator.

The goal is to create a light source which owns spectrum as close as possible to the real sunlight spectrum. Compared to the standard AM 1.5 G solar spectrum, arc sources usually

provide excessive ultraviolet photons while LED array light sources show infrared tails.[122] Therefore, filters are necessary to block unwanted part of the simulator spectrum. The solar simulator we apply is a xenon lamp with a built-in AM 1.5 G filter, Figure 1.9a. The light source provides ABB class certification defined by ASTM and IEC standards. To provide rigorous results, it is necessary to calibrate the light source depending on the bandgap of the studying semiconductor. Though the spectrum of solar simulator is very similar to the AM 1.5 G spectrum, the troughs resulted from absorption and scattering of air molecule and dust could still make a difference. For example, if a solar simulator was calibrated for the study of a 1.25 eV bandgap semiconductor, as the first significant trough lies at around 900 nm due to oxygen and water absorption, the researcher would decrease the light intensity by certain amount to compensate. However, if the solar simulator was used then for studying a 1.35 eV bandgap material, the compensation made before could underestimate the performance of this material.

A convenient way to make the calibration requires a certified Si diode which has a test report with the responsivity (R) as a function of wavelength. Then the quantum efficiency can be calculated through the following equation:

$$R = \eta \frac{e}{h\nu}$$

where the $h\nu$ is the photon energy, e is the elementary charge and η is the quantum efficiency. The total current can be found by the integration of multiplied results of the quantum efficiency and photon numbers at each wavelength (depending on the data resolution, one can choose the interval of 1 nm, 5 nm or 10 nm). The photon numbers as a function of wavelength can be converted from the AM 1.5 G spectrum. The wavelength range can be determined from the targeted semiconductor bandgap.

As the certified Si diode is expensive and fragile, the secure way for calibration in a lab is to use other normal Si diodes and calibrate them with the certified one and a monochromator (Figure 1.9b). The monochromator is the key instrument for measuring IPCE as mentioned in previous sections. By measuring the IPCE of both certified diode and a normal calibration diode, the IPCE or responsivity of the new calibration diode can be obtained. The calibration process remains the same. It is noteworthy that since excessive UV is produced by the solar simulator even with AM 1.5 G filter, all diodes should be test with casing that includes a filter, such as KG 3 filter.

1.6.2   Photoelectrochemical tests

The core tests for photoelectrodes are photoelectrochemical tests which include several three-electrode configuration tests that show performance-related results and stability tests that resemble the on-site operation. All PEC tests involve the PEC cell as the hub for all elements. The most frequently used cell is called "Cappuccino" cell designed at EPFL (Figure 1.10).[123,124]

Three electrodes include a reference electrode, a working electrode (the studying photoelectrode) and a counter electrode. Illumination on the clipped photoelectrode was allowed integrated quartz windows in the front and back, which has high transparency across the solar spectrum (Figure 1.10a, b). The material chosen for the cell was polyether ether ketone (PEEK) which is acid and alkali-resisting and can be mechanically processed easily. The cell was designed to hold around 50 mL of electrolyte, as the electrolyte can function as a filter and will start absorbing visible light if it's thick.[125] Generally, the criteria for choosing proper electrolyte mostly relies on the stability of the photoelectrode. Pourbaix diagrams which show stable phases with potential as a function of pH values are
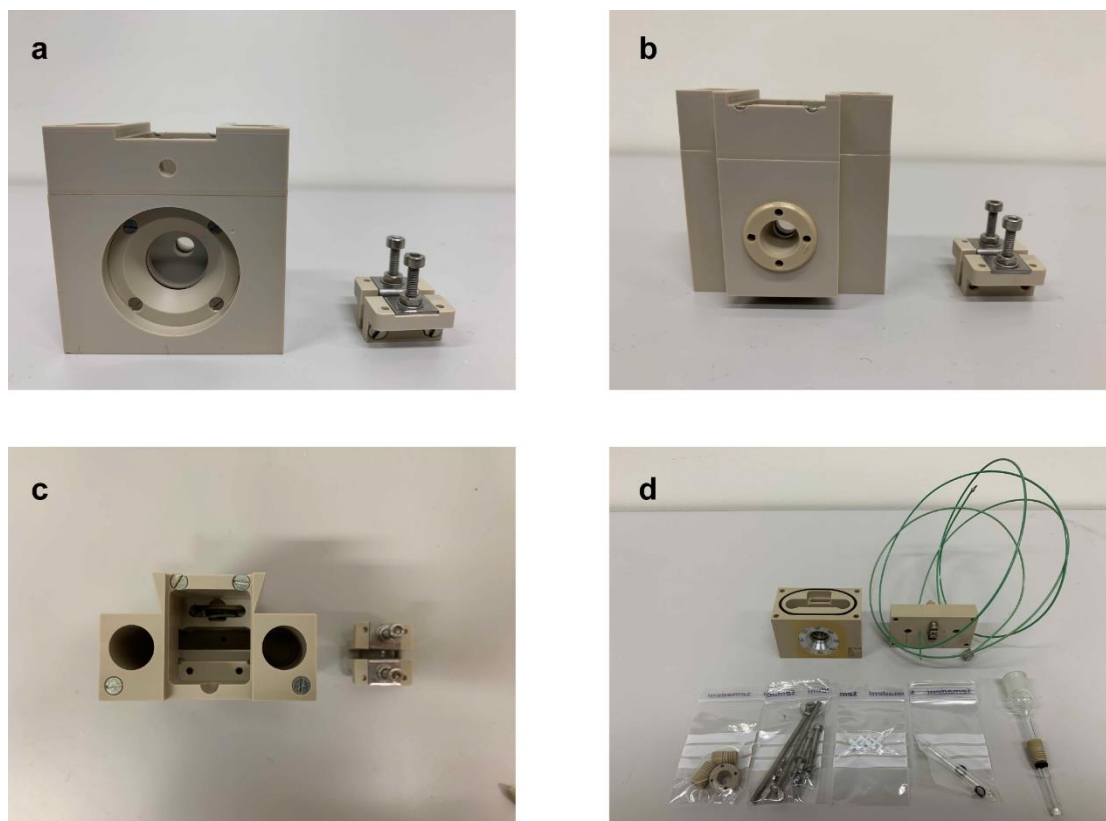

Figure 1.10 | a, Front view of Cappuccino PEC cell. b, Front view of Cappuccino PEC cell. c, Front view of Cappuccino PEC cell. d, Gas-tight Cappuccino PEC variant cell with accessories.

helpful. Considering the favored kinetics for water splitting reactions in acidic or alkaline electrolyte, one could choose more extreme pH electrolyte with viable hydrogen evolution or oxygen evolution catalysts. If neutral or near-neutral electrolytes are applied, a buffer solution could enhance the mass transport during PEC tests. The reference electrode should be selected properly depending on the electrolyte to avoid damage-resulted inaccuracy. The windows opened at both sides allow convenient study on front- and back-illumination, which may influence charge collection efficiencies. All electrodes are spatially separated and are inserted in the slots as shown in Figure 1.10c. The photoelectrode is clamped by the small holder in the right part of Figure 1.10c and inserted in the center of the cell. Contact was made between the titanium jacket of the holder and the conductive substrate of the photoelectrode. During stability tests, stirring is sometimes necessary as accumulated bubbles on the electrode surface will cause great resistance and scatter incident light simultaneously. The stir bars with 80 mm length could be put in the round slot inside the cell directly under the front window. The back window was designed to be replaceable. One could put another photoelectrode for tandem tests in the slot where back window was placed.

It is indispensable to quantify gas evolution during long-term stability tests especially for new photoelectrode materials, as the current recorded by potentiostat could be contributed by corrosion current of the photoelectrodes. In this case, faradaic efficiency will be tested with the gas-tight variant of Cappuccino cell (Figure 1.10d) connected to an in-situ gas chromatography (GC). Due to the limit of GC sensitivity, the photoelectrode should be able to provide stable photocurrent for at least tens of minutes depending on the photocurrent density. The calculated faradaic efficiency could fluctuate considerably due to bubble formation, gas accumulation in the cell headspace. Given enough testing duration, the faradaic efficiency will be close to 100% if the current is photocurrent. However, gas crossover could happen to decrease the efficiency even though the only faradaic reaction is water splitting. This could happen in cells that have close working and counter electrodes. A cell designed with membranes could avoid this problem.

1.6.3   Atomic layer deposition

ALD is a chemical vapor deposition technique which separate the normally mixed reactants into sequential exposures. Various materials now can be prepared by ALD including oxides, chalcogenides, halides and metals.[126,127] ALD offers excellent conformity with extreme thickness precision down to Angstrom level. The ability to switch precursors

during deposition can effectively control the composition in applications such as doping.[128] These unique features have made ALD a powerful tool in research.
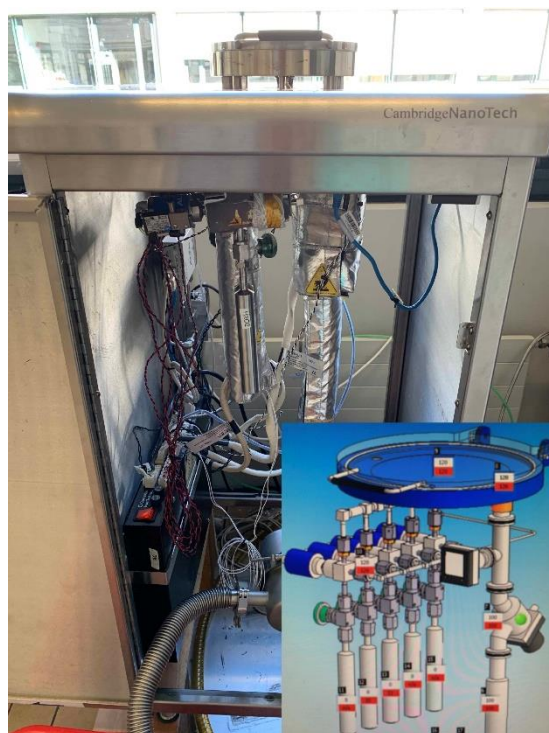
Figure 1.11 | Photo of a Savannah S100 thermal ALD from Veeco (Previous Cambridge Nanotech) with inset of the system illustration.

The ALD system we use for conformal junction construction is a thermal ALD as shown in Figure 1.11. The chamber is kept in vacuum to allow precursor desorption. Precursors are filled in stainless steel cylinders with a below valve. If necessary, heating jackets are equipped to provide precisely controlled heating for precursor, chamber and exhausting pipes. Central command boxes provide control on the electronic valves for particular pulse time and complicated sequences. Metal precursors are usually in bond with alkyls, halides, alkoxides and other radicals to have volatile properties. For solid precursors, the reactants are often heated to allow enough vapor generated during each deposition gap. Bubble kit that flows inert carrier gas into the precursor and then pumped into the chamber is also a good option. This allows better control on the pulsed precursor amount. However, overheating could decompose the precursor. In practice, precursor temperature will play an important role in having successful and reproducible depositions. Apart from the viable precursor temperature window, as the chamber temperature should be higher than that of precursor temperature to avoid condensation while the substrates have their limits

to the upper limit of the chamber temperature. A compromise is sometimes necessary.
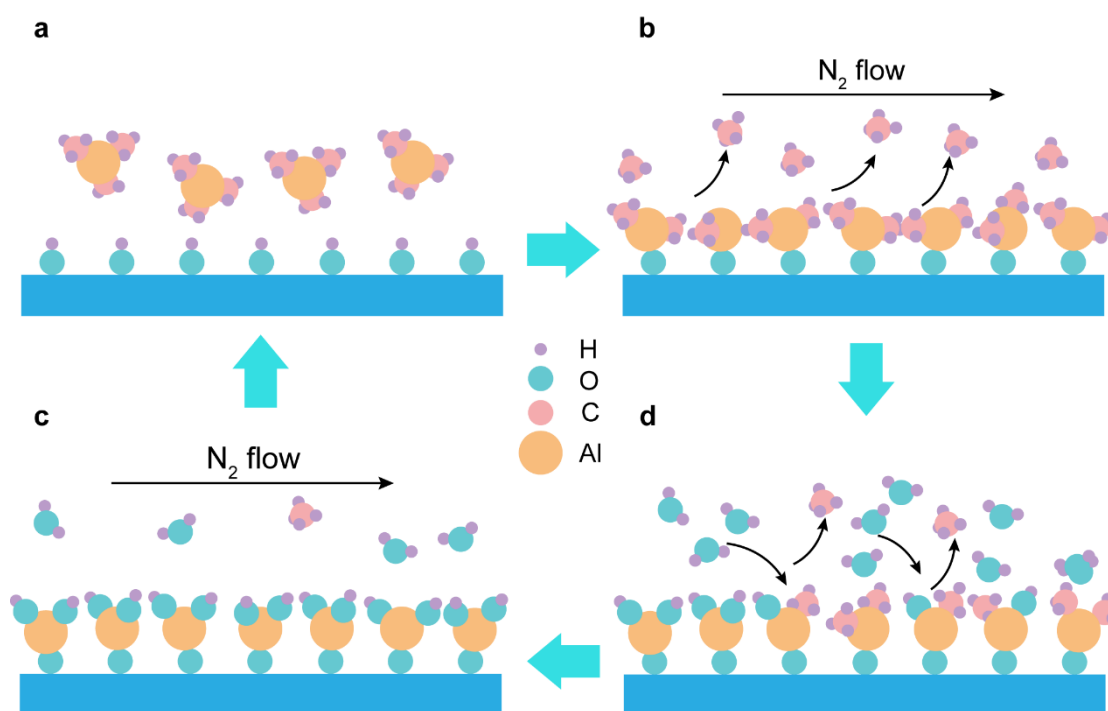
Figure 1.12 | Illustration on atomic layer deposition mechanism using Al_2O_3 deposition with Trimethylaluminum and H_2O as an example.

An ALD cycle was illustrated in Figure 1.12 taking the most studied Al_2O_3 deposition using trimethylaluminum (TMA) and water as an example. In Figure 1.12a, TMA vapor was pulsed into the chamber. If the substrate has hydroxyl terminated surface, TMA will be chemically absorbed and bonded in the first layer. As the chamber is heated in vacuum, with the help of continuous nitrogen flow, excessive layers absorbed with Van der Waals's force will be carried away, resulting in a monolayer of absorbed TMA. In the second step of a cycle in Figure 1.12d, oxidant (water) was pulsed into the chamber which will react with chemisorbed TMA and generate methane molecules. Excessive water and methane molecules are again carried away by nitrogen flows, leaving monolayer of Al_2O_3 with hydroxyl end for next cycle of deposition. Since the deposition is theoretically single layer deposition, the growth rate per cycle is usually less than 1 nm.[129] In the case of deposition on high-aspect ratio materials, exposure mode is applied. To allow penetration of precursor molecules into the deepest corner of the structured material, pump was blocked by an electronic valve to allow immersion of the substrate in precursor atmosphere instead of instant exposure to vacuum. The properties of the resulted coating could vary a lot depending on the oxidant and chamber (substrate) temperature. Growth rate could also be influenced by these parameters. To confirm the uniform coating of

wanted layers, testing wafers are usually applied as substrates, and the thicknesses of coated layers at various testing points in the chamber should be checked using ellipsometry or cross-section SEM.

1.7 References

(1) B. L. D. M. Brücher. Science Belongs to No One One—and to Everyone. *4Open* **2017**, *1*, E1.

(2) Internation Energy Agency. *Word Energy Balances: Overview. 2018* **2018**.

(3) International Energy Agency. *CO₂ Emissions from Fuel Combustion 2018: Overview*. **2018**.

(4) R. Buckley. Climate Change. *Adventure Tour. Manag.* **2010**, 123–135.

(5) M. Morris, C., Pehnt. *The Energy Transition*; 2014.

(6) H. P. Eugster; R. J. Spencer; I.-M. Chou; M. Sato. Fluid-Mineral Interactions: A Tribute to Thermochemistry of the Formation of Fossil Fuels; 1990.

(7) G. Bauer. Photovoltaic Solar Energy Conversion; 2012.

(8) G. N. Tiwari; A. Tiwari; Shyam. Handbook of Solar Energy: Theory, Analysis and Applications (Energy Systems in Electrical Engineering); 2016.

(9) U. Aswathanarayana. *Electricity Systems*; 2010.

(10)   G. Zini; P. Tartarini. Solar Hydrogen Energy Systems: Science and Technology for the Hydrogen Economy; 2012; Vol. 9788847019.

(11)   *Solar Hydrogen Generation*; Rajeshwar, K., McConnell, R., Licht, S., Eds.; Springer New York: New York, NY, 2008.

(12)   A. Fujishima; K. Honda. Electrochemical Photolysis of Water at a Semiconductor Electrode. *Nature* **1972**, *238* (5358), 37–38.

(13)   S. N. Agbo; T. Merdzhanova; S. Yu; H. Tempel; H. Kungl; R. A. Eichel; U. Rau; O. Astakhov. Photoelectrochemical Application of Thin-Film Silicon Triple-Junction Solar Cell in Batteries. *Phys. Status Solidi Appl. Mater. Sci.* **2016**, *213* (7), 1926–1931.

(14)   M. G. Walter; E. L. Warren; J. R. McKone; S. W. Boettcher; Q. Mi; E. A. Santori; N. S. Lewis. Solar Water Splitting Cells. *Chem. Rev.* **2010**, *110* (11), 6446–6473.

(15)   A. Heller. Hydrogen Evolving Solar Cells. *Catal. Rev.* **1984**, *26* (3–4), 655–681.

(16)   J. Jia; L. C. Seitz; J. D. Benck; Y. Huo; Y. Chen; J. W. D. Ng; T. Bilir; J. S. Harris; T. F.

Jaramillo. Solar Water Splitting by Photovoltaic-Electrolysis with a Solar-to-Hydrogen Efficiency over 30%. *Nat. Commun.* **2016**, *7*, 13237.

(17)   J. D. Prange; P. C. McIntyre; M. Gunji; C. E. D. Chidsey; S. Dühnen; Y. W. Chen; Y. Park. Atomic Layer-Deposited Tunnel Oxide Stabilizes Silicon Photoanodes for Water Oxidation. *Nat. Mater.* **2011**, *10* (7), 539–544.

(18)   K. Sivula; R. Van De Krol. Semiconducting Materials for Photoelectrochemical Energy Conversion. *Nat. Rev. Mater.* **2016**, *1* (2).

(19)   J. Ghijsen; L. H. Tjeng; J. van Elp; H. Eskes; J. Westerink; G. A. Sawatzky; M. T. Czyzyk. *Electronic Structure of Cu_2O and CuO*; 1988; Vol. 38.

(20)   M. Nolan; S. D. Elliott. The P-Type Conduction Mechanism in Cu_2O: A First Principles Study. *Phys. Chem. Chem. Phys.* **2006**, *8* (45), 5350–5358.

(21)   A. Paracchino; V. Laporte; K. Sivula; M. Grätzel; E. Thimsen. Highly Active Oxide Photocathode for Photoelectrochemical Water Reduction. *Nat. Mater.* **2011**, *10* (6), 456–461.

(22)   Q. Huang; Z. Ye; X. Xiao. Recent Progress in Photocathodes for Hydrogen Evolution. *J. Mater. Chem. A* **2015**, *3* (31), 15824–15837.

(23)   M. Stefik; M. Graetzel; M. Schreier; J. Azevedo; S. D. Tilley. Ruthenium Oxide Hydrogen Evolution Catalysis on Composite Cuprous Oxide Water-Splitting Photocathodes. *Adv. Funct. Mater.* **2013**, *24* (3), 303–311.

(24)   C. G. Morales-Guio; L. Liardet; M. T. Mayer; S. D. Tilley; M. Grätzel; X. Hu. Photoelectrochemical Hydrogen Production in Alkaline Solutions Using Cu_2O Coated with Earth-Abundant Hydrogen Evolution Catalysts. *Angew. Chemie - Int. Ed.* **2015**, *54* (2), 664–667.

(25)   L. Pan; J. H. Kim; M. T. Mayer; M. K. Son; A. Ummadisingu; J. S. Lee; A. Hagfeldt; J. Luo; M. Grätzel. Boosting the Performance of Cu_2O Photocathodes for Unassisted Solar Water Splitting Devices. *Nat. Catal.* **2018**, *1* (6), 412–420.

(26)   C. G. Morales-Guio; S. D. Tilley; H. Vrubel; M. Grätzel; X. Hu. Hydrogen Evolution from a Copper(I) Oxide Photocathode Coated with an Amorphous Molybdenum Sulphide Catalyst. *Nat. Commun.* **2014**, *5* (1), 3059.

(27)   H. Qi; J. Wolfe; D. Fichou; Z. Chen. Cu_2O Photocathode for Low Bias

Photoelectrochemical Water Splitting Enabled by NiFe-Layered Double Hydroxide Co-Catalyst. Sci. Rep. 2016, 6.

(28)   J. Azevedo; S. D. Tilley; M. Schreier; M. Stefik; C. Sousa; J. P. Araújo; A. Mendes; M. Grätzel; M. T. Mayer. Tin Oxide as Stable Protective Layer for Composite Cuprous Oxide Water-Splitting Photocathodes. *Nano Energy* **2016**, *24*, 10–16.

(29)   Z. Zhang; R. Dua; L. Zhang; H. Zhu; H. Zhang; P. Wang. Carbon-Layer-Protected Cuprous Oxide Nanowire Arrays for Efficient Water Reduction. *ACS Nano* **2013**, *7* (2), 1709–1717.

(30)   A. Paracchino; J. C. Brauer; J. E. Moser; E. Thimsen; M. Graetzel. Synthesis and Characterization of High-Photoactivity Electrodeposited Cu_2O Solar Absorber by Photoelectrochemistry and Ultrafast Spectroscopy. *J. Phys. Chem. C* **2012**, *116* (13), 7341–7350.

(31)   J. Luo; L. Steier; M. K. Son; M. Schreier; M. T. Mayer; M. Grätzel. Cu_2O Nanowire Photocathodes for Efficient and Durable Solar Water Splitting. *Nano Lett.* **2016**, *16* (3), 1848–1857.

(32)   Y. S. Lee; D. Chua; R. E. Brandt; S. C. Siah; J. V. Li; J. P. Mailoa; S. W. Lee; R. G. Gordon; T. Buonassisi. Atomic Layer Deposited Gallium Oxide Buffer Layer Enables 1.2 V Open-Circuit Voltage in Cuprous Oxide Solar Cells. *Adv. Mater.* **2014**, *26* (27), 4704–4710.

(33)   M. S. Prévot; N. Guijarro; K. Sivula. Enhancing the Performance of a Robust Sol-Gel-Processed p-Type Delafossite $CuFeO_2$ Photocathode for Solar Water Reduction. *ChemSusChem* **2015**, *8* (8), 1359–1367.

(34)   J. Husek; A. Cirri; S. Biswas; A. Asthagiri; L. R. Baker. Hole Thermalization Dynamics Facilitate Ultrafast Spatial Charge Separation in $CuFeO_2$ Solar Photocathodes. *J. Phys. Chem. C* **2018**, *122* (21), 11300–11304.

(35)   U. Kang; H. Park. A Facile Synthesis of $CuFeO_2$ and CuO Composite Photocatalyst Films for the Production of Liquid Formate from CO_2 and Water over a Month. *J. Mater. Chem. A* **2017**, *5* (5), 2123–2131.

(36)   U. Kang; S. K. Choi; D. J. Ham; S. M. Ji; W. Choi; D. S. Han; A. Abdel-Wahab; H. Park. Photosynthesis of Formate from CO_2 and Water at 1% Energy Efficiency via Copper Iron Oxide Catalysis. *Energy Environ. Sci.* **2015**, *8* (9), 2638–2643.

(37)   J. Gu; Y. Yan; J. W. Krizan; Q. D. Gibson; Z. M. Detweiler; R. J. Cava; A. B. Bocarsly. P-Type $CuRhO_2$ as a Self-Healing Photoelectrode for Water Reduction under Visible Light. *J. Am. Chem. Soc.* **2014**, *136* (3), 830–833.

(38)   S. Saadi; A. Bouguelia; M. Trari. Photocatalytic Hydrogen Evolution over $CuCrO_2$. *Sol. Energy* **2006**, *80* (3), 272–280.

(39)   J. R. Smith; T. H. Van Steenkiste; X. G. Wang. Thermal Photocatalytic Generation of H_2 over $CuAlO_2$ Nanoparticle Catalysts in H_2O. *Phys. Rev. B - Condens. Matter Mater. Phys.* **2009**, *79* (4), 041403.

(40)   A. Renaud; S. Jobic; F. Fabregat-Santiago; I. Herraiz-Cardona; B. Julián-López; L. Cario; S. Giménez; F. Odobel. Hole Conductivity and Acceptor Density of P-Type $CuGaO_2$ Nanoparticles Determined by Impedance Spectroscopy: The Effect of Mg Doping. *Electrochim. Acta* **2013**, *113*, 570–574.

(41)   Y. J. Jang; Y. Bin Park; H. E. Kim; Y. H. Choi; S. H. Choi; J. S. Lee. Oxygen-Intercalated $CuFeO_2$ Photocathode Fabricated by Hybrid Microwave Annealing for Efficient Solar Hydrogen Production. *Chem. Mater.* **2016**, *28* (17), 6054–6061.

(42)   Y. Oh; W. Yang; J. Kim; S. Jeong; J. Moon. Enhanced Photocurrent of Transparent $CuFeO_2$ Photocathodes by Self-Light-Harvesting Architecture. *ACS Appl. Mater. Interfaces* **2017**, *9* (16), 14078–14087.

(43)   J. Tan; Y. Oh; J. Moon; W. Yang; J. Park; H. Lee. Photoelectrodes Based on 2D Opals Assembled from Cu-Delafossite Double-Shelled Microspheres for an Enhanced Photoelectrochemical Response. *Nanoscale* **2018**, *10* (8), 3720–3729.

(44)   T. Arai; Y. Konishi; Y. Iwasaki; H. Sugihara; K. Sayama. High-Throughput Screening Using Porous Photoelectrode for the Development of Visible-Light-Responsive Semiconductors. *J. Comb. Chem.* **2007**, *9* (4), 574–581.

(45)   S. P. Berglund; F. F. Abdi; P. Bogdanoff; A. Chemseddine; D. Friedrich; R. Van De Krol. Comprehensive Evaluation of $CuBi_2O_4$ as a Photocathode Material for Photoelectrochemical Water Splitting. *Chem. Mater.* **2016**, *28* (12), 4231–4242.

(46)   N. T. Hahn; V. C. Holmberg; B. A. Korgel; C. B. Mullins. Electrochemical Synthesis and Characterization of P-$CuBi_2O_4$ Thin Film Photocathodes. *J. Phys. Chem. C* **2012**, *116* (10), 6459–6466.

(47)   Y. Nakabayashi; M. Nishikawa; Y. Nosaka. Fabrication of $CuBi_2O_4$ Photocathode through Novel Anodic Electrodeposition for Solar Hydrogen Production. *Electrochim. Acta* **2014**, *125* (3), 191–198.

(48)   S. Qu; Y. Yang; Y. Lei; Z. Wang; N. Nasori; D. Cao; L. Wen; Y. Mi; Z. Wang. P-Type $CuBi_2O_4$: An Easily Accessible Photocathodic Material for High-Efficiency Water Splitting . *J. Mater. Chem. A* **2016**, *4* (23), 8995–9001.

(49)   R. Patil; S. Kelkar; R. Naphade; S. Ogale. Low Temperature Grown $CuBi_2O_4$ with Flower Morphology and Its Composite with CuO Nanosheets for Photoelectrochemical Water Splitting. *J. Mater. Chem. A* **2014**, *2* (10), 3661–3668.

(50)   G. Sharma; Z. Zhao; P. Sarker; B. A. Nail; J. Wang; M. N. Huda; F. E. Osterloh. Electronic Structure, Photovoltage, and Photocatalytic Hydrogen Evolution with p-$CuBi_2O_4$ Nanocrystals. *J. Mater. Chem. A* **2016**, *4* (8), 2936–2942.

(51)   F. Wang; A. Chemseddine; F. F. Abdi; R. Van De Krol; S. P. Berglund. Spray Pyrolysis of $CuBi_2O_4$ Photocathodes: Improved Solution Chemistry for Highly Homogeneous Thin Films. *J. Mater. Chem. A* **2017**, *5* (25), 12838–12847.

(52)   D. Kang; J. C. Hill; Y. Park; K. S. Choi. Photoelectrochemical Properties and Photostabilities of High Surface Area $CuBi_2O_4$ and Ag-Doped $CuBi_2O_4$ Photocathodes. *Chem. Mater.* **2016**, *28* (12), 4331–4340.

(53)   J. Li; M. Griep; Y. Choi; D. Chu. Photoelectrochemical Overall Water Splitting with Textured $CuBi_2O_4$ as a Photocathode. *Chem. Commun.* **2018**, *54* (27), 3331–3334.

(54)   R. Venkatkarthick; C. K. Devi; L. J. Berchmans; S. Vasudevan; D. J. Davidson; G. Sozhan; S. Ravichanran. Photoelectrochemical Generation of Hydrogen Using P-Type $CaFe_2O_4$ Photocathodes. *J. Am. Chem. Soc. Commun.* **2010**, *132*, 17343–17345.

(55)   Y. Matsumoto; M. Omae; K. Sugiyama; E. Sato. New Photocathode Materials for Hydrogen Evolution: Calcium Iron Oxide ($CaFe_2O_4$) and Strontium Iron Oxide (Sr7Fe10O22). *J. Phys. Chem.* **2005**, *91* (3), 577–581.

(56)   Y. Matsumoto; K. Sugiyama; E. I. Sato. Improvement of $CaFe_2O_4$ Photocathode by Doping with Na and Mg. *J. Solid State Chem.* **1988**, *74* (1), 117–125.

(57)   K. Sekizawa; T. Nonaka; T. Arai; T. Morikawa. Structural Improvement of $CaFe_2O_4$ by Metal Doping toward Enhanced Cathodic Photocurrent. *ACS Appl. Mater. Interfaces*

2014, *6* (14), 10969–10973.

(58)   M. I. Díez-García; R. Gómez. Investigating Water Splitting with CaFe$_2$O$_4$ Photocathodes by Electrochemical Impedance Spectroscopy. *ACS Appl. Mater. Interfaces* **2016**, *8* (33), 21387–21397.

(59)   P. P. Sahoo; B. Zoellner; P. A. Maggard. Optical, Electronic, and Photoelectrochemical Properties of the p-Type Cu$_{3-x}$VO$_4$ Semiconductor. *J. Mater. Chem. A* **2015**, *3* (8), 4501–4509.

(60)   A. Kormányos; A. Thomas; M. N. Huda; P. Sarker; J. P. Liu; N. Poudyal; C. Janáky; K. Rajeshwar. Solution Combustion Synthesis, Characterization, and Photoelectrochemistry of CuNb$_2$O$_6$ and ZnNb$_2$O$_6$ Nanoparticles. *J. Phys. Chem. C* **2016**, *120* (29), 16024–16034.

(61)   L. Fuoco; N. King; D. Dougherty; P. A. Maggard; P. P. Sahoo; S. Stuart; Y. Liu. Copper Deficiency in the p-Type Semiconductor Cu$_{1-x}$Nb$_3$O$_8$. *Chem. Mater.* **2014**, *26* (6), 2095–2104.

(62)   J. Y. Chan; P. Watkins-Curry; N. King; P. A. Maggard; I. Sullivan. Flux-Mediated Syntheses, Structural Characterization and Low-Temperature Polymorphism of the p-Type Semiconductor Cu$_2$Ta$_4$O$_{11}$. *J. Solid State Chem.* **2015**, *236*, 10–18.

(63)   L. Fuoco; U. A. Joshi; P. A. Maggard. Preparation and Photoelectrochemical Properties of P-Type Cu$_5$Ta$_{11}$O$_{30}$ and Cu$_3$Ta$_7$O$_{19}$ Semiconducting Polycrystalline Films. *J. Phys. Chem. C* **2012**, *116* (19), 10490–10497.

(64)   F. F. Abdi; S. P. Berglund. Recent Developments in Complex Metal Oxide Photoelectrodes. *J. Phys. D. Appl. Phys.* **2017**, *50* (19), 193002.

(65)   G. K. Mor; K. Shankar; M. Paulose; O. K. Varghese; C. A. Grimes. Enhanced Photocleavage of Water Using Titania Nanotube Arrays. *Nano Lett.* **2005**, *5* (1), 191–195.

(66)   G. K. Mor; O. K. Varghese; M. Paulose; C. A. Grimes. Transparent Highly Ordered TiO$_2$ Nanotube Arrays via Anodization of Titanium Thin Films. *Adv. Funct. Mater.* **2005**, *15* (8), 1291–1296.

(67)   Z. Zhang; M. F. Hossain; T. Takahashi. Photoelectrochemical Water Splitting on Highly Smooth and Ordered TiO$_2$ Nanotube Arrays for Hydrogen Generation. *Int. J. Hydrogen Energy* **2010**, *35* (16), 8528–8535.

(68)   Z. Zhang; P. Wang. Optimization of Photoelectrochemical Water Splitting

Performance on Hierarchical TiO$_2$ Nanotube Arrays. *Energy Environ. Sci.* **2012**, *5* (4), 6506–6512.

(69)   Z. Zhang; M. F. Hossain; T. Takahashi. Photoelectrochemical Water Splitting on Highly Smooth and Ordered TiO$_2$ Nanotube Arrays for Hydrogen Generation. *Int. J. Hydrogen Energy* **2010**, *35* (16), 8528–8535.

(70)   R. C. Fitzmorris; X. Yang; J. Z. Zhang; A. Wolcott; G. Wang; A. Sobo; Y. Li; F. Qian. Nitrogen-Doped ZnO Nanowire Arrays for Photoelectrochemical Water Splitting. *Nano Lett.* **2009**, *9* (6), 2331–2336.

(71)   Y. Zhao; J. Z. Zhang; A. Wolcott; T. R. Kuykendall; W. A. Smith. Photoelectrochemical Study of Nanostructured ZnO Thin Films for Hydrogen Generation from Water Splitting. *Adv. Funct. Mater.* **2009**, *19* (12), 1849–1856.

(72)   K. Xie; N. Umezawa; N. Zhang; P. Reunchan; Y. Zhang; J. Ye. Self-Doped SrTiO$_3$ photocatalyst with Enhanced Activity for Artificial Photosynthesis under Visible Light. *Energy Environ. Sci.* **2011**, *4* (10), 4211–4219.

(73)   A. Dabirian; R. Van De Krol. High-Temperature Ammonolysis of Thin Film Ta$_2$O$_5$ Photoanodes: Evolution of Structural, Optical, and Photoelectrochemical Properties. *Chem. Mater.* **2015**, *27* (3), 708–715.

(74)   P. Salvador. Hole Diffusion Length in n-TiO$_2$ Single Crystals and Sintered Electrodes: Photoelectrochemical Determination and Comparative Analysis. *J. Appl. Phys.* **1984**, *55* (8), 2977–2985.

(75)   Chen, Z.; Dinh, H. N.; Miller, E. Photoelectrochemical Water Splitting - Standards, Experimental Methods, and Protocols; 2013.

(76)   Z. Liu; B. Pesic; K. S. Raja; R. R. Rangaraju; M. Misra. Hydrogen Generation under Sunlight by Self Ordered TiO$_2$ Nanotube Arrays. *Int. J. Hydrogen Energy* **2009**, *34* (8), 3250–3257.

(77)   M. Quintana; T. Edvinsson; A. Hagfeldt; G. Boschloo. Comparison of Dye-Sensitized ZnO and TiO$_2$ Solar Cells: Studies of Charge Transport and Carrier Lifetime. *J. Phys. Chem. C* **2007**, *111* (2), 1035–1041.

(78)   N. T. Hahn; H. Ye; D. W. Flaherty; A. J. Bard; C. B. Mullins. Reactive Ballistic Deposition of α-Fe$_2$O$_3$ Thin Films for Photoelectrochemical Water Oxidation. *ACS Nano*

2010, *4* (4), 1977–1986.

(79)   N. T. Hahn; C. B. Mullins. Photoelectrochemical Performance of Nanostructured Ti- and Sn-Doped α-Fe$_2$O$_3$ Photoanodes. *Chem. Mater.* **2010**, *22* (23), 6474–6482.

(80)   A. Kay; I. Cesar; M. Grätzel. New Benchmark for Water Photooxidation by Nanostructured α-Fe$_2$O$_3$ Films. *J. Am. Chem. Soc.* **2006**, *128* (49), 15714–15721.

(81)   I. Cesar; K. Sivula; A. Kay; R. Zboril; M. Grätzel. Influence of Feature Size, Film Thickness, and Silicon Doping on the Performance of Nanostructured Hematite Photoanodes for Solar Water Splitting. *J. Phys. Chem. C* **2009**, *113* (2), 772–782.

(82)   S. D. Tilley; M. Cornuz; K. Sivula; M. Grätzel. Light-Inducedwater Splitting with Hematite: Improved Nanostructure and Iridium Oxide Catalysis. *Angew. Chemie - Int. Ed.* **2010**, *49* (36), 6405–6408.

(83)   M. Grätzel; K. Sivula; J. Tucek; R. Zboril; R. Robert; F. Le Formal; A. Weidenkaff; J. Frydrych. Photoelectrochemical Water Splitting with Mesoporous Hematite Prepared by a Solution-Based Colloidal Approach. *J. Am. Chem. Soc.* **2010**, *132* (21), 7436–7444.

(84)   G. Wang; Y. Ling; D. A. Wheeler; K. E. N. George; K. Horsley; C. Heske; J. Z. Zhang; Y. Li. Facile Synthesis of Highly Photoactive α-Fe$_2$O$_3$-Based Films for Water Oxidation. *Nano Lett.* **2011**, *11* (8), 3503–3509.

(85)   Y. Ling; G. Wang; J. Reddy; C. Wang; J. Z. Zhang; Y. Li. The Influence of Oxygen Content on the Thermal Activation of Hematite Nanowires. *Angew. Chemie - Int. Ed.* **2012**, *51* (17), 4074–4079.

(86)   S. C. Riha; B. M. Klahr; E. C. Tyo; S. Seifert; S. Vajda; M. J. Pellin; T. W. Hamann; A. B. F. Martinson. Atomic Layer Deposition of a Submonolayer Catalyst for the Enhanced Photoelectrochemical Performance of Water Oxidation with Hematite. *ACS Nano* **2013**, *7* (3), 2396–2405.

(87)   L. Steier; J. Luo; M. Schreier; M. T. Mayer; T. Sajavaara; M. Grätzel. Low-Temperature Atomic Layer Deposition of Crystalline and Photoactive Ultrathin Hematite Films for Solar Water Splitting. *ACS Nano* **2015**, *9* (12), 11775–11783.

(88)   S. Zeng; K. Tang; T. Li; Z. Liang; D. Wang; Y. Wang; W. Zhou. Hematite Hollow Spindles and Microspheres: Selective Synthesis, Growth Mechanisms, and Application in Lithium Ion Battery and Water Treatment. *J. Phys. Chem. C* **2007**, *111* (28), 10217–10225.

(89)   M. Barroso; S. R. Pendlebury; A. J. Cowan; J. R. Durrant. Charge Carrier Trapping, Recombination and Transfer in Hematite (α-Fe_2O_3) Water Splitting Photoanodes. *Chem. Sci.* **2013**, *4* (7), 2724–2734.

(90)   A. Pu; J. Deng; M. Li; J. Gao; H. Zhang; Y. Hao; J. Zhong; X. Sun. Coupling Ti-Doping and Oxygen Vacancies in Hematite Nanostructures for Solar Water Oxidation with High Efficiency. *J. Mater. Chem. A* **2014**, *2* (8), 2491–2497.

(91)   T. Hisatomi; F. Le Formal; M. Cornuz; J. Brillet; N. Tétreault; K. Sivula; M. Grätzel. Cathodic Shift in Onset Potential of Solar Oxygen Evolution on Hematite by 13-Group Oxide Overlayers. *Energy Environ. Sci.* **2011**, *4* (7), 2512–2515.

(92)   D. A. Wheeler; Y. Li; J. Z. Zhang; G. Wang; Y. Ling. Sn-Doped Hematite Nanostructures for Photoelectrochemical Water Splitting. *Nano Lett.* **2011**, *11* (5), 2119–2125.

(93)   R. Liu; Z. Zheng; J. Spurgeon; X. Yang. Enhanced Photoelectrochemical Water-Splitting Performance of Semiconductors by Surface Passivation Layers. *Energy Environ. Sci.* **2014**, *7* (8), 2504–2517.

(94)   J. Kiwi; M. Grätzel. Colloidal Redox Catalysts for Evolution of Oxygen and for Light-Induced Evolution of Hydrogen from Water. *Angew. Chemie Int. Ed. English* **1979**, *18* (8), 624–626.

(95)   D. K. Zhong; J. Sun; H. Inumaru; D. R. Gamelin. Solar Water Oxidation by Composite Catalyst/α-Fe_2O_3 Photoanodes. *J. Am. Chem. Soc.* **2009**, *131* (17), 6086–6087.

(96)   A. Kudo; K. Ueda; H. Kato; I. Mikami. Photocatalytic O_2 Evolution under Visible Light Irradiation on $BiVO_4$ in Aqueous $AgNO_3$ Solution. *Catal. Letters* **1998**, *53* (3/4), 229–230.

(97)   Z. Zhao; W. Luo; Z. Li; Z. Zou. Density Functional Theory Study of Doping Effects in Monoclinic Clinobisvanite $BiVO_4$. *Phys. Lett. Sect. A Gen. At. Solid State Phys.* **2010**, *374* (48), 4919–4927.

(98)   S. P. Berglund; D. W. Flaherty; N. T. Hahn; A. J. Bard; C. B. Mullins. Photoelectrochemical Oxidation of Water Using Nanostructured $BiVO_4$ Films. *J. Phys. Chem. C* **2011**, *115* (9), 3794–3802.

(99)   J. Su; L. Guo; S. Yoriya; C. A. Grimes. Aqueous Growth of Pyramidal-Shaped $BiVO_4$

Nanowire Arrays and Structural Characterization: Application to Photoelectrochemical Water Splitting. *Cryst. Growth Des.* **2010**, *10* (2), 856–861.

(100)   Y. Liang; T. Tsubota; L. P. A. Mooij; R. Van De Krol. Highly Improved Quantum Efficiencies for Thin Film BiVO$_4$ Photoanodes. *J. Phys. Chem. C* **2011**, *115* (35), 17594–17598.

(101)   D. K. Zhong; S. Choi; D. R. Gamelin. Near-Complete Suppression of Surface Recombination in Solar Photoelectrolysis by "Co-Pi" Catalyst-Modified W:BiVO$_4$. *J. Am. Chem. Soc.* **2011**, *133* (45), 18370–18377.

(102)   H. Ye; J. Lee; J. S. Jang; A. J. Bard. Rapid Screening of BiVO$_4$-Based Photocatalysts by Scanning Electrochemical Microscopy (SECM) and Studies of Their Photoelectrochemical Properties. *J. Phys. Chem. C* **2010**, *114* (31), 13322–13328.

(103)   A. Srivastav; A. Verma; A. Banerjee; S. A. Khan; M. Gupta; V. R. Satsangi; R. Shrivastav; S. Dass. Gradient Doping - A Case Study with Ti-Fe$_2$O$_3$ towards an Improved Photoelectrochemical Response. *Phys. Chem. Chem. Phys.* **2016**, *18* (48), 32735–32743.

(104)   J. Su; L. Guo; N. Bao; C. A. Grimes. Nanostructured WO$_3$/BiVO$_4$ Heterojunction Films for Efficient Photoelectrochemical Water Splitting. *Nano Lett.* **2011**, *11* (5), 1928–1933.

(105)   X. Shi; I. Y. Choi; K. Zhang; J. Kwon; D. Y. Kim; J. K. Lee; S. H. Oh; J. K. Kim; J. H. Park. Efficient Photoelectrochemical Hydrogen Production from Bismuth Vanadate-Decorated Tungsten Trioxide Helix Nanostructures. *Nat. Commun.* **2014**, *5* (1), 4775.

(106)   Y. Pihosh; I. Turkevych; K. Mawatari; J. Uemura; Y. Kazoe; S. Kosar; K. Makita; T. Sugaya; T. Matsui; et al. Photocatalytic Generation of Hydrogen by Core-Shell WO$_3$/BiVO$_4$ Nanorods with Ultimate Water Splitting Efficiency. *Sci. Rep.* **2015**, *5* (1), 11141.

(107)   T. W. Kim; K. S. Choi. Nanoporous BiVO4photoanodes with Dual-Layer Oxygen Evolution Catalysts for Solar Water Splitting. *Science.* **2014**, *343* (6174), 990–994.

(108)   Y. Kuang; Q. Jia; G. Ma; T. Hisatomi; T. Minegishi; H. Nishiyama; M. Nakabayashi; N. Shibata; T. Yamada; et al. Ultrastable Low-Bias Water Splitting Photoanodes via Photocorrosion Inhibition and in Situ Catalyst Regeneration. *Nat. Energy* **2017**, *2* (1), 16191.

(109)   M. Zhong; T. Hisatomi; Y. Kuang; J. Zhao; M. Liu; A. Iwase; Q. Jia; H. Nishiyama; T.

Minegishi; et al. Surface Modification of CoO Loaded $BiVO_4$ Photoanodes with Ultrathin p-Type NiO Layers for Improved Solar Water Oxidation. *J. Am. Chem. Soc.* **2015**, *137* (15), 5053–5060.

(110)   B. Klahr; S. Gimenez; F. Fabregat-Santiago; J. Bisquert; T. W. Hamann. Photoelectrochemical and Impedance Spectroscopic Investigation of Water Oxidation with "Co-Pi"-Coated Hematite Electrodes. *J. Am. Chem. Soc.* **2012**, *134* (40), 16693–16700.

(111)   Y. Ma; S. R. Pendlebury; A. Reynal; F. Le Formal; J. R. Durrant. Dynamics of Photogenerated Holes in Undoped $BiVO_4$ Photoanodes for Solar Water Oxidation. *Chem. Sci.* **2014**, *5* (8), 2964–2973.

(112)   B. Dam; R. van de Krol; L. Han; A. H. M. Smets; F. F. Abdi; M. Zeman. Efficient Solar Water Splitting by Enhanced Charge Separation in a Bismuth Vanadate-Silicon Tandem Photoelectrode. *Nat. Commun.* **2013**, *4* (1), 2195.

(113)   L. Han; F. F. Abdi; R. Van De Krol; R. Liu; Z. Huang; H. J. Lewerenz; B. Dam; M. Zeman; A. H. M. Smets. Efficient Water-Splitting Device Based on a Bismuth Vanadate Photoanode and Thin-Film Silicon Solar Cells. *ChemSusChem* **2014**, *7* (10), 2832–2838.

(114)   Y. Hou; X. Y. Li; Q. D. Zhao; X. Quan; G. H. Chen. Electrochemical Method for Synthesis of a $ZnFe_2O_4/TiO_2$ Composite Nanotube Array Modified Electrode with Enhanced Photoelectrochemical Activity. *Adv. Funct. Mater.* **2010**, *20* (13), 2165–2174.

(115)   K. J. McDonald; K. S. Choi. Synthesis and Photoelectrochemical Properties of $Fe_2O_3/ZnFe_2O_4$ Composite Photoanodes for Use in Solar Water Oxidation. *Chem. Mater.* **2011**, *23* (21), 4863–4869.

(116)   A. Sheikh; A. Yengantiwar; M. Deo; S. Kelkar; S. Ogale. Near-Field Plasmonic Functionalization of Light Harvesting Oxide-Oxide Heterojunctions for Efficient Solar Photoelectrochemical Water Splitting: The $AuNP/ZnFe_2O_4/ZnO$ System. *Small* **2013**, *9* (12), 2091–2096.

(117)   A. A. Tahir; K. G. U. Wijayantha. Photoelectrochemical Water Splitting at Nanostructured $ZnFe_2O_4$ Electrodes. *J. Photochem. Photobiol. A Chem.* **2010**, *216* (2–3), 119–125.

(118)   J. H. Kim; Y. J. Jang; J. H. Kim; J. W. Jang; S. H. Choi; J. S. Lee. Defective $ZnFe_2O_4$ nanorods with Oxygen Vacancy for Photoelectrochemical Water Splitting. *Nanoscale* **2015**, *7* (45), 19144–19151.

(119)   A. G. Hufnagel; C. Scheu; D. Fattakhova-Rohlfing; T. Bein; K. Peters; A. Müller. Zinc Ferrite Photoanode Nanomorphologies with Favorable Kinetics for Water-Splitting. *Adv. Funct. Mater.* **2016**, *26* (25), 4435–4443.

(120)   J. H. Kim; J. H. Kim; J. W. Jang; J. Y. Kim; S. H. Choi; G. Magesh; J. Lee; J. S. Lee. Awakening Solar Water-Splitting Activity of $ZnFe_2O_4$ Nanorods by Hybrid Microwave Annealing. *Adv. Energy Mater.* **2015**, *5* (6), 1401933.

(121)   S. Zhang; X. Wang; Z. Li; N. Zhang; Y. Guo; Q. Qian; Z. Zou.   A Facile Spray Pyrolysis Method to Prepare Ti-Doped $ZnFe_2O_4$ for Boosting Photoelectrochemical Water Splitting . *J. Mater. Chem. A* **2017**, *5* (16), 7571–7577.

(122)   Z. Chen; H. N. Dinh; E. Miller. Photoelectrochemical Water Splitting Standards, Experimental Methods, and Protocols; 2013.

(123)   T. Bosserez; J. Rongé; J. Van Humbeeck; S. Haussener; J. Martens. Design of Compact Photoelectrochemical Cells for Water Splitting. *Oil Gas Sci. Technol. IFP Energies Nouv. Ó* **2015**.

(124)   T. Lopes; L. Andrade; H. A. Ribeiro; A. Mendes. Characterization of Photoelectrochemical Cells for Water Splitting by Electrochemical Impedance Spectroscopy. *Int. J. Hydrogen Energy* **2010**, *35* (20), 11601–11608.

(125)   S. Haussener; C. Xiang; J. M. Spurgeon; S. Ardo; N. S. Lewis; A. Z. Weber. Modeling, Simulation, and Design Criteria for Photoelectrochemical Water-Splitting Systems. *Energy Environ. Sci.* **2012**, *5* (12), 9922.

(126)   G. Popov; M. Mattinen; T. Hatanpää; M. Vehkamäki; M. Kemell; K. Mizohata; J. Räisänen; M. Ritala; M. Leskelä. Atomic Layer Deposition of PbI_2 Thin Films. *Chem. Mater.* **2019**, *31* (3), 1101–1109.

(127)   R. W. Johnson; A. Hultqvist; S. F. Bent. A Brief Review of Atomic Layer Deposition: From Fundamentals to Applications. *Mater. Today* **2014**, *17* (5), 236–246.

(128)   A. Paracchino; V. Laporte; K. Sivula; M. Grätzel; E. Thimsen. Highly Active Oxide Photocathode for Photoelectrochemical Water Reduction. *Nat. Mater.* **2011**, *10* (6), 456–461.

(129)   M. Knez; K. Nielsch; L. Niinistö. Synthesis and Surface Engineering of Complex Nanostructures by Atomic Layer Deposition. *Adv. Mater.* **2007**, *19* (21), 3425–3438.

(130)   W. Yang; J. Moon. Recent Advances in Earth-Abundant Photocathodes for Photoelectrochemical Water Splitting. *ChemSusChem* **2018**, 1–12.

(131)   Y. Zhang; Y. Cui; P.-C. Hsu; Y. Qiu; R. Zhang; G. Zhou; Z. Liang; W. Liu; W. Chen; et al.   Efficient Solar-Driven Water Splitting by Nanocone $BiVO_4$ -Perovskite Tandem Cells . *Sci. Adv.* **2016**, *2* (6), e1501764.

(132)   X. Zhu; N. Guijarro; Y. Liu; P. Schouwink; R. A. Wells; F. Le Formal; S. Sun; C. Gao; K. Sivula. Spinel Structural Disorder Influences Solar-Water-Splitting Performance of $ZnFe_2O_4$ Nanorod Photoanodes. *Adv. Mater.* **2018**, *30* (34), 1801612.

2 Enhancing Electron Transport in Cu-based Photocathodes with p-n Heterojunctions

This chapter is based on related research in two peer-reviewed publications:

1. **L. Pan**; J. H. Kim; M. T. Mayer; M. K. Son; A. Ummadisingu; J. S. Lee; A. Hagfeldt; J. Luo; M. Grätzel. Boosting the Performance of Cu_2O Photocathodes for Unassisted Solar Water Splitting Devices. *Nat. Catal.* **2018**, *1* (6), 412–420.

2. Y. X. Yu[§]; **L. Pan**[§]; M. K. Son; M. T. Mayer; W. De Zhang; A. Hagfeldt; J. Luo; M. Grätzel. Solution-Processed Cu_2S Photocathodes for Photoelectrochemical Water Splitting. ACS Energy *Lett.* **2018**, *3* (4), 760–766. ([§] These authors contributed equally to this work)

The content in this chapter is adapted from the versions before editorial change.

In p-type semiconductors, electrons are minority carriers whose electronic properties such as diffusion length and carrier density are inferior to majority carriers, which could limit photoelectrode performance when they are applied as photoabsorbers. This chapter includes two works on forming p-n heterojunctions using n-type layers and p-type photoabsorbers to efficiently separate charges. Both cases have shown the importance of smooth electron transport by precise band energy level alignment, giving unprecedented photoelectrochemical performances.

2.1 Introduction

2.1.1 Research progress of Cu$_2$O photocathodes

Hydrogen fuel generated through solar water splitting offers a green and sustainable energy source and addresses the issue of solar intermittency.[1] Though efforts have been devoted to this area in the past several decades, there is still no solar water splitting device fulfilling the requirements of high efficiency, long term stability and low cost concurrently.[2,3] The challenge stands that efficient photoelectrodes are generally composed of expensive semiconductor photoabsorbers and noble metal catalysts while inexpensive and Earth-abundant photoelectrodes generally exhibit low efficiency. To solve this dilemma, efforts are focused on two main directions, one is to search for new materials and the other is to improve existing inexpensive photoelectrodes.[3] In the latter, new benchmark performance pushing the frontier of the field is desired.

Due to their low cost, high abundance and facile preparation methods, metal oxide semiconductors play important roles in both the photocatalytic and photoelectrochemical approaches for solar water splitting.[4,5] Among them, Cu$_2$O is one of the most promising materials whose photoelectrochemical performance in the water splitting reaction is the highest among all oxides. The modern era of Cu$_2$O photocathodes started from the seminal work using atomic layer deposited protection layers to prevent Cu$_2$O from photodecomposition.[6] Following that, the stability has been further improved by applying thicker TiO$_2$ protection layers and using RuO$_x$ as the hydrogen evolution catalysts.[7] Inspired by Cu$_2$O photovoltaic cells developments,[8–10] Delaunay's group increased the photovoltage of Cu$_2$O photocathode to 1.0 V for solar water splitting using Ga$_2$O$_3$ as an n-type layer.[11] However, realizing a Cu$_2$O photocathode with the merits of current state-of-the-art devices is demanding. Along with balancing light absorption depth and minority carrier diffusion length, band alignment must be considered at each junction to minimize photovoltage loss.

In this chapter, a new Cu$_2$O photocathode was demonstrated. Advances were achieved using nano-structured photoelectrodes in combination with Ga$_2$O$_3$ as the electron selective layer and TiO$_2$ as a protection layer. The nanowire radial heterojunction guarantees simultaneous enhancement of light absorption and charge transport, and the Ga$_2$O$_3$ layer enables better band alignment that reduces interfacial recombination. With X-ray photoelectron spectroscopy and UV-vis absorption spectroscopy, band alignment of

Cu_2O was studied with conventionally used aluminum doped zinc oxide (AZO) and highly optimized Ga_2O_3 in detail. The mechanism behind the photovoltage augmentation was elucidated.

2.1.2   The case of p-type Cu_2S photocathodes.

With the merits of p-type conductivity, proper bandgap, low toxicity, and high absorption coefficient ($>10^4$ cm^{-1}),[12–15] Cu_2S is regarded as a promising material for solar energy conversion. Indeed, it has been widely studied in photovoltaics (PV) development since 1960s. With a direct bandgap of 1.8 eV and an indirect bandgap of 1.2 eV, it can theoretically deliver a power conversion efficiency of 30% as a single junction PV cell.[16] Historically, Cu_2S/CdS heterojunction PV devices approached a solar to electricity conversion efficiency of 10%.[17] There are many distinct crystalline phases and stoichiometry of copper sulfide, such as chalcocite (Cu_2S), djurleite ($Cu_{1.96}S$), digenite ($Cu_{1.8}S$), anilite ($Cu_{1.75}S$) and covellite (CuS).[18,19] However, only Cu_2S can generate free carriers at temperature below 90 °C, as the excess copper deficiencies in other compounds could lead to very high hole concentrations, resulting in a degenerately doped semiconductor which is unsuitable for conventional PV application.[15,20] Therefore, controlling the stoichiometry to achieve the accurate Cu_2S phase is highly important for solar energy application.

Methods to prepare Cu_2S films include spray pyrolysis,[21] atomic layer deposition,[12,15,22] pulsed chemical vapor deposition,[23,24] electrodeposition,[25] and solid state reaction.[26,27] However, most of these films are not photoactive because of the poor control of stoichiometry. In this work, an indirect solution process via ion exchange reaction was used to prepare Cu_2S from CdS films. The Cu_2S obtained from Cu^+ exchange of CdS is fully stoichiometric, known as the low-chalcocite phase, which is often used in normal structure CdS/Cu_2S solar cells where CdS is the bottom layer.[28] The Cu_2S phase was confirmed by XRD and its stoichiometry was verified by XPS. Furthermore, as a photocathode for water splitting, the Cu_2S electrode should be inverted in structure, with the CdS layer on top of the Cu_2S layer. To avoid the oxidation and phase change of Cu_2S during the deposition process of CdS, we developed a modified chemical bath deposition (CBD) method by adding a reductive agent in the CdS precursor solution. This method results in high quality Cu_2S and CdS p-n junction.

To achieve stable and efficient solar water splitting with Cu_2S/CdS photocathodes, we deposited TiO_2 on the electrode surface as the protection layer and RuO_x as the hydrogen

evolution catalyst. The resulting Cu_2S photocathodes exhibited a photocurrent density up to 7.0 mA cm^{-2} at -0.3 V versus RHE and an onset potential of 0.48 V vs RHE under AM 1.5 G simulated sunlight illumination for photoelectrochemical water reduction. This performance is comparable to the commonly studied Cu_2O photocathodes.[29–31] Nevertheless, its smaller bandgap makes it more appealing than Cu_2O to be used as a bottom photoabsorber for tandem solar water splitting devices.[32,33] To our best knowledge, this is the first time that solution processed Cu_2S film demonstrates appreciable performance for solar water splitting, which could stimulate more studies on Cu-based photocathodes in the future.
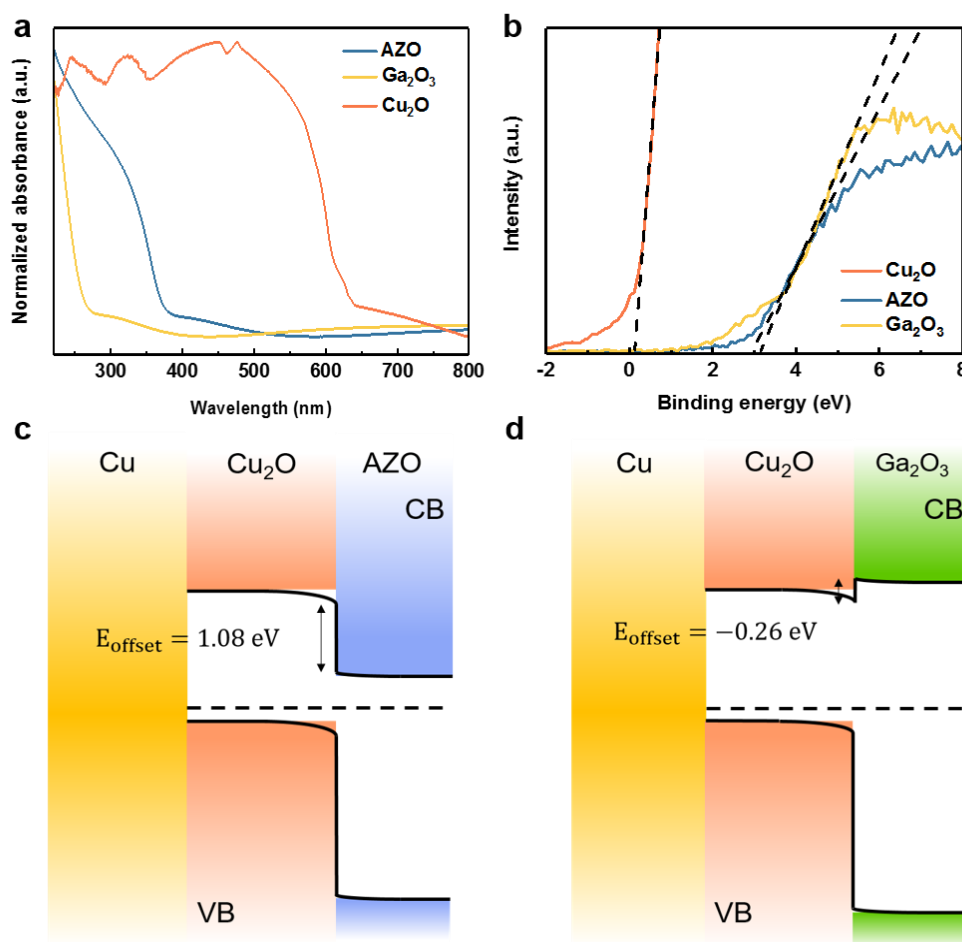

Figure 2.1 | Band energy diagrams derived from absorption and XPS measurement. a, UV-vis absorption spectra and b, valence band edge spectra of Cu_2O, AZO and Ga_2O_3. Equilibrium band edge diagrams of c, Cu_2O/AZO and d, Cu_2O/Ga_2O_3 heterojunctions with different conduction band offsets assuming pinning of the band edges of the semiconductors at the interfaces.

2.2 Results and discussion

2.2.1 Band energy level alignment of the Cu_2O photocathode

It is reported that the nanowire structure can elevate the photocurrent density of Cu_2O electrodes.[34] However, the shortcoming of low photovoltage still needs to be addressed. In a Cu_2O heterojunction device, the photovoltage is limited by the Fermi level difference between Cu_2O and the n-type layer, so choosing an appropriate n-type layer is crucial for achieving high photovoltages. For our Cu_2O nanowire devices, n-type oxide layers were deposited using ALD to form coaxial heterojunctions. To investigate the band alignment in detail, UV-vis absorption spectroscopy and X-ray photoelectron spectroscopy (XPS) were carried out, and the results are shown in Figure 2.1a and 2.1b, respectively. Cu_2O, AZO and Ga_2O_3 show optical band gaps of 2 eV, 3.4 eV and 5 eV, respectively, as derived from Tauc plots assuming a direct allowed transition (Figure 2.2).[35]
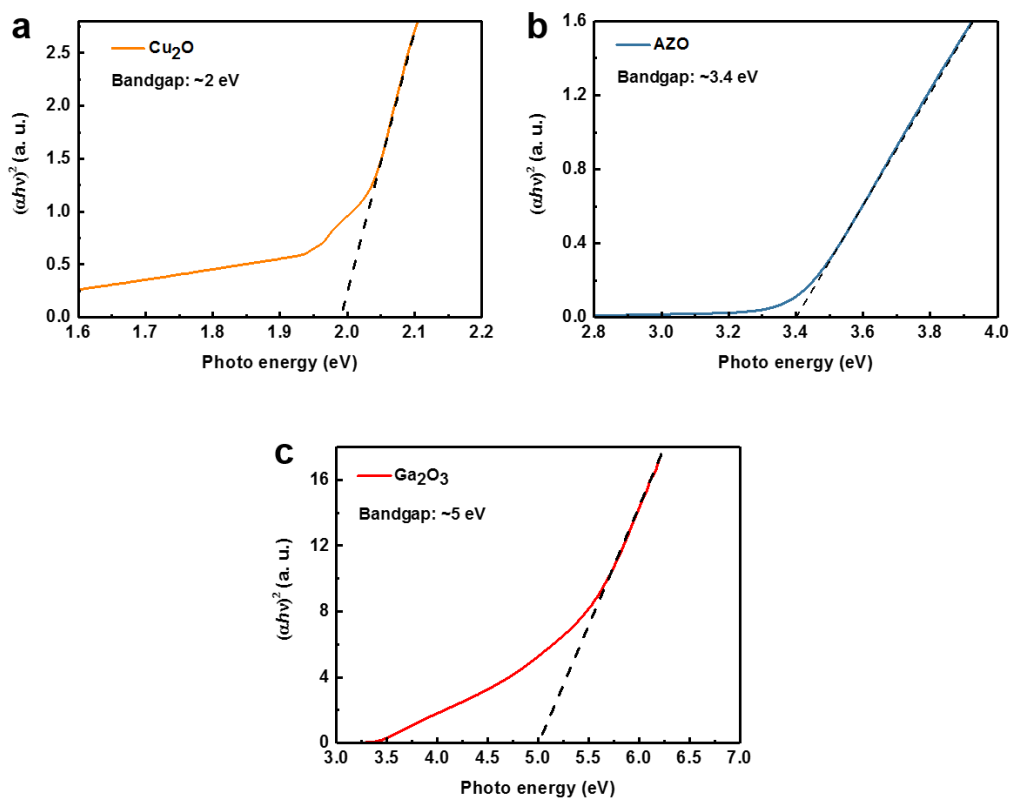

Figure 2.2 | Tauc plots of a, Cu_2O, b, AZO and c, Ga_2O_3.

The valence band levels of Cu_2O, AZO and Ga_2O_3 were determined from linear extrapolation of the valence band edge spectra measured by XPS. The band offsets were determined by the Kraut method through XPS, using core-level offsets from hetero-

junction samples and the band gaps of individual samples (Figure 2.3).
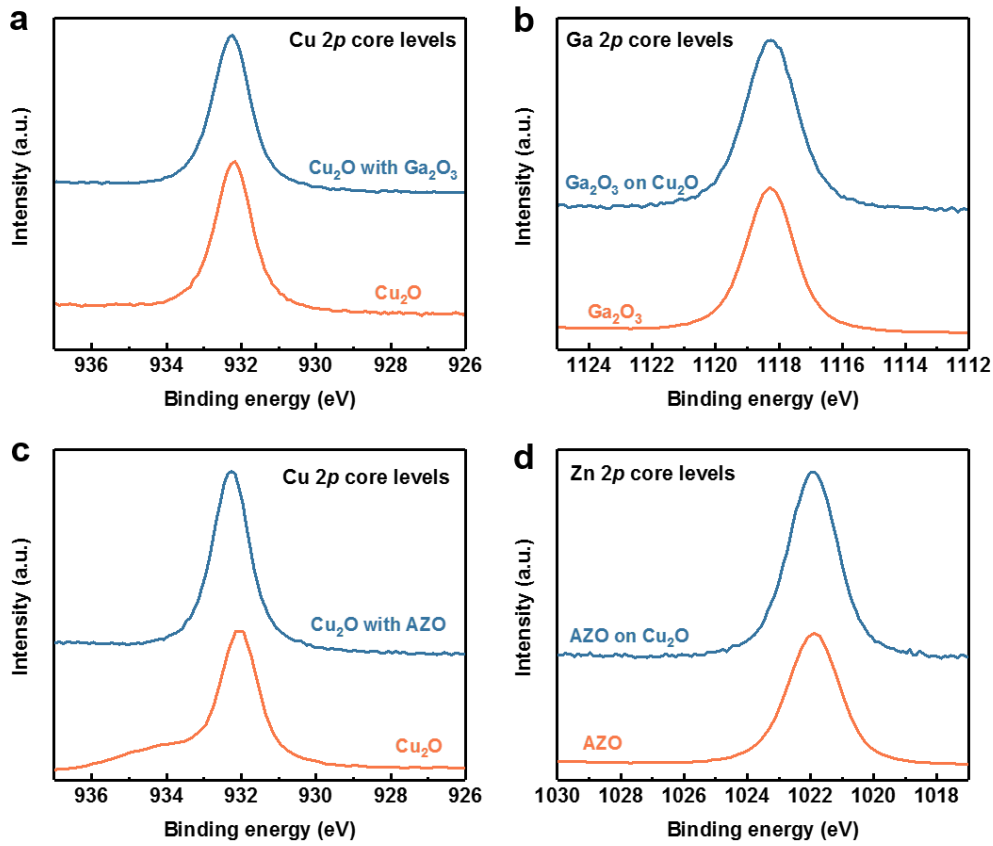

Figure 2.3 | Core levels spectra. a, Cu 2*p* core levels of bulk Cu_2O and with a thin Ga_2O_3 overlayer. b, Ga 2*p* core levels of bulk Ga_2O_3 and in a thin overlayer sample. c, Cu 2*p* core levels of bulk Cu_2O and with a thin AZO overlayer. d, Zn 2*p* core levels of bulk AZO and in a thin overlayer sample.

Using the optical band gaps and valence band levels, we constructed the band energy diagrams of Cu_2O with AZO and Ga_2O_3, as shown in Figure 2.1c and 2.1d, respectively. A large conduction band offset of 1.08 eV was discovered in the sample with the AZO layer, which could limit the maximum separation of quasi-Fermi levels in the two oxides under illumination. The sample with Ga_2O_3 layer, in contrast, displaying an insignificantly small band offset, maximizes the Fermi level offset between the two oxides and should therefore exhibit a much larger photovoltage. This is despite the spike-type conduction band offset that was formed, which may render interface-recombination to become a dominant factor. Doping the electron selective layer to raise its donor density can effectively mitigate the recombination, further enhancing the photovoltage.

2.2.2 Cu_2O photoelectrodes with Ga_2O_3 layer and RuO_x catalysts

For fabricating full devices, the core-shell Cu_2O/Ga_2O_3 NW arrays were coated by ALD TiO_2
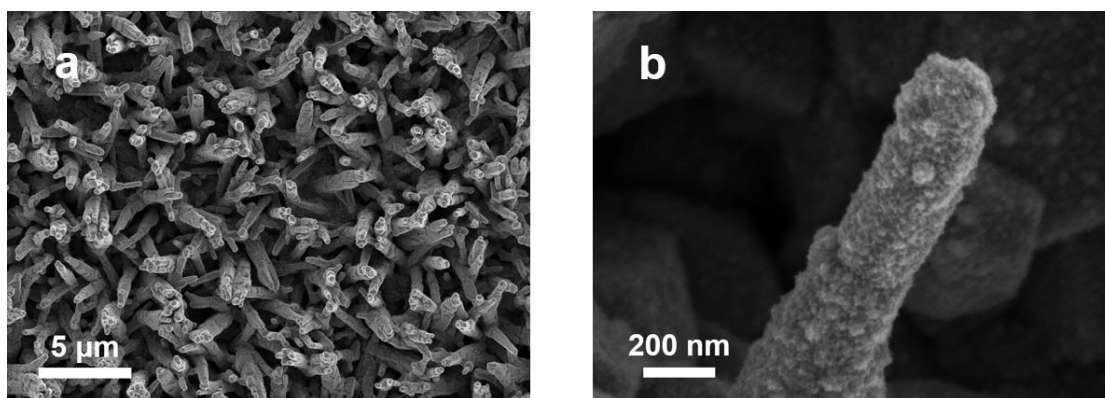
Figure 2.4 | Scanning electron micrographs of RuO_x modified Cu_2O photoelectrode. a, Top view image. b, High resolution image focused on a single wire.

layers, enabling electron conduction and protection against corrosion. To enhance the surface charge injection and reaction kinetics, RuO_x was then deposited as the hydrogen
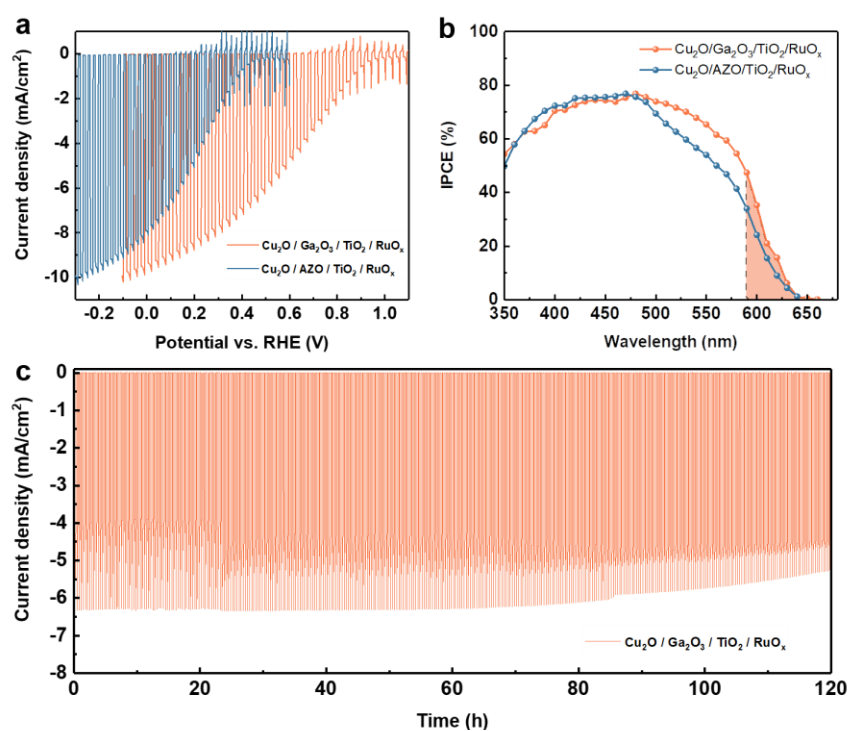

Figure 2.5 | Photoelectrochemical performance of Cu_2O nanowire photocathodes. a, *J-E* response under simulated one sun AM 1.5 G chopped illumination for Cu_2O nanowire photocathodes with $AZO/TiO_2/RuO_x$ and $Ga_2O_3/TiO_2/RuO_x$. b, Corresponding wavelength dependent IPCE measurement. Shadow area represents the contribution of excitonic effect in total quantum yield. c, Stability test at a fixed bias of 0.5 V vs. RHE with chopped illumination and continuous stirring. Electrolyte was renewed twice during the test. All measurements were performed in pH 5 electrolyte.
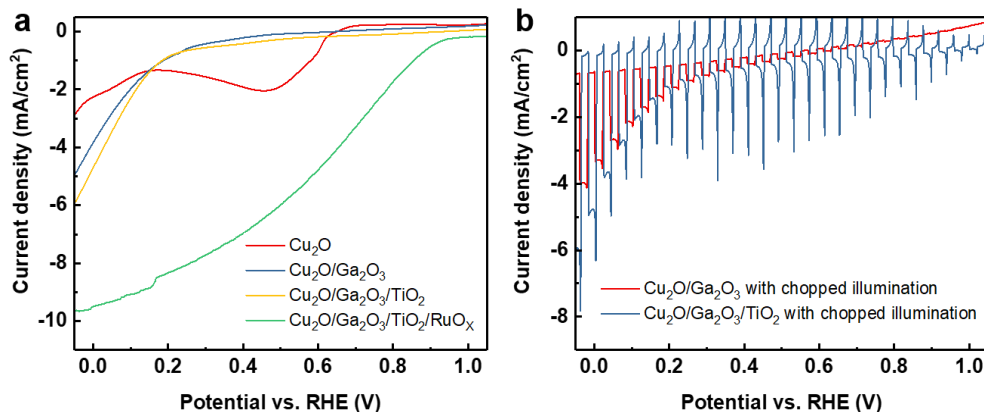
Figure 2.6 | Linear sweep voltammetry of Cu_2O nanowire photocathodes. a, Cu_2O photocathodes tested with different overlayer situations in pH 5 buffer electrolytes under continuous simulated AM 1.5 G illumination. b, Cu_2O photocathodes tested with Ga_2O_3 and Ga_2O_3/TiO_2 overlayers in pH 5 buffer electrolytes under chopped AM 1.5 G illumination.

evolution catalyst on the surface of the electrode. SEM images (Figure 2.4) reveal that the $Cu_2O/Ga_2O_3/TiO_2$ nanostructures are covered with the RuO_x catalyst. Cu_2O NW photocathode devices employing AZO and Ga_2O_3 as electron selective layers were tested in pH 5 electrolyte under chopped illumination (Figure 2.5). Compared to the devices with AZO layer, the photoelectrodes with Ga_2O_3 show a 0.5 V anodic shift in onset potential. Remarkably, at 0.5 V vs. RHE, samples with the Ga_2O_3 layer already delivers a photocurrent density of 6.5 mA cm^{-2}, which is just the onset for the sample with AZO. Moreover, at 0 V vs. RHE, current density reaches almost 10 mA cm^{-2} (Figure 2.5a). Comparisons of Cu_2O photocathodes with different n-type layers were made to show the effect of each layer (Figure 2.6).

A photoelectrochemical test was carried out in 3 different pH electrolytes under standard simulated AM 1.5G illumination (Figure 2.7). Although no apparent current density difference was observed in the region more negative than 0.2 V vs. RHE, the onset potential shifted to more positive values when the testing environment was more alkaline. This is due to the change in the hydrogen binding energy for different pH values, which is also reported for other photoelectrodes or hydrogen evolution reaction catalysts.[36,37] The dark current was negligible across the potential range tested, showing the blocking ability of the heterojunctions. The IPCE results are presented in Figure 2.5b. With a broad plateau response across the wide absorption range, the sample outperforms systems shown in most previous reports.[7,11] It is worth mentioning that a considerable quantum yield in the long wavelength range was obtained due to excitonic effects present in our samples, as
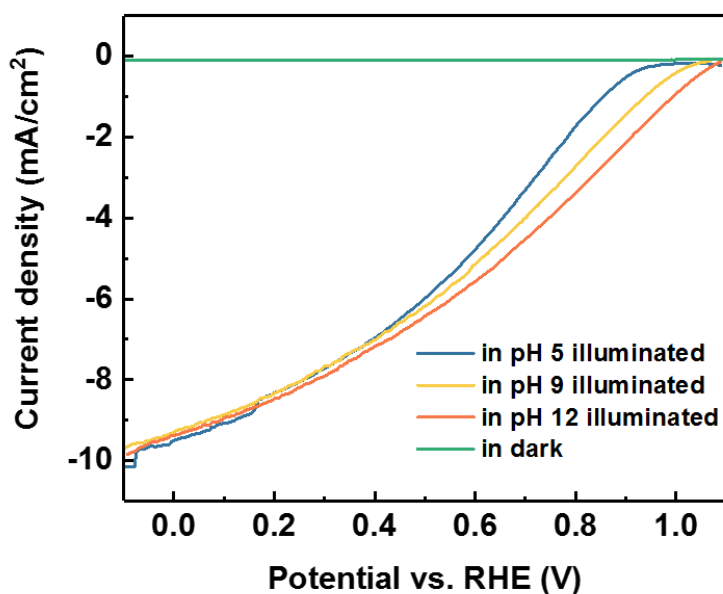
Figure 2.7 | Linear sweep voltammetry of Cu_2O nanowire photocathodes with RuO_x as hydrogen evolution catalyst tested in buffer electrolytes of different pH under simulated AM 1.5 G illumination.
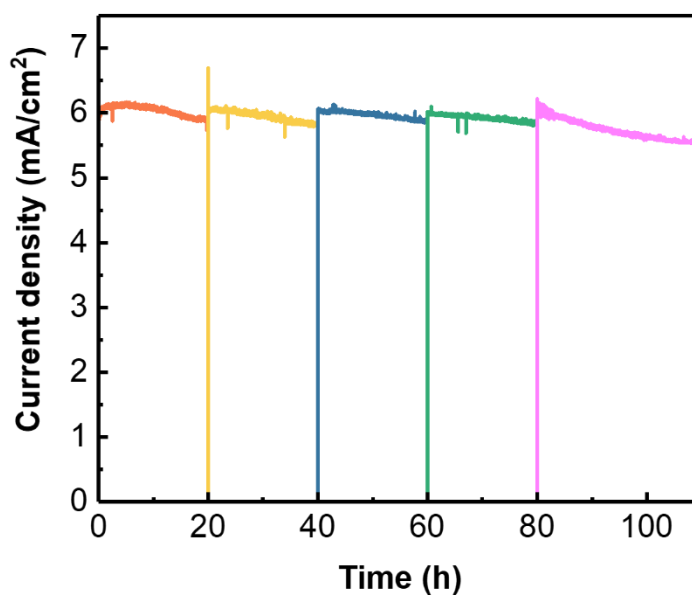

Figure 2.8 | Stability test with continuous illumination. Test was done in pH 5 buffer solution at the fixed bias of 0.5 V vs. RHE with continuous illumination and stirring. Electrolyte was refreshed for 4 times with 20-hour interval.

illustrated in the shadow area, between the electronic band gap (2.1 eV, 590 nm) and optical band gap (1.91 eV, 650 nm) of Cu_2O.[38] The photocurrent in this region accounts for ~6% of total current, though more excitonic effects could be expected from free carrier
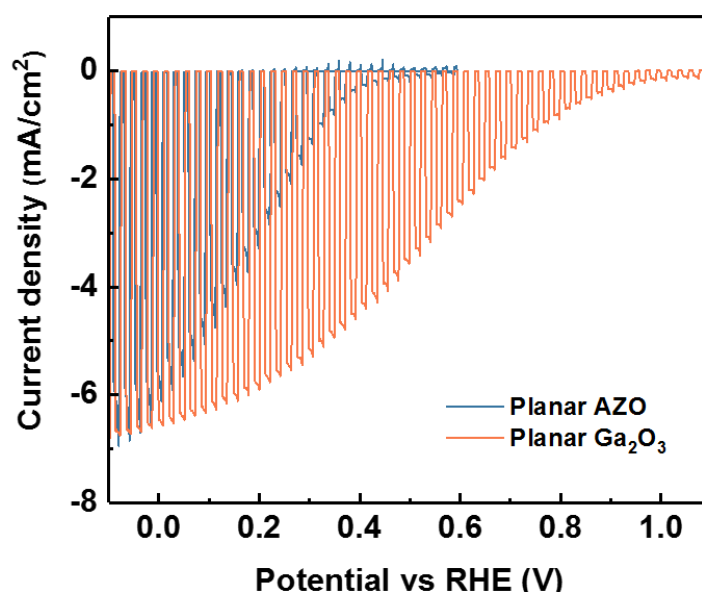
Figure 2.9 | Linear sweep voltammetry of planar Cu_2O photocathodes with AZO or Ga_2O_3 as buffer layer tested under chopped AM 1.5G illumination in a pH 5 electrolyte.

relaxation processes in the part that has excitation energies greater than 2.1 eV, a region where the photoluminescence spectra indicate that excitons are also generated.

In addition to large photocurrent density and high photovoltage, long term stability is another important challenge for solar water splitting devices. The Cu_2O photocathode with a 100 nm TiO_2 overlayer was tested under continuous stirring and chopped illumination with 10 min intervals for light and dark to simulate intermittent solar irradiation. Impressively, our sample is stable for more than 100 h in a pH 5 electrolyte at a bias potential of 0.5 V vs. RHE (Figure 2.5c), which is a significant step towards the criterion of a standalone overall PEC water splitting cell in a parallel tandem configuration. Stability under continuous illumination (Figure 2.8) was also studied with an electrolyte-refresh-strategy similar to a previous report.[39] The performance was demonstrated of a photocurrent density of 10 mA cm^{-2}, a photovoltage exceeding 1 V and stability beyond 100 h sets a new benchmark for Cu_2O towards solar water splitting. To show the wide applicability of the Ga_2O_3 layer on samples with different structures, studies were also carried out on planar Cu_2O samples made by electrochemical deposition. With a similar onset shift obtained for planar Cu_2O samples using a Ga_2O_3 layer (Figure 2.9), It is suggested that the enhancement in photovoltage is solely due to the advantages offered by the Ga_2O_3 layer. With the possibility of making semitransparent planar Cu_2O photocathodes, improved tandem devices with even higher solar-to-hydrogen conversion
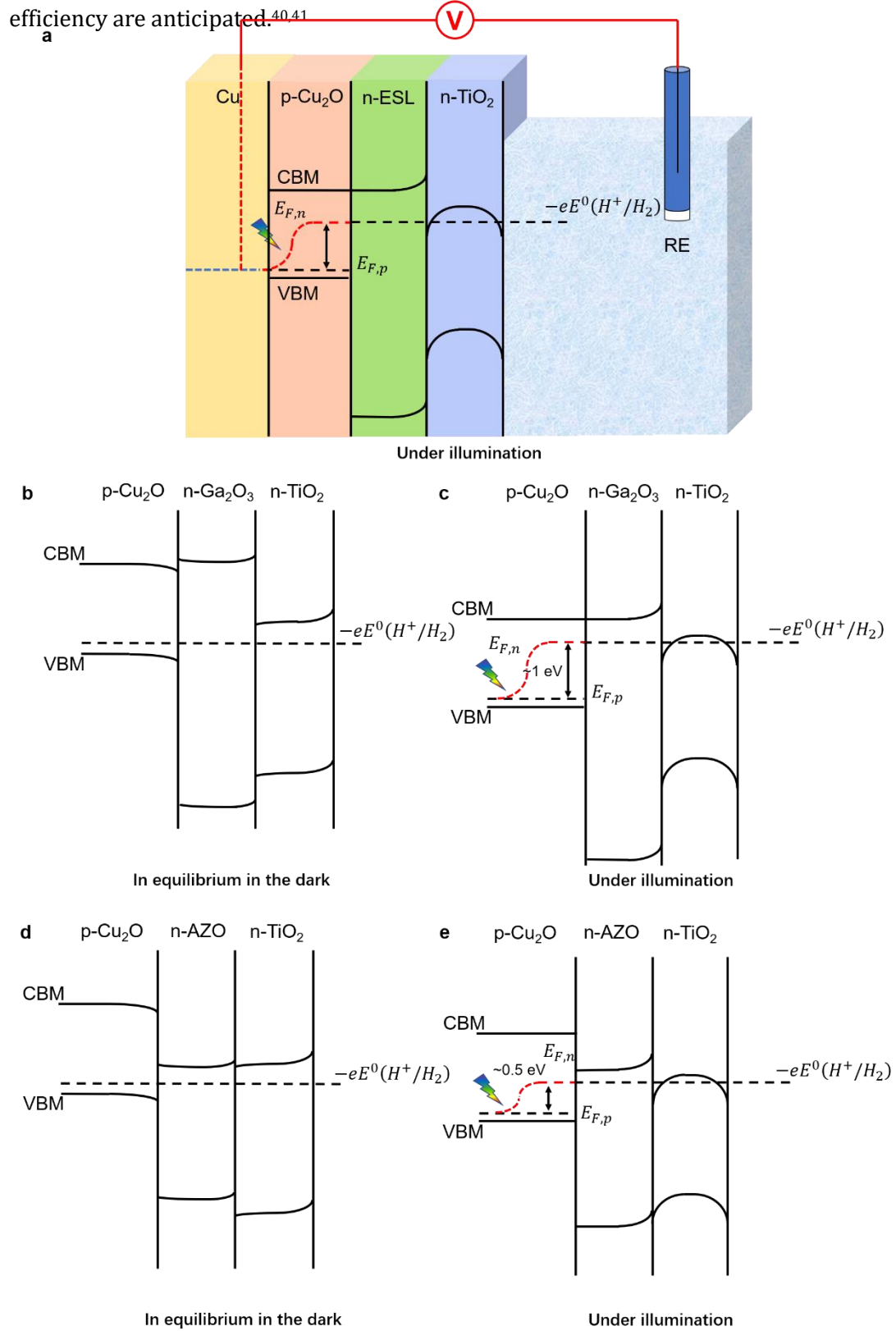
efficiency are anticipated.[40,41]

Figure 2.10 | Schematic illustration of PEC measurement and band diagrams for Cu₂O photocathodes.

a, Schematic illustration of Cu₂O/Ga₂O₃/TiO₂ photocathodes measurements under illumination. band

diagrams of b,c, Cu₂O/Ga₂O₃/TiO₂ and d,e, Cu₂O/AZO/TiO₂ in equilibrium in the dark and under
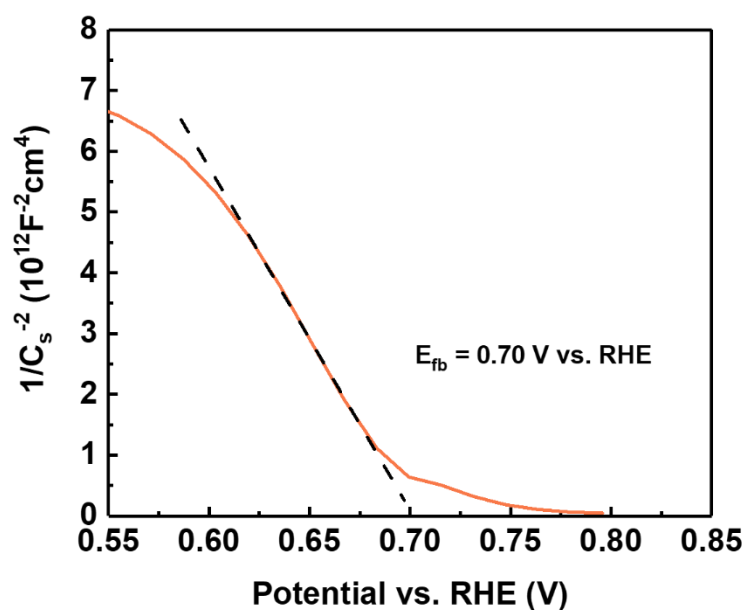
illumination.

Figure 2.11 | Mott-Schottky plot. Tested in pH 9 carbonate buffer solution with bare Cu_2O.

Distinct from many other metal oxide photoelectrodes for water splitting, the Cu_2O photoelectrode is a buried p-n junction. The origin of the electrical field for charge separation is the p-n junction between Cu_2O and the n-type layer rather than the semiconductor-electrolyte junction. Thus, the photovoltage of Cu_2O photoelectrode we measure originates from the quasi-Fermi level difference between the p-type Cu_2O and the n-type layer instead of the difference between flatband potential and reversible hydrogen potential, Figure 2.10a. Electrochemical impedance spectroscopy (EIS) measurement was carried out on a bare Cu_2O photoelectrode in pH 9 solution, and the Mott-Schottky plot of the data is shown in Figure 2.11. Based on the Mott–Schottky equation, the flatband potential of Cu_2O is determined to be 0.70 V vs. RHE, which is consistent with the literature.[6,34,42] However, we would not be able to achieve an onset potential of more positive than 0.7 V if the onset potential of the Cu_2O photoelectrode is determined by the flatband potential. Moreover, apart from serving as the protection layer, the TiO_2 layer functions as an ohmic contact as its conduction band minimum (CBM) is well aligned with the hydrogen evolution potential.[43] Thus, here the CBM of TiO_2 has no influence on the onset potential of the Cu_2O photocathode. To illustrate the above discussion, band diagrams of $Cu_2O/AZO/TiO_2$ and $Cu_2O/Ga_2O_3/TiO_2$ junctions in the dark and under illumination are depicted, Figure 2.10 b,c,d,e.
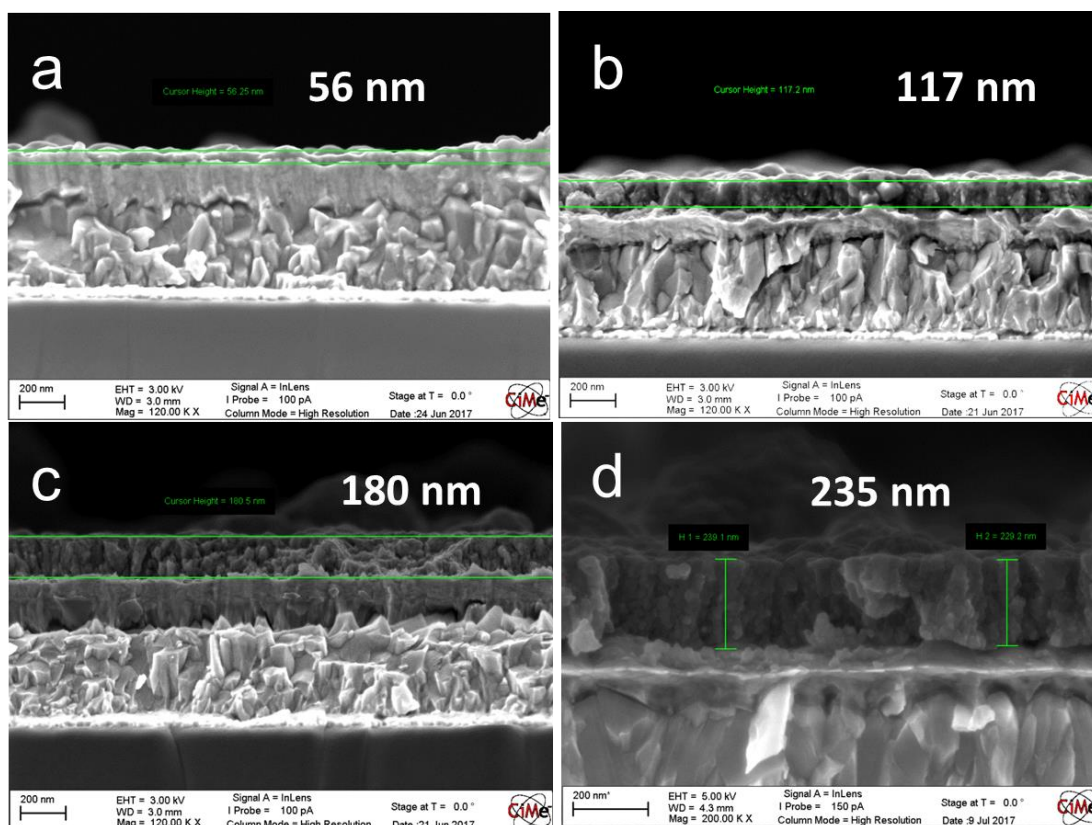
2.2.3   Preparation of pure Cu$_2$S film via cation exchange reaction.

Figure 2.12 | Cross-section SEM images of CdS films formed on FTO-Au substrates following different numbers of CBD treatments: a, one, b, two, c, three and d, four.

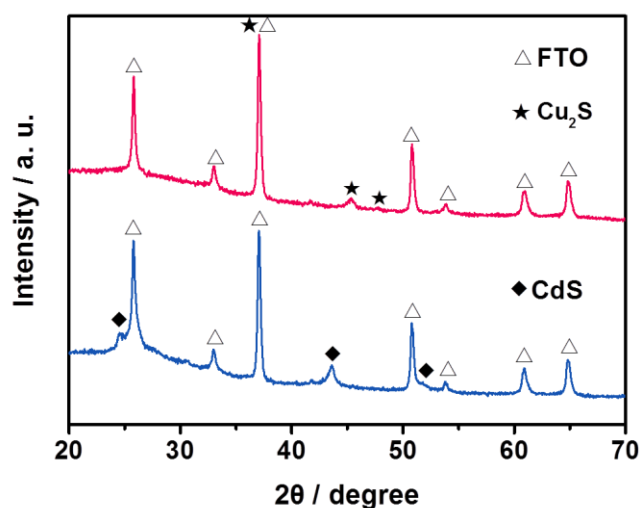The Cu$_2$S films were prepared from CdS films via solution processed cation exchange

Figure 2.13 | X-ray diffraction patterns of prepared films on FTO substrates before (blue) and after (red) ion exchange reaction.

reactions. Firstly, CdS films were deposited on Au coated FTO substrates by the traditional CBD method.[44] The Au layer was used to form an ohmic contact for efficient hole collection.[30] Each CBD deposition cycle resulted in a film with a thickness of around 60 nm. In order to get thick CdS films, we repeated the deposition several times. With four deposition cycles, we obtained CdS films with a thickness around 240 nm, Figure 2.12. Then, CdS films were immersed into the Cu$^+$ aqueous solution for the ion exchange reaction. With enough time, the CdS film would be completely transformed into Cu$_2$S, even for the films that were deposited for four times with a thickness of more than 200 nm. The thorough transformation was confirmed by the XRD patterns presented in Figure 2.13.

The CdS samples presented in this figure are deposited via four CBD cycles on bare FTO substrates. The diffraction peaks at 2θ of 24.6°, 43.6° and 51.8° match well with the hexagonal CdS pattern (JCPDS 75-1545). After the ion exchange reaction, these peaks disappeared and new peaks corresponding to hexagonal Cu$_2$S pattern (JCPDS 84-0209) at 2θ of 37.0°, 45.4° and 47.8° emerged, indicating the complete transformation of CdS into Cu$_2$S.
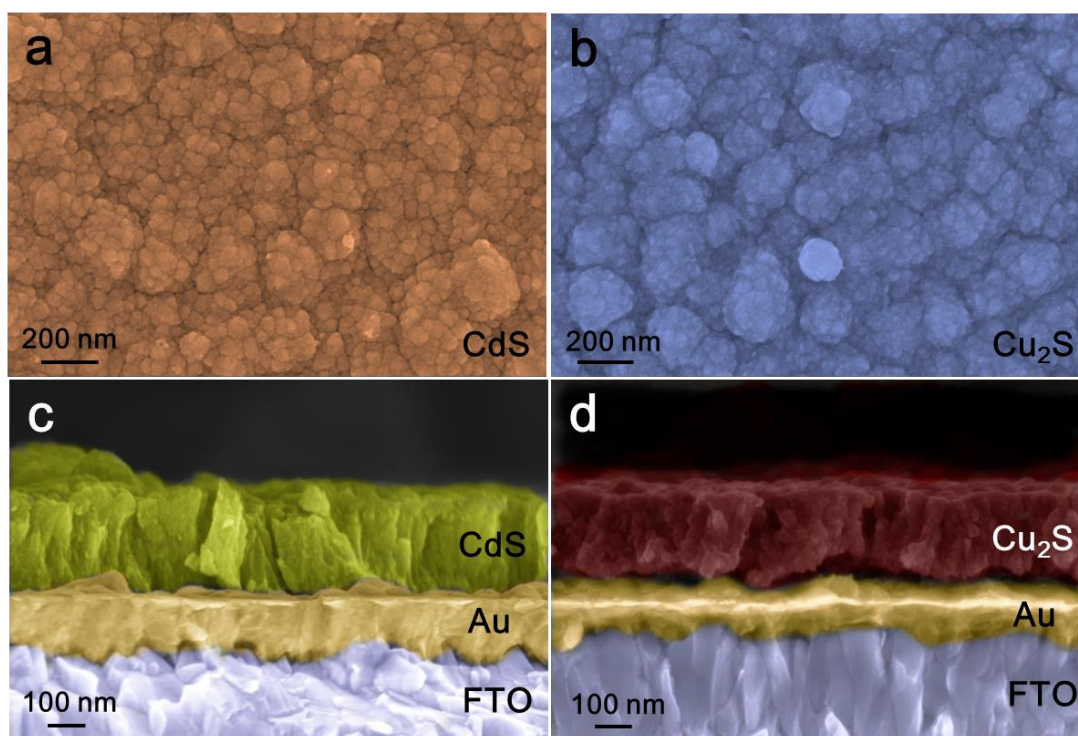

Figure 2.14 | Top surface a,b, and cross-section c,d, false-colored scanning electron microscopy images of CdS and Cu$_2$S films on Au/FTO substrates. The CdS film was prepared by repeating the chemical bath deposition four times.

Figure 2.14 displays the top surface and cross-section SEM images of the CdS film deposited via four CBD cycles and the derived Cu_2S film from the ion exchange reaction. The CdS film shows a relatively flat surface with small crystalline grains ranging from several nanometers to 50 nm, and it has a thickness of ~235 nm, Figure 2.14a and 2.14c. After cation exchange reaction with Cu^+ forming Cu_2S, the morphology and the thickness of the film were preserved with high fidelity due to the solidarity of the anionic framework, a hallmark of cation exchange in chalcogenides, Figure 2.14b and 2.14d.[45] This might be favored by the hexagonal crystal structure of both CdS and Cu_2S with similar unit cell sizes.
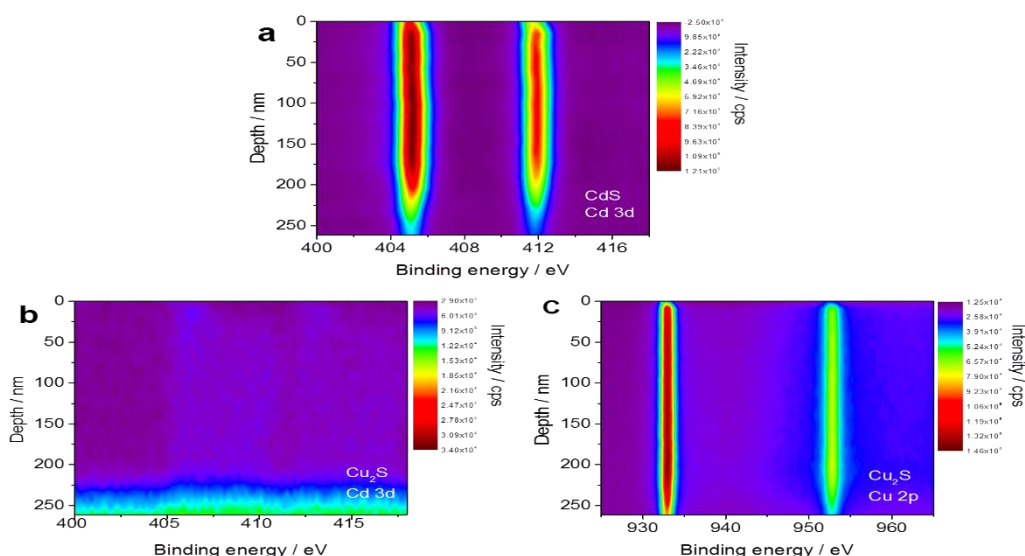

Figure 2.15 | X-ray photoelectron spectroscopy depth profiles of CdS and Cu_2S films. a, Cd 3d spectra of as-deposited CdS film (4 CBD cycles). b, Cd 3d and c, Cu 2p spectra after CBD transformation of CdS to Cu_2S. After cation exchange reaction, the Cu 2p signal from Cu_2S is present throughout the whole film, whereas Cd 3d peaks disappear.

To further verify the stoichiometry, we carried out XPS depth profiling measurements on the CdS film after 4 CBD cycles and the as derived Cu_2S film, Figure 2.15. The binding energies of 405.2 and 412.0 eV in the spectra corresponded to Cd $3d_{5/2}$ and Cd $3d_{3/2}$ core levels, respectively. These peaks remained at the same position across the depth of the film, indicating its homogeneity, Figure 2.15a. After the cation exchange reaction, the peaks of Cd 3d disappeared even at the bottom part of the film, Figure 2.15b, confirming the complete Cd ion replacement across the film. The new peaks at 932.7 eV and 952.5 eV belonged to the binding energies of Cu $2p_{3/2}$ and Cu $2p_{1/2}$ core levels, respectively, Figure 2.15c, and no satellite peaks were found in the higher binding energy region, which was consistent with the standard reference XPS spectrum of Cu 2p in Cu_2S.[24] Furthermore, the atomic ratio of Cu to S was verified to be 33 to 17 in the film, confirming the Cu_2S phase.
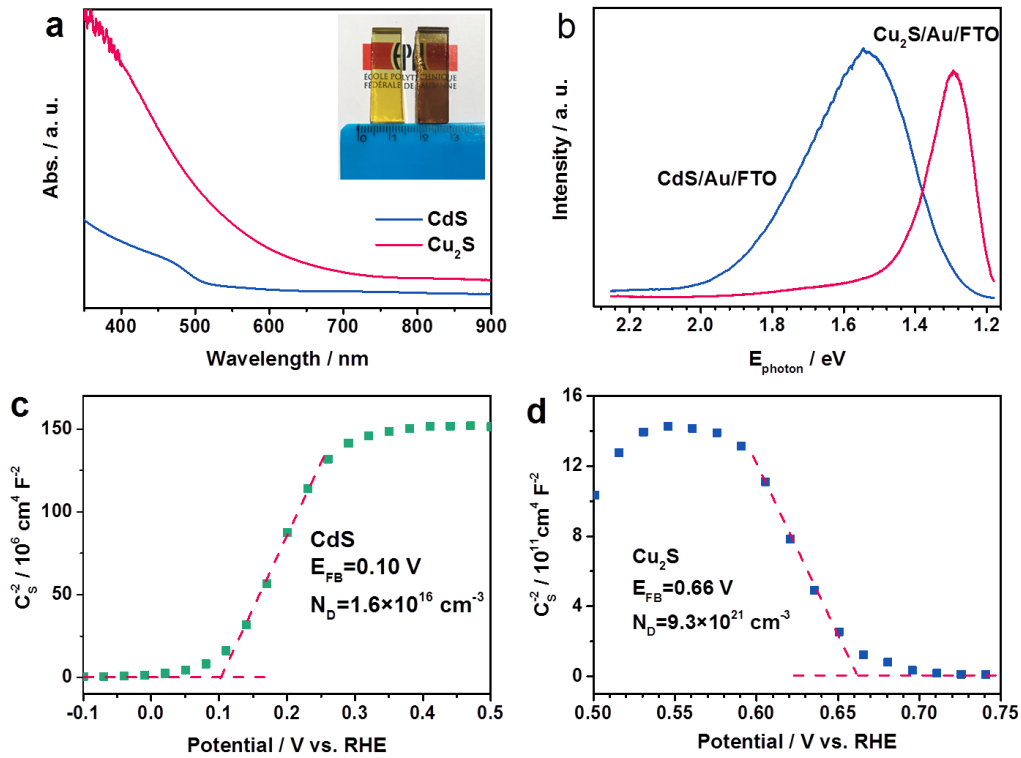
2.2.4   Optical and photoelectrochemical properties of Cu$_2$S films.

Figure 2.16 | a, UV-Vis absorption spectra of CdS and Cu$_2$S films measured in the transmission mode, b, Photoluminescence spectra of CdS and Cu$_2$S film performed at room temperature, and Mott−Schottky plots of c, CdS, d, Cu$_2$S films obtained from electrochemical impedance measurements in the dark in an electrolyte solution of 0.5 M Na$_2$SO$_4$ and 0.1 M KH$_2$PO$_4$ at pH 5.0 with an AC amplitude of 25 mV and a frequency of 259.75 Hz (other frequencies are presented in Figure 2.18).

The optical absorption properties of the films on FTO substrates were characterized by UV-vis-NIR spectrophotometer in the transmission mode, Figure 2.16a. The yellow CdS film absorbs from UV to the visible wavelength range with an absorption edge at 520 nm,
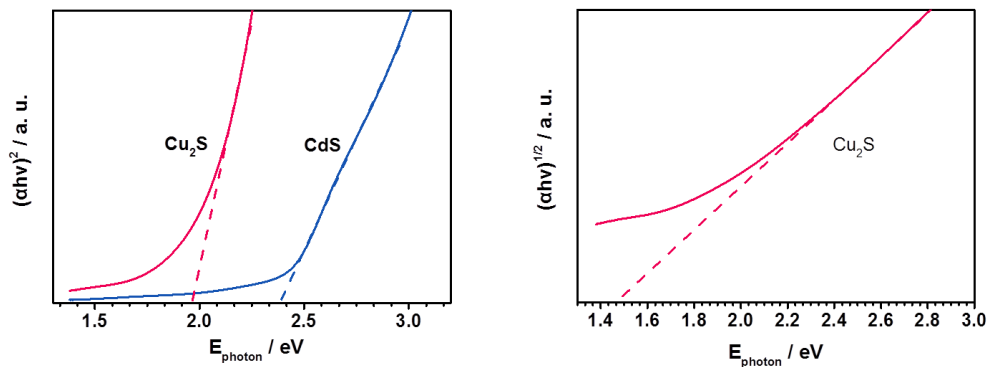

Figure 2.17 | Tauc plots of CdS and Cu$_2$S films in the transmission mode.

corresponding to a direct bandgap of 2.39 eV calculated from Tauc plot, Figure 2.17. After cation exchange with Cu^+, the color of the film turns brown which is apparent from the photo of the samples in the inset. Thus, the absorption of Cu_2S film extends to long wavelength range up to the infrared region. However, because the optical transition is indirect, there is no sharp absorption edge in the curve. Nevertheless, the derived Tauc plot of Cu_2S revealed a direct and an indirect bandgap of 1.96 and 1.47 eV, respectively, Figure 2.17. Under 532 nm laser excitation, the CdS film on Au coated FTO substrate shows a broad band emission centered around 1.54 eV, Figure 2.16b, which is known as the "red" emission and is related to sulfur vacancies.[46] After ion exchange, the "red" emission disappeared. The Cu_2S film only exhibits a strong photoluminescence near the band edge region with a peak centered at 1.29 eV, indicating the complete conversion and the excellent photoelectronic property of the film.
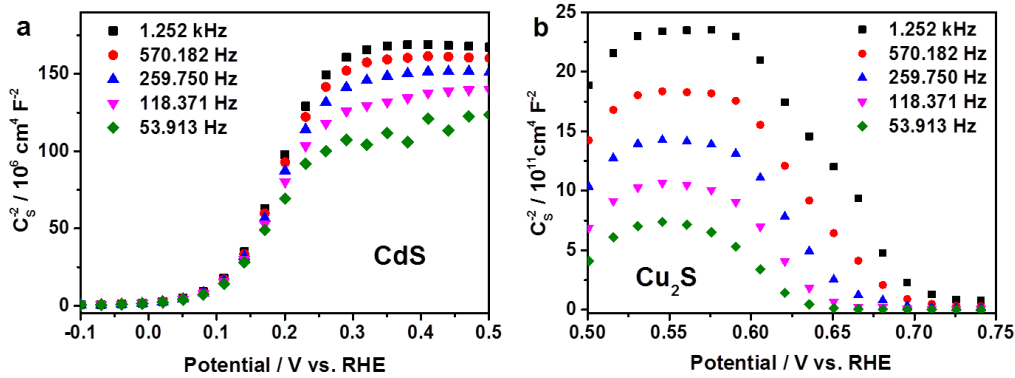

Figure 2.18 | Mott−Schottky plots of a, CdS and b, Cu_2S films obtained from electrochemical impedance measurements in the dark in an electrolyte solution of 0.5 M Na_2SO_4 and 0.1 M KH_2PO_4 at pH 5.0 with an AC amplitude of 25 mV at different frequencies.

In addition to the optical properties, the charge carrier density and the flat band potential of the materials are also important parameters for photoelectrochemical water splitting. We derived charge carrier densities (N_A) and flat band potentials (E_{fb}) of planar CdS and Cu_2S electrodes from electrochemical impedance spectroscopy (EIS) measurements using the Mott−Schottky equation,

$$\left(\frac{A}{C_{bulk}}\right)^2 = \frac{2}{e\varepsilon_r\varepsilon_0 N_A}\left(E - E_{fb} - \frac{kT}{e}\right)$$

where e is the elementary charge, ε_r = 8.9 and $\sim$4 are the relative permittivity of CdS[47] and Cu_2S,[28] respectively, ε_0 is the permittivity of vacuum, k is Boltzmann constant, and T is the absolute temperature. The active area, A, is roughness corrected for both samples. The

roughness factor was estimated from SEM images taken in cross-sectional and top view and was on average 1.2 for both samples. The positive slope of the linear region in the Figure 2.16c indicates the n-type characteristic of the CdS film, whereas a negative slope confirms the p-type characteristic of Cu_2S film, Figure 2.16d. The measured flat band potentials of planar CdS and Cu_2S samples were 0.10 and 0.66 V *versus* RHE, respectively, and their charge carrier densities were found to be 1.6×10^{16} and 9.3×10^{21} cm^{-3}, respectively. These results indicate that the Cu_2S and CdS films are suitable for constructing a p-n junction for solar water splitting, which are in the similar range as other reports on CdS[44] and Cu_2S[19].

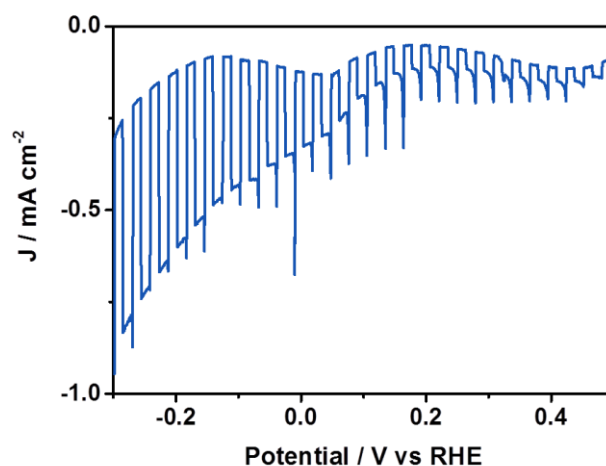### 2.2.5 PEC performance of the $Cu_2S/CdS/TiO_2/RuO_x$ photoelectrode

Figure 2.19 | Chopping LSV curve of $Cu_2S/CdS/TiO_2/RuO_x$ film in which CdS layer was prepared by conventional NH_3 based CBD method.

In order to use Cu_2S for photoelectrochemical water splitting, a protection layer must be employed, as bare Cu_2S is unstable under water splitting conditions. Furthermore, to enhance charge separation, formation of a buried p-n junction on Cu_2S is demanded. Here, we used CdS as an n-type buffer layer and TiO_2 as a surface protection layer. Conventional CdS CBD methods use high concentration of $NH_3 \cdot H_2O$ as the complexing agent, which will gradually dissolve and leading to partial oxidation of the Cu_2S film, decreasing photoelectrochemical performance, Figure 2.19. To overcome this issue, we added N_2H_4 as a reductive agent in the deposition solution and used NH_4Cl as a pH buffer. With this novel method, the oxidation of Cu_2S during the deposition of CdS was prevented, resulting in films with high photoactivity. The CdS layer is around 10-15 nm in thickness as revealed from the SEM image in Figure 2.20a. The TiO_2 protection layer was deposited by ALD,
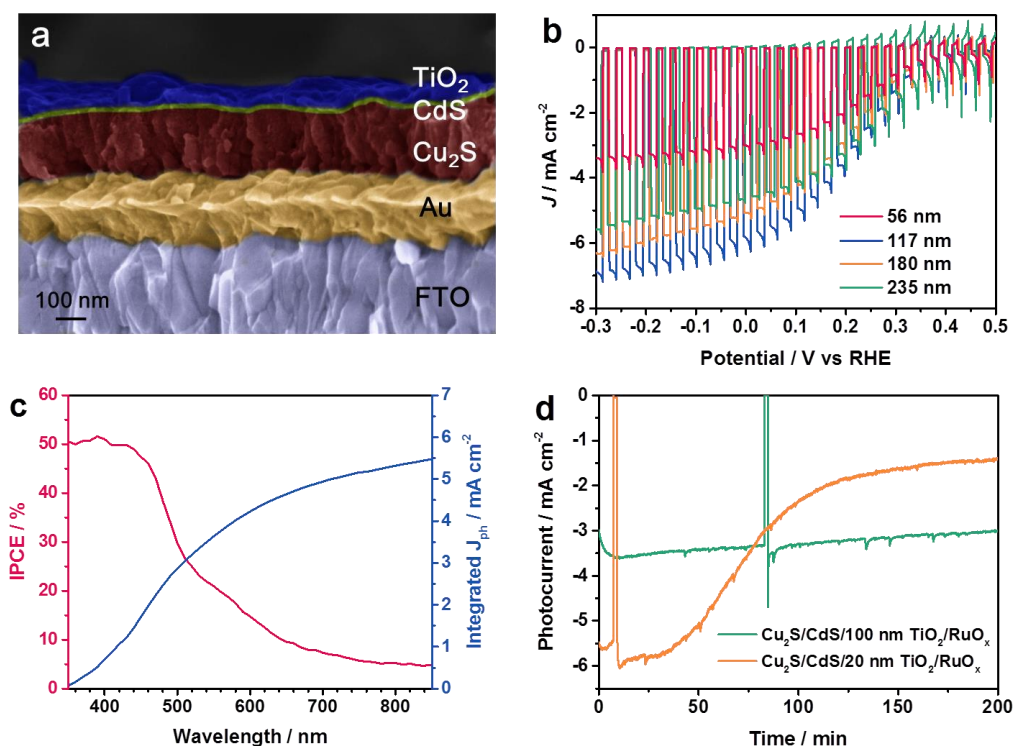
Figure 2.20 | Photoelectrochemical properties and morphology of the Cu_2S photocathodes. a, Cross-section false-colored SEM image of the optimized Cu_2S photocathode ($FTO/Au/Cu_2S/CdS/TiO_2$) with the Cu_2S layer thickness of *ca*. 120 nm. b, *J*−E curves of Cu_2S photocathodes with different thickness under simulated chopped AM 1.5G illumination. c, IPCE spectra under monochromatic illumination of the optimized Cu_2S photocathode at an applied bias of 0 V vs RHE. d, Photocurrent density measured under constant bias at 0 V vs RHE under simulated AM 1.5G illumination. All measurements were performed in pH 5.0 electrolyte.

enabling homogenous and uniform coating on the surface of the Cu_2S-CdS film. To improve the charge transfer from electrode to electrolyte, the hydrogen evolution reaction (HER) catalyst RuO_x with thickness around 40 nm was deposited on the surface by photoelectrochemical deposition, Figure 2.21.[29]

The photoelectrochemical performance of the completed Cu_2S photocathodes ($Cu_2S/CdS/TiO_2/RuO_x$) was evaluated in pH 5 electrolyte, Figure 2.20b. Based on the thickness of the Cu_2S absorber layer (corresponding to the initial CdS layer thickness varied by repeating the CBD deposition cycles), the electrodes exhibited different photocurrent densities. Initially, the photocurrent density increased as the Cu_2S layer became thicker. However, above a Cu_2S layer thickness of 120 nm, the photocurrent density started to decrease. This might be because of the balance between light absorption
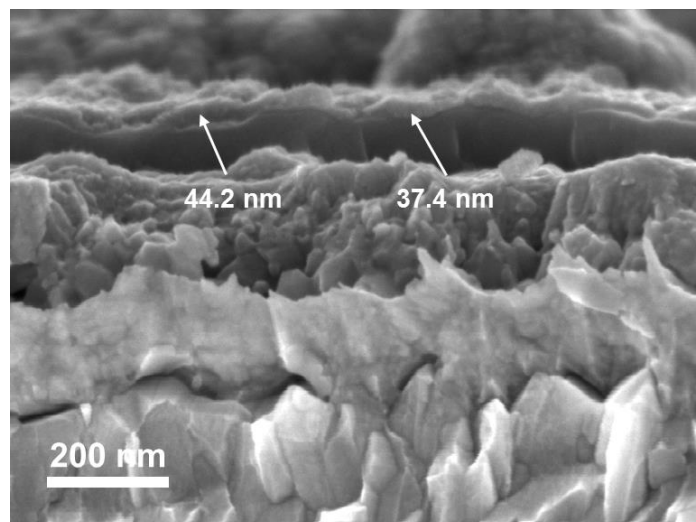
Figure 2.21 | Cross-section scanning electron microscopy images of FTO/Au/Cu$_2$S/CdS/TiO$_2$ (100 nm)/RuO$_x$ photocathode (Arrow indicates the thickness of RuO$_x$ layer)

and carrier transport as the minority carrier diffusion length of Cu$_2$S is around 100 to 400 nm, and thicker films will reduce the electron collection efficiency. The optimized Cu$_2$S photocathode reached a photocurrent density of around 7.0 mA cm^{-2} at -0.3 V versus RHE. The cross-section SEM image of this electrode is illustrated in Figure 2.20a. Incident photon to current efficiency (IPCE) measurement was carried out at 0 V versus RHE to show the wavelength dependent photoresponse of the electrode, Figure 2.20c. In agreement with the absorption spectrum of the Cu$_2$S, the electrode showed a broad response from the ultraviolet to the near-infrared range with a peak efficiency of 51% at 400 nm, confirming the excellent light-harvesting capability. Integrating the IPCE over the standard AM 1.5G spectrum generated a photocurrent density of around 5.5 mA cm^{-2}, consistent with the value obtained from chopped light current–voltage measurement. The stability of the sample was characterized by chronoamperometry measurements at 0 V versus RHE under continuous illumination, Figure 2.20d. With a thin TiO$_2$ (20 nm) layer, the photocurrent showed a quick decay after 50 min continuous illumination. This might be due to the insufficient surface coverage with few ALD cycles, leaving pinholes inside the film. In order to achieve better stability, we used a thicker TiO$_2$ protection layer (100 nm), which enabled 90% retention of the photocurrent after continuous illumination test for 200 min. However, the photocurrent of the sample with thick TiO$_2$ (100 nm) protection layer is lower than that of samples with thinner TiO$_2$ (20 nm) layer, which might be due to increased resistance of the TiO$_2$ layer. The brief drop to zero current, resulting from shortly blocking the illumination at ~80 min shows that the measured current is indeed from photoexcitation. After the stability measurement, no obvious damage is observable
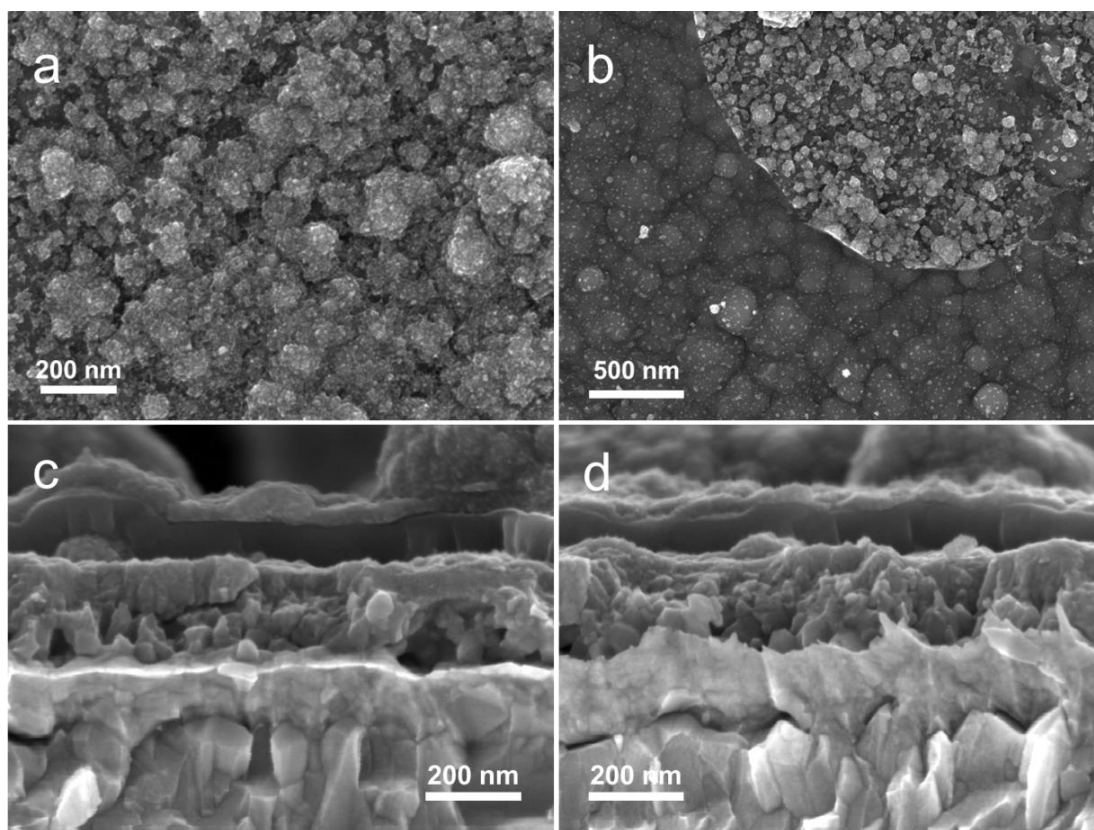
72

Figure 2.22 | Top surface a,b, and cross section c,d, scanning electron microscopy images of FTO/Au/Cu$_2$S/CdS/TiO$_2$ (100 nm)/RuO$_x$ photocathode after stability test

from the top view and cross-section SEM images, Figure 2.22. Degradation might be due to the slow penetration of protons through the amorphous TiO$_2$ ions, which attacked the junction underneath.

2.2.6   Band alignments of Cu$_2$S/CdS junction

To derive the band alignment at the Cu$_2$S-CdS junction, we carried out UV-Vis-NIR absorption and XPS measurements. The bandgaps of Cu$_2$S and CdS films were determined to be 1.47 and 2.39 eV, respectively from the Tauc plots, Figure 2.17. The corresponding valence band maximum (VBM) for Cu$_2$S and CdS were fitted to be 0.14 and 1.24 eV, respectively, from the Fermi level by linear extrapolation of the low binding energy region near the Fermi edge, Figure 2.23a. From these results, we derived the band diagram of the Cu$_2$S and CdS heterojunction as illustrated in Figure 2.23b, which is similar to the reported band alignment of Cu$_2$S/CdS thin film solar cells.[48] They form a type II junction, spontaneous electron transfer from n-CdS to p-Cu$_2$S equalizes their Fermi level, setting up an electrical field that assists in electron extraction from the Cu$_2$S to the CdS layer. Without the CdS layer, the Cu$_2$S/ TiO$_2$/RuO$_x$ photocathode showed obvious dark current and very
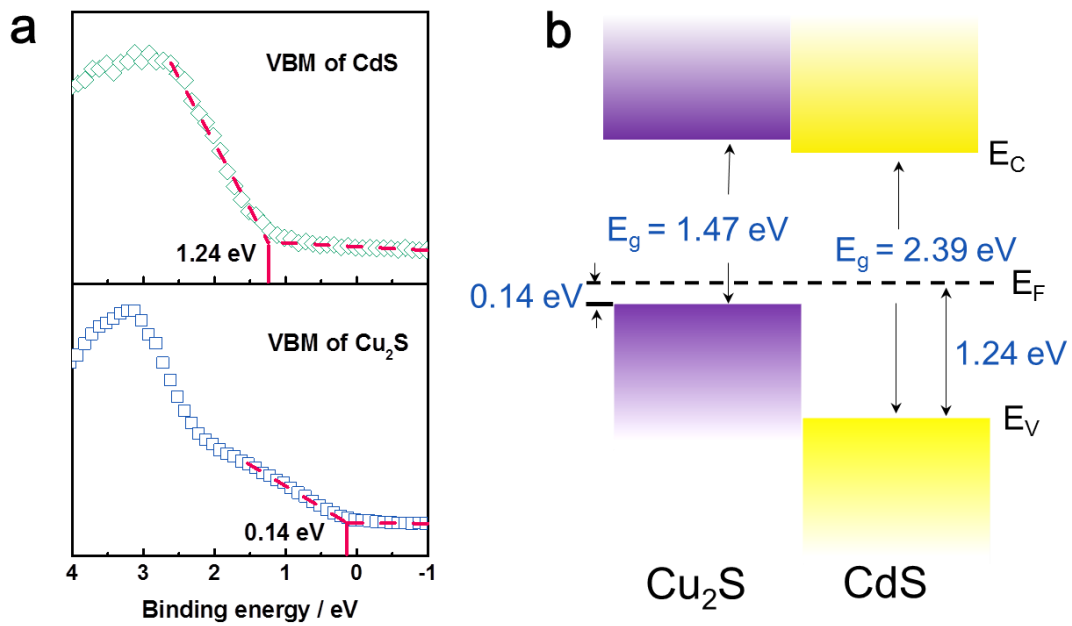
Figure 2.23 | a, Valence band spectra of CdS and Cu$_2$S films, b, Schematic band energy diagram of Cu$_2$S and CdS heterojunction.

low photocurrent due to the high recombination rate of charge carriers in the Cu$_2$S layer, Figure 2.24.

To our knowledge, this is the first time that solution processed Cu$_2$S has been used for solar water splitting with impressive performance. Because of its small bandgap, it is an appealing bottom photoelectrode for tandem solar water splitting devices. To further
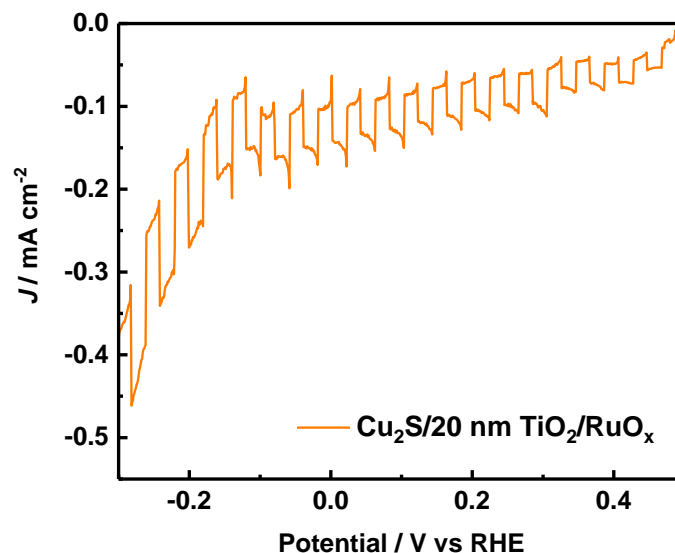
Figure 2.24 $J{-}E$ curves of Cu$_2$S/TiO$_2$ (20nm)/RuO$_x$ photocathode under simulated chopped AM 1.5G illumination in pH 5.0 electrolyte.

increase the photocurrent density, nanostructured electrodes will be used in the future to ensure sufficient light harvesting and provide a short electron transport pathway at the same time. New buffer layers with appropriate band alignment to Cu_2S should be studied to replace the toxic CdS. Though Cu_2S photoelectrodes demonstrated a relative stable performance with thick protection layer, their stability issue and light filtering remains a problem, which can be addressed by using a buffer layer which is transparent in the visible and impairs the copper diffusion.

2.3 Conclusion

In both cases, remarkable performance was achieved by building p-n heterojunctions for efficient charge separation. Apart from enhanced photocurrent densities, the photovoltage of Cu_2O was improved by 0.5 V, rendering the new Cu_2O photocathode a 1 V photovoltage, which is one of the best among all photocathodes. From the detailed band energy analysis, we verified the origin of the photovoltage gain in the appropriate band alignment between p-type Cu_2O and n-type Ga_2O_3. This is also valid in the case of the Cu_2S/CdS junction. With the advantage of nanostructured Cu_2O photoabsorber, which allows the establishment of a radial heterojunction, and in the case of Cu_2S, an optimized CBD process resulting in a pure Cu_2S phase, unprecedent performances were achieved for both Cu_2O and Cu_2S photocathodes. In particular, due to the development of Cu_2O, a record efficiency of unassisted oxide solar water splitting tandem system was possible. This will be discussed in detail in the following chapters. The successful heterojunction engineering examples will provide a strategy, which could be beneficial for development and understanding of both PEC and PV devices.

2.4 Methods

2.4.1 Fabrication of Cu_2O photocathodes

Preparation of Cu_2O nanowire photoelectrodes. F-doped SnO_2 substrates (FTO, G2E TEC-15) were cleaned by sequential ultrasonic treatments in 2% Hellmanex water solution (30 min), acetone (15 min) and deionized water (15 min). Then, 1.5 μm of Cu (99.995%) was sputtered on FTO using Alliance-Concept DP 650 with a growth rate of 2.65 nm s^{-1}. Samples are subsequently anodized in 3 M KOH (99.98%, metal basis) solution to form $Cu(OH)_2$ nanowires as precursor. Using a large area gold-coated FTO glass as the counter electrode, anodization was performed at a constant current density of 6 mA cm^{-2} at room temperature until a compliance voltage of 2 V was reached. After being rinsed with copious amounts of water, samples were dried in air overnight. To transform $Cu(OH)_2$ into Cu_2O, samples are annealed at 600 °C in a tube furnace under high purity Argon (Ar) flow (99.9995%, ALPHAGAZ) for 4 h. Following that, an extra blocking layer of Cu_2O was coated on Cu_2O nanowire samples by 30 min electrodeposition in a buffered copper sulfate solution. For the preparation of the buffered copper sulfate solution, 7.98 g of $CuSO_4$, 21.77 g of K_2HPO_4, and 67.5 g of lactic acid were dissolved in 250 mL of H_2O, and the pH of electrolyte was adjusted to 12 using a KOH (2 M) solution; the final solution totals around 1 L. Cu_2O blocking layers were deposited at a constant current density of -0.1 mA cm^{-2} (galvanostatic mode) using a source meter (Keithley 2400) in a two-electrode configuration (a Pt mesh served as the counter electrode). This deposition condition was also used for the preparation of planar Cu_2O samples, with the exception that the deposition time was 100 min.

Atomic layer deposition of overlayers. Atomic layer deposition coating was implemented with a thermal ALD system (Savannah 100, Cambridge Nanotech). The top part of the sample was masked by Kapton tape for protecting the electric contact area prior to the deposition of thin n-type semiconductor layers. For preparation of Cu_2O NW samples with Al: ZnO (AZO) layer, 20 nm of AZO, followed by 20 nm of TiO_2 was coated using the previous described configurations. For the preparation of Cu_2O NW samples with a Ga_2O_3 layer, exposure mode was employed for better coverage over the nanowires. Gallium oxide was deposited at a substrate temperature of 150 °C using Bis(μ-dimethylamino)tetrakis(dimethylamino)digallium (98%, STREM Chemicals) as the gallium precursor and deionized water as the oxidant. The gallium precursor was heated

to 130 °C to provide enough vapor pressure, and it was introduced into the chamber under a nitrogen flow of 10 sccm, with 1 s pulse time, 2 s exposure time and 30 s pumping time. The growth rate for Ga_2O_3 on test silicon wafers with native oxide was determined by ellipsometry (Sopra GES 5E) on test silicon wafers with native oxide, and found to be approximately 1.5 Å per cycle. For all Cu_2O photocathodes with Ga_2O_3 layer, 135 cycles of Ga_2O_3 were deposited, resulting in thickness of approximately 20 nm. TiO_2 was deposited at a substrate temperature of 150 °C using Tetrakis(dimethylamino)titanium (99.999%, Sigma) with a precursor temperature of 75 °C. Hydrogen peroxide (50% in water, stabilized, Aldrich) was used as the oxidant. H_2O_2 was stored in 4 °C and the cylinder was freshly refilled before each deposition. Using a nitrogen flow of 5 sccm, TiO_2 was deposited at an approximate growth rate of 0.59 Å per cycle with 0.1 s pulse time, 2 s exposure time and 30 s pumping time. Deposition cycle numbers are determined by the required thickness and calculated using the previously mentioned growth rate. Samples for the 100-hour stability test were protected with a 100 nm TiO_2 ALD layers and all other samples were protected with 20 nm TiO_2 layers deposited by ALD.

RuO_x hydrogen evolution catalyst deposition. For the RuO_x and the nickel molybdenum (NiMo) catalysts used in this study, galvanostatic photoelectrochemical deposition was employed. In the case of the RuO_x deposition, the process used was similar to that of previously described. Briefly, the deposition was done in a 1.3 mM $KRuO_4$ solution at a current density of -28 µA cm^{-2} under simulated one sun illumination. Deposition time was fixed at 6 min. A platinum wire was used as the counter electrode.

2.4.2 Materials, optical and photoelectrochemical characterizations

Materials characterizations. XRD patterns were acquired with a Bruker D8 Discover diffractometer in the Bragg-Brentano geometry, using Cu Kα radiation and Ni β-filter. Diffraction spectra were recorded between 2θ of 20° and 80° at a scan rate of 1° min^{-1} with a step width of 0.02°. Raman spectra were carried out on a LabRAM HR Raman spectrometer using a 532 nm laser for excitation. A high-resolution scanning electron microscope (SEM) (Zeiss Merlin) with in-lens detector was used for SEM imaging. X-ray photoelectron spectroscopy (XPS) was carried out using a PHI VersaProbe II scanning XPS microprobe (Physical Instruments AG). Analysis was performed using a monochromatic Al Kα X-ray source of 24.8 W power with a beam size of 100 µm. The spherical capacitor analyser was set at 45° take-off angle with respect to the sample surface. The pass energy was 46.95 eV yielding a full width at half maximum of 0.91 eV for the Ag 3d 5/2 peak.

Samples experienced less than 6 min of ambient air exposure during transfer and mounting.

Photoelectrochemical and electrochemical characterization. The photo-electrochemical performance of samples was evaluated in a three-electrode configuration using Cu_2O photocathodes as the working electrode, a Pt wire as the counter electrode and Ag/AgCl/sat. KCl as the reference electrode. For measurements in solutions of different pH, the pH 5.0 buffer was prepared using a combination of 0.5 M Na_2SO_4 and 0.1 M phosphate solution, while the pH 9.0 buffer was made by adjusting pH of 0.1 M Na_2CO_3 and 0.1 M $NaHCO_3$ solution and the pH 12 solution was prepared by tuning pH of 0.2 M KOH solution. A potentiostat/galvanostat (BioLogic, SP-200) was used to acquire the photoresponse under chopped illumination from a LCS-100 solar simulator (Newport, Class ABB) with an AM 1.5G filter. The PEC cell was fixed at a position determined by measuring the short-circuit current on a calibrated silicon diode with a KG 3 filter. Calibration was carried out across the relevant wavelength range of 300-800 nm. All linear sweep voltammetry scan rates were 10 mV s^{-1}. Incident photon to current efficiency (IPCE) was measured under light from 300 W Xe lamp through a monochromator (TLS-300XU, Newport). The photoresponse was compared with that of a calibrated Si photodiode (FDS100-CAL, Thorlabs) to determine the IPCE at each wavelength. Tests were carried out using chronoamperometry at 0 V vs. RHE in a homemade cell with a quartz window (Edmund Optics). Steady current was recorded 5 seconds later than wavelength shift with white LED bias to minimize transient current interference. For the 100-h stability test, the electrolyte was replaced several times. Current density was examined with a chronoamperometry technique at a potential of 0.5 V vs. RHE with continuous stirring and light chopping at 10 min interval for both light and dark. The EIS measurement was carried out for bare Cu_2O nanowire sample in pH 9 carbonate buffer solution. The space-charge capacitance (C_{SC}) of semiconductor varies as a function of the applied potential according to the Mott-Schottky equation shown below. Flat band potential E_{fb} and charge carrier density can be extracted from the x-intercept and the slope of the plot using this equation:

$$\left(\frac{A}{C_{bulk}}\right)^2 = \frac{2}{e\varepsilon\varepsilon_0 N_A}\left(E - E_{fb} - \frac{kT}{e}\right)$$

where e is the electron charge, ε = 7.5 is used as the relative permittivity of Cu_2O,[49] ε_0 is the permittivity of vacuum, T is in thermodynamic temperature and E is the applied potential. As shown in the Figure 2.11, the flat band potential is about +0.70 V vs. RHE and

the carrier concentration calculated is around 1.40×10^{18} cm^{-3}, which agreed with previous results.[42,50] Potential values were transformed to the reversible hydrogen electrode scale through the equation: $E_{RHE} = E_{Ag/AgCl(KCl\ sat.)}$ + 0.197 V +0.059 V * pH.

Photoelectrochemical measurements of photoanodes and tandem system were performed with standard three-electrode configurations; photoanode as the working electrode, Pt mesh as the counter electrode and Ag/AgCl (3M KCl) as the reference electrode. The scan rate for the current-voltage (*J-V*) curve was 20 mV/sec. For water oxidation experiments, 0.2 M potassium borate (KBi) electrolyte (made by using DI water, 1.0 M KOH (Samjun, >99%) and H_3BO_3 (≥99%, Sigma Aldrich) (pH ~9.0) was used as the main electrolyte. Electrolyte was used after purged with Ar gas (30 minutes) to remove dissolved oxygen. To measure the degree of charge separation, 1.0 M Na_2SO_3 (>98%, Sigma Aldrich) was added to the main electrolyte. Potentials were recorded with correction by the Nernst relation $E_{RHE} = E_{Ag/AgCl(KCl\ sat.)}$ + 0.197 V +0.059 V * pH, in which $E_{Ag/AgCl}$ is applied bias potential and 0.209 is a conversion factor from the Ag/AgCl electrode to the RHE scale. All electrochemical data were recorded by using a potentiostat (IviumStat, Ivium Technologies). A 300 W Xenon lamp was used to make simulated 1 sun light irradiation condition (AM 1.5G, 100 mW/cm^2) by using a solar simulator (Oriel 91160) with an AM 1.5G filter calibrated with a reference cell certified by the National Renewable Energy Laboratories, USA.

Optical measurements. The UV-vis absorption spectra of the AZO and Ga_2O_3 samples on quartz substrates were characterized by a UV–vis-NIR Spectrophotometer (Cary) in transmission mode, and the absorption spectra Cu_2O was derived from the Kubelka–Munk theory using diffuse reflectance spectra measured with an integrating sphere. UV-vis absorbance of $BiVO_4$ film was measured with a UV-vis spectrometer (UV-2401PC, Shimadzu). As a reference, BaSO4 powder attached on FTO was used. The optical band gaps of Cu_2O, AZO and Ga_2O_3 were determined from liner extrapolation of Tauc plots, $(\alpha h\nu)^{1/n}$ versus ($h\nu$) curve assuming direct allowed transition ($n = 1/2$). Steady state photoluminescence spectra were acquired with a LabRAM HR Raman spectrometer with a 532 nm laser for excitation. Confocal laser scanning fluorescence images were captured at 25°C using Leica Application Suite X software on a confocal laser scanning microscope (Leica TCS SP8). A HC PL APO oil objective (63x/1.40) was used. A pulsed white light laser (set at 514 nm) was used for excitation. Identical excitation power and gain settings (values set to obtain the best dynamic range of the PMT detectors) were used to capture both images (and both channels in each image). Single plane 512x512 images were

obtained from a unidirectional scan (400 Hz speed) with line accumulation of 12. The pinhole size was 1 Airy unit. Acquisition was done at a resolution of 72 nm in xy and an image bit depth of 8. Both the channels were pseudo-colored. Then, linear brightness and contrast adjustments done equally to identical channels in both images. The scale bars for the pseudo color assignment after these adjustments are shown with the images.

2.4.3 Fabrication of Cu$_2$S photocathodes

CdS film by Chemical Bath Deposition. Firstly, 150 nm Au was coated on FTO as substrates by DC sputtering at room temperature with Alliance-Concept DP 650 system. The CdS film was then deposited onto the Au surface by chemical bath deposition as reported elsewhere.[51] Typically, the substrates were immersed in 40 mL aqueous solution containing 133 mg Cd(CH$_3$COO)$_2$·2H$_2$O (Sigma-Aldrich, 98%), 134 mg NH$_4$Cl (Fluka, ≥99.5%) and 5 mL 25% NH$_3$·H$_2$O (VWR Chemicals, Analytical) and heated to 70 °C. Then 10 mL aqueous solution with 1.25 g (NH$_2$)$_2$CS (Sigma-Aldrich, ≥99.0%) was added into the previous solution to form CBD solution. The deposition solution was mildly stirred at 70 °C for 10 min. Then the substrates were taken out of the solution, rinsed with water and dried with air gun. CdS films with various thicknesses were formed by repeating this procedure with different numbers of CBD treatments.

Cation exchange to Cu$_2$S Films. The cation exchange reaction was performed in a 100 mL 3-neck flask according to a previous report.[26] Firstly, 30 mL 1.0 M HCl solution was neutralized to pH 7.0 by dropwise addition of 35 wt% hydrazine (N$_2$H$_4$) solution (Aldrich) (please note that the reaction of HCl and hydrazine involves corrosive, flammable, and toxic substances and is highly exothermic, and must be performed with great care). Additional deionized water was added to get a 50 mL solution. The solution was then purged with argon gas throughout the whole reaction process. After being purged for 5 min at room temperature, 0.40 g CuI (Riedel-de Haën, ≥99%) was quickly added to the solution and the temperature was raised to 90 °C. Then CdS films with different thickness were immersed into the solution for 30 minutes to achieve the total conversion to Cu$_2$S.

CBD of CdS layer on Cu$_2$S films. The CdS top interface layer was also formed by CBD, but employing a variation of the method described above for thick CdS films. The CBD solution was made by dissolving 160 mg Cd(CH$_3$COO)$_2$·2H$_2$O, 134 mg NH$_4$Cl, 3 mL 25% NH$_3$·H$_2$O and 180 μL 35 wt% hydrazine solution into 40 mL deionized water. It was heated to 70 °C and the Cu$_2$S films were immersed in to the solution for 1.5 min. Then, 10 mL aqueous solution with 1.25 g (NH$_2$)$_2$CS was added and the mixture solution kept at 70 °C for 6 min.

Then the substrates were taken out of the solution, rinsed with water and dried with air gun.

Atomic Layer Deposition of TiO₂ as Protecting Layer. The protecting layers were deposited by ALD (Savannah 100, Cambridge Nanotech).[34] TiO_2 was deposited at 150 °C using tetrakis-dimethylamino titanium (TDMAT) and H_2O as the Ti and O precursors, respectively. To ensure appreciable vapor pressure, TDMAT was heated to 75 °C. Typically, 340 cycles and 1700 cycles deposition gives 20 nm and 100 nm TiO_2 film, respectively.

Deposition of RuOₓ as a catalyst. For the deposition of RuO_x catalysts, a 15 mL solution containing 4.0 mg of $KRuO_4$ was used.[7] The catalyst solution was fresh made before each deposition. Typically, samples were catalyzed at a current density of -30 µA cm^{-2} for 15 min under illumination.

2.4.4   Materials and photoelectrochemical characterizations

Material Characterizations. The XRD patterns were acquired with PANalytical Empyrean system (Theta-Theta, 240mm) equipped with a PIXcel-1D detector, Bragg-Brentano beam optics and parallel beam optics, using Cu Kα radiation (1.540598 Å) and a Ni β-filter. Spectra were acquired with reflection transmission spinner from $2\theta = 20°–80°$ at a scan rate of 1° min^{-1} and the reflection patterns were matched to the PDF-4+ database (ICDD). The optical properties of the films were characterized with a Cary 5 UV–Vis-NIR spectrophotometer. Absorbance spectra were calculated according to Kubelka–Munk theory. The morphology of the films was characterized using a high-resolution scanning electron microscope (ZEISS Merlin). X-Ray Photoelectron Spectroscopy (XPS) measurements were carried out using a PHI VersaProbe II scanning XPS microprobe (Physical Instruments AG, Germany). Analysis was performed using a monochromatic Al Kα X-ray source of 24.8 W power with a beam size of 100 µm. The spherical capacitor analyser was set at 45° take-off angle with respect to the sample surface. The pass energy was 46.95 eV yielding a full width at half maximum of 0.91 eV for the Ag 3d 5/2 peak. Curve fitting was performed using the PHI Multipak software.

Photoelectrochemical Measurements. The photoelectrochemical performance of the photocathodes was studied using a Bio-Logic SP-200 electrochemical workstation to acquire the photoresponse under simulated AM 1.5G illumination (100 mW cm^{-2}) from 100W ozone free Xenon lamp equipped with an AM 1.5 G filter (Oriel LCS-100, Newport), calibrated with a silicon diode. Current–voltage measurements were carried out in a

three-electrode configuration with the Cu_2S photocathodes as the working electrode, a Pt mesh as the counter electrode and Ag/AgCl/sat. KCl as the reference electrode, in an electrolyte solution of 0.5 M Na_2SO_4 and 0.1 M KH_2PO_4 at pH 5.0. A scan rate of 10 mV s^{-1} in the cathodic direction was used to acquire the data. IPCE measurements were performed under monochromator in a tunable light source system (TLS-300XU, Newport) with white LED light bias in three-electrode configuration at 0 V versus reversible hydrogen electrode. Comparison with a calibrated Si photodiode (Thorlabs FDS100-CAL) allowed the calculation of the IPCE. The stability of the electrodes was characterized with chronoamperometry at 0 V versus RHE under chopped and simulated AM 1.5G illumination (100 mW cm^{-2}). Electrochemical impedance spectroscopy measurements were conducted on bare CdS and Cu_2S electrodes in the dark in an electrolyte solution of 0.5 M Na_2SO_4 and 0.1 M KH_2PO_4 at pH 5.0 with an AC amplitude of 25 mV and frequency from 0.1 Hz to 1 MHz. Photoluminescence spectra were carried out on LabRAM HR Raman spectrometer with 532 nm laser.

2.5 References

(1) S. D. Tilley; M. T. Mayer; N.-G. Park; J. Luo; M. Gratzel; H. J. Fan; M. Schreier; M. K. Nazeeruddin; J.-H. Im. Water Photolysis at 12.3% Efficiency via Perovskite Photovoltaics and Earth-Abundant Catalysts. *Science.* **2014**, *345* (6204), 1593–1596.

(2) M. G. Walter; E. L. Warren; J. R. McKone; S. W. Boettcher; Q. Mi; E. A. Santori; N. S. Lewis. Solar Water Splitting Cells. *Chem. Rev.* **2010**, *110* (11), 6446–6473.

(3) J. W. Ager; M. R. Shaner; K. A. Walczak; I. D. Sharp; S. Ardo. Experimental Demonstrations of Spontaneous, Solar-Driven Photoelectrochemical Water Splitting. *Energy Environ. Sci.* **2015**, *8* (10), 2811–2824.

(4) F. E. Osterloh. Inorganic Nanostructures for Photoelectrochemical and Photocatalytic Water Splitting. *Chem. Soc. Rev.* **2013**, *42* (6), 2294–2320.

(5) K. Sivula; R. Van De Krol. Semiconducting Materials for Photoelectrochemical Energy Conversion. *Nat. Rev. Mater.* **2016**, *1* (2).

(6) A. Paracchino; V. Laporte; K. Sivula; M. Grätzel; E. Thimsen. Highly Active Oxide Photocathode for Photoelectrochemical Water Reduction. *Nat. Mater.* **2011**, *10* (6), 456–461.

(7) M. Stefik; M. Graetzel; M. Schreier; J. Azevedo; S. D. Tilley. Ruthenium Oxide Hydrogen Evolution Catalysis on Composite Cuprous Oxide Water-Splitting Photocathodes. *Adv. Funct. Mater.* **2013**, *24* (3), 303–311.

(8) T. Minami; Y. Nishi; T. Miyata. Effect of the Thin Ga2O3 Layer in n^+-ZnO/n-Ga_2O_3/p-Cu_2O Heterojunction Solar Cells. *Thin Solid Films* **2013**, *549*, 65–69.

(9) M. Tadatsugu; N. Yuki; M. Toshihiro. High-Efficiency Cu_2O-Based Heterojunction Solar Cells Fabricated Using a Ga_2O_3 Thin Film as N-Type Layer. *Appl. Phys. Express* **2013**, *6* (4), 44101.

(10) Y. S. Lee; D. Chua; R. E. Brandt; S. C. Siah; J. V. Li; J. P. Mailoa; S. W. Lee; R. G. Gordon; T. Buonassisi. Atomic Layer Deposited Gallium Oxide Buffer Layer Enables 1.2 V Open-Circuit Voltage in Cuprous Oxide Solar Cells. *Adv. Mater.* **2014**, *26* (27), 4704–4710.

(11) C. Li; T. Hisatomi; O. Watanabe; M. Nakabayashi; N. Shibata; K. Domen; J. J. Delaunay. Positive Onset Potential and Stability of Cu_2O-Based Photocathodes in Water

Splitting by Atomic Layer Deposition of a Ga$_2$O$_3$ Buffer Layer. *Energy Environ. Sci.* **2015**, *8* (5), 1493–1500.

(12)   E. Thimsen; Q. Peng; A. B. F. Martinson; M. J. Pellin; J. W. Elam. Ion Exchange in Ultrathin Films of Cu$_2$S and ZnS under Atomic Layer Deposition Conditions. *Chem. Mater.* **2011**, *23* (20), 4411–4413.

(13)   S. C. Riha; R. D. Schaller; D. J. Gosztola; G. P. Wiederrecht; A. B. F. Martinson. Photoexcited Carrier Dynamics of Cu$_2$S Thin Films. *J. Phys. Chem. Lett.* **2014**, *5* (22), 4055–4061.

(14)   I. Minguez-Bacho; M. Courté; H. J. Fan; D. Fichou. Conformal Cu$_2$S-Coated Cu$_2$O Nanostructures Grown by Ion Exchange Reaction and Their Photoelectrochemical Properties. *Nanotechnology* **2015**, *26* (18), 185401.

(15)   S. C. Riha; S. Jin; S. V. Baryshev; E. Thimsen; G. P. Wiederrecht; A. B. F. Martinson. Stabilizing Cu$_2$S for Photovoltaics One Atomic Layer at a Time. *ACS Appl. Mater. Interfaces* **2013**, *5* (20), 10302–10309.

(16)   W. Shockley; H. J. Queisser. Detailed Balance Limit of Efficiency of *p-n* Junction Solar Cells. *J. Appl. Phys.* **1961**, *32* (3), 510–519.

(17)   P. K. Bhat; S. R. Das; D. K. Pandya; K. L. Chopra. Back Illuminated High Efficiency Thin Film Cu$_2$S/CdS Solar Cells. *Sol. Energy Mater.* **1979**, *1* (3–4), 215–219.

(18)   T. D. Sands; J. Washburn; R. Gronsky. High Resolution Observations of Copper Vacancy Ordering in Chalcocite (Cu$_2$S) and the Transformation to Djurleite (Cu$_{1.97 \text{ to } 1.94}$S). *Phys. status solidi* **1982**, *72* (2), 551–559.

(19)   P. Kar; S. Farsinezhad; X. Zhang; K. Shankar. Anodic Cu$_2$S and CuS Nanorod and Nanowall Arrays: Preparation, Properties and Application in CO$_2$ Photoreduction. *Nanoscale* **2014**, *6* (23), 14305–14318.

(20)   A. M. Al-Dhafiri; G. J. Russell; J. Woods. Degradation in CdS-Cu$_2$S Photovoltaic Cells. *Semicond. Sci. Technol.* **1992**, *7* (8), 1052–1057.

(21)   S.-Y. Wang; W. Wang; Z.-H. Lu. Asynchronous-Pulse Ultrasonic Spray Pyrolysis Deposition of Cu$_x$S (X=1, 2) Thin Films. *Mater. Sci. Eng. B* **2003**, *103* (2), 184–188.

(22)   A. B. F. Martinson; S. C. Riha; E. Thimsen; J. W. Elam; M. J. Pellin. Structural, Optical, and Electronic Stability of Copper Sulfide Thin Films Grown by Atomic Layer Deposition.

Energy Environ. Sci. **2013**, *6* (6), 1868.

(23)   I. Carbone; Q. Zhou; B. Vollbrecht; L. Yang; S. Medling; A. Bezryadina; F. Bridges; G. B. Alers; J. T. Norman; et al. Pulsed Chemical Vapor Deposition of Cu_2S into a Porous TiO_2 Matrix. *J. Vac. Sci. Technol. A Vacuum, Surfaces, Film.* **2011**, *29* (5), 051505.

(24)   S. Siol; H. Sträter; R. Brüggemann; J. Brötz; G. H. Bauer; A. Klein; W. Jaegermann. PVD of Copper Sulfide (Cu_2S) for PIN-Structured Solar Cells. *J. Phys. D. Appl. Phys.* **2013**, *46* (49), 495112.

(25)   K. Anuar; Z. Zainal; M. . Hussein; N. Saravanan; I. Haslina. Cathodic Electrodeposition of Cu_2S Thin Film for Solar Energy Conversion. *Sol. Energy Mater. Sol. Cells* **2002**, *73* (4), 351–365.

(26)   A. B. Wong; S. Brittman; Y. Yu; N. P. Dasgupta; P. Yang. Core–Shell CdS–Cu_2S Nanorod Array Solar Cells. *Nano Lett.* **2015**, *15* (6), 4096–4101.

(27)   J. B. Rivest; P. K. Jain. Cation Exchange on the Nanoscale: An Emerging Technique for New Material Synthesis, Device Fabrication, and Chemical Sensing. *Chem. Soc. Rev.* **2013**, *42* (1), 89–96.

(28)   X. Liu; M. T. Mayer; D. Wang. Understanding Ionic Vacancy Diffusion Growth of Cuprous Sulfide Nanowires. *Angew. Chemie Int. Ed.* **2010**, *49* (18), 3165–3168.

(29)   J. M. Luther; P. K. Jain; T. Ewers; A. P. Alivisatos. Localized Surface Plasmon Resonances Arising from Free Carriers in Doped Quantum Dots. *Nat. Mater.* **2011**, *10* (5), 361–366.

(30)   A. Paracchino; V. Laporte; K. Sivula; M. Grätzel; E. Thimsen. Highly Active Oxide Photocathode for Photoelectrochemical Water Reduction. *Nat. Mater.* **2011**, *10* (6), 456–461.

(31)   P. Dias; M. Schreier; S. D. Tilley; J. Luo; J. Azevedo; L. Andrade; D. Bi; A. Hagfeldt; A. Mendes; et al. Transparent Cuprous Oxide Photocathode Enabling a Stacked Tandem Cell for Unbiased Water Splitting. *Adv. Energy Mater.* **2015**, *5* (24), 1501537.

(32)   C. Li; T. Hisatomi; O. Watanabe; M. Nakabayashi; N. Shibata; K. Domen; J.-J. Delaunay. Positive Onset Potential and Stability of Cu_2O-Based Photocathodes in Water Splitting by Atomic Layer Deposition of a Ga_2O_3 Buffer Layer. *Energy Environ. Sci.* **2015**, *8* (5), 1493–1500.

(33)   J. Luo; S. D. Tilley; L. Steier; M. Schreier; M. T. Mayer; H. J. Fan; M. Grätzel. Solution Transformation of Cu_2O into $CuInS_2$ for Solar Water Splitting. *Nano Lett.* **2015**, *15* (2), 1395–1402.

(34)   J. Luo; L. Steier; M. K. Son; M. Schreier; M. T. Mayer; M. Grätzel. Cu_2O Nanowire Photocathodes for Efficient and Durable Solar Water Splitting. *Nano Lett.* **2016**, *16* (3), 1848–1857.

(35)   B. D. Viezbicke; S. Patel; B. E. Davis; D. P. Birnie. Evaluation of the Tauc Method for Optical Absorption Edge Determination: ZnO Thin Films as a Model System. *Phys. Status Solidi Basic Res.* **2015**, *252* (8), 1700–1710.

(36)   R. E. Brandt; M. Young; H. H. Park; A. Dameron; D. Chua; Y. S. Lee; G. Teeter; R. G. Gordon; T. Buonassisi. Band Offsets of N-Type Electron-Selective Contacts on Cuprous Oxide (Cu_2O) for Photovoltaics. *Appl. Phys. Lett.* **2014**, *105* (26).

(37)   E. A. Kowalczyk; K. W.; G. R.; W. P. Precise Determination of the Valence Band Edge in X Ray Photoemission Spectra Application to Measurement of Semiconductor Interface Potentials. *Phys. Rev. Lett.* **1980**, *44* (24), 1620–1623.

(38)   S. T. Omelchenko; Y. Tolstova; H. A. Atwater; N. S. Lewis. Excitonic Effects in Emerging Photovoltaic Materials: A Case Study in Cu_2O. *ACS Energy Lett.* **2017**, *2* (2), 431–437.

(39)   Y. Kuang; Q. Jia; G. Ma; T. Hisatomi; T. Minegishi; H. Nishiyama; M. Nakabayashi; N. Shibata; T. Yamada; et al. Ultrastable Low-Bias Water Splitting Photoanodes via Photocorrosion Inhibition and in Situ Catalyst Regeneration. *Nat. Energy* **2017**, *2* (1), 16191.

(40)   A. Mendes; M. Grätzel; J. Azevedo; A. Hagfeldt; M. T. Mayer; P. Dias; L. Andrade; S. D. Tilley; D. Bi; et al. Transparent Cuprous Oxide Photocathode Enabling a Stacked Tandem Cell for Unbiased Water Splitting. *Adv. Energy Mater.* **2015**, *5* (24), 1501537.

(41)   M. K. Son; L. Steier; M. Schreier; M. T. Mayer; J. Luo; M. Grätzel. A Copper Nickel Mixed Oxide Hole Selective Layer for Au-Free Transparent Cuprous Oxide Photocathodes. *Energy Environ. Sci.* **2017**, *10* (4), 912–918.

(42)   L. Gao; X. Qian; T. Hang; M. Li; P. Zhang; Q. Xu; Y. Qu.   Electrodeposition of Cu_2O Nanostructure on 3D Cu Micro-Cone Arrays as Photocathode for Photoelectrochemical Water Reduction . *J. Electrochem. Soc.* **2016**, *163* (10), H976–H981.

(43)   P. C. K. Vesborg; O. Hansen; I. Chorkendorff; A. B. Laursen; T. Pedersen; B. Seger. Using TiO$_2$ as a Conductive Protective Layer for Photocathodic H$_2$ Evolution . *J. Am. Chem. Soc.* **2013**, *135* (3), 1057–1064.

(44)   M. Li; R. Zhao; Y. Su; Z. Yang; Y. Zhang. Carbon Quantum Dots Decorated Cu$_2$S Nanowire Arrays for Enhanced Photoelectrochemical Performance. *Nanoscale* **2016**, *8* (16), 8559–8567.

(45)   H. Khallaf; I. O. Oladeji; G. Chai; L. Chow. Characterization of CdS Thin Films Grown by Chemical Bath Deposition Using Four Different Cadmium Sources. *Thin Solid Films* **2008**, *516* (21), 7306–7312.

(46)   J. Aguilar-Hernández; J. Sastre-Hernández; N. Ximello-Quiebras; R. Mendoza-Pérez; O. Vigil-Galán; G. Contreras-Puente; M. Cárdenas-García. Photoluminescence Studies on CdS-CBD Films Grown by Using Different S/Cd Ratios. *Thin Solid Films* **2006**, *511–512*, 143–146.

(47)   I. Vamvasakis; A. Trapali; J. Miao; B. Liu; G. S. Armatas. Enhanced Visible-Light Photocatalytic Hydrogen Production Activity of Three-Dimensional Mesoporous p-CuS/n-CdS Nanocrystal Assemblies. *Inorg. Chem. Front.* **2017**, *4* (3), 433–441.

(48)   G. Liu; T. Schulmeyer; J. Brötz; A. Klein; W. Jaegermann. Interface Properties and Band Alignment of Cu$_2$S/CdS Thin Film Solar Cells. *Thin Solid Films* **2003**, *431–432*, 477–482.

(49)   T. E. Jenkins; H. Tamura; D. Trivich; J. W. Hodby; C. Schwab.   Cyclotron Resonance of Electrons and of Holes in Cuprous Oxide, Cu$_2$O . *J. Phys. C Solid State Phys.* **2002**, *9* (8), 1429–1439.

(50)   C. Li; Y. Li; J. J. Delaunay. A Novel Method to Synthesize Highly Photoactive Cu$_2$O Microcrystalline Films for Use in Photoelectrochemical Cells. *ACS Appl. Mater. Interfaces* **2014**, *6* (1), 480–486.

(51)   H. Khallaf; I. O. Oladeji; G. Chai; L. Chow. Characterization of CdS Thin Films Grown by Chemical Bath Deposition Using Four Different Cadmium Sources. *Thin Solid Films* **2008**, *516* (21), 7306–7312.

3 Tail-states Assisted Hole Transport in Cu$_2$O Photocathodes with CuSCN Hole Transport Layer

This chapter is adapted from a submitted article: **L. Pan**; Y. Liu; L. Yao; D. Ren; K. Sivula; M. Grätzel; A. Hagfeldt. Cu$_2$O Photocathodes with Band-tail States Assisted Hole Transport for Standalone Solar Water Splitting. **2019**, Submitted.

This version is based on the version before editorial change.

This chapter focuses on improving charge transport on the other side of the photoelectrode echoing last chapter. Though Au was used as an excellent back contact for Cu$_2$O photocathodes owing to the perfect matching between Au work function and Cu$_2$O valence band energy, it has disadvantages such as high cost and opacity which could hinder large-scale and tandem applications. The results in this chapter show that due to its excellent electronic properties, electrodeposited CuSCN can effectively function as the hole transport layer for Cu$_2$O photocathodes. A detailed band energy characterization revealed that the band-tail states assisted hole transport is playing an important role between Cu$_2$O and CuSCN.

3.1 Introduction

As one of the solutions for future energy demand, solar energy shows promise to substitute fossil fuels without sacrificing our standard of living. Photoelectrochemical (PEC) solar energy conversion further addresses the intermittency of sunlight to meet the need for long-term energy storage. In the most studied field of solar-to-hydrogen (STH) conversion, oxide-based photoelectrodes are attractive due to their high abundance, economical fabrication and excellent stability.[1–3] Among all oxide photocathodes where hydrogen is generated during solar water splitting, Cu_2O photocathodes hold the champion performance rivaling that of many photovoltaic (PV) semiconductor based photocathodes.[4] However, Rome wasn't built in a day. Starting from the ground-breaking work by Paracchino et al. where the Cu_2O photocathode was protected by atomic layer deposition (ALD) layers of TiO_2, Cu_2O photocathodes are giving meaningful photocurrent with hours of stable operation.[5] Then, efforts are made on surface catalysts to enable better stability in electrolyte of various pH values.[6–8] To achieve optimized light absorption and minority carrier transfer, the photoabsorber Cu_2O was nano-structured via high-temperature processes, resulting in an simultaneously enhanced photocurrent density and stability.[9,10] Most recently, another significant advance was realized by building a more efficient coaxial heterojunction of Ga_2O_3/Cu_2O.[11,12] With excellent photovoltage of around 1 V versus reversible hydrogen electrode (RHE), which is the highest among all single-junction photocathodes, an all-oxide standalone tandem system with unprecedented 3% STH efficiency was demonstrated, proving the potential of Cu_2O photocathodes for solar energy conversion commercialization.[12]

Till now, state-of-the-art Cu_2O photocathodes are still employing gold as the back contact due to the matching between the gold work function and Cu_2O valence band level.[5,10,12] In addition to gold scarcity, gold is not a selective contact for the conducting carriers, which can cause considerable amount of recombination. Moreover, Au absorbs extensively from visible to infrared light, leading to the difficulty of making transparent Cu_2O photocathodes.[13] Since Cu_2O is often used as front absorber due to its relatively large bandgap, the opacity would hinder the establishment of an efficient tandem based on Cu_2O photocathodes. To our best knowledge, only nickel oxide-based materials were studied as the hole transport layer (HTL) for the Cu_2O photocathode. Nevertheless, a two-step process, including thermal annealing, was required in both cases.

In this study, we report, for the first time, the use of CuSCN as effective hole transport material for Cu$_2$O photocathodes. Overall PEC performance improvement was achieved with solution-processed CuSCN layers, featuring excellent fill factors. Material, optical and electronic properties of two types of CuSCN with different structures were characterized and compared. Furthermore, band-tail assisted hole-transport was uncovered for efficient hole-selective conduction between Cu$_2$O and CuSCN. To show the multiple advantages of employing CuSCN as the HTL, a PEC-PV tandem was optimized and demonstrated, delivering 4.55% STH efficiency.

3.2 Results and discussion

3.2.1 Characterization of CuSCN films
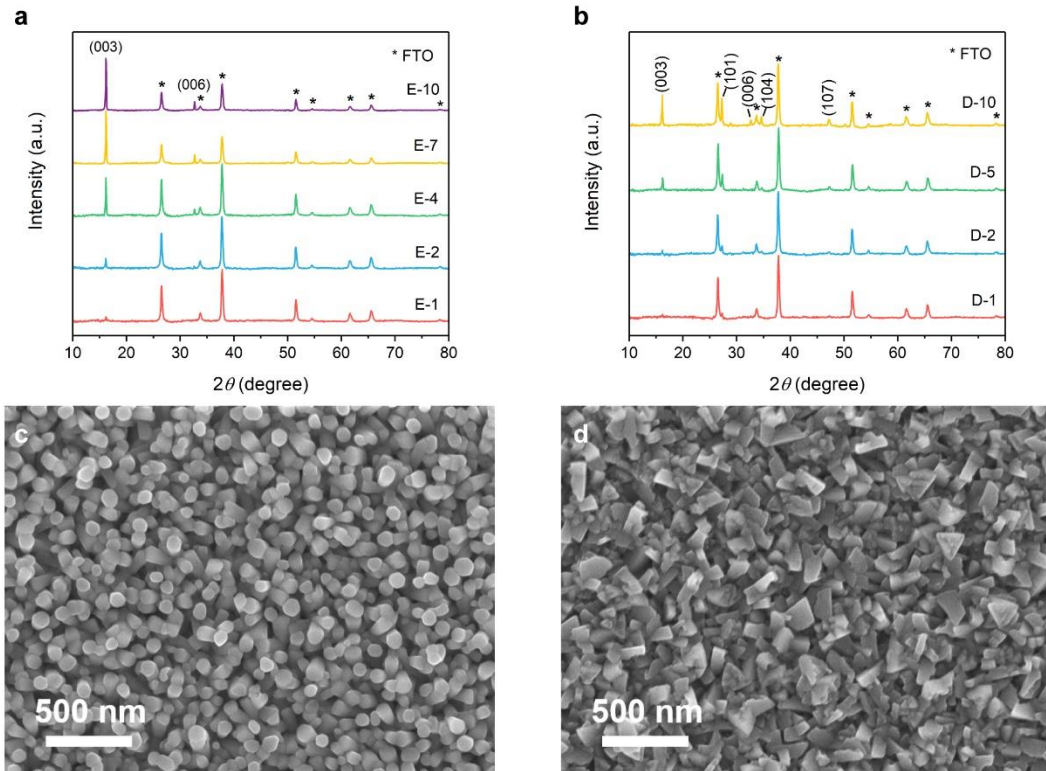
Figure 3.1 | XRD patterns and SEM imaging of CuSCN films. a, XRD patterns of CuSCN-E on FTO substrates with various electrodeposition duration. b, XRD patterns of CuSCN-D on FTO substrates with various electrodeposition duration. Numbers in sample names denote the electrodeposition duration in minutes. Indexes were extracted from PDF cards of #01-077-0451 for FTO and #29-0581 for CuSCN. c, Top-view image of CuSCN-E with 2 min electrodeposition. d, Top-view image of CuSCN-D with 2 min electrodeposition.

CuSCN has extensive applications in opto/electronic devices.[14] Apart from its exceptional optical transparency, chemical stability and hole transport properties, processing versatility is also considered one of the merits of CuSCN for manufacturing electronic devices. Previous reports on electrodeposition of CuSCN on a rotating disk revealed that the growth of nanostructured CuSCN is limited by mass transport.[15,16] Extensive studies varied deposition parameters including bath composition, temperature, pH values to tune its morphology, orientation and nanostructures.[15-20] In order to attain precise stoichiometry and reliable successful rate, we maintained the 1:1 molar ratio of [Cu²⁺]:[SCN⁻] in both electrolytes but differed the chelating agent, which will effectively

change the solution pH.[17,19] The solution containing ethylenediaminetetraacetic acid (EDTA) shows a pH value of 1.6, whereas the one with diethanolamine (DEA) gives a pH value of 8.2. Phase composition and crystalline structure of the resulting films (the one with EDTA was denoted as CuSCN-E and the one with DEA is denoted as CuSCN-D) were analyzed by X-ray diffractometry (XRD) as shown in Figure 3.1a, b. Both films show diffraction peaks that are indexed to the rhombohedral β-CuSCN (JCPDS No. 29-0581). No impurity peaks are visible other than those of fluorine-doped tin oxide (FTO) substrates (marked with asterisks, JCPDS No. 01-077-0451). While the CuSCN-D shows 4 major diffraction peaks of (003), (101), (104) and (107) featuring (101) and (003) peaks, CuSCN-E has a preferred orientation along the (001) direction with sharp shapes indicating high crystallinity. The samples prepared in acidic bath show only (001) direction peaks of increasing intensity with longer deposition. In contrast, CuSCN-D shows both pronounced peaks of (003) and (101) as duration gets longer. Comparing the two films with 10 min electrodeposition, relative intense peaks are obtained with CuSCN-E series, implying better crystallinity. These results associate properly with scanning
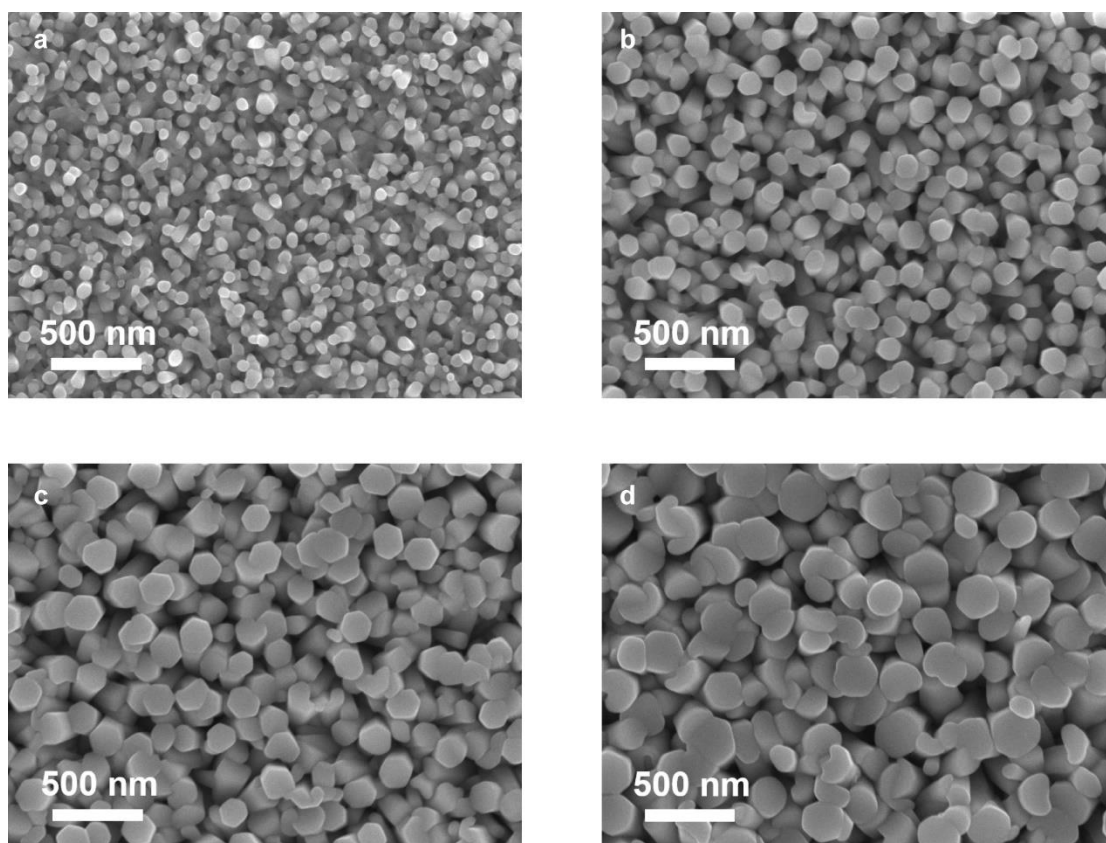

Figure 3.2 | Top-view scanning electron micrographs of CuSCN-E with a, 1 min, b, 4 min, c, 7 min and d, 10 min electrodeposition.
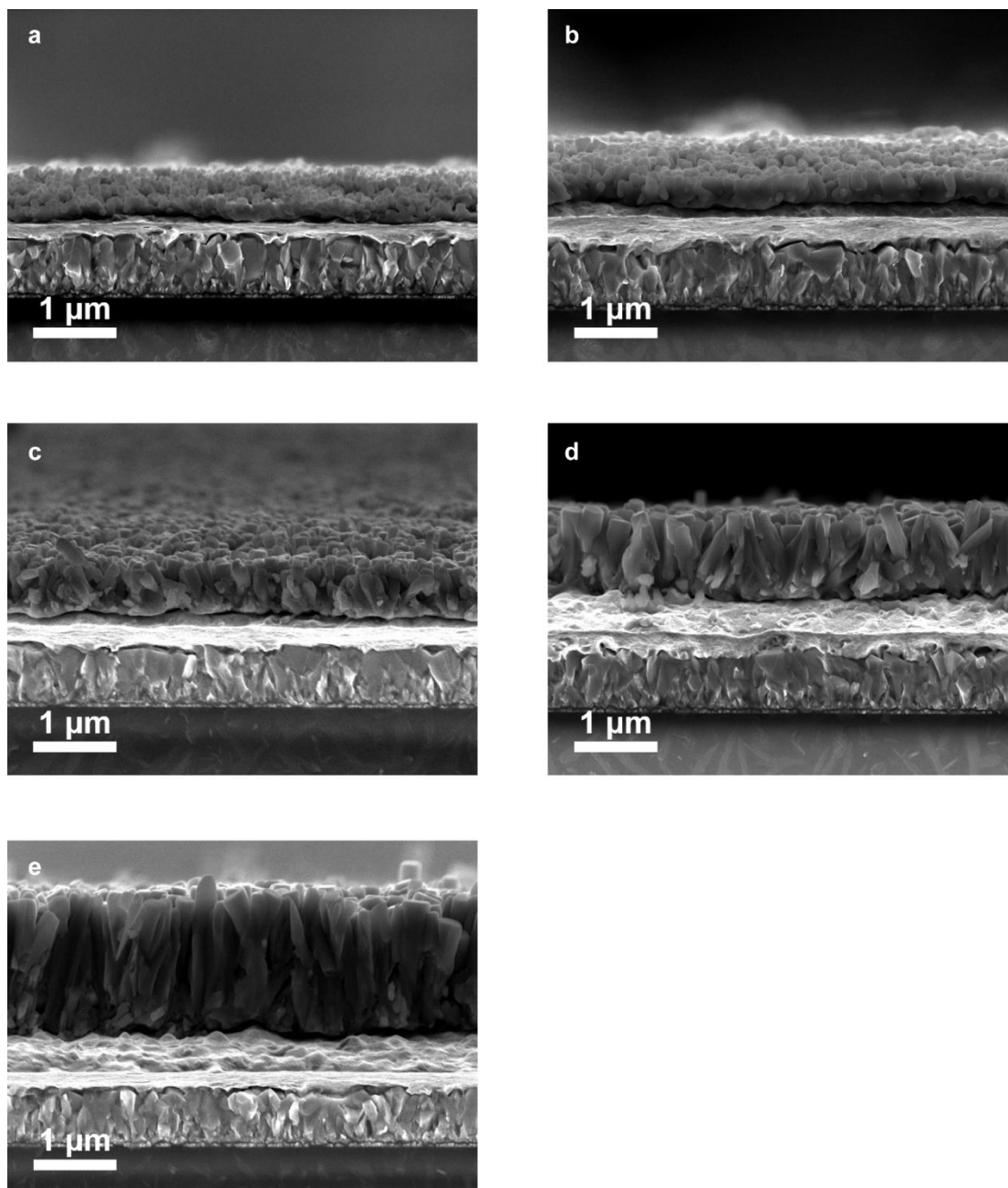
electron microscope (SEM) images.

Figure 3.3 | Cross-section scanning electron micrographs of CuSCN-E with a, 1 min, b, 2 min, c, 4 min, d, 7 min and e, 10 min electrodeposition.

Both top-view and cross-section SEM images are collected on samples with various deposition duration. Similar to electrodeposition in other acidic electrolyte, samples produced with EDTA show dense and vertical nanorods morphology (Figure 3.1c).[18,19,21] As expected in XRD analysis, the films exhibit well-defined columnar crystals with uniform diameters. The strong preferential orientation along the *c*-axis is logically corresponding
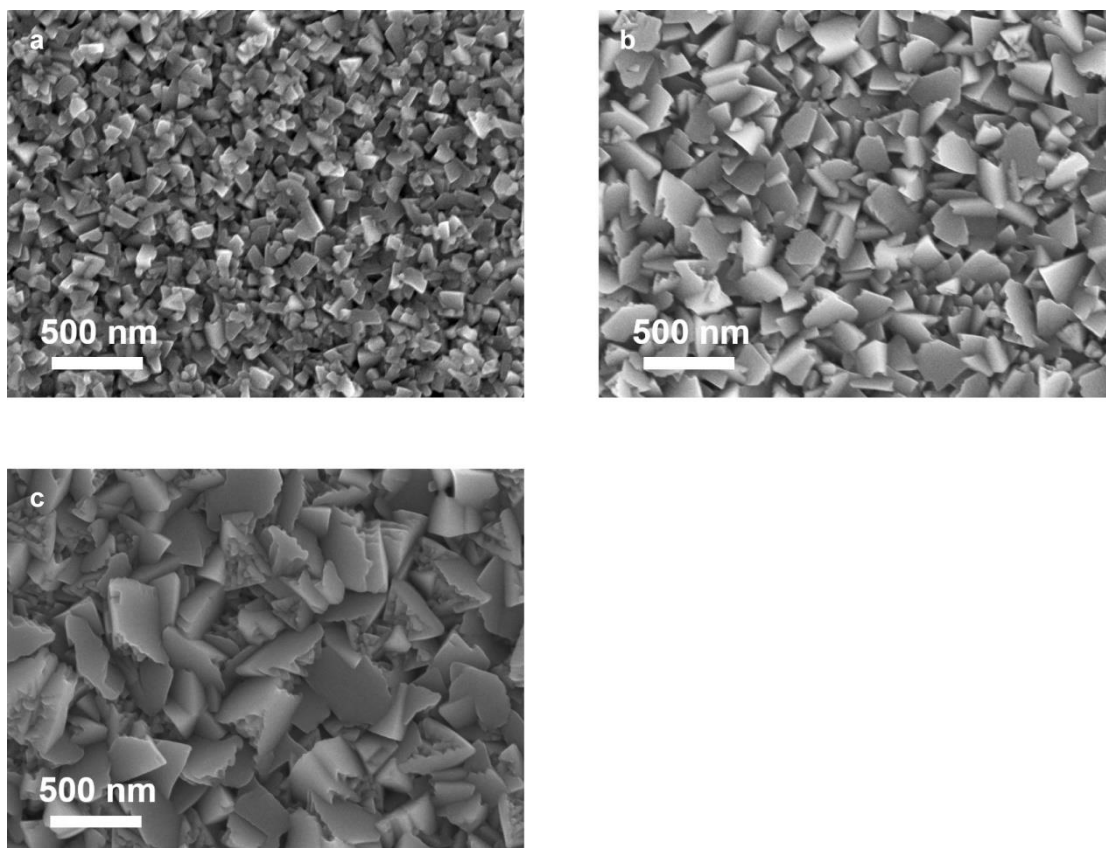
to the longitudinal direction of the nanorods.[18]

Figure 3.4 | Top-view scanning electron micrographs of CuSCN-D with a, 1 min, b, 5 min and c, 10 min electrodeposition.

While the deposition duration gets longer, nanorod diameters increase from approximately 100 nm to 300 nm, losing its diameter uniformity (Figure 3.2). This shows that the nanorods are formed due to mass transport limit, because the reactant, [Cu(SCN)+], is quickly depleted among the nanorods so a pillar-like structure is developed.[15] Corresponding cross-section images (Figure 3.3) show not only the thickening of the film but also the enhanced density, as the space among the columns are filled gradually. Figure 3.1d shows image of CuSCN-D. Rugged grains are closely packed with well-defined structure. As the films get thicker, grains get larger with more noticeable plain surface and broken edges (Figure 3.4). Drastic structure difference exhibited here has been explained by the difference between existing copper complexes that form at different pH.[19,22] A closer look at the cross-section images (Figure 3.5) reveals that though the surface of film is rough, the film is continuous, which promises negligible leaking of electrons when functioning as the HTL. Thickness growth rate was estimated using linear
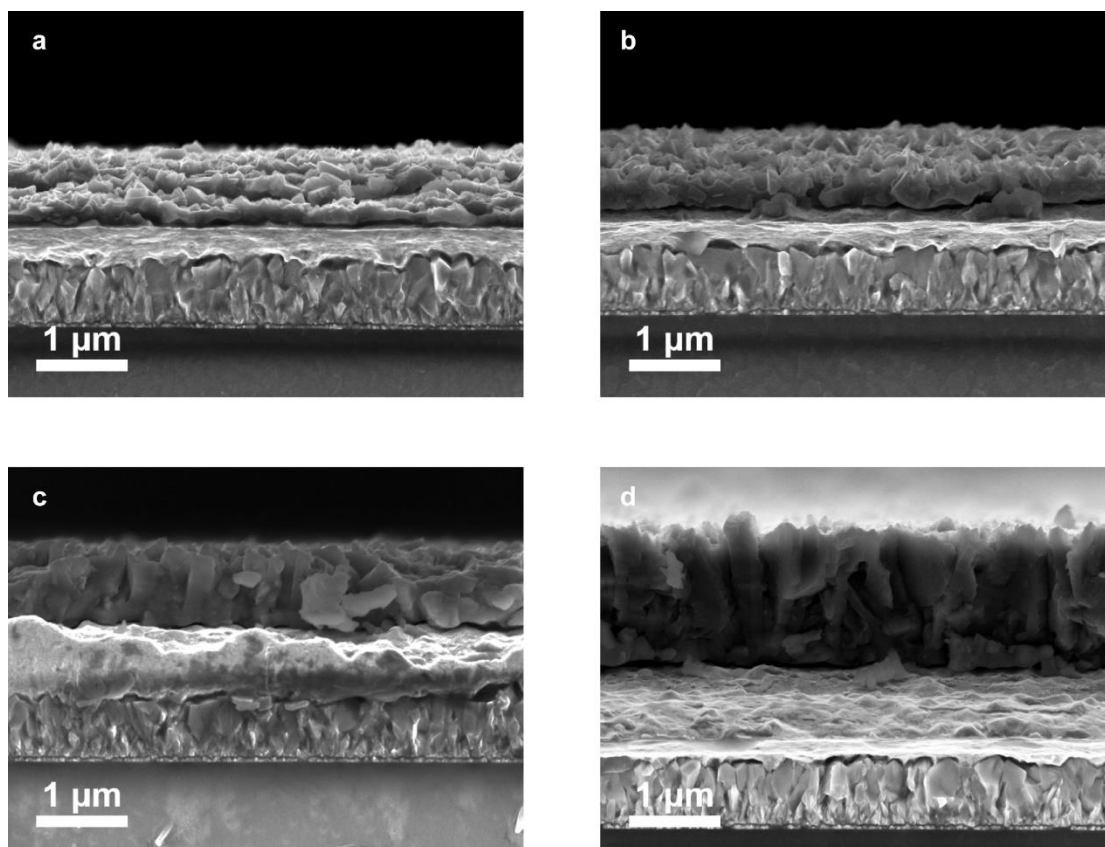
Figure 3.5 | Cross-section scanning electron micrographs of CuSCN-D with a, 1 min, b, 2 min, c, 5 min and d, 10 min electrodeposition.

fitting of SEM cross-section thicknesses from 3 independent batches prepared with the same configuration. Growth rates of 141.5 nm min^{-1} and 150.0 nm min^{-1} were respectively estimated for EDTA and DEA assisted depositions (Figure 3.6). A thorough X-ray photoelectron spectroscopy (XPS) study has been carried out on the CuSCN films. The
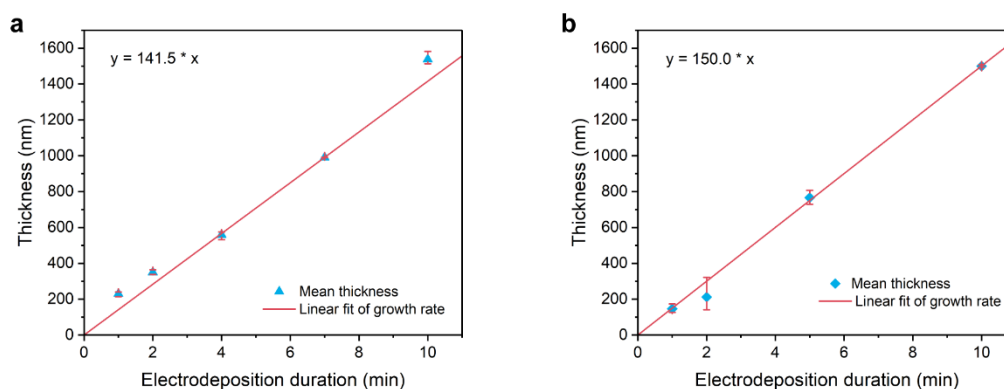

Figure 3.6 | CuSCN growth rate linear fitting. a, Growth rate of 141.5 nm per minute determined for CuSCN-E, b, Growth rate of 150.0 nm per minute determined for CuSCN-D.

survey results resemble the ones in literature validating the presence of Cu, S, C and N, and indicate a trace amount of oxygen, which is due to inevitable contamination on the surface of the samples, Figure 3.7.[23–25]
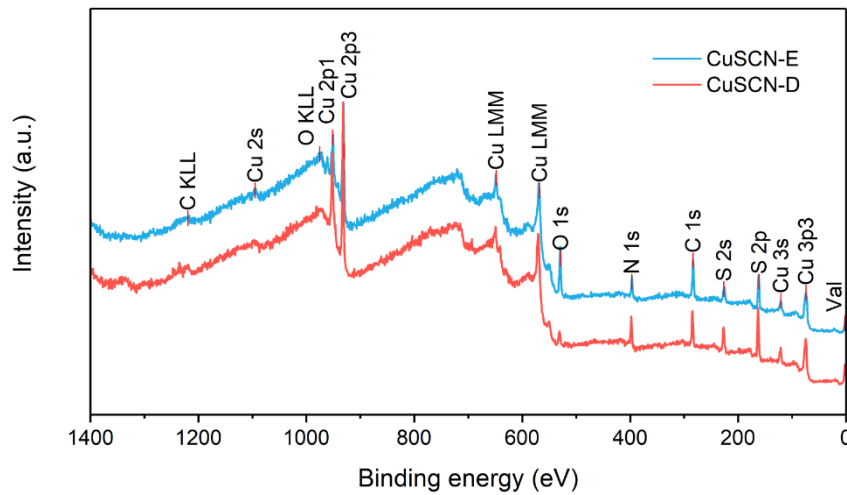

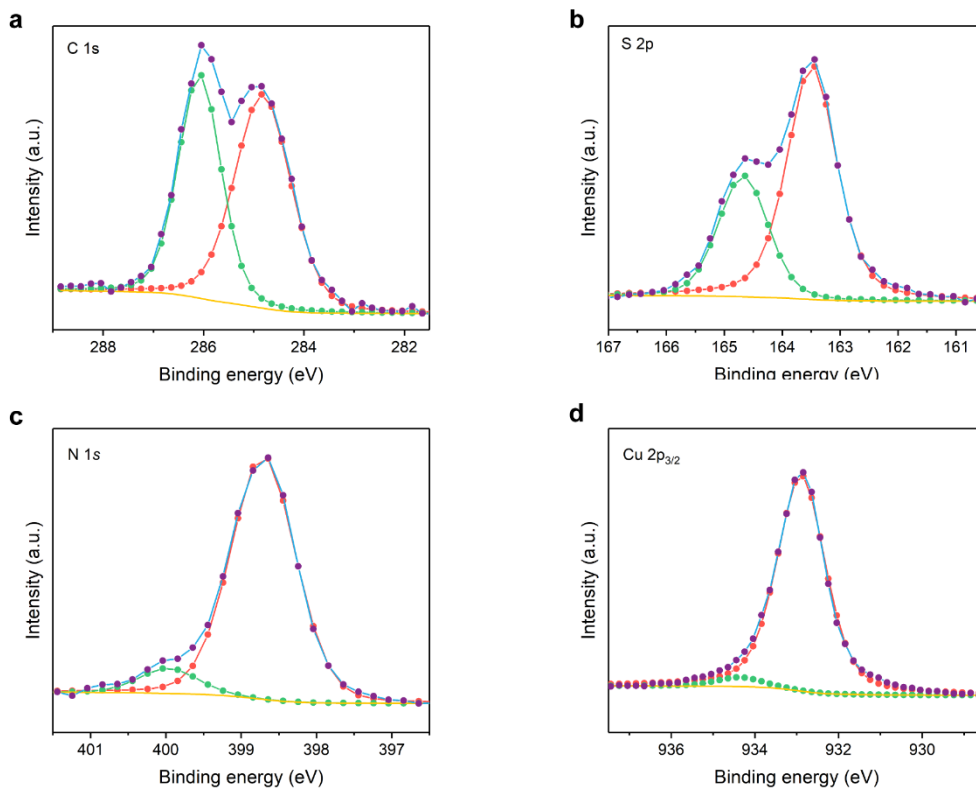Figure 3.7 | XPS survey spectra of CuSCN films with 2 min electrodeposition.

Figure 3.8 | High-resolution deconvoluted XPS spectra of CuSCN-E films with 2 min electrodeposition. a, carbon 1s spectra, b, S 2p spectra, c, N 1s spectra, d, Cu 2p$_{3/2}$ spectra.
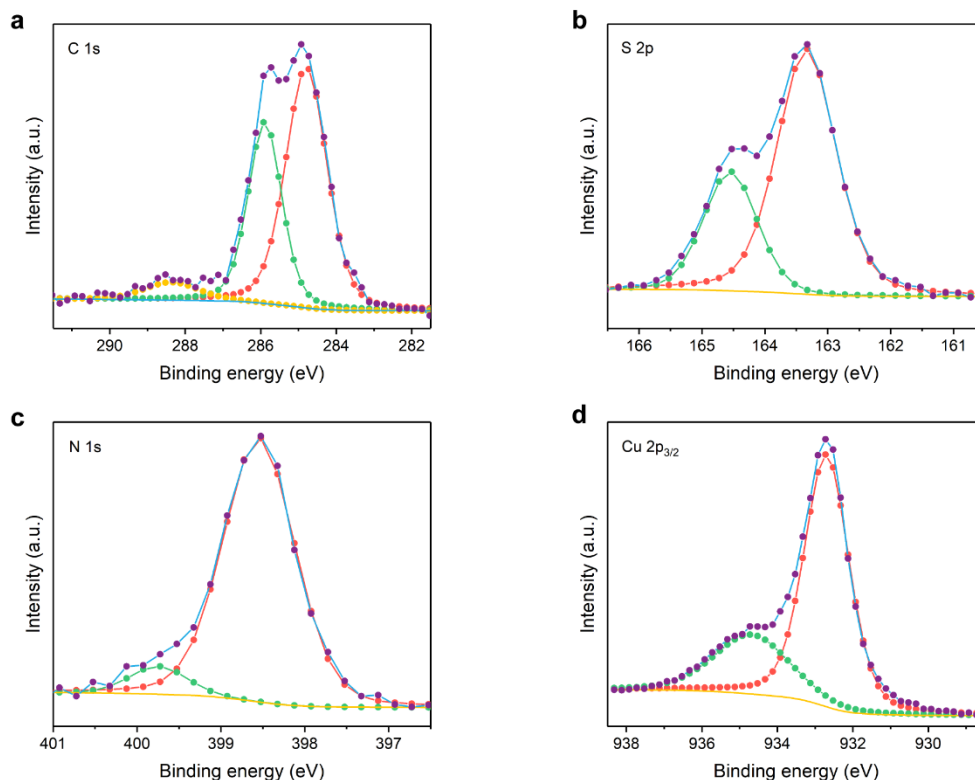
Figure 3.9 | High-resolution deconvoluted XPS spectra of CuSCN-D films with 2 min electrodeposition. a, carbon 1s spectra, b, S 2p spectra, c, N 1s spectra, d, Cu 2p$_{3/2}$ spectra.

High-resolution spectra of selected elements in CuSCN films prepared with different chelating agents were collected and presented in Figure 3.8 and 3.9. It is conceivable that covalent carbon binding in CuSCN will substantially contribute to the C 1s spectra, therefore the peak at 284.8 eV, which is ascribed to aliphatic carbon contamination, was used for calibration after deconvolution. The other major peak in the C 1s spectrum located at 286 eV corresponds to the sp-state carbon in $-C \equiv N$, while the small one at 288.2 is due to C-O bond of impurities (Figure 3.8a and 3.9a).[23,26] The peak in the S 2p region is formed by doublets of S 2p$_{3/2}$ and S 2p$_{1/2}$ which were deconvoluted to two peaks at 163.5 eV and 164.6 eV. Both can be ascribed to sulfur in -S-C form (Figure 3.8b and 3.9b). Similar patterns are also acquired from both CuSCN films for N 1s spectra where the main deconvoluted peak at 398.3 eV probably corresponds to nitrogen in nitrile form (Figure 3.8c and 3.9c). In both Cu 2p$_{3/2}$ spectra, the curve peaks at 932.8 eV, which can be assigned to Cu^{1+} in CuSCN (Figure 3.8d and 3.9d). No obvious distinction occurs between these two films until we focus on the binding energy of 934.7 eV, where only the CuSCN-D show a relatively large peak. This peak has been observed and usually interpreted to either CuO, Cu$_2$O or Cu^{2+} species in other CuSCN XPS research.[23,25–27] We then carefully checked both
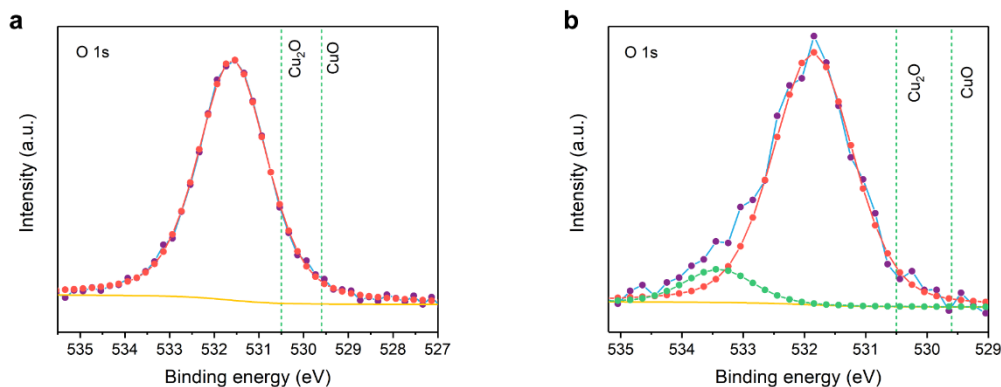
Figure 3.10 | High-resolution deconvoluted O 1s XPS spectra of a, the CuSCN-E film, b, the CuSCN-D film.

O 1s spectra as shown in Figure 3.10. The prominent peak at 531.6 eV is inevitable on samples exposed to the atmosphere due to contamination such as water. Peaks at binding energies of 529.6 eV and 530.5 eV, which respectively represent O 1s core level features of CuO and Cu₂O, did not appear.[27] However, an intriguing peak at 533.4 eV emerges only in the O 1s spectrum of CuSCN-D. This peak is regarded as evidence of metal carbonates, metal hydroxides or organic C-O bond.[28,29] Combining with the exclusive Cu signals of the CuSCN-D, we suggest the presence of Cu(II) carbonate hydroxide which is probably derived from Cu(II) species of CuSCN-D in the alkaline electrolyte. This result correlates with the hysteresis we observed in CuSCN-D during the Space-Charge Limited Current (SCLC) measurement discussed in the following sections. In addition to the XRD analysis, it implies that CuSCN-D owns a relatively defective crystal with unconsolidated structure compared to the highly crystalline columnar CuSCN-E.

3.2.2   PEC performance of the photocathode

Cu₂O, Ga₂O₃ and TiO₂ layers were deposited onto CuSCN in sequence to construct the photoelectrode with the structure shown in Figure 3.11a.[12] RuOₓ was photoelectrochemically deposited as the hydrogen evolution catalyst.[8,10] The new photocathode was tested with the conventional one (without CuSCN layer) by linear sweep voltammetry (LSV) in pH 5 buffer solution. The LSV curves are shown in Figure 3.11b. Distinct from the performance of conventional samples, which exhibits onset potential of 1 V versus RHE and current density of around 6.4 mA cm^{-2} at 0 V versus RHE with relatively poor fill factor, the photocathode with CuSCN layer shows globally
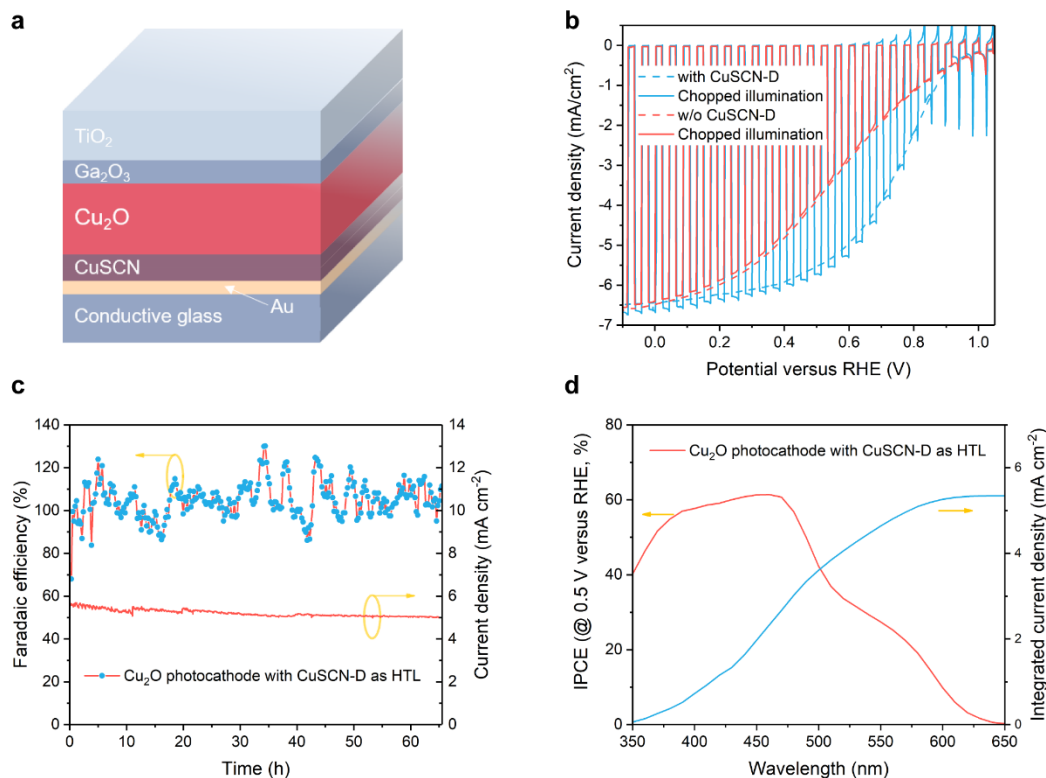
Figure 3.11 | Structure and PEC performance of CuSCN-incorporated Cu_2O photocathodes. a, A schematic diagram of the CuSCN-incorporated Cu_2O photocathode configuration. b, Current density-potential (*J-E)* responses of Cu_2O photocathodes with or w/o CuSCN-D layer under simulated one-sun illumination (air mass 1.5 G spectrum) in pH 5 buffered electrolyte (scan rate 10 mV/s). c, Stability test at fixed bias of 0.5 V versus RHE and corresponding Faradaic efficiency for hydrogen evolution in pH 5 buffered electrolyte under simulated one-sun illumination. d, Wavelength-dependent IPCE and integrated current density of Cu_2O photocathodes with CuSCN-D layer. All photocathode tests are carried out on photocathodes with 2 min electrodeposited CuSCN-D layers.

enhanced photocurrent featuring an excellent fill factor. Specifically, the current density of new photocathode at 0.6 V versus RHE is around 5.3 mA cm⁻² comparing to 3 mA cm⁻² of the standard one. The PEC performance tested under chopped illumination (solid line) confirmed that both photocathodes are giving photocurrent instead of corrosion current. In the following systematic study, we varied the film thicknesses of both films by altering electrodeposition duration and tested their PEC behavior (Figure 3.12).

Though both types of CuSCN films show best performance with 2-min electrodeposition samples, the Cu_2O photocathodes with CuSCN-D shows drastic photocurrent difference when changing deposition duration. We believe this phenomenon has strong connection to the structure of the films. Since CuSCN-E possesses nanorod morphology, the minimum
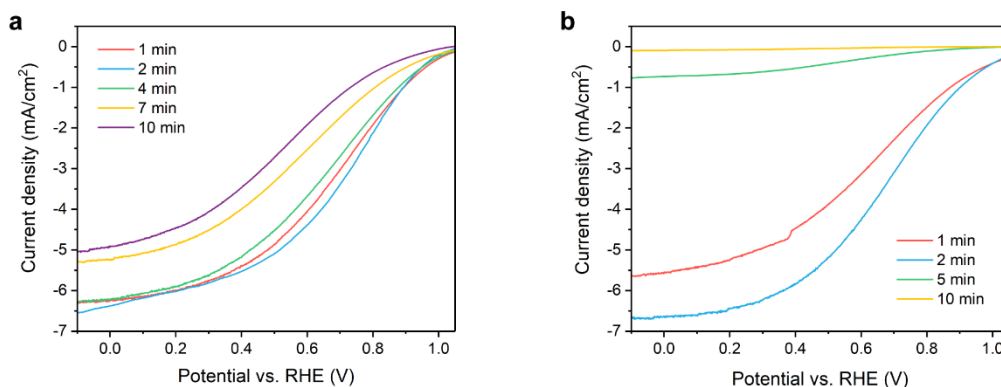
Figure 3.12 | Current density-potential (*J-V*) responses of Cu$_2$O photocathodes with a, CuSCN-E and b, CuSCN-D resulted from various electrodeposition duration as noted. All tests are carried out in pH 5 buffered electrolyte with simulated one-sun illumination. (AM 1.5 G spectrum, scan rate 10 mV/s, three-electrode configuration)

thickness of the film should be calculated using the root of the rod, which could be much smaller than the overall film thickness. Additionally, the growth rate of CuSCN-D is larger than that of CuSCN-E and the orientation could contribute to the variation as well. Nevertheless, the best cases with both films show improved fill factor, highlighting the 2-min CuSCN-D with overall enhanced PEC performance. The early onset potential with enhanced fill factor could boost the photocathode performance significantly in applications such as tandem devices and photo-redox reactions. In Figure 3.11c, the wavelength dependent incident photon-to-current conversion efficiency (IPCE) was carried out to reveal spectral response. Please note that here the IPCE was recorded at 0.5 V versus RHE as this value is more meaningful under tandem configurations. IPCE values around 60% was observed starting from short visible light region until 470 nm, where the lowest direct allowed optical gap lies, proving the outstanding quantum efficiency of Cu$_2$O photocathodes.[30,31] Importantly, the integrated IPCE values with the AM 1.5 G spectrum yields current density of around 5.4 mA cm^{-2}, validating the simulation precision of our light source. Finally, the whole device was subjected to long-term operation with gas quantification, Figure 3.11d. After 60 hours of continuous test, the photocurrent drops from 5.3 mA cm^{-2} to approximately 5.0 mA cm^{-2}. Despite the large fluctuation caused by large cell headspace, the Faradaic efficiency remained at around 100 % during the whole test, justifying the positive contribution of CuSCN as the HTL for Cu$_2$O photocathodes.
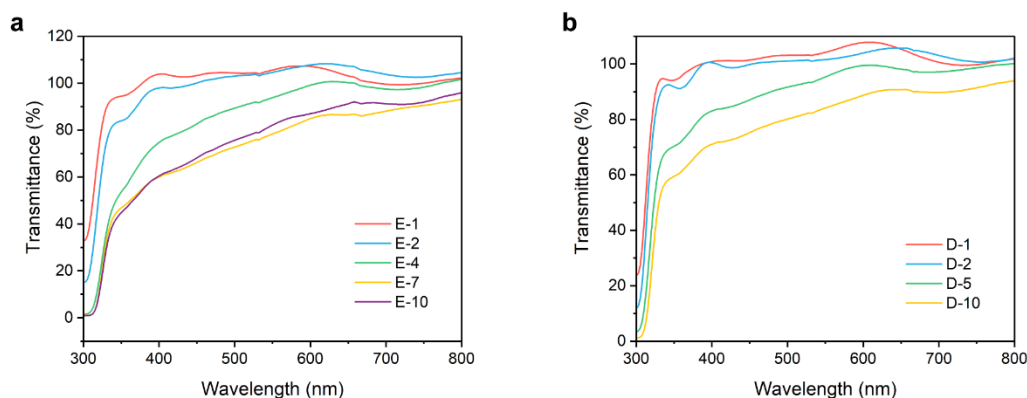
3.2.3　Hole conducting mechanism

Figure 3.13 | Transmittance spectra of CuSCN measured on FTO glass. a, CuSCN-E samples with 5 thicknesses. b, CuSCN-D samples with 4 thicknesses. Numbers in sample names denote the electrodeposition duration in minutes.

To understand the PEC behavior, both films are characterized by optical, electrochemical and electronic measurement. Examination of transmittance are carried out on CuSCN coated FTO glass. As shown in Figure 3.13, CuSCN films prepared with short deposition duration (1 min and 2 min) show excellent transparency for wavelengths longer than 400 nm regardless of choices of chelating agents. While films get thicker with longer deposition, transparency decreases.
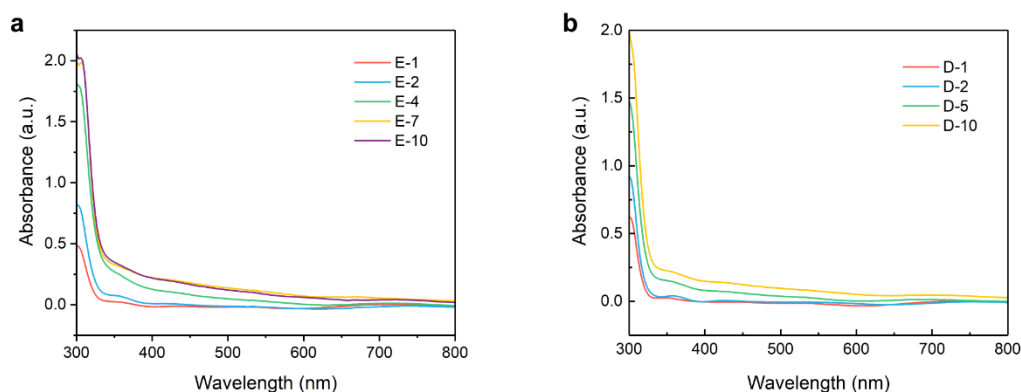

Figure 3.14 | Absorbance spectra converted from CuSCN transmittance data above. a, CuSCN-E samples with 5 thicknesses. b, CuSCN-D samples with 4 thicknesses. Numbers in sample names denote the electrodeposition duration in minutes.

To clearly see the wavelength dependent absorption, absorbance spectra was obtained by converting the transmittance data, Figure 3.14. Steep absorption line arises at around 360 nm, which separates the UV region and visible region and their distinct absorbing behaviors. However, for thicker films, absorption extends into the visible part. Absorption
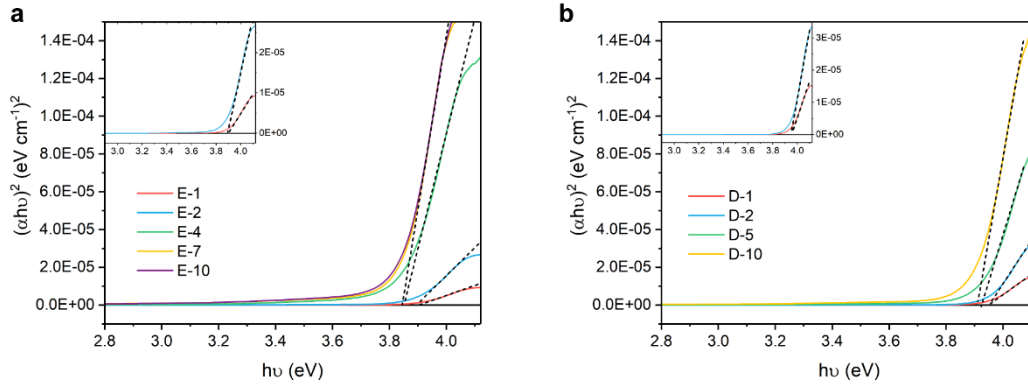
Figure 3.15 | Tauc plots of CuSCN on FTO substrates with linear extrapolation. a, CuSCN-E samples with 5 thicknesses. Inset graph shows enlarged extrapolation and cross of sample CuSCN-E-1 and CuSCN-E-2. b, CuSCN-D samples with 4 thicknesses. Numbers in sample names denote the electrodeposition duration in minutes. Inset graph shows enlarged extrapolation and cross of sample CuSCN-D-1 and CuSCN-D-2.

data was then used to extract optical bandgap by plotting $(\alpha h\nu)^n$ against $h\nu$ according to the Tauc's Equation,

$$\alpha h\nu = A(h\nu - E_G)^{1/n}$$

where "A" is proportionality constant; "$h\nu$" is photon energy displayed in "eV" and "E_g" refers to the bandgap of the material. Though the question on the nature of the CuSCN bandgap remains open, we consider it direct ($n = 2$) as suggested in most cases.[23,32] The linear region is extrapolated to the x-axis, Figure 3.15. The enlarged fitting with thinner films is shown in the inset. Optical bandgaps of 3.84-3.95 eV for all CuSCN were determined, which are in good agreement with reported results for p-type CuSCN.[18,23,32] Yet the values get reduced with increasing film thickness up to 1.5 μm. It is reminded that the optical transparency and the bandgap absorption has a strong dependence on grain sizes and crystallinity, because the concentration of localized states resulting from crystal defects will decrease due to an increase in crystal quality. It is notable that the crystallinity is improved with thicker films as discussed above, the trend is opposite to those of typical examples.[18,33] We suggest that the morphology plays a role here as the dimension of the crystals is of the order of the exciton Bohr radius of the semiconductor. Meanwhile, domains of slightly different chemical structure can also influence the absorption edge.[24]

A band gap of 2.02 eV was found for Cu_2O with the above method (Figure 3.16).
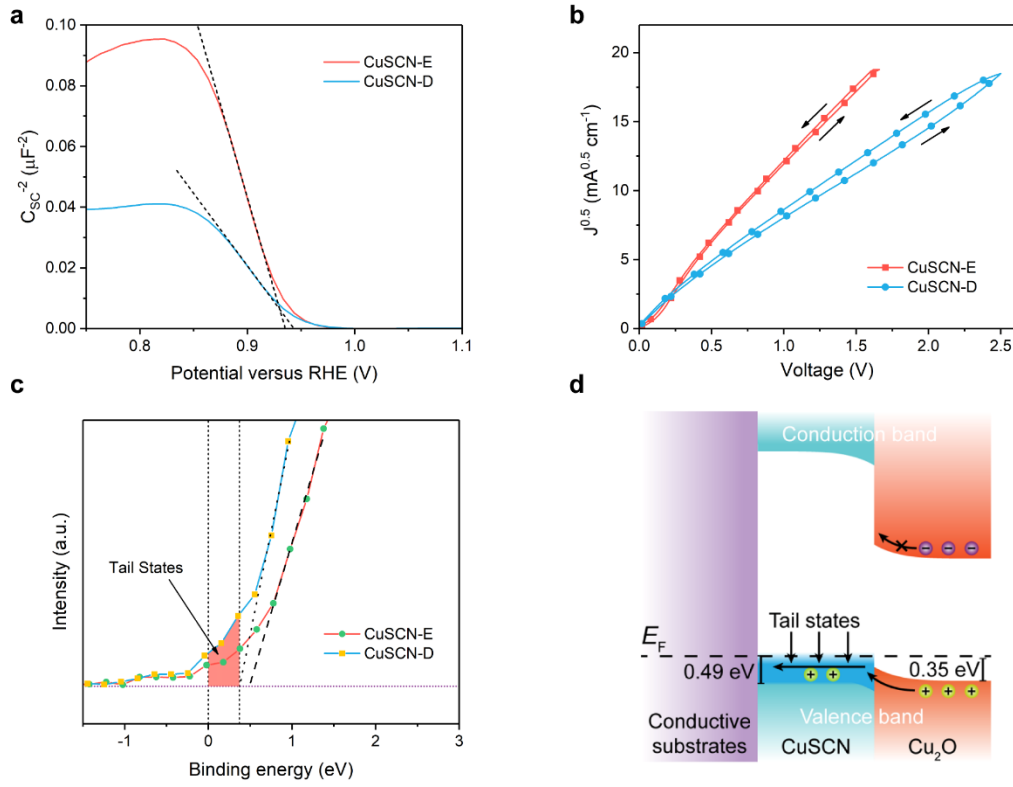

Figure 3.17 | Electronic properties of CuSCN layers and hole transport mechanism. a, Mott-Schottky plot of CuSCN layers tested in 1 M Na_2SO_4 solution. b, SCLC measurement on different CuSCN layers. c, Enlarged valence band spectra with shadowed area denoting the band-tail states. d, Band energy diagrams showing the band-tail assisted hole transport between Cu_2O and CuSCN.
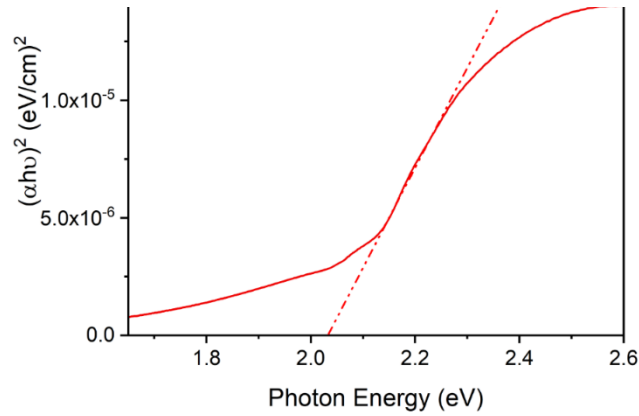

Figure 3.16 | Mott-Schottky plot of Cu_2O. Tests are carried out in pH 9 carbonate buffer on Cu_2O photocathode without ALD layers.

To evaluate the electric conductivity of the films, the majority carrier density and mobility are acquired by Mott-Schottky and SCLC methods, respectively. According to the Mott-

Schottky equation,

$$\frac{1}{C^2} = \frac{2}{\varepsilon\varepsilon_0 e N_A A^2}\left(-V + V_{fb} - \frac{kT}{e}\right)$$

where C is the interfacial capacitance, ε is the dielectric constant of CuSCN, N_A is the density states of acceptors in CuSCN, V is the applied potential and V_{fb} is the flat band potential. The negative slopes of the linear part are clearly indicating the p-type nature of CuSCN films (Figure 3.17a).
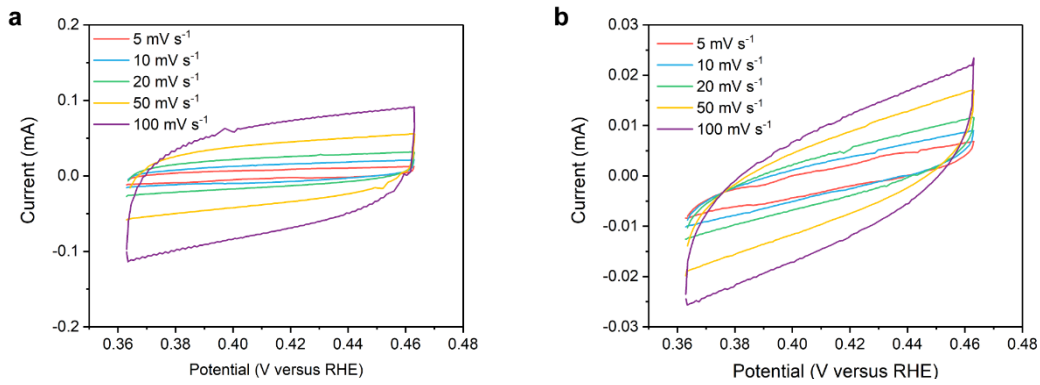

Figure 3.18 | Cyclic voltammograms of CuSCN films. Tests are carried out in 1 M Na$_2$SO$_4$ solution with various scan rates on a, CuSCN-E-2 and b, CuSCN-D-2.

By calculating the slopes and assuming that the dielectric constant is invariable, one can obtain the hole concentrations for both films. However, a flat surface does not reflect the real surface morphology, which may lead to an overestimation of the carrier density.[18] Therefore, we assessed surface roughness by measuring the double-layer capacitance in quiescent electrolyte and compared it to that of mercury/electrolyte interface whose roughness is assumed to be unity. Cyclic voltammograms were collected with various scan rates in a potential window where Faradaic current is minimal (Figure 3.18).

The charging current, i_c, is used to estimate the double layer capacitance, C_{dl}, using the following equation:

$$i_c = \nu C_{dl}$$

With the cylindrical CuSCN structure, the specific capacitance of CuSCN-E is around 7 times larger than that of CuSCN-D (Figure 3.19).
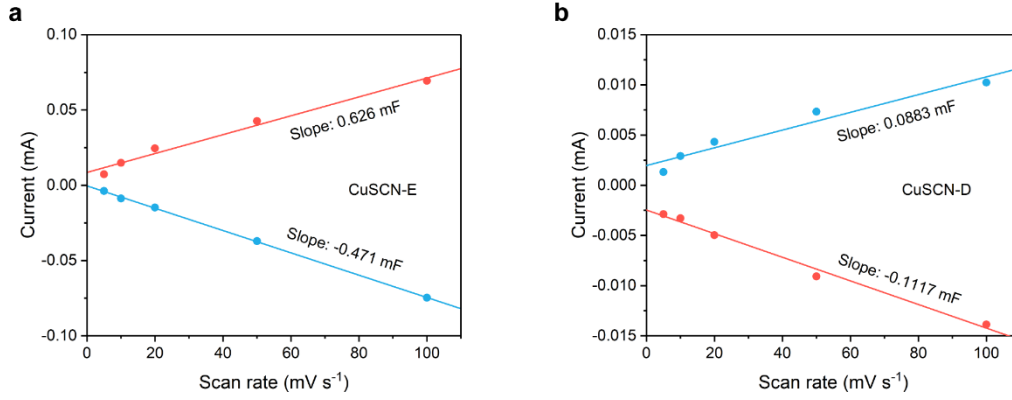
Figure 3.19 | The cathodic (blue) and anodic (red) charging currents as a function of scan rate with linear extrapolation. Currents are recorded at 0.41 V vsersus RHE.

Assuming a specific capacitance of 20 μF cm^{-2}, the roughness factors are calculated to be 21.29 and 4.165 for CuSCN-E and CuSCN-D, respectively.[34] With the correction of surface roughness, if the ε (ε = 5.1) is considered constant, the carrier density of CuSCN-E and CuSCN-D are correspondingly determined to be $8,65 \times 10^{16}$ cm^{-3} and 1.59×10^{18} cm^{-3}.[35] The hole mobility was obtained from trap-free SCLC regime of hole only devices (FTO/Au/CuSCN-E or CuSCN-D/MoO₃/Ag). The current density-voltage (*J-V*) characteristics of the hole only devices were exhibited in Figure 3b. In trap-free SCLC regime, the current density is known to follow the Mott-Gurney Law as follows,

$$J = \frac{8}{9} \mu_h \varepsilon \varepsilon_0 \frac{V^2}{L^3}$$

where μ_h is free carrier mobility, ε_0 is the vacuum permittivity, and L is the CuSCN film thickness. ε is the relative permittivity, reported to be 5.1 for CuSCN.[35] By fitting the *J-V*
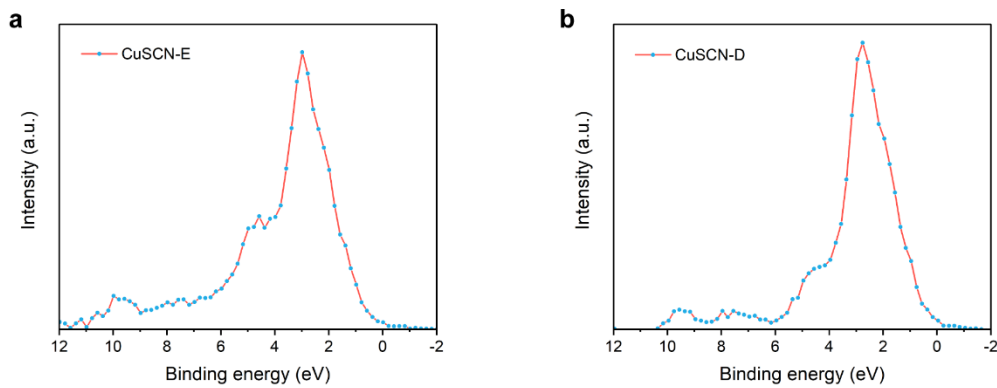

Figure 3.20 | XPS valence band spectra. a, Tested on sample CuSCN-E. b, Tested on sample CuSCN-D.

curves, the μ_h of CuSCN-E and CuSCN-D is calculated to be 0.78 ± 0.06 and 0.34 ± 0.06 cm^2 V^{-1} s^{-1}, respectively. As p-type semiconductors rarely show mobilities beyond 1 cm^2 V^{-1} s^{-1},

these values remain high.[36,37] The excellent hole mobilities of CuSCN-E and CuSCN-D are favorable for extracting photo-generated holes and suppressing the interfacial recombination. It is noticeable that CuSCN-D based hole only devices show a more pronounced hysteresis phenomenon, compared to the devices with CuSCN-E. Such a
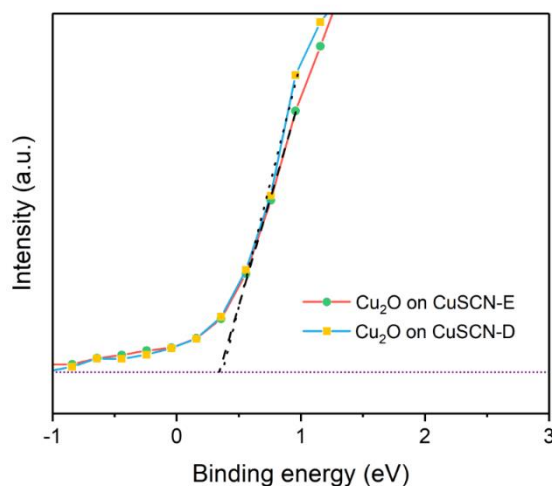

Figure 3.21 | Enlarged valence band spectra of Cu_2O.

hysteresis phenomenon has often been observed in ion-contained devices, such as the emerging perovskite solar cells.[38] As previous discussions evidenced that CuSCN-E has higher crystallinity while CuSCN-D shows relatively loose structure bearing more defects that support the predominant p-type conductivity, the more pronounced hysteresis curves in CuSCN-D hole only devices is interpreted as the migration of residual ions considering a thick CuSCN layer is used for hole only devices.[14] In summary, the CuSCN-D films own higher hole conductivity relative to the CuSCN-E counterparts, which was expressed in the form of better fill factor during PEC tests. Based on the results, we suggest that CuSCN with a less crystalline structure, which bears more defects could potentially be beneficial for hole transport.

The XPS valence band spectra are acquired to analyze the electronic structures of CuSCN. The characteristic valence band signals show excellent consistency with the reported density of states calculations concerning number of featured peaks and energy positions after subtracting a Shirley background.[39–42] The prominent peak of Cu 3d orbital is well-resolved at around 3 eV whereas other features arising between 3 eV and 12 eV can be attributed to the covalent bonding in the CuSCN (Cu-S, S-C, and C≡N bonds), Figure 3.20.

The VBMs are found to be 0.49 eV for CuSCN-E and 0.37 eV for CuSCN-D relative to the

Fermi level by linear extrapolation, which corresponds well with reported results acquired from both XPS and ultraviolet photoelectron spectroscopy (UPS), Figure 3.17c.[40,41,43] (1.2) Small barriers will be formed between Cu_2O/CuSCN interface during hole transport, as the valence band maximum (VBM) of Cu_2O is approximately 0.35 eV, Figure 3.21. In general, the barrier will reduce the open-circuit voltage and impede efficient hole extraction. Although the barrier in CuSCN-D devices is small, and tunneling may overcome the barrier, the device performance with thick CuSCN-D (as thick as 750 nm) contradicts with this assumption. Therefore, we infer that holes should be transported through a transport energy level.

A close analysis at the density of states near the valence band edge reveals the existence of band-tail states, as shown in the shadow region of Figure 3.17c. The possible contribution of carbon layer to the tail intensity has been ruled out by employing argon plasma etching before data acquiring. It is generally considered that these states within the bandgap originate from internal strain, composition variations, surface crystal or chemical defects.[14] In the case of solution-processed CuSCN films, acceptor-like states would appear near the Fermi level due to structural defects or composition variations through electrical field-effect measurements.[41,43] Previous reports of CuSCN-based dye-sensitized cells and field-effect transistors, along with DFT calculations, have predicted that the enhanced hole conductivity of CuSCN is due to acceptor-like states above VBM and they should occur near the Fermi level which can even extend to the Fermi level owing to their broad energetic distribution.[35,40,41] The noticeable tail signals arranging from 0.37 eV to -0.25 eV observed in the valence band spectra clearly prove the assumption. By comparing the acceptor levels with experimental evidence, these defects are mostly suggested to be Cu vacancies. In addition to that, S vacancies (or equivalently, CN vacancies) are also possible to contribute to shallow degenerated levels, provided the vacancy occurs at a significant concentration.[40]

Based on the above information and discussion, we constructed the band diagrams to illustrate the hole conducting mechanism in Figure 3.17d. Though CuSCN-D and Cu_2O have close valence band edges, the conduction band minimum of CuSCN is much higher than that of Cu_2O, resulting in a 2-eV bandgap difference. The large conduction band offset at the CuSCN/Cu_2O interface generates a huge barrier for electrons to inject, thus electron-hole recombination is reduced in CuSCN. Although the valence band offset could hinder hole transporting from Cu_2O to CuSCN, the band-tail states existence renders a smooth hole transport without experiencing the barrier (via valence band). Specifically, the hole

injection barrier was reduced by the transport pathway, without heavy doping to shift Fermi level.

3.3 Conclusion

PEC water splitting relies on efficient charge separation and transport. In this work, we have demonstrated the use of CuSCN as an effective HTL for Cu$_2$O photocathodes, which resulted in overall enhanced performance. Two types of CuSCN films with different structures were fabricated by simple solution processes. Detailed analysis of optical, electrochemical and electronic characterization suggest that a defective structure could be beneficial for hole conduction in CuSCN. Moreover, band-tail states assisted hole transport was discovered between Cu$_2$O and CuSCN. This work stands as the first one that use CuSCN as an efficient HTL layer in Cu$_2$O photocathodes. Considering the optoelectronic and cost advantages of CuSCN material, future application such as tandem water splitting devices with improved performance become possible.

3.4 Methods

3.4.1 Fabrication of the photocathodes

Preparation of CuSCN films. Prior to deposition, FTO substrates were cleaned with ultrasonic in 2% Hellmanex solution (20 min), acetone (20 min), ethanol (20 min) and deionized water (20 min). Opaque samples are prepared on gold coated substrates while transparent samples are fabricated directly on cleaned FTO. 100 nm of Au was sputtered using Alliance Concept DP 650 with uniform mode. CuSCN-E is prepared by electrodeposition in aqueous solution containing 12 mM $CuSO_4$ and equivalent amount of EDTA and KSCN whereas CuSCN-D is fabricated in aqueous solution containing 15 mM $CuSO_4$, 67.5 mM DEA and 45 mM KSCN. EDTA and DEA were added before adding KSCN to prevent $Cu(SCN)_2$ precipitate formation. The pH of EDTA-contained precursor solution and DEA-contained precursor solution are 1.6 and 8.2, respectively. A standard three-electrode configuration was used for electrochemical deposition with Pt counter electrode and Ag/AgCl/sat. KCl reference electrode. All films are prepared using chronoamperometry technique with various duration. The deposition potentials of CuSCN-E and CuSCN-D respectively are -0.3 V and -0.45 V versus reference electrode.

Fabrication of Cu_2O photocathodes. all Cu_2O photocathodes are prepared on CuSCN films for different conditions except conventional control samples with previously described method.[12] Cu_2O was electrodeposited in a buffered copper sulfate solution. To prepare the solution, 7.98 g $CuSO_4$, 67.5 g lactic acid and 21.77 g K_2SO_4 were dissolved in 250 ml H_2O followed by a pH adjustment to pH 10 with 2 M KOH aqueous solution. The electrodeposition of Cu_2O was performed in galvanostat mode with current density of -0.1 mA cm^{-2}. A large piece of platinum was used as the counter electrode and an Ag/AgCl/sat. KCl electrode is used as reference. Deposition duration was varied according to the main text. ALD was carried out for depositing Ga_2O_3 and TiO_2 layers with Savannah 100 (Cambridge NanoTech) thermal ALD system. The thicknesses of Ga_2O_3 and TiO_2 layers typically are both 20 nm and controlled by number of cycles of ALD. Gallium oxide was deposited using bis(μ-dimethylamino)tetrakis(dimethylamino)digallium (98%, Stream Chemicals) and TiO_2 was deposited using tetrakis(dimethylamino)titanium (99.999%, Sigma). The chamber is stabilized at 150 °C and flushed with 10 sccm nitrogen gas (99.9995%, Carbagas). Specially, samples for 60-hour stability test were protected with 100 nm TiO_2. RuO_x catalyst was photoelectrochemically deposited under galvanostatic

mode as previously described.[8] Briefly, the deposition was carried out in 1.3 mM KRuO$_4$ precursor solution for 6 min with constant current density of -28 µA cm^{-2} under simulated light illumination. Platinum wire was used as counter electrode.

3.4.2 Materials, optical, electronic and photoelectrochemical characterizations

Materials Characterization. The phase composition of the as-prepared films was analyzed by X-ray diffraction (XRD) on an Empyrean system with PIXcel-1D detector and Cu Kα radiation. Diffraction patterns were recorded between 2θ of 10° and 80° at a scan rate of 1° min^{-1} with a step width of 0.02^o. SEM images were collected with a high-resolution scanning electron microscope (Zeiss Merlin) equipped with the in-lens detector. X-ray photoelectron spectroscopy (XPS) measurements were performed with PHI VersaProbe II scanning XPS microprobe using a monochromatic Al Kα X-ray of 24.8 W power with a beam size of 100 µm. The spherical capacitor analyzer was set at 45% take-off angle with respect to the sample surface. All peaks are calibrated using adventitious C 1s peak of 284.8 eV to correct charge shift of binding energies after deconvolution. Valence band spectra were acquired after argon plasma etching to avoid the adventitious carbon layer contribution. Curve fitting was performed using PHI Multipak software after Shirley background subtraction. SEM images are collected using a high-resolution scanning electron microscope (Zeiss Merlin) with in-lens dector.

Photoelectrochemical analysis. All photoelectrochemical and electrochemical analysis was done using SP-300 potentiostat with EIS module (BioLogic Science Instruments). PEC performance was characterized in homemade PEEK cells with three-electrode configuration, where Cu$_2$O photocathode is the working electrode, Pt wire is the counter electrode and Ag/AgCl/sat. KCl is the reference electrode. Including stability tests, PEC performance is measured in a pH 5 buffer solution which contains 0.5 M Na$_2$SO$_4$, 0.1 M sodium phosphate with an LCS-100 solar simulator (class ABB, Newport, with air mass 1.5 G filter) providing illumination. The intensity was controlled by light path distance which is determined by measuring the short-circuit current of a calibrated silicon diode with KG 3 filter. Calibration was done across the range between 300-800 nm dependent on photoabsorber bandgap. All linear-sweep voltammetry uses scan rate of 10 mV s^{-1}. The IPCE was measured by comparing wavelength-dependent photoresponse at certain potential of photoelectrodes and a silicon photodiode (FDS100-CAL, Thorlabs) under light from 300 W xenon lamp through a monochromator (TLS-300XU, Newport). At each wavelength stair, current 5 s after wavelength shift was recorded. Electrochemical

impedance measurement was carried out for CuSCN and Cu$_2$O in 1 M Na$_2$SO$_4$ solution. The space-charge capacitance was recorded at various applied potential. Potential values were transformed to the reversible hydrogen electrode scale using the following equation:

$$E_{RHE} = E_{Ag/AgCl(KCl\,sat.)} + 0.197\,V + 0.059\,V \times pH$$

Surface roughness of CuSCN was estimated by comparing the double-layer capacitance of the electrode/electrolyte interface to that of the mercury/electrode interface.[34] measuring the double-layer capacitance was determined using cyclic voltammetry (CV) measurements. The non-Faradaic potential window was first identified from initial CV scans. All measured current in this region is assumed to be double-layer charging current. The C_{dl} equals to the slope of the line by linear fitting where i_C is function of v. The electrochemically active surface area (ECSA) was calculated by dividing C_{dl} of the electrode by that of liquid mercury electrode. Thereafter, the roughness factor is found by comparing the ECSA to apparent electrode are.

Optical measurements. Optical data of films were acquired using a UV-vis-NIR spectrophotometer (Cary) in transmission mode. All films are tested on FTO substrates using the FTO transmittance curve as background. Corresponding absorption spectra were derived according to Kubelka-Munk theory. The optical bandgap of Cu$_2$O was determined from linear extrapolation of Tauc plots assuming direct allowed transition (n = 2)

Hole mobility characterization. Hole only devices with the structure of FTO/Au/CuSCN/MoO$_3$/Ag were fabricated to determine hole mobility of CuSCN-E and CuSCN-D. To construct the hole only device with the function of blocking the electron injection under bias, firstly, a layer of Au (100 nm) was sputtered on top of FTO. Then, EDTA- and DEA- CuSCN with a thickness of 1.5 μm were electrodeposited by the method described above. The CuSCN thickness was obtained from a calibration curve between electrodeposition time and film thickness (examined by cross-sectional SEM images). After that, the substrates were transferred to a vacuum chamber. 10 nm MoO$_3$ and 100 nm Ag were evaporated sequentially under a pressure of 1×10^{-6} mbar through a shadow mask (area defined as 28 mm^2). The current density-voltage characteristics of the devices were tested by Keithley 2400 source measure unit under dark condition. The averaged mobility data is acquired from three devices and calculated from the forward *J-V* scan.

Gas quantification. The amount of hydrogen evolved from a homemade gas-tight PEC cell

was quantified by a gas chromatograph (HP 5890, molecular sieve 5 L column) equipped with a thermal conductivity detector. Gas products were sampled every 11 min using argon carrier gas.

3.5 References

(1)   K. Sivula; R. Van De Krol. Semiconducting Materials for Photoelectrochemical Energy Conversion. *Nat. Rev. Mater.* **2016**, *1* (2).

(2) W. Yang; J. Moon. Recent Advances in Earth-Abundant Photocathodes for Photoelectrochemical Water Splitting. *ChemSusChem* **2018**, 1–12.

(3) Y. Yang; S. Niu; D. Han; T. Liu; G. Wang; Y. Li. Progress in Developing Metal Oxide Nanomaterials for Photoelectrochemical Water Splitting. *Adv. Energy Mater.* **2017**, *7* (19), 1700555.

(4) S. D. Tilley. Recent Advances and Emerging Trends in Photo-Electrochemical Solar Energy Conversion. *Adv. Energy Mater.* **2019**, *9* (2), 1802877.

(5) A. Paracchino; V. Laporte; K. Sivula; M. Grätzel; E. Thimsen. Highly Active Oxide Photocathode for Photoelectrochemical Water Reduction. *Nat. Mater.* **2011**, *10* (6), 456–461.

(6) C. G. Morales-Guio; S. D. Tilley; H. Vrubel; M. Graẗzel; X. Hu. Hydrogen Evolution from a Copper(I) Oxide Photocathode Coated with an Amorphous Molybdenum Sulphide Catalyst. *Nat. Commun.* **2014**, *5* (I), 1–7.

(7) C. G. Morales-Guio; L. Liardet; M. T. Mayer; S. D. Tilley; M. Grätzel; X. Hu. Photoelectrochemical Hydrogen Production in Alkaline Solutions Using Cu₂O Coated with Earth-Abundant Hydrogen Evolution Catalysts. *Angew. Chemie - Int. Ed.* **2015**, *54* (2), 664–667.

(8) M. Stefik; M. Graetzel; M. Schreier; J. Azevedo; S. D. Tilley. Ruthenium Oxide Hydrogen Evolution Catalysis on Composite Cuprous Oxide Water-Splitting Photocathodes. *Adv. Funct. Mater.* **2013**, *24* (3), 303–311.

(9) Z. Zhang; R. Dua; L. Zhang; H. Zhu; H. Zhang; P. Wang; W. Desalination; E. Science; E. Division; et al. Carbon-Layer-Protected Cuprous. **2013**, No. 2, 1709–1717.

(10)   J. Luo; L. Steier; M. K. Son; M. Schreier; M. T. Mayer; M. Grätzel. Cu₂O Nanowire Photocathodes for Efficient and Durable Solar Water Splitting. *Nano Lett.* **2016**, *16* (3), 1848–1857.

(11)   C. Li; T. Hisatomi; O. Watanabe; M. Nakabayashi; N. Shibata; K. Domen; J. J.

Delaunay. Positive Onset Potential and Stability of Cu₂O-Based Photocathodes in Water Splitting by Atomic Layer Deposition of a Ga₂O₃ Buffer Layer. *Energy Environ. Sci.* **2015**, *8* (5), 1493–1500.

(12)   L. Pan; J. H. Kim; M. T. Mayer; M. K. Son; A. Ummadisingu; J. S. Lee; A. Hagfeldt; J. Luo; M. Grätzel. Boosting the Performance of Cu₂O Photocathodes for Unassisted Solar Water Splitting Devices. *Nat. Catal.* **2018**, *1* (6), 412–420.

(13)   A. Mendes; M. Grätzel; J. Azevedo; A. Hagfeldt; M. T. Mayer; P. Dias; L. Andrade; S. D. Tilley; D. Bi; et al. Transparent Cuprous Oxide Photocathode Enabling a Stacked Tandem Cell for Unbiased Water Splitting. *Adv. Energy Mater.* **2015**, *5* (24), 1501537.

(14)   P. Pattanasattayavong; V. Promarak; T. D. Anthopoulos. Electronic Properties of Copper(I) Thiocyanate (CuSCN). *Adv. Electron. Mater.* **2017**, *3* (3), 1–12.

(15)   L. Sun; K. Ichinose; T. Sekiya; T. Sugiura; T. Yoshida. Cathodic Electrodeposition of P-CuSCN Nanorod and Its Dye-Sensitized Photocathodic Property. *Phys. Procedia* **2011**, *14*, 12–24.

(16)   T. Iwamoto; Y. Ogawa; L. Sun; M. S. White; E. D. Glowacki; M. C. Scharber; N. S. Sariciftci; K. Manseki; T. Sugiura; et al. Electrochemical Self-Assembly of Nanostructured CuSCN/Rhodamine B Hybrid Thin Film and Its Dye-Sensitized Photocathodic Properties. *J. Phys. Chem. C* **2014**, *118* (30), 16581–16590.

(17)   C. Liu; W. Wu; K. Liu; M. Li; G. Hu; H. Xu. Orientation Growth and Electrical Property of CuSCN Films Associated with the Surface States. *CrystEngComm* **2012**, *14* (20), 6750–6754.

(18)   X. Gan; K. Liu; X. Du; L. Guo; H. Liu. Bath Temperature and Deposition Potential Dependences of CuSCN Nanorod Arrays Prepared by Electrochemical Deposition. *J. Mater. Sci.* **2015**, *50* (24), 7866–7874.

(19)   C. Chappaz-Gillot; R. Salazar; S. Berson; V. Ivanova. Insights into CuSCN Nanowire Electrodeposition on Flexible Substrates. *Electrochim. Acta* **2013**, *110*, 375–381.

(20)   Y. Selk; T. Yoshida; T. Oekermann. Variation of the Morphology of Electrodeposited Copper Thiocyanate Films. *Thin Solid Films* **2008**, *516* (20), 7120–7124.

(21)   W. Sun; C. Huang; Y. Li; H. Peng; Z. Bian; S. Ye; Z. Liu; W. Yan. CuSCN-Based Inverted Planar Perovskite Solar Cell with an Average PCE of 15.6%. *Nano Lett.* **2015**, *15* (6), 3723–

3728.

(22)   C. Chappaz-Gillot; R. Salazar; S. Berson; V. Ivanova. Room Temperature Template-Free Electrodeposition of CuSCN Nanowires. *Electrochem. commun.* **2012**, *24* (1), 1–4.

(23)   D. Aldakov; C. Chappaz-Gillot; R. Salazar; V. Delaye; K. A. Welsby; V. Ivanova; P. R. Dunstan. Properties of Electrodeposited CuSCN 2D Layers and Nanowires Influenced by Their Mixed Domain Structure. *J. Phys. Chem. C* **2014**, *118* (29), 16095–16103.

(24)   D. Ramírez; G. Riveros; K. Álvarez; B. González; C. J. Pereyra; E. A. Dalchiele; R. E. Marotti; D. Ariosa; F. Martín; et al. Electrochemical Synthesis of CuSCN Nanostructures, Tuning the Morphological and Structural Characteristics: From Nanorods to Nanostructured Layers. *Mater. Sci. Semicond. Process.* **2017**, *68* (June), 226–237.

(25)   P. Pattanasattayavong; G. O. N. Ndjawa; K. Zhao; K. W. Chou; N. Yaacobi-Gross; B. C. O'Regan; A. Amassian; T. D. Anthopoulos. Electric Field-Induced Hole Transport in Copper(i) Thiocyanate (CuSCN) Thin-Films Processed from Solution at Room Temperature. *Chem. Commun.* **2013**, *49* (39), 4154–4156.

(26)   T. Du; J. Li; D. J. Payne; N. Wijeyasinghe; L. Tsetseris; H. Faber; Y.-H. Lin; P. Pattanasattayavong; F. Yan; et al. Copper(I) Thiocyanate (CuSCN) Hole-Transport Layers Processed from Aqueous Precursor Solutions and Their Application in Thin-Film Transistors and Highly Efficient Organic and Organometal Halide Perovskite Solar Cells. *Adv. Funct. Mater.* **2017**, *27* (35), 1701818.

(27)   N. S. Mcintyre; M. G. Cook. X-Ray Photoelectron Studies on Some Oxides and Hydroxides of Cobalt, Nickel, and Copper. *Anal. Chem.* **1975**, *47* (13), 2208–2213.

(28)   D. Briggs; G. Beamson. XPS Studies of the Oxygen 1s and 2s Levels in a Wide Range of Functional Polymers. *Anal. Chem.* **1993**, *65* (11), 1517–1523.

(29)   D. A. Salvatore; K. E. Dettelbach; J. R. Hudkins; C. P. Berlinguette. Near-Infrared-Driven Decomposition of Metal Precursors Yields Amorphous Electrocatalytic Films. *Sci. Adv.* **2015**, *1* (2).

(30)   B. K. Meyer; A. Polity; D. Reppin; M. Becker; P. Hering; P. J. Klar; T. Sander; C. Reindl; J. Benz; et al. Binary Copper Oxide Semiconductors: From Materials towards Devices. *Phys. Status Solidi Basic Res.* **2012**, *249* (8), 1487–1509.

(31)   C. Malerba; F. Biccari; C. Leonor Azanza Ricardo; M. D'Incau; P. Scardi; A. Mittiga.

Absorption Coefficient of Bulk and Thin Film Cu$_2$O. *Sol. Energy Mater. Sol. Cells* **2011**, *95* (10), 2848–2854.

(32)   P. Pattanasattayavong; N. Yaacobi-Gross; K. Zhao; G. O. N. Ndjawa; J. Li; F. Yan; B. C. O'Regan; A. Amassian; T. D. Anthopoulos. Hole-Transporting Transistors and Circuits Based on the Transparent Inorganic Semiconductor Copper(I) Thiocyanate (CuSCN) Processed from Solution at Room Temperature. *Adv. Mater.* **2013**, *25* (10), 1504–1509.

(33)   E. R. Shaaban. Microstructure Parameters and Optical Properties of Cadmium Ferrite Thin Films of Variable Thickness. *Appl. Phys. A Mater. Sci. Process.* **2014**, *115* (3), 919–925.

(34)   J. H. Lunsford; T. J. Johnson; E. F. Vansant; Y. Ben Taarit; W. Jolly; K. G. Caulton; H. Lunsford; C. Com-; A. Press; et al. Mechanism of Formation Of. *J. Am. Chem. Soc.* **1975**, *91* (24), 1412–1415.

(35)   P. Pattanasattayavong; A. D. Mottram; F. Yan; T. D. Anthopoulos. Study of the Hole Transport Processes in Solution-Processed Layers of the Wide Bandgap Semiconductor Copper(I) Thiocyanate (CuSCN). *Adv. Funct. Mater.* **2015**, *25* (43), 6802–6813.

(36)   J. A. Caraveo-Frescas; P. K. Nayak; H. A. Al-Jawhari; D. B. Granato; U. Schwingenschlögl; H. N. Alshareef. Record Mobility in Transparent P-Type Tin Monoxide Films and Devices by Phase Engineering. *ACS Nano* **2013**, *7* (6), 5160–5167.

(37)   A. T. Marin; A. Kursumovic; A. Chen; L. A. Dunlop; D. Muñoz-Rojas; C. Yeoh; H. Wang; J. L. MacManus Driscoll; D. C. Iza; et al.   Growth of ∼5 cm^2 V^{-1} s^{-1} Mobility, p-Type Copper(I) Oxide (Cu$_2$O) Films by Fast Atmospheric Atomic Layer Deposition (AALD) at 225°C and Below . *AIP Adv.* **2012**, *2* (4), 042179.

(38)   Y. Wang; X. Liu; Z. Zhou; P. Ru; H. Chen; X. Yang; L. Han. Reliable Measurement of Perovskite Solar Cells. *Adv. Mater.* **2019**, *61646* (2008), 1803231.

(39)   W. Ji; L.-Y. Chen; G.-Q. Yue; S. Wu; H.-B. Zhao; Y. Jia; F.-S. Ke; S.-Y. Wang. Electronic Structures and Optical Properties of CuSCN with Cu Vacancies. *J. Korean Phys. Soc.* **2012**, *60* (8), 1253–1257.

(40)   J. E. Jaffe; T. C. Kaspar; T. C. Droubay; T. Varga; M. E. Bowden; G. J. Exarhos. Electronic and Defect Structures of CuSCN. *J. Phys. Chem. C* **2010**, *114* (19), 9111–9117.

(41)   T. Du; J. Li; D. J. Payne; N. Wijeyasinghe; L. Tsetseris; H. Faber; Y.-H. Lin; P.

Pattanasattayavong; F. Yan; et al. Copper(I) Thiocyanate (CuSCN) Hole-Transport Layers Processed from Aqueous Precursor Solutions and Their Application in Thin-Film Transistors and Highly Efficient Organic and Organometal Halide Perovskite Solar Cells. *Adv. Funct. Mater.* **2017**, *27* (35), 1701818.

(42)　　D. Hines; H. Cohen; T. Bendikov; G. Hodes; P. V. Kamat; Y. Itzhaik.　Band Diagram and Effects of the KSCN Treatment in TiO$_2$/Sb$_2$S$_3$/CuSCN ETA Cells . *J. Phys. Chem. C* **2015**, *120* (1), 31–41.

(43)　　M. Kim; S. Park; J. Jeong; D. Shin; J. Kim; S. H. Ryu; K. S. Kim; H. Lee; Y. Yi. Band-Tail Transport of CuSCN: Origin of Hole Extraction Enhancement in Organic Photovoltaics. *J. Phys. Chem. Lett.* **2016**, *7* (14), 2856–2861.

4 Improving Light Absorption and Charge Extraction by Reworking the Cu$_2$O Photoabsorber

This chapter includes part of the research in a peer-reviewed publication: **L. Pan**; J. H. Kim; M. T. Mayer; M. K. Son; A. Ummadisingu; J. S. Lee; A. Hagfeldt; J. Luo; M. Grätzel. Boosting the Performance of Cu$_2$O Photocathodes for Unassisted Solar Water Splitting Devices. *Nat. Catal.* **2018**, *1* (6), 412–420 and ongoing work of single-crystal Cu$_2$O photoelectrode.

At the heart of photoelectrodes lies the semiconductor photoabsorber. Previous chapters are focused on improving the electron and hole transport by building heterojunctions with Cu$_2$O, while this chapter will focus on the photoabsorber itself. The nanowire Cu$_2$O can harvest scattered light more efficiently while reduces the electron diffusion distance before injection into the catalysts. With conformal and uniform coating of ALD layers and Earth-abundant catalysts, coaxial heterojunction is formed and the whole electrode could deliver meaningful performance in alkaline electrolyte. The second part of this chapter shows the anisotropic opto/electronic properties of Cu$_2$O semiconductor. The successful preparation of single-crystal Cu$_2$O allows high-quality fundamental photoelectrochemical and optical characterizations and offers views for future photoelectrode development.

4.1 Introduction

Cu$_2$O, a p-type semiconductor, has high hole mobility and favorable energy band positions for solar water splitting. Various preparation methods have been proved viable such as electrodeposition,[1,2] magnetron sputtering,[3] chemical vapor deposition[4] and thermal annealing.[5,6] The preparation methods have impacts on morphology, phases, orientation and optoelectronic properties.[1,5] The nanowire photoabsorber has the advantage of larger surface area and higher light absorption compared to the planar structure.[5,6] In the meantime, charge transport and light absorption paths are decouple to allow more efficient electron injection into the catalysts for p-type semiconductors. With the natural advantages of atomic layer deposition, conformal coating of Ga$_2$O$_3$ layer resulted in the radial heterojunction for effective charge separation. Lastly, the increased surface area lowers the work load of catalyst per geometric area.

Before the application of ALD, Cu$_2$O photoelectrodes are tested without the protection layer. The direct contact between Cu$_2$O and electrolyte causes serious corrosion, especially with illumination.[2,5] Efforts are made to change the crystal orientation of Cu$_2$O by adjusting parameters of electrodeposition. It was found that the (111) facet exhibits more stable PEC operation.[7] However, due to the low regularity of crystal orientations, studies on anisotropic optoelectronic properties are not supported. In the second part of this chapter, the single-crystal Cu$_2$O was synthesized by electrochemical epitaxy. Moreover, Cu$_2$O films with 3 orientations were successfully fabricated which provide a perfect platform for optical, electrochemical and photoelectrochemical studies.

4.2 Results and discussion

4.2.1 An all Earth-abundant Cu$_2$O nanowire photoelectrode

Though RuO$_x$ is an effective hydrogen evolution catalyst, its scarcity hinders the large-scale deployment of Cu$_2$O photoelectrodes. In addition, it is not stable in alkaline electrolytes, as demonstrated in Figure 4.1.

The photocurrent dropped by 30% within 8 hours of test using a pH 9 buffer solution. As most of the Earth-abundant electrocatalysts for the oxygen evolution reaction (OER) operate in alkaline electrolytes and tandem devices are imperative for maximizing the utilization of sunlight and driving complete water splitting, it is essential to design our
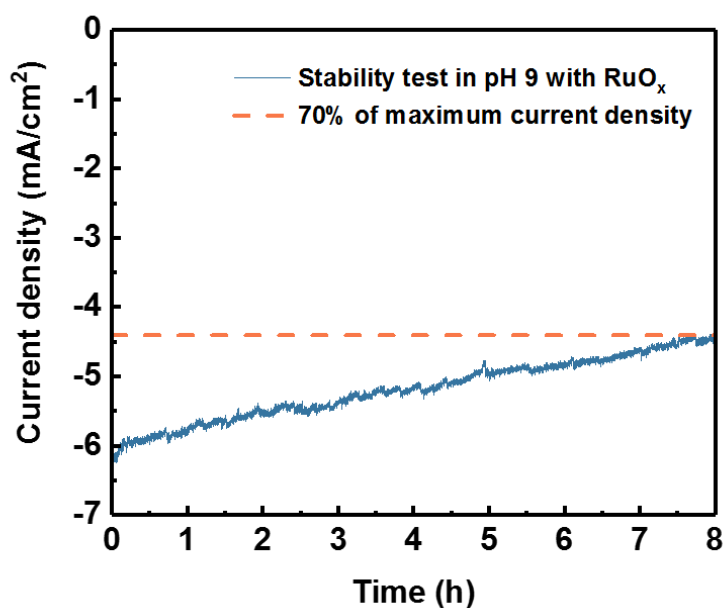
Figure 4.1 | Stability test of Cu₂O photoelectrode with RuO_x catalyst in a pH 9 buffer electrolyte with continuous illumination and stirring.
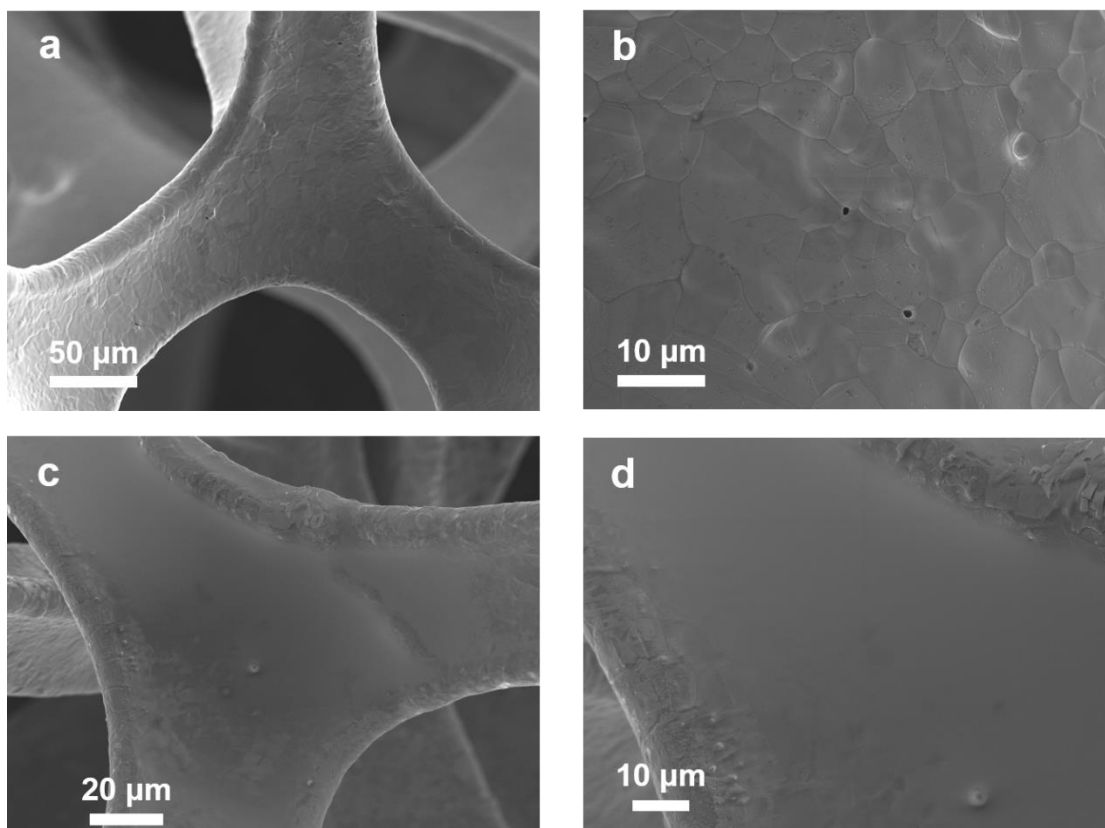

Figure 4.2 | SEM images of nickel foam and NiMo coated nickel foam. a, b, SEM images of bare nickel foam. c, d, SEM images of nickel foam after the electrodeposition of NiMo.

photocathodes to be able to operate in alkaline working environments. Thus, developing

a photocathode using an Earth-abundant HER catalyst with stable performance in alkaline electrolytes is of great importance.
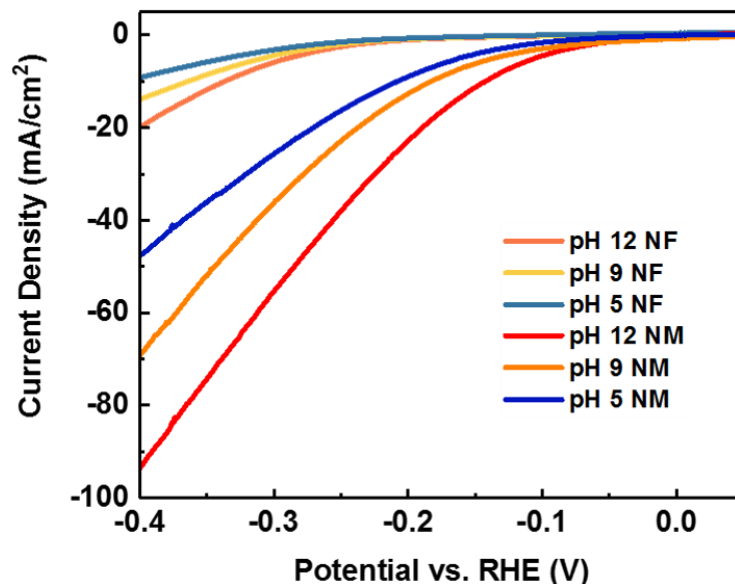

Figure 4.3 | Linear sweep voltammetry of nickel foam (NF) and NiMo coated nickel foam (NM) in buffer electrolytes of different pH.

A promising substitute for noble metal catalysts, NiMo showed remarkable activity and stability in alkaline electrolytes.[8,9] Thus, we chose NiMo as the electrocatalyst for our electrode. To estimate the catalytic activity of NiMo, we examined its activity by coating it on nickel foam, through electrochemical deposition for 4 min with a negative current density of 1.5 mA cm^{-2}. After deposition, the rough surface of nickel foam consisting of visible grains and cavities was uniformly covered by a smooth NiMo catalyst layer (Figure 4.2). The electrocatalytic performances of both bare nickel foam and NiMo-modified nickel foam was evaluated in 3 different pH electrolytes (pH 5, pH 9, pH 12) (Figure 4.3).

In general, at different pH, the NiMo samples showed similar onset potentials for the HER while different trends in the current density appeared when we scanned though more negative values. The catalyst operating in pH 12 electrolyte had a steeper slope compared to that obtained for the two other electrolyte with pH of 5 and 9, leading to overpotentials of 130 mV, 180 mV and 220 mV at 10 mA cm^{-2} current density, respectively. This is probably due to different kinetic rates for H$_2$O dissociation in solutions of different pHs.[10] The bare Ni foam was also tested as a control experiment. However, the current density contribution from Ni foam at ~200 mV overpotential was negligible in different electrolytes, clarifying the excellent HER performances of the NiMo catalyst.

We then photo-electrodeposited NiMo onto Cu$_2$O NW photoelectrodes. After deposition, the morphology of the electrode was well preserved (Figure 4.4a and 4.4b). Taking a closer look, the NiMo catalyst is visible in the form of tiny particles coated homogenously on the surface of the electrode, rivaling the uniformity of atomic layer deposition and contrasting previous reports that showed that NiMo aggregated into large particles (Figure 4.4c). We further carried out scanning transmission electron microscopy (STEM) coupled with energy-dispersive X-ray spectroscopy (EDX) elemental mapping measurements on an individual Cu$_2$O NW to closely study the overlayer coating. In Figure 4.4d, the bright field image reveals that each Cu$_2$O nanowire consists of several large crystal grains connected along one direction. Cu element mapping confirmed this result (Figure 4.4e). In the EDX maps (Figure 4.4 f-k) of other elements, we see that the
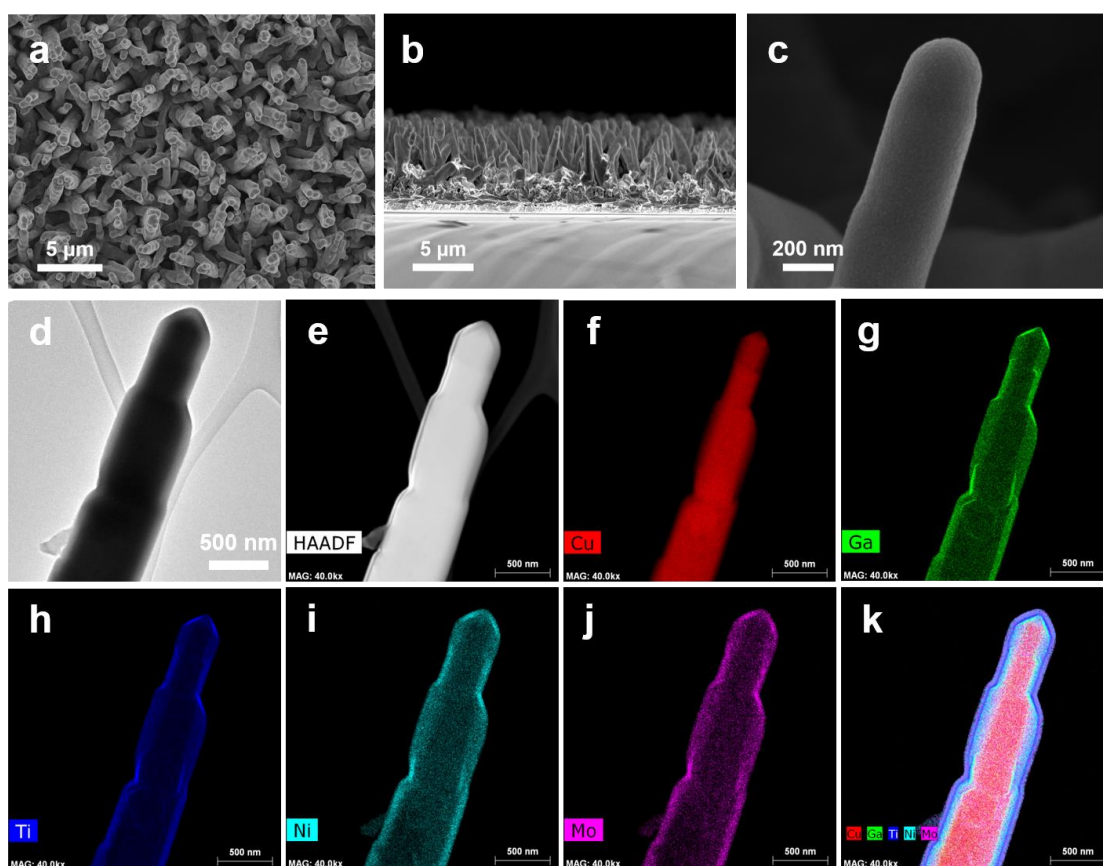

Figure 4.4 | Electron microscopy of NiMo modified Cu$_2$O photocathodes. a, Top view SEM image of NiMo coated Cu$_2$O nanowire photocathodes. b, Cross-section image of cleaved Cu$_2$O photocathodes. c, Magnified SEM image focused on a single nanowire. d, High resolution transmission electron micrograph of Cu$_2$O NW photoelectrode. e, High-angle annular dark-field (HAADF) image of Cu$_2$O NW photoelectrode. f-j, Elemental mapping images of Cu, Ga, Ti, Ni and Mo, respectively. k, Combined elemental mapping image of Cu Ga, Ti, Ni and Mo.
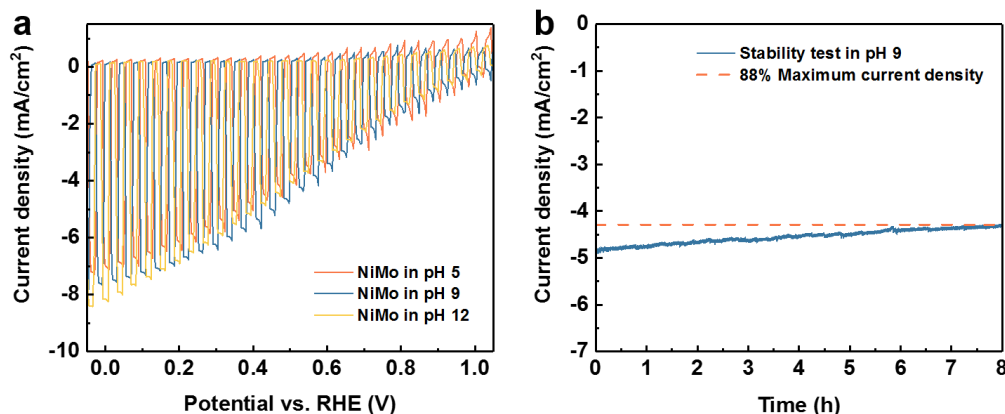
Figure 4.5 | Photoelectrochemical measurement on NiMo modified Cu$_2$O photocathodes. a, *J-E* response under simulated AM 1.5 G chopped illumination in different pH buffer solutions. b, Chronopotentiometry measurement on NiMo modified Cu$_2$O photocathode in pH 9 buffer solution with continuous illumination and stirring.

sequential distribution of each layer forms a radial p-n junction with well-defined thicknesses for each layer. This enables efficient charge separation and collection, both of which are essential aspects. Moreover, when combined with the homogeneous coating of the NiMo catalyst, effective utilization of charges is ensured, resulting in excellent device performance.

Photoelectrochemical tests were carried out in 3 electrolytes of different pH values, under standard simulated AM 1.5 G illumination. When NiMo was employed in the nanowire samples, the onset potential was further improved to more than 1.0 V (positive) vs. RHE for all pH values examined (Figure 4.5a). Unlike the RuO$_x$ modified samples, NiMo modified ones exhibited similar onset behavior but showed recognizable differences in the peak current density at 0 V vs. RHE. The current density for the NiMo modified photocathode reaches 8.2 mA cm^{-2} at 0 V vs. RHE, which is comparable to that of the RuO$_x$ modified sample. The long-term stability of NiMo modified Cu$_2$O NW photoelectrodes in an alkaline electrolyte was evaluated under continuous AM 1.5 G illumination at 0.5 V vs. RHE (Figure 4.5b). After 8 h, the current density retained ~90% of its maximum value. Considering the excellent stability of NiMo as an electrocatalyst in an alkaline electrolyte, the decrease is probably due to degradation caused by electrolyte penetration into the amorphous TiO$_2$ layer.[8,11] Studies have already shown that treatment of TiO$_2$ can effectively improve overall stability.[12]
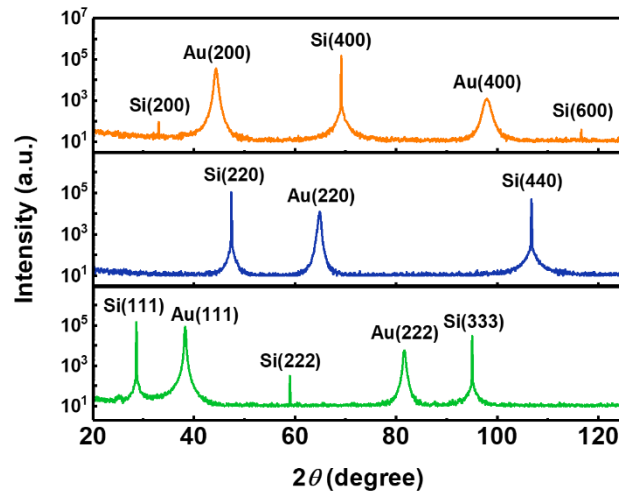
4.2.2 Cu₂O single-crystal photocathodes

Figure 4.6 | XRD patterns of single-crystal Au films on Si wafer with various crystal orientations.

The Cu$_2$O single-crystal film was prepared via a simple and inexpensive method.[13] As the lattice matching agent between Si and Cu$_2$O, gold layer was grown by electrochemical
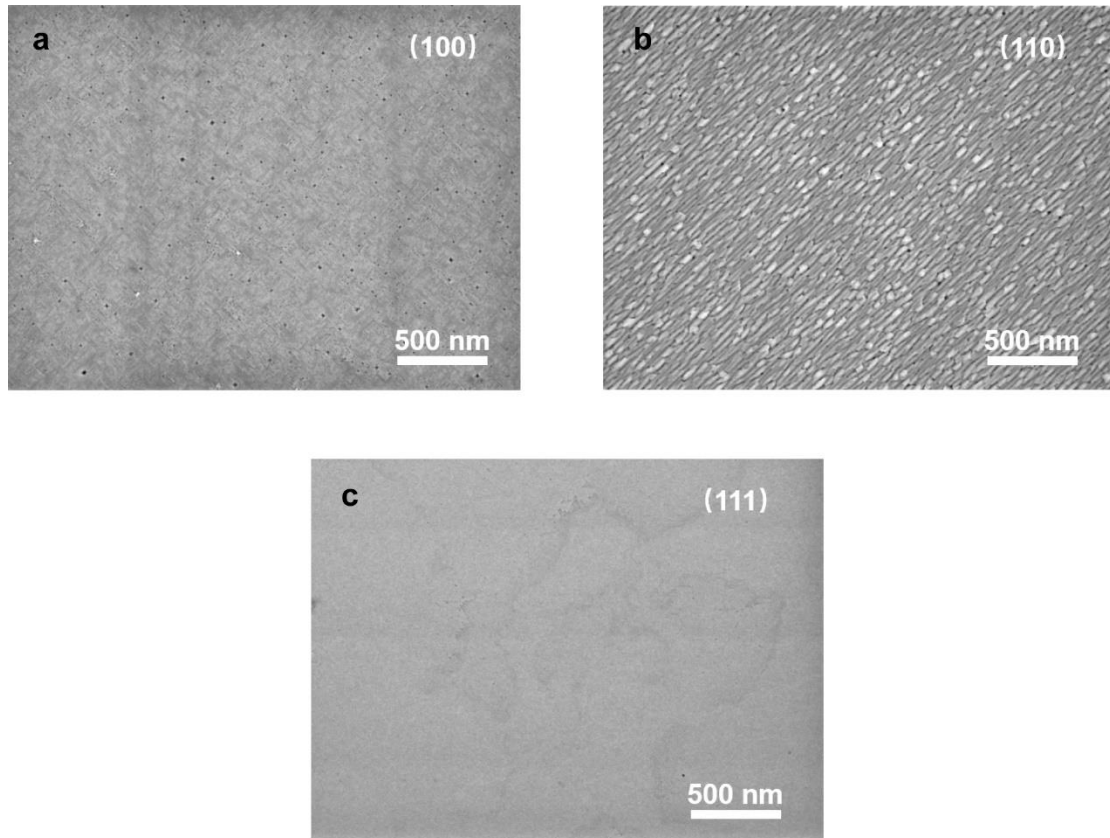

Figure 4.7 | Top-view SEM images of epitaxial Au films on Si wafers of a, (100) crystal orientation, b, (110) crystal orientation and c, (111) crystal orientation.
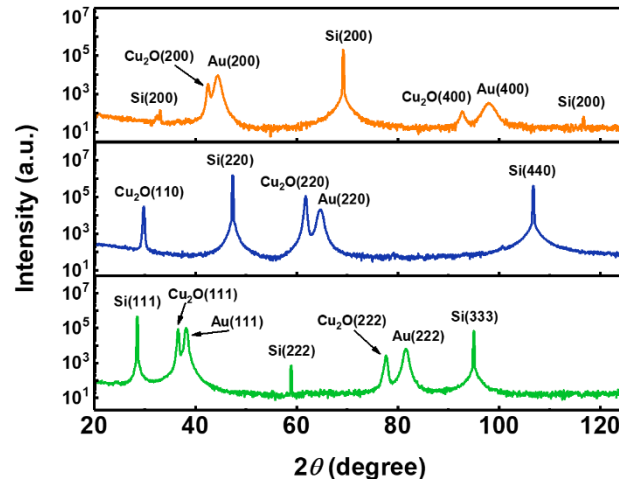
Figure 4.8 | XRD patterns of single-crystal Cu₂O/Au/Si films with various crystal orientations of (100) (orange), (110) (blue) and (111) (green).

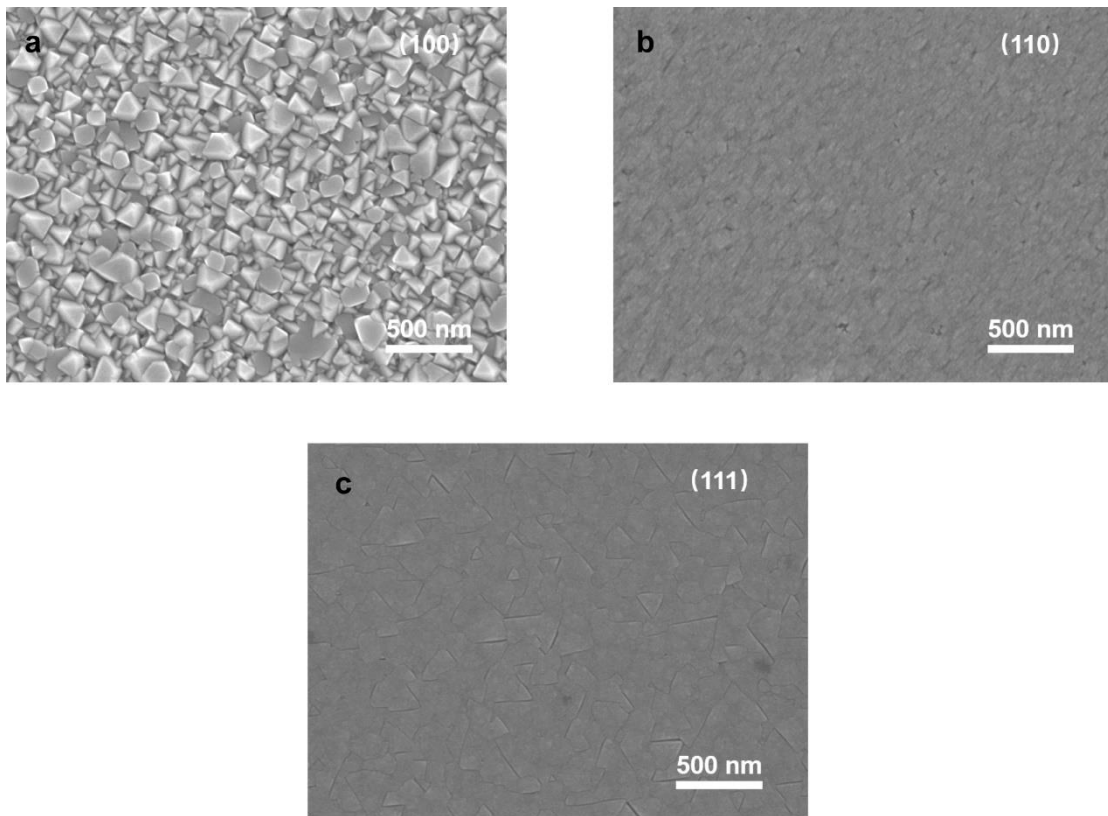Figure 4.9 | Top-view SEM images of epitaxial Cu₂O/Au/Si films of a, (100) crystal orientation, b, (110) crystal orientation and c, (111) crystal orientation.

epitaxy. Then, since the lattice mismatch between gold and Cu₂O is less than 4.7%, the Cu₂O epitaxial growth was possible. Moreover, orientations of films are adjustable due to the nature of epitaxy. If there's need for lifting-off, a native SiOₓ film can be formed through

photooxidation. In both cases of optical and electrochemical studies, single-crystal materials offer perfect platform for optical and electronic studies as its properties are well-defined. Therefore, Cu_2O single-crystal films with 3 orientations are prepared.

The first epitaxy happens during the electrodeposition of Au on Si wafers as 4 unit meshes of Au coincides with 3 unit meshes of Si. Three films of different orientations are characterized by XRD as shown in Figure 4.6. Please note that the y-axis shows log of intensity, so even small impurity peak will be noticeable. However, no impurity matter or phases are found proving the high-quality of the films. Then to observation on the morphology of the film were realized using scanning electron microscope. In Figure 4.7, drastic differences are found among the morphologies of Au films with various orientations. Though small pin holes with size of around 10 nm are found in the (100) Au film, the film is smooth and uniform. The other films are even smoother compared to other studies of epitaxial Au films, hallmark of epitaxial films.[14] Then Cu_2O was electrodeposited epitaxially on Au films. Again, XRD patterns with log of intensity as y-axis was acquired (Figure 4.8). Only Cu_2O with 3 crystal orientations are found in each film, validating the success of electrochemical epitaxy. SEM top-view images are shown in Figure 4.9. In the Cu_2O (100) film, large grains of cubic Cu_2O crystals with average sizes of 100 nm were observed. Both (110) and (111) films are relatively smoother, featuring the triangles formed by flattening of cubic corners.
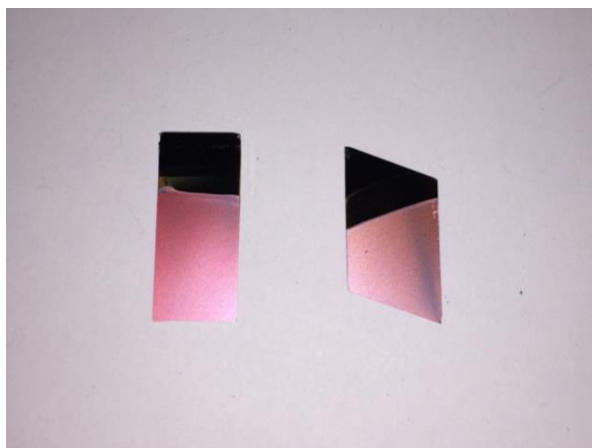
Figure 4.10 | Photo of $Cu_2O/Au/TiO_2$ photoelectrode.

The photoelectrochemical behavior of single-crystal Cu_2O films with three orientations are tested after coating of ALD layers and RuO_x catalyst. One would expect increased performance using single-crystal photocathodes as single-crystal photocathodes owns defect-free crystals with minimum grain boundaries. Both defects and grain boundaries are considered electron-hole recombination centers which are detrimental to

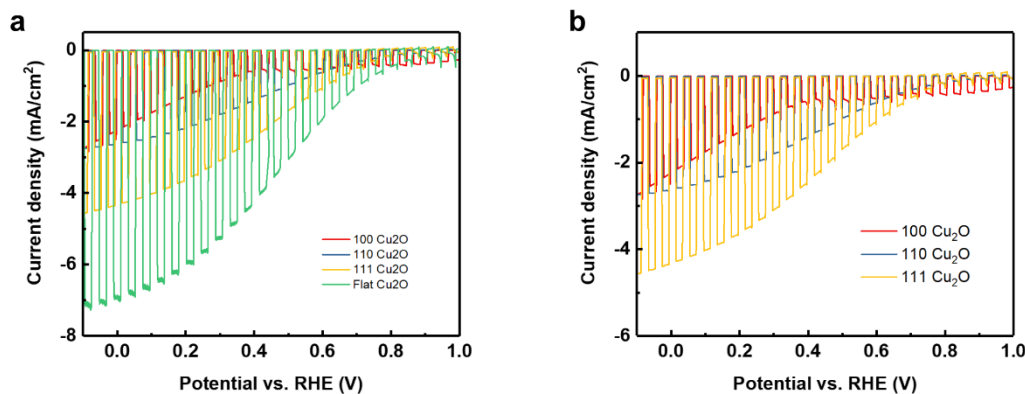Figure 4.11 | a, *J-V* curves of single-crystal and polycrystalline Cu₂O photocathodes under simulated solar illumination with Air Mass 1.5 G spectrum in pH 5 buffered electrolyte. b, *J-V* responses of single-crystal Cu₂O photocathodes with 3 orientations under simulated solar illumination with Air Mass 1.5 G spectrum in pH 5 buffered electrolyte.

photoelectrochemical performance.[15,16] However, as the top of the crystal is very smooth, the photoelectrode reflect like a mirror, Figure 4.10. A great deal of light is reflected directly at the surface resulting in a considerable loss of photons. The comparison between performance of conventional flat photocathodes and single-crystal photocathodes are shown in Figure 4.11a. This problem could be solved in two ways. The first is to apply the anti-reflection layer. Considering the practical application in electrolyte, only limited stable oxide layers which match the refractive indexes could be used. The other way requires controlled etching to create rough surface of Cu₂O while maintaining the bulk to be unharmed.[15,17] Interesting information was found in Figure 4.11b which shows PEC performance among single-crystal Cu₂O of three orientations. Apparently, the best performance provided by (111) Cu₂O photocathodes while the Cu₂O with (100) orientation shows the worst. The results correlate well with a report on facet-dependent electric conductivity where they find the 111-111 plane has the highest conductivity while the 100-100 plane owns the lowest. Further anisotropic property studies using terahertz spectroscopy, electrochemical impedance and high-resolution TEM are envisaged.

4.3 Conclusion

This chapter concludes studies on Cu₂O photoabsorber. First by nano-structuring the Cu₂O photocathode, light absorption was enhanced as more scattering light can be absorbed in the jungle of Cu₂O nanowires. Meanwhile, the decoupled light absorption and charge diffusion paths improved the electron transport within the photoelectrodes. With the

coating of ALD layers, radial junction was formed resulting in record performance among such material. The anisotropic properties were studied with single-crystal Cu$_2$O films of various orientations. It was found that the Cu$_2$O with (111) orientation exhibits the best performance due to better electric conductivity. The successful fabrication of single-crystal Cu$_2$O provides a perfect platform for future fundamental research.

4.4 Methods

4.4.1   Fabrication of Earth-abundant Cu$_2$O photocathodes.

Preparation of Cu$_2$O nanowire photoelectrodes. F-doped SnO$_2$ substrates (FTO, G2E TEC-15) were cleaned by sequential ultrasonic treatments in 2% Hellmanex water solution (30 min), acetone (15 min) and deionized water (15 min). Then, 1.5 μm of Cu (99.995%) was sputtered on FTO using Alliance-Concept DP 650 with a growth rate of 2.65 nm s^{-1}. Samples are subsequently anodized in 3 M KOH (99.98%, metal basis) solution to form Cu(OH)$_2$ nanowires as precursor. Using a large area gold-coated FTO glass as the counter electrode, anodization was performed at a constant current density of 6 mA cm^{-2} at room temperature until a compliance voltage of 2 V was reached. After being rinsed with copious amounts of water, samples were dried in air overnight. To transform Cu(OH)$_2$ into Cu$_2$O, samples are annealed at 600 °C in a tube furnace under high purity Argon (Ar) flow (99.9995%, ALPHAGAZ) for 4 h. Following that, an extra blocking layer of Cu$_2$O was coated on Cu$_2$O nanowire samples by 30 min electrodeposition in a buffered copper sulfate solution. For the preparation of the buffered copper sulfate solution, 7.98 g of CuSO$_4$, 21.77 g of K$_2$HPO$_4$, and 67.5 g of lactic acid were dissolved in 250 mL of H$_2$O, and the pH of electrolyte was adjusted to 12 using a KOH (2 M) solution; the final solution totals around 1 L. Cu$_2$O blocking layers were deposited at a constant current density of −0.1 mA cm^{-2} (galvanostatic mode) using a source meter (Keithley 2400) in a two-electrode configuration (a Pt mesh served as the counter electrode). This deposition condition was also used for the preparation of planar Cu$_2$O samples, with the exception that the deposition time was 100 min.

Atomic layer deposition of overlayers. Atomic layer deposition (ALD) coating was implemented with a thermal ALD system (Savannah 100, Cambridge Nanotech). The top part of the sample was masked by Kapton tape for protecting the electric contact area prior to the deposition of thin n-type semiconductor layers. For preparation of Cu$_2$O NW samples with Al: ZnO (AZO) layer, 20 nm of AZO, followed by 20 nm of TiO$_2$ was coated using the previous described configurations. For the preparation of Cu$_2$O NW samples with a Ga$_2$O$_3$ layer, exposure mode was employed for better coverage over the nanowires. Gallium oxide was deposited at a substrate temperature of 150 °C using Bis(μ-dimethylamino)tetrakis(dimethylamino)digallium (98%, STREM Chemicals) as the

gallium precursor and deionized water as the oxidant. The gallium precursor was heated to 130 °C to provide sufficient vapor pressure, and it was introduced into the chamber under a nitrogen flow of 10 sccm, with 1 s pulse time, 2 s exposure time and 30 s pumping time. The growth rate for Ga$_2$O$_3$ on test silicon wafers with native oxide was determined by ellipsometry (Sopra GES 5E) on test silicon wafers with native oxide, and found to be approximately 1.5 Å per cycle. TiO$_2$ was deposited at a substrate temperature of 150 °C using Tetrakis(dimethylamino)titanium (99.999%, Sigma) with a precursor temperature of 75 °C. Hydrogen peroxide (50% in water, stabilized, Aldrich) was used as the oxidant. H$_2$O$_2$ was stored in 4 °C and the cylinder was freshly refilled before each deposition. Using a nitrogen flow of 5 sccm, TiO$_2$ was deposited at an approximate growth rate of 0.59 Å per cycle with 0.1 s pulse time, 2 s exposure time and 30 s pumping time. Deposition cycle numbers are determined by the required thickness and calculated using the previously mentioned growth rate. Samples for the100-hour stability test were protected with a 100 nm TiO$_2$ ALD layers and all other samples were protected with 20 nm TiO$_2$ layers deposited by ALD.

NiMo hydrogen evolution catalyst deposition. NiMo was electrodeposited onto Ni foam. Prior to the deposition, Ni foam was immersed in 32% hydrochloric acid for 3 min to remove the native oxide layer. The solution used for deposition was modified from the one used by McKone et al.[18] NiMo was deposited from a sulfamate solution with 32.5 g Ni(SO$_3$NH$_2$)$_2$, 3 g H$_3$BO$_3$ and 0.5 g NaMoO$_4$ in 100 mL solution under constant current for 2 min (current density of -1.5 mA cm^{-2}) using a platinum mesh as the counter electrode. Photoelectrodeposition of NiMo on the Cu$_2$O electrode was carried out under simulated AM 1.5G illumination at the same current density as electrodeposition for 180 s. The active area, ranging from 0.25 - 0.8 cm^2, was determined by applying opaque epoxy mask before catalyst deposition.

4.4.2   Fabrication of single-crystal Cu$_2$O photocathodes

Electrodeposition of Au film on Si wafers. The single-crystal electrochemical epitaxial method was modified from previous report.[13] Degenerate Si wafers (Sil'Tronix) with resistivity of 0.004-0.005 Ωcm of 3 orientations namely (100)±0.02°, (110)±0.02° and (111)±0.02° were first cleaned in 5% hydrofluoric acid solution for 30 seconds. Then wafers were soaked in 90 °C hot deionized water for 15 min to grow a new layer of SiO$_x$. A second dipping in 5% hydrofluoric acid was applied to remove the oxide layer followed by rinsing with deionized water. All electrodepositions were implemented immediately after

the above cleaning procedures. Au was electrodeposited in an aqueous plating solution of 0.05 mM $HAuCl_4$, 1 mM KCL, 1 mM H_2SO_4 and 100 mM K_2SO_4 with three-electrode configuration. Ag/AgCl reference electrode and Pt foil counter electrode were applied. Chronoamperometry technique (Bio-Logic SP-300) at -1.9 V versus Ag/AgCl reference pre-polarized potential was applied for various durations with stirring at 400 rpm. All films are rinsed with copious amount of deionized water and dried naturally in air.

Electrodeposition of Cu_2O on Au/Si substrates. Cu_2O was electrodeposited using similar processes in previous chapters while keeping the electrodepositing current density at -0.01 mA cm^{-2}. Durations may vary depending on the desired thickness. ALD layers and catalysts are deposited using the same procedures as reported before.[19]

4.4.3 Materials and photoelectrochemical characterizations

Materials characterizations. XRD patterns were acquired with a Bruker D8 Discover diffractometer in the Bragg-Brentano geometry, using Cu Kα radiation and Ni β-filter. Diffraction spectra were recorded between 2θ of 20° and 80° at a scan rate of 1° min^{-1} with a step width of 0.02°. A high-resolution scanning electron microscope (SEM) (Zeiss Merlin) with in-lens detector was used for SEM imaging. Transmission electron microscopy was done on Technai Osiris (FEI) and energy-dispersive X-ray (EDX) elemental mapping were carried out in scanning transmission electron microscopy (STEM) mode.

Photoelectrochemical characterization. The photoelectrochemical performance of samples was evaluated in a three-electrode configuration using Cu_2O photocathodes as the working electrode, a Pt wire as the counter electrode and Ag/AgCl/sat. KCl as the reference electrode. For measurements in solutions of different pH, the pH 5.0 buffer was prepared using a combination of 0.5 M Na_2SO_4 and 0.1 M phosphate solution, while the pH 9.0 buffer was made by adjusting pH of 0.1 M Na_2CO_3 and 0.1 M $NaHCO_3$ solution and the pH 12 solution was prepared by tuning pH of 0.2 M KOH solution. A potentiostat/galvanostat (BioLogic, SP-300) was used to acquire the photoresponse under chopped illumination from an LCS-100 solar simulator (Newport, Class ABB) with an AM 1.5G filter. The PEC cell was fixed at a position determined by measuring the short-circuit current on a calibrated silicon diode with a KG 3 filter. Calibration was carried out across the relevant wavelength range of 300-800 nm. All linear sweep voltammetry scan rates were 10 mV s^{-1}.

4.5 References

(1) A. Paracchino; J. C. Brauer; J. E. Moser; E. Thimsen; M. Graetzel. Synthesis and Characterization of High-Photoactivity Electrodeposited Cu₂O Solar Absorber by Photoelectrochemistry and Ultrafast Spectroscopy. *J. Phys. Chem. C* **2012**, *116* (13), 7341–7350.

(2) A. Paracchino; V. Laporte; K. Sivula; M. Grätzel; E. Thimsen. Highly Active Oxide Photocathode for Photoelectrochemical Water Reduction. *Nat. Mater.* **2011**, *10* (6), 456–461.

(3) H. Zhu; J. Zhang; C. Li; F. Pan; T. Wang; B. Huang. Cu₂O Thin Films Deposited by Reactive Direct Current Magnetron Sputtering. *Thin Solid Films* **2009**, *517* (19), 5700–5704.

(4) S. Eisermann; A. Kronenberger; A. Laufer; J. Bieber; G. Haas; S. Lautenschläger; G. Homm; P. J. Klar; B. K. Meyer. Copper Oxide Thin Films by Chemical Vapor Deposition: Synthesis, Characterization and Electrical Properties. *Phys. status solidi* **2012**, *209* (3), 531–536.

(5) Z. Zhang; R. Dua; L. Zhang; H. Zhu; H. Zhang; P. Wang. Carbon-Layer-Protected Cuprous Oxide Nanowire Arrays for Efficient Water Reduction. *ACS Nano* **2013**, *7* (2), 1709–1717.

(6) J. Luo; L. Steier; M. K. Son; M. Schreier; M. T. Mayer; M. Grätzel. Cu₂O Nanowire Photocathodes for Efficient and Durable Solar Water Splitting. *Nano Lett.* **2016**, *16* (3), 1848–1857.

(7) Q.-B. Ma; J. P. Hofmann; A. Litke; E. J. M. Hensen. Cu₂O Photoelectrodes for Solar Water Splitting: Tuning Photoelectrochemical Performance by Controlled Faceting. *Sol. Energy Mater. Sol. Cells* **2015**, *141*, 178–186.

(8) J. R. McKone; B. F. Sadtler; C. A. Werlang; N. S. Lewis; H. B. Gray. Ni-Mo Nanopowders for Efficient Electrochemical Hydrogen Evolution. *ACS Catal.* **2013**, *3* (2), 166–169.

(9) Y. Wang; G. Zhang; W. Xu; P. Wan; Z. Lu; Y. Li; X. Sun. A 3D Nanoporous Ni-Mo Electrocatalyst with Negligible Overpotential for Alkaline Hydrogen Evolution. *ChemElectroChem* **2014**, *1* (7), 1138–1144.

(10)   D. Strmcnik; P. P. Lopes; B. Genorio; V. R. Stamenkovic; N. M. Markovic. Design Principles for Hydrogen Evolution Reaction Catalyst Materials. *Nano Energy* **2016**, *29*, 29–36.

(11)   N. V. Krstajić; V. D. Jović; L. Gajić-Krstajić; B. M. Jović; A. L. Antozzi; G. N. Martelli. Electrodeposition of Ni-Mo Alloy Coatings and Their Characterization as Cathodes for Hydrogen Evolution in Sodium Hydroxide Solution. *Int. J. Hydrogen Energy* **2008**, *33* (14), 3676–3687.

(12)   J. Azevedo; L. Steier; P. Dias; M. Stefik; C. T. Sousa; J. P. Araújo; A. Mendes; M. Graetzel; S. D. Tilley. On the Stability Enhancement of Cuprous Oxide Water Splitting Photocathodes by Low Temperature Steam Annealing. *Energy Environ. Sci.* **2014**, *7* (12), 4044–4052.

(13)   N. K. Mahenderkar; Q. Chen; Y. C. Liu; A. R. Duchild; S. Hofheins; E. Chason; J. A. Switzer. Epitaxial Lift-off of Electrodeposited Single-Crystal Gold Foils for Flexible Electronics. *Science.* **2017**, *355* (6330), 1203–1206.

(14)   J. A. Switzer; J. C. Hill; N. K. Mahenderkar; Y. C. Liu. Nanometer-Thick Gold on Silicon as a Proxy for Single-Crystal Gold for the Electrodeposition of Epitaxial Cuprous Oxide Thin Films. *ACS Appl. Mater. Interfaces* **2016**, *8* (24), 15828–15837.

(15)   H. S. Han; S. Shin; D. H. Kim; I. J. Park; J. S. Kim; P. S. Huang; J. K. Lee; I. S. Cho; X. Zheng. Boosting the Solar Water Oxidation Performance of a BiVO₄ Photoanode by Crystallographic Orientation Control. *Energy Environ. Sci.* **2018**, *11* (5), 1299–1306.

(16)   Z. Wang; Y. Inoue; T. Hisatomi; R. Ishikawa; Q. Wang; T. Takata; S. Chen; N. Shibata; Y. Ikuhara; et al. Overall Water Splitting by Ta₃N₅ Nanorod Single Crystals Grown on the Edges of KTaO₃ Particles. *Nat. Catal.* **2018**, *1* (10), 756–763.

(17)   F. Amano; T. Ebina; B. Ohtani. Enhancement of Photocathodic Stability of P-Type Copper(I) Oxide Electrodes by Surface Etching Treatment. *Thin Solid Films* **2014**, *550*, 340–346.

(18)   J. R. McKone; E. L. Warren; M. J. Bierman; S. W. Boettcher; B. S. Brunschwig; N. S. Lewis; H. B. Gray. Evaluation of Pt, Ni, and Ni–Mo Electrocatalysts for Hydrogen Evolution on Crystalline Si Electrodes. *Energy Environ. Sci.* **2011**, *4* (9), 3573.

(19)   L. Pan; J. H. Kim; M. T. Mayer; M. K. Son; A. Ummadisingu; J. S. Lee; A. Hagfeldt; J. Luo; M. Grätzel. Boosting the Performance of Cu₂O Photocathodes for Unassisted Solar

Water Splitting Devices. *Nat. Catal.* **2018**, *1* (6), 412–420.

5 Standalone Solar Water Splitting Devices with Cu$_2$O Photocathodes

This chapter is based on related research in two peer-reviewed publications:

1. **L. Pan**; J. H. Kim; M. T. Mayer; M. K. Son; A. Ummadisingu; J. S. Lee; A. Hagfeldt; J. Luo; M. Grätzel. Boosting the Performance of Cu$_2$O Photocathodes for Unassisted Solar Water Splitting Devices. *Nat. Catal.* **2018**, *1* (6), 412–420.

2. **L. Pan**; Y. Liu; L. Yao; D. Ren; K. Sivula; M. Grätzel; A. Hagfeldt. Cu$_2$O Photocathodes with Band-tail States Assisted Hole Transport for Standalone Solar Water Splitting. **2019**, Submitted.

This version is based on the edition before editorial change.

After previous studies on several aspects of the Cu$_2$O photocathodes, this chapter presents two tandem devices based on the above-mentioned photoelectrodes. The first PEC-PEC tandem system comprises the nanostructured Cu$_2$O photocathodes with radial heterojunction. Using the state-of-the-art BiVO$_4$ photoanode as the front absorber and Cu$_2$O photocathode as the rear one, an unassisted all-oxide tandem was established delivering record solar-to-hydrogen efficiency of such kind. In the second PEC-PV tandem, the Cu$_2$O photocathode was serially connected with a perovskite solar cell. The CuSCN layer developed in chapter 4 allow the planar photoelectrode to be transparent, which creates new possibility of using Cu$_2$O photocathodes as front absorber. Due to the more extensive utilization of solar spectrum, a higher efficiency was achieved.
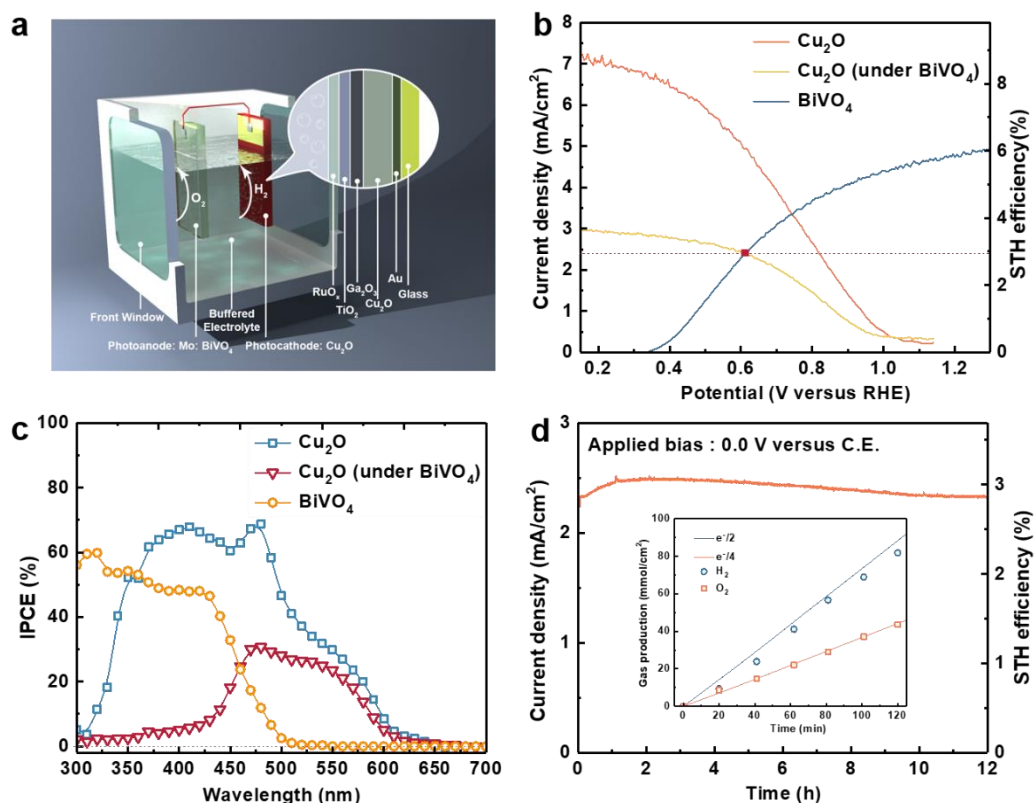
5.1 Introduction

Figure 5.1 | Unassisted all-oxide solar water splitting. a, Illustration of all-oxide tandem solar water splitting device consists of Cu_2O as photocathode and Mo: $BiVO_4$ as photoanode without bias. b, J-E response under simulated AM 1.5G chopped illumination for Cu_2O photocathodes, Mo: $BiVO_4$ photoanode and Cu_2O photocathodes behind photocathodes in 0.2 M Pottasium borate (pH 9.0). Crossing point gives ~2.4 mA/cm^2 and ~3 % solar-to-hydrogen efficiency. c, Corresponding wavelength dependent IPCE spectra. d, Unbiased stability test tandem system in 0.2 M Pottasium borate (pH 9.0). Inset shows the corresponding gas measurement for both photocathode and photoanode.

As mentioned in the first chapter, it is necessary to build tandem devices for efficient solar water splitting due to limitations of single photoabsorber. Recent fast development of oxide photoelectrodes has shown both high light harvesting efficiency and high APCE (charge separation efficiency), however, general great performance of photocathodes and photoanodes do not guarantee high performance of tandem cell: even though InP based photocathodes give ~4.2% half-cell efficiency, it's parallel tandem cell with $BiVO_4$ gives only 0.5 % STH effiiciency.[1] Generally, tandems with oxide-based photoelectrodes delivers STH efficiency of 0.3-1.0%.[2–5]

Inspired by the advancement of Cu$_2$O photocathodes in chapter 3 and 4, inexpensive and efficient tandem devices are expected. In this chapter, an all-oxide PEC-PEC tandem and a PEC-PV tandem based on Cu$_2$O photocathodes are established. Discussions on further improvement of such devices inspired by problems arose during research are presented.

5.2 Results and discussion

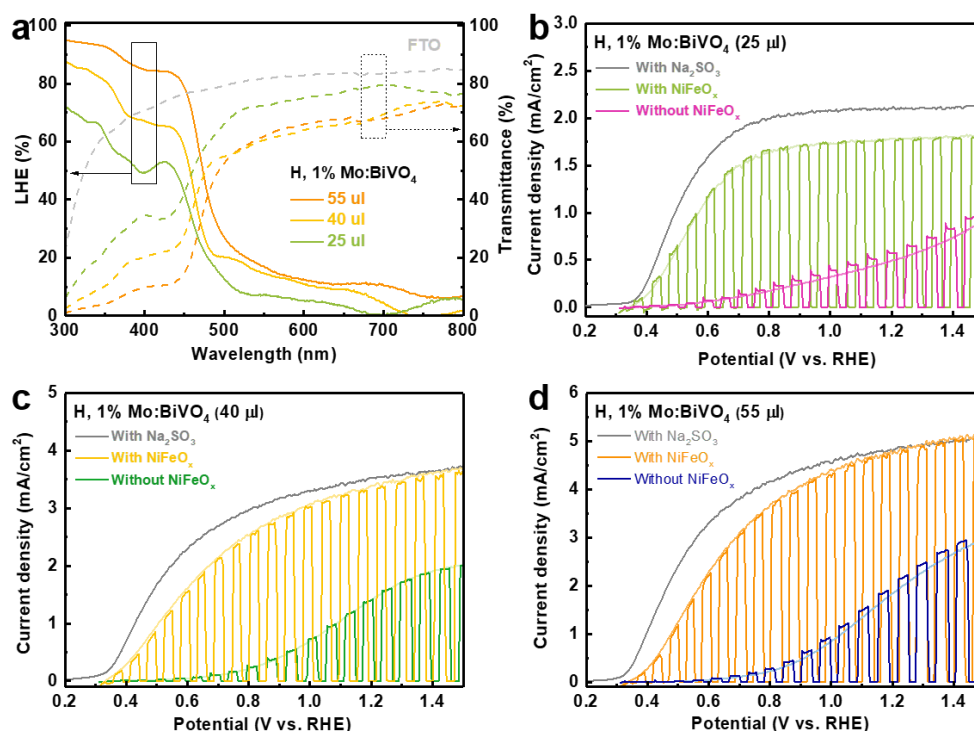### 5.2.1 All-oxide PEC-PEC based on Cu$_2$O photocathodes and BiVO$_4$ photoanodes.

Figure 5.2 | Optical and photoelectrochemical properties of Mo: BiVO$_4$. a, Light harvesting efficiency and transmittance spectra of hydrogen treated Mo: BiVO$_4$ photoanodes with different precursor loading. b-d, *J-E* responses of Mo: BiVO$_4$ photoanodes of 25 μl, 40 μl, 55 μl precursor loading tested with/without NiFeO$_x$ catalyst in pH 9 borate electrolyte with/without sacrificial agent.

To demonstrate the remarkable performance of the new Cu$_2$O photocathode, an overall unassisted solar water splitting tandem device was constructed by pairing it with the state-of-the-art BiVO$_4$ photoanode.[6,7] The detailed configuration of the device is shown in Figure 5.1a, where the light passes first through the front BiVO$_4$ absorber before reaching the Cu$_2$O absorber. In this configuration, the wider bandgap BiVO$_4$ (2.4 eV) absorbs photons of the higher energy, while lower energy photons are absorbed by Cu$_2$O (2.0 eV

band gap). Given that the two photoelectrodes are electronically connected in series, the tandem device current density is limited by the electrode producing the lower photocurrent, and a balanced generation of photocurrents between the two electrodes is therefore desired. To achieve optimal current matching, we fabricated BiVO$_4$ photoanodes of different transparency by varying the precursor volume.

The transmittance of these samples and their associated PEC performance are presented in Figure 5.2. Though the nano-structured Cu$_2$O photocathode has higher plateau current density than the planar one, its comparably lower fill factor results in lower current density at the potential range which is critical for tandem operation, Figure 5.3.
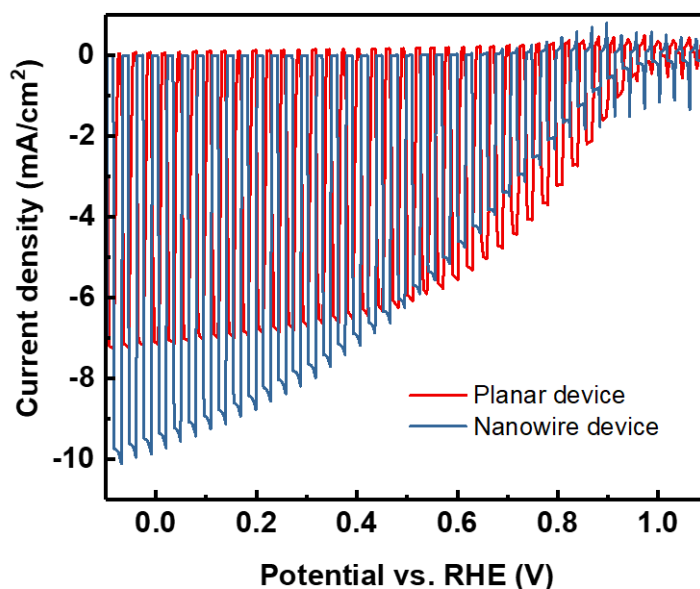

Figure 5.3 | Linear sweep voltammetry of planar photocathodes with electrodeposited Cu$_2$O (planar) and annealed Cu$_2$O (nanowire) tested under chopped AM 1.5G illumination in a pH 5 electrolyte.

Thus, we choose the planar Cu$_2$O samples for the tandem demonstration. The PEC performances of the planar Cu$_2$O photocathode with and without BiVO$_4$ photoanodes of different transparency as filters are presented in Figure 5.4. The operating current density of the overall unassisted tandem solar water splitting device can be predicted by overlapping the *J-E* curves of both electrodes and observing the point at which they overlap, Figure 5.1b. The highest current density of ~2.45 mA cm^{-2} was predicted using the BiVO$_4$ photoanode prepared with the 55 μl precursor solution as illustrated in Figure 5.5. The IPCE responses of both electrodes show their complimentary spectral responses in Figure 5.1c. In the wavelength range around 500 nm, where BiVO$_4$ photoanodes almost stopped absorbing photons with higher wavelengths, the Cu$_2$O photocathode still loses a
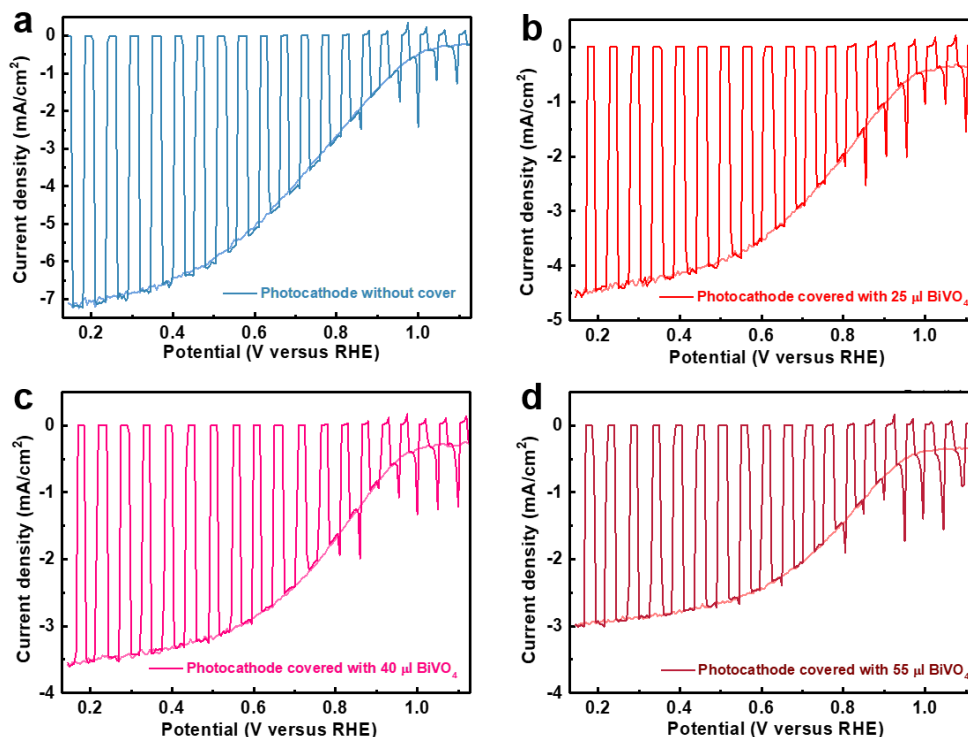
Figure 5.4 | Photoelectrochemical performance of Cu₂O photocathode under different cover conditions. a-d, *J-E* responses of Cu₂O photocathode tested in pH 9 borate buffer solution without/with cover of photoanode prepared with different precursor loading.

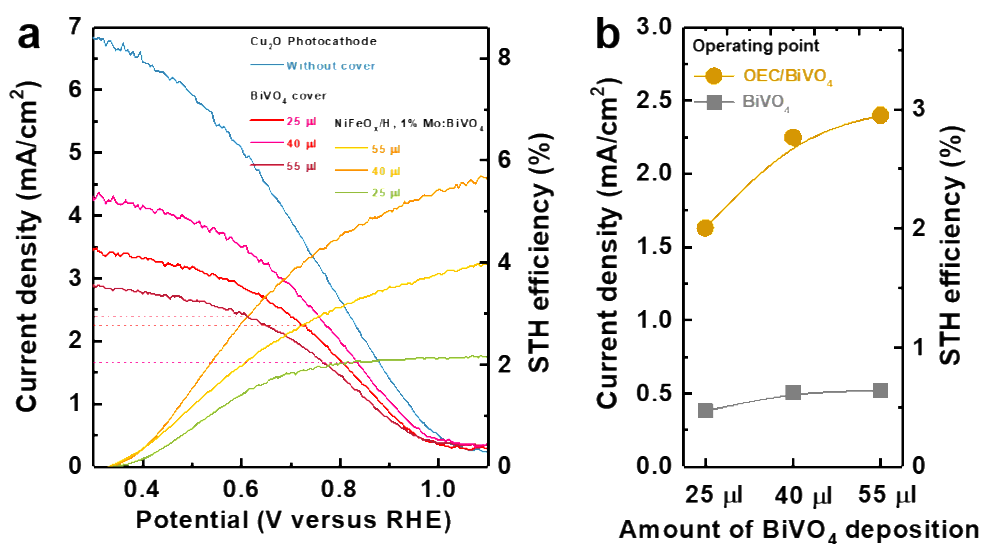considerable amount of efficiency, which is probably due to scattering and reflection at

Figure 5.5 | Optimization of operating point for tandem cell using different thickness of Mo: BiVO₄ photoanodes. a, Overlaid *J-E* responses of Cu₂O photocathodes and Mo: BiVO₄ photoanodes with NiFeOₓ catalyst. b, Summarized operating current density and efficiency of tandem cells.

the electrode-electrolyte and the gas-liquid interface. Though the band gaps of both

*Ref No.	Photocathodes	Photoanodes	**Electrolyte (pH)	***Efficiency	Ref
1	Pt/n/p-Si	Co-Pi/Mo:BiVO4	0.5 M KPi (pH 7.0)	Tandem STH: 0.57%	
2	Pt/a-n/p-Si	NiFeOx/Fe2O3	0.5 M KPi (pH 11.8)	Tandem STH: 0.57%	
3	Pt/TiO_2/Zn:InP	Co-Pi/BiVO4	0.1 M KPi (pH 7)	Parallel scheme STH: 0.5 %	
4	Pt/In_2S_3/CdS/Cu_2ZnSnS_4	NiOOH/BiVO4	0.2 M NaPi (pH 6.5)	Parallel scheme HC-STH: 0.28 %	
5	Pt/Mo/Ti/CdS/In_2S_3/(ZnSe)$_{0.85}$($CuIn_{0.7}Ga_{0.3}Se_2$)$_{0.15}$/Mo/SLG/Ti	NiFeOx/BiVO4	1.0 M KBi (pH 9.2)	Parallel scheme STH: 1.0 %	
6	Pt/Mo/Ti/(ZnSe)$_{0.85}$(CIGS)$_{0.15}$/Mo/SLG	NiFeOx/BiVO4	0.5 M KBi (pH 9.5)	Parallel scheme STH: 0.91 %	
7	Pt/ZnS/CdS/(ZnSe)$_{0.85}$($CuIn_{0.7}Ga_{0.3}Se_2$)$_{0.15}$/Mo/SLG	NiFeOx/BiVO4	0.5 M KBi (pH 9.5)	Parallel scheme STH: 0.6 %	
8	Pt/CdS/$CuGa_3Se_5$/(Ag,Cu)$GaSe_2$/Mo/SLG	NiOOH/FeOOH/ 1% Mo:BiVO4	0.1 M KPi (pH 7)	Tandem STH: 0.67% (2 h stability)	
9	RuO_2/TiO_2/AZO/Cu_2O/Au	Co-Pi/W:BiVO4	0.5 M KPi (pH 7.0)	Tandem STH: 1.0% (retained<5 minutes)	
This work	RuO_x/TiO_2/Ga_2O_3/Cu_2O/Au	NiFeO$_x$/reduced 1% Mo:BiVO$_4$	0.5 M KBi (pH 9.0)	STH: 3.0% +12 stability	

Table 6.1 | Reports of photocathode – photoanode D4 cell for overall water splitting (2012~2017).

*Reports are arranged in year, but not in actual publication date.

**KPi: potassium biphosphate, NaPi: sodium biphosphate, KBi: Potassium borate.

***light source of all results is AM 1.5 G, 100 mW/cm^2 (1 sun) unless denoted. Materials are denoted as stable if constant potential operation was demonstrated without serious efficiency drop (<25%).

photoelectrodes are not perfect for two-absorber tandem, the absorption mismatch gives reasonable efficiencies.

The standalone unassisted solar water splitting device comprising of the Cu_2O photocathode and $BiVO_4$ photoanode exhibits a current density as predicted in Figure 5.1b. The device showed stable performance with less than 10% loss under continuous illumination for 12 hours (Figure 5.1d). A peak current density of ~2.5 mA cm^{-2} was achieved after operation for 1 hour, which corresponds to a STH conversion efficiency exceeding 3%. To the best of our knowledge, this is by far the highest efficiency reported for unbiased PEC water splitting devices with oxide-only semiconductors (See Table 6.1).

With great advances of the state-of-the-art Cu_2O photocathodes, a huge leap from previous record efficiencies of tandems which combine two absorbers (oxides and Si, CIGS or CZTS photoelectrodes) with less than 1% STH efficiency was realized. A gas measurement was also carried out to quantify the H_2 and O_2 gases evolved (Figure 5d inset). Owing to the large head space of the PEC cell and the Ar purging, the initial Faradaic efficiencies for H_2 and O_2 were not ideal, however it reaches almost 100% afterwards showing the legitimacy of the new record.

5.2.2   PEC-PV tandem with the CuSCN based Cu_2O photocathode

The solar-blind CuSCN layer is ideal for allowing the transmission of unabsorbed solar energy for rear photoabsorber that could provide extra bias. Here, we choose the perovskite solar cell (PSC) as the rear absorber and simulated their individual photocurrent for a PEC-PV tandem device. Based on an AM 1.5 G photon flux spectrum and IPCE data of Cu_2O photocathodes (front absorber) and PSCs (rear absorber, masked with the photocathodes), the electron fluxes are calculated as shown in Figure 5.6a. With high IPCE, Cu_2O is efficiently harvesting short-wavelength solar energy, yet leaving large amount of energy untapped due to its relatively large bandgap. As the rear photoabsorber, PSC collected the rest of the solar energy till 850 nm. With two absorbers, most of the solar spectrum is well-covered. Based on the concept, we designed the arrangement of all parts in Figure 5.6b, where two basic parts of PEC photoelectrode and PSC cell are wired and placed closely back-to-back to minimized light scattering loss. Carrier paths are shown as well. When the system is illuminated, photo-generated electrons in Cu_2O are collected and injected to the surface RuO_x catalyst to reduce water, while the holes will recombine with electrons from the PSC through the wire. Holes from PSC are conducted to the counter electrode back in the PEC cell for oxygen evolution reactions. Iridium oxide
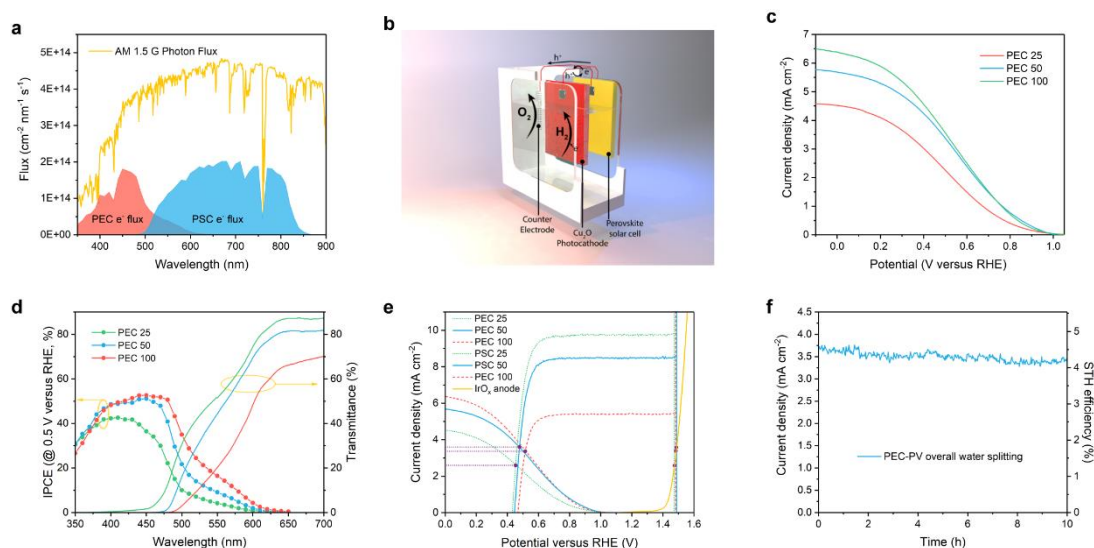
Figure 5.6 | Standalone solar water splitting. a, Plot of photon flux based on AM 1.5 G spectrum and expected electron fluxes of photocathode and PV calculated from wavelength-dependent IPCE responses of photocathode at 0.5 V versus RHE and PV at short circuit. b, Illustration of PEC-PV tandem configuration based on CuSCN-incorporated Cu_2O photocathode, PSC and IrO_x anode. c, *J-E* responses of transparent Cu_2O photocathodes with various thicknesses. Numbers in sample names denote the electrodeposition duration of Cu_2O in minutes. d, Wavelength-dependent IPCE of transparent Cu_2O photocathodes biased at 0.5 V versus RHE and corresponding transmittance spectra. e, Estimated tandem operating current density by overlaying *J-E* curves of photocathodes, *J-V* curves of PV cells and linear sweep voltammetry of IrO_x anode. f, Chronoamperometry of assembled PEC-PV tandem tested under simulated one-sun illumination in pH 5 buffered electrolyte with zero bias.

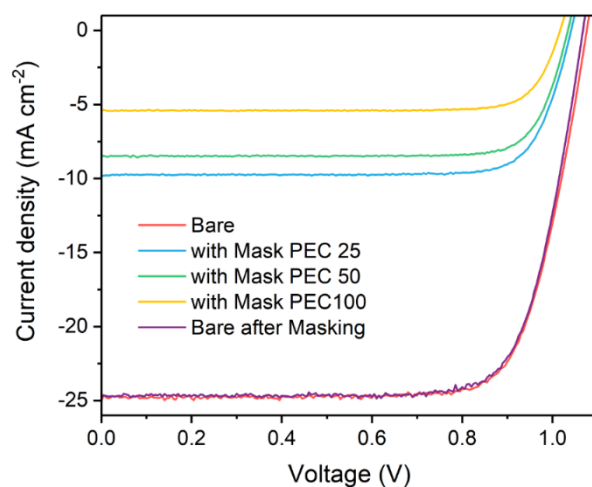was selected as the counter electrode material due to its greatest catalytic activity.[8]

Figure 5.7 | The current density-voltage (*J-V*) curves of PSCs. Samples are tested under simulated AM 1.5 G illumination at 100 mW cm^{-2}.

As two parts are connected in series, their photocurrents must match. To this end, It is necessary to find the balance between sufficient light absorption in Cu$_2$O for good PEC performance and necessary transparency that permits proper PSC operation, gold layer is removed and 3 thicknesses of Cu$_2$O (PEC 25, PEC 50 and PEC 100, where the numbers denote the duration in minutes) are explored by changing the electrodeposition duration.[9] All performance is lowered without the Au contact due to increased resistance. Though sample with the thinnest Cu$_2$O shows only 4.5 mA cm^{-2} at 0 V versus RHE, the sample

Conditions	V$_{OC}$	J$_{SC}$	FF	PCE	J$_{SC}$ (IPCE)
Bare	1.076	25.06	75.3	20.33	24.9
MASK PEC 25	1.041	9.81	79.8	8.17	9.34
MASK PEC 50	1.034	8.54	81.3	7.22	7.93
MASK PEC 100	1.017	5.43	81.4	4.48	4.38
Bare (after Masking)	1.068	24.68	76.6	20.2	N/A

Table 6.2 | Performance Summary of applied PSCs.

of 50 min electrodeposition exhibits similar performance to the 100 min one. Corresponding transmittance and IPCE at 0.5 V versus RHE were measured (Figure 5.6d). Compared to the opaque sample, IPCE of all 3 samples are showing a global decline of around 7%. Two phenomena are noteworthy. First, as film gets thicker, both the absorption and IPCE gets more significant at longer wavelength. This correlates well with the negative relation between extinction coefficient and wavelength.[10] In other words, thick films are necessary to absorb substantial photons in long-wavelength region. Second, though the photons with energy smaller than the band gap will interact weakly with the semiconductor, the transmittance at long-wavelength region (> 600 nm) decreases along with film thickness. We suggest this is possibly due to an increase of scattering caused by larger roughness in thicker films.

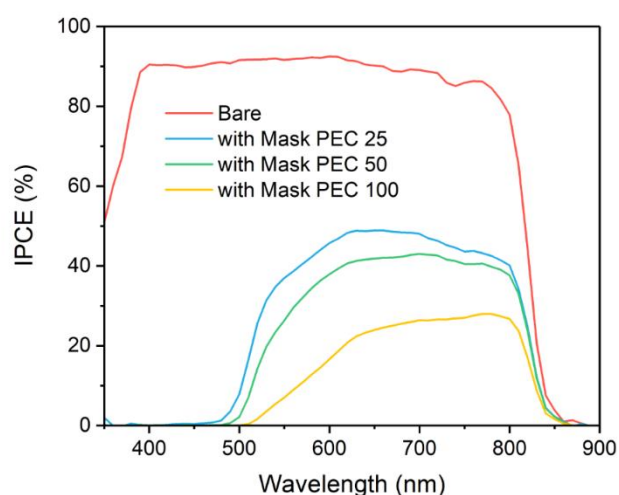The PSCs employed here are 2D/3D PSCs which exhibit an open-circuit voltage (V_{OC}) of

Figure 5.8 | Wavelength-dependent IPCE of PSCs.

1.076 V, short-circuit current density of 25.06 mA cm^{-2} and fill factor of 75.3% (Figure 5.7 and Table 6.2). The PV performance with transparent Cu_2O photocathodes as masks is also shown in Figure 5.7. Because of the undesirable energy loss with thick Cu_2O mask in long-wavelength region, the PSC with PEC 100 mask is giving only 4.48% conversion efficiency. However, the PSC with PEC 50 mask is giving similar efficiency (7.22%) value to the one with PEC 25 mask (8.17%). Corresponding IPCEs are shown in Figure 5.8. Clearly, considerable number of lower-energy photons that were wasted by Cu_2O were not used by the PSC. Combining with the photocathode optical data, we suggest that optical loss at interfaces contributes significantly.

To predict the tandem operating current density, we overlapped the *J-V* curves of photocathodes, PSCs and the counter electrode (Figure 5.6e). As both photocathodes and the counter electrode curves are fixed, the PV curves are shifted while matching the current densities of both crossing points with the other electrodes. Current densities of 2.59, 3.62 and 3.37 mA cm^{-2} are found for tandem system with PEC 25, PEC 50 and PEC 100 front electrodes, respectively. Then PEC 50 was selected and connected with other parts as the schematic shown in Figure 4b and tested with simulated 1 sun illumination for 10 hours under two-electrode configuration. The current density is shown in Figure 5.6f. A slightly larger current density of 3.72 mA cm^{-2} is observed at the beginning of the test compared to the estimated current density, which is probably due to activation in both the photocathode and the PSC.[9,11,12] STH efficiency was calculated with by the following equation considering 100% Faradaic efficiency,

$$\eta_{STH} = \frac{j_{ph} \times 1.23\ V}{P_{in}}$$

Where j_{ph} is the photocurrent density of the system, 1.23 V is the electromotive force for water splitting and P_{in} is the power of incident illumination, taken as 100 mW cm^{-2} for AM 1.5 G spectrum with 1 sun intensity. The corresponding η_{STH} was determined to be 4.55% and dropped 8.8% after 10-hour operation. As the photocathodes have been proved stable for tens of hours with gas quantification, we assume the degradation origins from the PSC due to high humidity around the PEC cell.

5.3 Conclusion and outlooks

The value here represents one of the highest efficiencies achieved by unbiased solar water splitting devices using oxide photoelectrodes.[13,14] Nevertheless, we concluded several approaches to improve the tandem performance. First, considerable amount of energy was unexploited in the form of optical loss. Scattering and reflection at interfaces could be minimized by making a monolithic device which integrate photoabsorbers and electrocatalysts into one neat piece. Quite a few high-efficiency devices fabricated in this style hold the potential of even lower cost because of simple structure.[15,16] Then, even though we applied electrocatalysts that are among the best performers, the slow kinetics for hydrogen evolution reaction (HER) and oxygen evolution reaction (OER) in near-neutral electrolyte leads to considerable burden on the system. To relieve the situation, one can either improve the catalysts by nano-structuring or transfer the system to more alkaline solution (OER is more sluggish and most good OER catalysts work in alkaline electrolyte). In the latter case, new protecting strategies should be developed to allow meaningful operation duration. Lastly, there're still space for both Cu$_2$O photocathodes and PSCs to be optimized for this application. A careful examination of the Figure 5.6e, revealed that the working potential didn't lie at the max power point of either cells. To bring the curves together, higher photovoltage is desired. A photovoltage of 1 V is certainly not the limit of Cu$_2$O considering its 2-eV bandgap. Since the photovoltage is determined by the Fermi level difference of its built-in junction, one can shift, most probably, the Fermi level of Ga$_2$O$_3$ by doping Sn^{4+}, for example.[12] On the other hand, as one of the advantage of PSCs, their composition is tunable, where large photocurrent density can be sacrificed for higher V$_{OC}$.[17,18]

In summary, we demonstrated a new Cu$_2$O photocathode with benchmark performance.

To show the advancement of the electrode, we constructed an overall unassisted tandem solar water splitting device with the-state-of-the-art $BiVO_4$ photoanode, achieving a record STH conversion efficiency of ~3% for all-oxide based devices. In the case of Cu_2O photocathodes with CuSCN as HTL, an overall improvement was achieved in planar devices. Considering the excellent optical and electronic properties of CuSCN, a standalone PEC-PV tandem was constructed with state-of-the-art perovskite solar cell delivering STH efficiency of 4.55%. Though this efficiency stands as the highest among all Cu_2O based dual-absorber tandems, several suggestions based on our results show considerable space for future development.

5.4 Methods

5.4.1   Fabrication of counter electrodes, photoelectrodes and perovskite solar cells.

Preparation of Cu₂O nanowire photoelectrodes. The nanowire Cu_2O photoelectrodes used here are the same as the ones described in chapter 3 and the Cu_2O photoelectrodes with CuSCN layer are prepared as described in chapter 4.

Preparation of BiVO₄ films. All following chemicals used in this study were of analytical grade and used without further purification. $BiVO_4$ film was prepared by a modified metal-organic decomposition (MOD) method with a slight modification from our previous procedure.[6] Thus, 0.2 M $Bi(NO_3)$ •5H₂O (99.8%; Kanto Chemicals) dissolved in acetic acid (99.7%; Kanto Chemicals), 0.03 M $VO(acac)_2$ (98.0%; Sigma Aldrich) and 0.03 M $MoO_2(acac)_2$ (98.0%; Sigma Aldrich) in acetyl acetone (>99.0%; Kanto Chemicals) were prepared as a precursor solution. Then stoichiometric amount of each precursor was mixed to complete a precursor solution. For Mo doping, Bi:(V+Mo) = 1:1 atomic ratio was applied for 1% Mo: $BiVO_4$ films. For fabrication of the $BiVO_4$ film, 55~25 µl of solution was dropped on FTO glass (2 cm x 2.5 cm) and dried for 15 min in Ar atmosphere. The FTO glass (TEC 8; Pilkington) was cleaned by using acetone and ethanol with ratio of 1: 5, and washed with copious amount of deionized water and finally stored in acetone before usage. The greenish transparent precursor film was calcined at 550 ℃ for 30 mins to form a yellow $BiVO_4$ film. After the annealing process, 2 cm x 2.5 cm $BiVO_4$/FTO was split to obtain photoanodes with a net irradiation area of 0.54 cm² connected by silver paste and copper wire and sealed with epoxy resin.

Hydrogen treatment of metal oxide films. Hydrogen treatment was conducted using borohydride decomposition method reported by Hao et al.[19] First, 16 mmol of $NaBH_4$ (>98%; Sigma Aldrich) was put into a 200 ml alumina crucible and another smaller alumina bottle (15 ml) was put on the $NaBH_4$ powder. In this smaller bottle, as-prepared metal oxide film (2 cm x 2.5 cm) was placed and finally 200 ml alumina crucible was covered with an alumina cover. This reactor was put in already-heated furnace at 500 ℃ for 30 min. Then the crucible was immediately taken out from the furnace and naturally cooled down.

NiFeOx co-catalyst deposition on the BiVO₄ film. The $NiFeO_x$ co-catalysts were deposited utilizing photo-assisted electrodeposition under AM 1.5G illumination according to the

reported procedure with variation based on NiOOH/FeOOH double layer OEC.[20] 30 mg of $Fe(SO_4)_2 \cdot 7H_2O$ (≥99%; Sigma Aldrich) and 10 mg of $Ni(SO_4)_2 \cdot 6H_2O$ (99%; Sigma Aldrich) were put in glass bottle and 100 ml of 0.5 M $KHCO_3$ (pH of 8.3, 30 min Ar gas purged before usage) was put in, resulting transparent and yellow solution. Existence of bicarbonate anion deters premature oxidation of Fe_2^+ ion to iron hydroxide precipitation which resemble orange dust. Photoelectrodeposition was conducted using as prepared precursor solution on photoelectrode. Linear sweep voltammetry was applied with bias of -0.3 V to 0.5 V versus reference electrode (Ag/AgCl) for 4~6 times under illumination (AM 1.5G, 100 mW/cm²). Sequential linear sweep voltammetry gave reduced current density and this suggests that over deposition of $NiFeO_x$ could occur at certain point. After deposition, photoelectrode was taken out and washed with copious about of DI water. Photoelectrode was stored in Ar gas filled bottle before usage.

Fabrication of perovskite solar cells. The 3D perovskite active layer was deposited on a freshly-prepared FTO/c-TiO_2/m-TiO_2 substrate and a two-step spin-coating method is applied with addition of 200 μL chlorobenzene. The 3D perovskite solution precursor is prepared by dissolving lead iodide, formamidinium iodide and methylammonium iodide, methylammonium iodide and cesium iodide in dimethylformamide (DMF) and ultra-dry dimethyl sulfoxide (DMSO) under mild heating at 70 °C. The bilayer perovskite cell was fabricated by 10 s post-dipping treatment in a isopropanol solution which contains lead iodide and Pentafluorophenylethyl ammonium iodide (FEAI). The residual FEAI solution was removed by spin-coating, followed by 10 min annealing at 120 °C. All processes were done in a nitrogen glovebox. To coat hole transporting layer, Spiro-OMeTAD was dissolved in chlorobenzene with dopants of lithium bistrifluorosulfonyl imide and 4-tert-butyl pyridine and spin-coated on the perovskite film. The gold electrode was thermally evaporated onto the surface of HTL with mask. A thin layer of MgF_2 was E-beam evaporated under room temperature with thikness of 140 nm.

IrO_x electrode preparation. The IrO_x anode was prepared according literature.[9] Briefly, a piece of titanium foil (99.7%, Sigma Aldrich) was etched in boiling 1 M oxalic acid solution for 1 hour. Then 30 μL of 0.2 M H_2IrCl_6 solution was drop cast on the foil followed by 500 °C calcination in air for 10 min. The above steps are repeated for three times, resulting in the deposition of 6.3 mg of IrO_x deposited on the surface.

5.4.2   Photoelectrochemical characterization and gas quantification

Photoelectrochemical   and   electrochemical   characterization.   The

photoelectrochemical performance of samples was evaluated in a three-electrode configuration using Cu$_2$O photocathodes as the working electrode, a Pt wire as the counter electrode and Ag/AgCl/sat. KCl as the reference electrode. For measurements in solutions of different pH, the pH 5.0 buffer was prepared using a combination of 0.5 M Na$_2$SO$_4$ and 0.1 M phosphate solution, while the pH 9.0 buffer was made by adjusting pH of 0.1 M Na$_2$CO$_3$ and 0.1 M NaHCO$_3$ solution and the pH 12 solution was prepared by tuning pH of 0.2 M KOH solution. A potentiostat/galvanostat (BioLogic, SP-200) was used to acquire the photoresponse under chopped illumination from an LCS-100 solar simulator (Newport, Class ABB) with an AM 1.5G filter. The PEC cell was fixed at a position determined by measuring the short-circuit current on a calibrated silicon diode with a KG 3 filter. Calibration was carried out across the relevant wavelength range of 300-800 nm. All linear sweep voltammetry scan rates were 10 mV s^{-1}. Incident photon to current efficiency (IPCE) was measured under light from 300 W Xe lamp through a monochromator (TLS-300XU, Newport). The photoresponse was compared with that of a calibrated Si photodiode (FDS100-CAL, Thorlabs) to determine the IPCE at each wavelength. Tests were carried out using chronoamperometry at 0 V vs. RHE in a homemade cell with a quartz window (Edmund Optics). Potential values were transformed to the reversible hydrogen electrode scale through the equation: E_{RHE} = $E_{Ag/AgCl(KCl\ sat.)}$ + 0.197 V +0.059 V * pH.

Photoelectrochemical measurements of photoanodes and tandem system were performed with standard three-electrode configurations; photoanode as the working electrode, Pt mesh as the counter electrode and Ag/AgCl (3M NaCl) as the reference electrode. The scan rate for the current-voltage (*J-V*) curve was 20 mV/sec. For water oxidation experiments, 0.2 M potassium borate (KBi) electrolyte (made by using DI water, 1.0 M KOH (Samjun, >99%) and H$_3$BO$_3$ (≥99%, Sigma Aldrich) (pH ~9.0) was used as the main electrolyte. Electrolyte was used after purged with Ar gas (30 minutes) to remove dissolved oxygen. To measure the degree of charge separation, 1.0 M Na$_2$SO$_3$ (>98%, Sigma Aldrich) was added to the main electrolyte. Potentials were recorded with correction by the Nernst relation E_{RHE} = $E_{Ag/AgCl(KCl\ sat.)}$ + 0.197 V +0.059 V * pH, in which E$_{Ag/AgCl}$ is applied bias potential and 0.209 is a conversion factor from the Ag/AgCl electrode to the RHE scale. All electrochemical data were recorded by using a potentiostat (IviumStat, Ivium Technologies). A 300 W Xenon lamp was used to make simulated 1 sun light irradiation condition (AM 1.5G, 100 mW/cm^2) by using a solar simulator (Oriel 91160) with an AM 1.5G filter calibrated with a reference cell certified by the National Renewable Energy

Laboratories, USA.

Photoelectrochemical H$_2$ and O$_2$ evolution measurements. Using Ar as a carrier gas, the amounts of H$_2$ and O$_2$ gases evolved from the PEC cell were analyzed using a gas chromatograph (HP5890, molecular sieve 5 L column) equipped with a thermal conductivity detector (TCD). Light source and electrolyte were the same as those used for above PEC measurements, and the gas products were sampled every 20 mins.

Photovoltaic performance tests. Solar cells are measured using 300 W xenon light source (Oriel) with Schott K113 filter (Praezisions Glas & optic GmbH). Light intensity was calibrated by silicon photodiode for each measurement. A Keithley 2400 was used to drive and record current-voltage scan with scan rate of 50 mV s^{-1}. Cell mask area is a 0.16 cm^2 square. IPCE was carried out using monochromator (Arkeo & Ariadne, Cicci reserch) equipped with a 300 W xenon lamp.

Tandem testing. Active area of transparent PEC electrode with RuO$_x$ catalyst was defined by opaque epoxy (Loctite Hysol 9461). Homemade IrO$_x$ electrode was positioned at the side in the pH 5 buffer electrolyte. Perovskite was centered and put closely against the back quartz window of the cell. The connections of PEC-PV and PV-IrO$_x$ anode are built with copper wire by ultrasonic soldering. Specifically, the electron collecting contact of PV cell was connected to the back contact of photocathode while the hole collecting contact was connect to the anode. The same solar simulator was used to the one in PEC analysis. Current was recorded using chronoamperometry at zero bias potential.

5.5 References

(1) Y. Yu; S. R. Leone; H. Zhang; P. Yang; S. W. Eaton; N. A. Gibson; S. Aloni; N. Kornienko. Growth and Photoelectrochemical Energy Conversion of Wurtzite Indium Phosphide Nanowire Arrays. *ACS Nano* **2016**, *10* (5), 5525–5535.

(2) H. Kaneko; T. Minegishi; M. Nakabayashi; N. Shibata; Y. Kuang; T. Yamada; K. Domen. A Novel Photocathode Material for Sunlight-Driven Overall Water Splitting: Solid Solution of ZnSe and Cu(In,Ga)Se$_2$. *Adv. Funct. Mater.* **2016**, *26* (25), 4570–4577.

(3) T. Minegishi; T. Harada; Y. Kuang; F. Jiang; S. Ikeda; Gunawan; K. Domen.   Pt/In$_2$S$_3$ /CdS/Cu$_2$ZnSnS$_4$ Thin Film as an Efficient and Stable Photocathode for Water Reduction under Sunlight Radiation . *J. Am. Chem. Soc.* **2015**, *137* (42), 13691–13697.

(4) T. Higashi; H. Kaneko; T. Minegishi; H. Kobayashi; M. Zhong; Y. Kuang; T. Hisatomi; M. Katayama; T. Takata; et al. Overall Water Splitting by Photoelectrochemical Cells Consisting of (ZnSe)$_{0.85}$(CuIn$_{0.7}$Ga$_{0.3}$Se$_2$)$_{0.15}$ Photocathodes and BiVO$_4$ Photoanodes. *Chem. Commun.* **2017**, *53* (85), 11674–11677.

(5) J. H. Kim; H. Kaneko; T. Minegishi; J. Kubota; K. Domen; J. S. Lee. Overall Photoelectrochemical Water Splitting Using Tandem Cell under Simulated Sunlight. *ChemSusChem* **2016**, *9* (1), 61–66.

(6) J. H. Kim; Y. Jo; J. H. Kim; J. W. Jang; H. J. Kang; Y. H. Lee; D. S. Kim; Y. Jun; J. S. Lee. Wireless Solar Water Splitting Device with Robust Cobalt-Catalyzed, Dual-Doped BiVO$_4$ Photoanode and Perovskite Solar Cell in Tandem: A Dual Absorber Artificial Leaf. *ACS Nano* **2015**, *9* (12), 11820–11829.

(7) J. H. Kim; J. W. Jang; Y. H. Jo; F. F. Abdi; Y. H. Lee; R. Van De Krol; J. S. Lee. Hetero-Type Dual Photoanodes for Unbiased Solar Water Splitting with Extended Light Harvesting. *Nat. Commun.* **2016**, *7*, 13380.

(8) C. C. L. McCrory; S. Jung; I. M. Ferrer; S. M. Chatman; J. C. Peters; T. F. Jaramillo. Benchmarking Hydrogen Evolving Reaction and Oxygen Evolving Reaction Electrocatalysts for Solar Water Splitting Devices. *J. Am. Chem. Soc.* **2015**, *137* (13), 4347–4357.

(9) A. Mendes; M. Grätzel; J. Azevedo; A. Hagfeldt; M. T. Mayer; P. Dias; L. Andrade; S. D. Tilley; D. Bi; et al. Transparent Cuprous Oxide Photocathode Enabling a Stacked Tandem

Cell for Unbiased Water Splitting. *Adv. Energy Mater.* **2015**, *5* (24), 1501537.

(10)   C. Malerba; F. Biccari; C. Leonor Azanza Ricardo; M. D'Incau; P. Scardi; A. Mittiga. Absorption Coefficient of Bulk and Thin Film Cu$_2$O. *Sol. Energy Mater. Sol. Cells* **2011**, *95* (10), 2848–2854.

(11)   J. Luo; L. Steier; M. K. Son; M. Schreier; M. T. Mayer; M. Grätzel. Cu$_2$O Nanowire Photocathodes for Efficient and Durable Solar Water Splitting. *Nano Lett.* **2016**, *16* (3), 1848–1857.

(12)   L. Pan; J. H. Kim; M. T. Mayer; M. K. Son; A. Ummadisingu; J. S. Lee; A. Hagfeldt; J. Luo; M. Grätzel. Boosting the Performance of Cu$_2$O Photocathodes for Unassisted Solar Water Splitting Devices. *Nat. Catal.* **2018**, *1* (6), 412–420.

(13)   J. H. Kim; J. W. Jang; Y. H. Jo; F. F. Abdi; Y. H. Lee; R. Van De Krol; J. S. Lee. Hetero-Type Dual Photoanodes for Unbiased Solar Water Splitting with Extended Light Harvesting. *Nat. Commun.* **2016**, *7* (1), 13380.

(14)   W. Vijselaar; P. Westerik; J. Veerbeek; R. M. Tiggelaar; E. Berenschot; N. R. Tas; H. Gardeniers; J. Huskens. Spatial Decoupling of Light Absorption and Catalytic Activity of Ni-Mo-Loaded High-Aspect-Ratio Silicon Microwire Photocathodes. *Nat. Energy* **2018**, *3* (3), 185–192.

(15)   A. Heller. Hydrogen Evolving Solar Cells. *Catal. Rev.* **1984**, *26* (3–4), 655–681.

(16)   W. H. Cheng; M. H. Richter; M. M. May; J. Ohlmann; D. Lackner; F. Dimroth; T. Hannappel; H. A. Atwater; H. J. Lewerenz. Monolithic Photoelectrochemical Device for Direct Water Splitting with 19% Efficiency. *ACS Energy Lett.* **2018**, *3* (8), 1795–1800.

(17)   N. J. Jeon; J. H. Noh; W. S. Yang; Y. C. Kim; S. Ryu; J. Seo; S. Il Seok. Compositional Engineering of Perovskite Materials for High-Performance Solar Cells. *Nature* **2015**, *517* (7535), 476–480.

(18)   J.-D. Decoppet; A. Abate; F. Giordano; M. Grätzel; P. Gao; A. Hagfeldt; C. Renevier; K. Schenk; D. Bi; et al. Efficient Luminescent Solar Cells Based on Tailored Mixed-Cation Perovskites. *Sci. Adv.* **2016**, *2* (1), e1501170.

(19)   Y. Hao; J. Deng; L. Zhou; X. Sun; J. Zhong. Depth-Reduction Induced Low Onset Potential of Hematite Photoanodes for Solar Water Oxidation. *RSC Adv.* **2015**, *5* (39), 31086–31090.

(20)   F. Yu; Y. Wang; L. Sun; L. Bai; H. Li; F. Li. An Iron-Based Thin Film as a Highly Efficient Catalyst for Electrochemical Water Oxidation in a Carbonate Electrolyte. *Chem. Commun.* **2016**, *52* (33), 5753–5756.

6 Conclusions and Outlooks

Photoelectrochemical water splitting provides a fascinating solution to both future energy demand and current environmental problems. State-of-the-art photoelectrodes have achieved significant development in the last 10 years. Yet, the desire for robust, efficient and economic PEC processes was not satisfied. The studies in this thesis took the development of the Cu_2O photocathode, an inexpensive p-type oxide semiconductor, as an example to unfold the course of pushing a promising photoelectrode towards standalone solar water splitting device.

In the first part, electron transport was enhanced by constructing a p-n heterojunction with well-aligned band energy levels. Since the electrons are the minority carriers in p-type semiconductors, their electronic properties are inferior to that of majority ones, thus their transport is a key limiting factor for the overall performance of photoelectrodes. Yet an efficient charge separation and a smooth charge conduction could result in significant improvement. This was allowed by the Cu_2O/Ga_2O_3 junction, which effectively separates the photo-generated electron-hole pairs with the built-in p-n junction that owns large Fermi level difference. Moreover, thorough characterizations revealed the excellent conduction band matching between Cu_2O and Ga_2O_3, which guarantees efficient electron transport. The resulted unprecedent photocurrent density of around 10 mA cm^{-2} at 0 V versus RHE represents the best performance of its kind as shown in Figure 6.1.[1] In the meantime, the photovoltage of 1 V stands as one of the best among all photocathodes
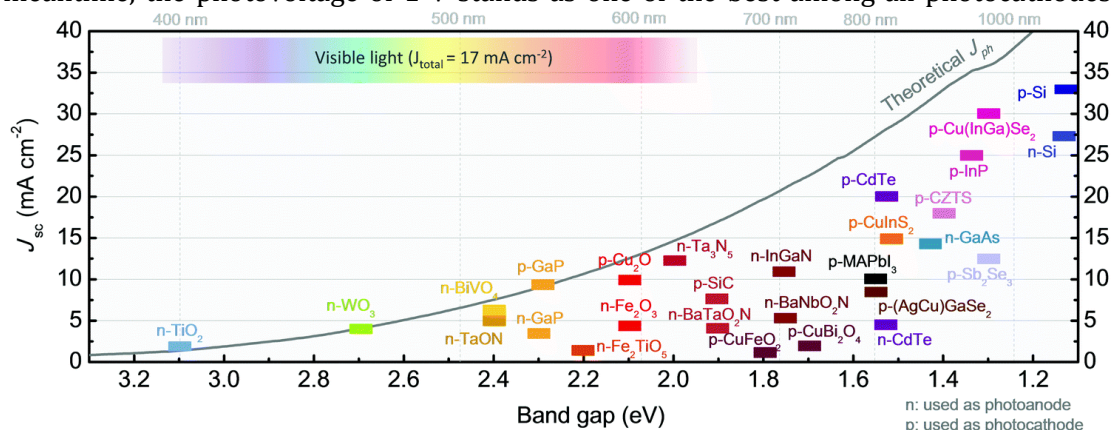

Figure 6.1 | Reported short-circuit photocurrent density of photoelectrodes for PEC water splitting under 1 sun illumination. Current recorded at 0.0 V versus RHE for photocathodes and 1.23 V versus RHE for photoanodes.

including photovoltaic material-based ones.

Since the photovoltage is determined by the Fermi level difference in the p-n junction, it could be further improved by adjusting the Fermi level in either semiconductor. One simple way is to push the Fermi level of Ga_2O_3 up via doping it with Sn or Si. This method could also increase the conductivity of the Ga_2O_3 layer and reduce the resistance in Ga_2O_3/TiO_2 junction. However, the dopant activation needs annealing at high temperature, which could damage the Cu_2O layer.[2] Therefore, a proper fabrication method is necessary other than thermal ALD.

The second part focuses on the hole transport at the other side of the photoelectrode echoing the first part. Au was used as the ohmic contact for Cu_2O photocathodes due to the perfect matching between Au work function and Cu_2O valence band. However, noble metals are scarce and costly. Meanwhile, Au could conduct both electrons and holes, resulting in considerable amount of electron-hole recombination at the back contact. Electrodeposited CuSCN was applied as the hole transport material for Cu_2O photocathodes for the first time. Apart from the excellent electronic properties of the solution-processed CuSCN, band-tail states assisted hole transport was discovered via thorough band energy level analysis. Due to the selective hole conduction, planar Cu_2O photoelectrodes exhibit outstanding fill factor. The optical advantage of CuSCN further unlocks the key of applying Cu_2O as the front photoabsorber in a tandem device. Though CuSCN functions as an effective hole transport material for Cu_2O photocathodes, its electronic properties could be optimized during fabrication. Plenty of examples can be referred to the research on perovskite solar cells.[3–5] Generally, two kinds of modifications are presented. The first is to change the stoichiometry or the structure of CuSCN. These modifications could have substantial impact on the mobility, carrier density, dielectric constant and electronic structure.[6–8] The other way is to modify the CuSCN with foreign particles, i.e. doping.[3,9] Both ways could further improve the hole conduction in Cu_2O photocathodes, and in return favor its application in various kinds of electronic devices.

As both the electron and hole transfer have been improved, the focus was shifted to the photoabsorber itself in the third part. The photoabsorber is the place where the conversion from photons to photo-generated carriers happens. Its structure has significant impact for light absorption and charge extraction. Nanowire structure has the benefit of harvesting scattered light with multiple absorption inside the wire jungle. More importantly, with this configuration, the electrons only have to travel the radius of the wire

to reach the electrode surface, while, the holes, with longer diffusion length, can still be collected by the back contact. The increased real surface area could also ease the workload of the integrated catalyst. With the advantage of ALD coating and underpotential electrodeposition, conformal radial heterojunction and catalyst decoration was achieved. Apart from the structure of Cu_2O, the crystal orientation of it is also important. The anisotropic PEC performance of Cu_2O photocathode implies that the Cu_2O with different crystal orientation could exhibit distinct charge transport properties. The successful fabrication of single-crystal Cu_2O and Au films provides perfect platforms for fundamental studies on anisotropic optical and electronic behaviors. Transmission mode carrier absorption spectroscopy and terahertz spectroscopy could be two of the methods that fit the material structure. Provided that suitable sampling technique was possible to fabricate electron-transparent thin samples while reserving the atomic regularity of the single crystal, the types of defects in Cu_2O which contributes to its semiconductor properties can be observed in aberration-corrected TEMs. However, the single-crystal photoelectrodes suffer from serious reflection. Controlled etching which enhances the surface disorder while keeping the well-defined crystal bulk could be an option as shown in Figure 6.2.

200 nm	EHT = 5.00 kV	Signal A = InLens	Stage at T = 0.0 °	
	WD = 3.6 mm	I Probe = 150 pA		
	Mag = 50.00 K X	Column Mode = High Resolution	Date :26 Jul 2018	CiMe
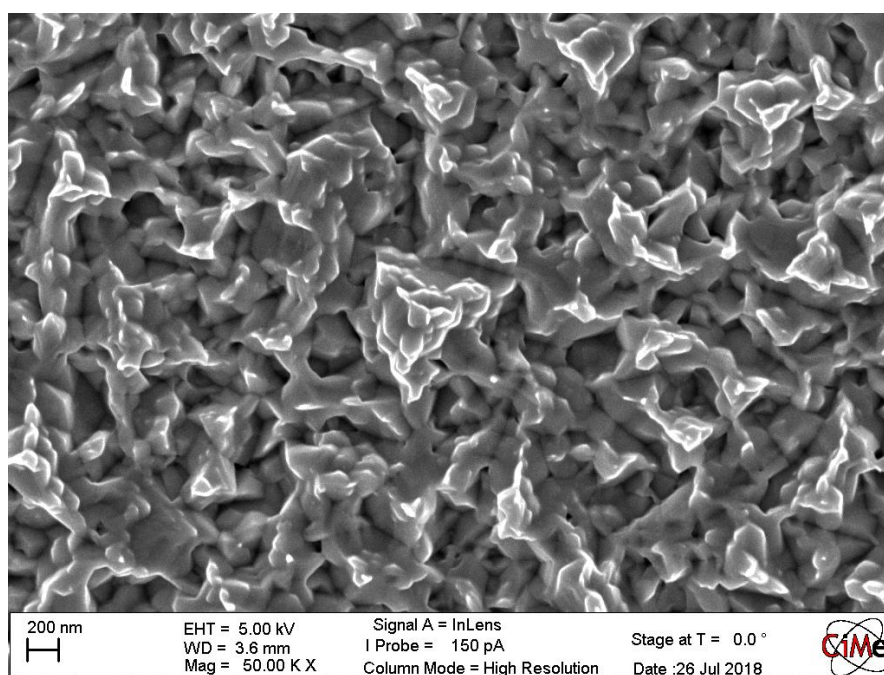
Figure 6.2 | SEM image of etched Cu_2O photocathode surface by NH_3 with controlled duration.

The final part of the thesis concludes two early attempts to build Cu_2O-based tandems for unassisted solar water splitting. With dual-absorber configuration, the theoretical

efficiency could be improved to 34% compared to that of 19% with single-absorber.[10] However, in practice, interfaces between different phases could cause scattering and reflection, which results in considerable amount of optical loss. Since a unit solar water splitting device includes two photoabsorbers connected in series, the problems initiated by the matching of current between two absorbers could greatly reduce the overall solar-to-hydrogen efficiency. Besides, the absorption spectra of both photoabsorbers should cover as much of the solar spectrum as they can while keeping the economical configuration. Detailed solutions to the above problems are proposed at the end of chapter 5.

This thesis merely concludes the development of Cu_2O photocathodes in a short period. During the research of Cu_2O photocathodes, the idea of future application was always kept in mind. However, it is always difficult and irresponsible to judge whether an emerging technique will be applied in the future. There are plenty of space for this technology to further develop while more technoeconomic analysis are also indispensable to provide advice to the administration. In addition, the knowledge and methods associated with semiconductors and catalysts acquired could be valuable to the advance in other areas. I hope the examples of advancing the performance of the Cu_2O photoelectrode in multiple aspects towards a standalone solar water splitting device could be a humble reference to people who are interested in this area.

7 Acknowledgements

First and foremost, I would like to thank my PhD advisor Prof. Ander Hagfeldt. I am thankful for the opportunity of doing my PhD offered by him, a highly respected and erudite physical chemist. It is a privilege to learn from his profound knowledge of electrochemistry and semiconductor physics. I really appreciate the luxurious freedom, support and trust he provided during my research, which I believe is the reason for such an enjoyable experience. Thank him for those inspiring and enjoyable discussions, and for his help in life when I needed it the most. His kindness will always be kept in heart.

I would also like to thank Prof. Michael Grätzel, my unofficial co-advisor. Due to the close collaborations between LSPM and LPI, he is offering advice and help from the very beginning of my PhD. As one of the most respected physical chemists in the world, he shared knowledge and vision without reservation. Thank him for those many fruitful discussions and recommendations. His advice and opinions are valuable and will help me in the future as well.

I want to thank my previous colleagues Prof. Matthew T. Mayer and Prof. Jingshan Luo. Matt has been patient and conscientious in showing me from the basic technique of using a swagelok to the deriving of the band bending in a band diagram. You have been a great mentor and friend to me. I do appreciate your sharing of knowledge and scientific spirit. Jingshan did a great help for me to blend in with such large international groups. Your working attitude and passion has been valuable to my PhD experience. Thank you for so many encouraging discussions and generous support. It is lucky to meet you guys at the beginning of my PhD.

I owe special thanks to Prof. Yuxiang Yu, Marko Stojanovic, Dr. Xuerun Li and Ms. Chuanlan Zhang for your generous help during my life in Switzerland. It won't be an easy experience without your great help.

I would like to thank my collaborators Dr. Jin-hyun Kim, Dr. Liang Yao, Prof. Kevin Sivula. I couldn't achieve any of the work without your constructive advice and contribution.

I thank my fellow PhD students at EPFL, Dr. Marcel Shreier, Dr. Ludmilla Steier, Dr. Amita Ummadisingu, Dr. Norman Pellet, Dr. Bitao Dong, Dr. Yasemin Saygili, Mr. Zaiwei Wang, Dr. Jeannette Kadro, Mr. Runze Mao, Mr. Lichen Bai, Dr. Sadig Aghazada, Dr. Valeriu Scutelnic,
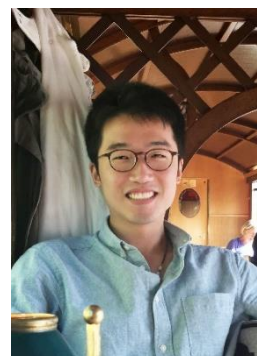
8 Curriculum Vitae

Linfeng PAN

liampan@outlook.com

+41 78 860 75 31

Chemin du Bochet 18, Ecublens VD,

Education

Jul 2015 - Jun 2019	**Swiss Federal Institute of Technology, Lausanne**, Switzerland.
	PhD in Chemistry and Chemical Engineering
	Advisor: Prof. Anders Hagfeldt
Sep 2012 - Jun 2015	**East China University of Science and Technology**, Shanghai, China.
	MSc in Material Science
	Advisor: Prof. Huagui Yang.
Sep 2008 - Jun 2012	**Nanjing Tech University**, Nanjing, China.
	BSc in Material Science and Engineering

Research Experience

- Pushed solar water splitting performance using oxide semiconductor towards standalone devices with record efficiency.
- Developed advanced fabrication methods for heterojunctions and catalysts fabrication with understanding of optoelectronic properties using spectroscopic characterizations.
- Established a research subgroup to explore the electrocatalytic water splitting field as a team leader during master study.
- Extensive collaboration in the fields of perovskite solar cell and CO_2 electroreduction.
- Designed, built and maintained equipment as laboratory manager.

Publications

1. **L. Pan**; J. H. Kim; M. T. Mayer; M. K. Son; A. Ummadisingu; J. S. Lee; A. Hagfeldt; J. Luo; M. Grätzel. Boosting the Performance of Cu2O Photocathodes for Unassisted Solar Water Splitting Devices. *Nat. Catal.* 2018, *1* (6), 412–420.

2. Y. X. Yu[§]; **L. Pan**[§]; M. K. Son; M. T. Mayer; W. De Zhang; A. Hagfeldt; J. Luo; M. Grätzel. Solution-Processed Cu2S Photocathodes for Photoelectrochemical Water Splitting. **ACS Energy *Lett*.** 2018, *3* (4), 760–766.

3. Y. Liu; S. Akin; **L. Pan**; R. Uchida; N. Arora; J. Milic; A. Hinderhofer; F. Schrerber; A. Uhl; S. Zakeeruddin; A. Hagfeldt; M. I. Dar; M. Grätzel. Ultra-hydrophobic 3D/2D Fluoroarene Bilayer-Based Water-Resistant Perovskite Solar Cells with Efficiencies Exceeding 22%. *Sci. Adv*. 2019, Accepted.

4. Y. Li; P. Liu; **L. Pan**; H. Wang; Z. Yang; L. Zheng; P. Hu; H. Zhao; L. Gu; H. Yang. Local Atomic Structure Modulations Activate Metal Oxide as Electrocatalyst for Hydrogen Evolution in Acidic Water. *Nat. Commun.* 2015, *6* (May).

5. L. Steier; S. Bellani; H. C. Rojas; **L. Pan**; M. Laitinen; T. Sajavaara; F. Di Fonzo; M. Grätzel; M. R. Antognazza; et al. Stabilizing Organic Photocathodes by Low-Temperature Atomic Layer Deposition of TiO 2. *Sustain. Energy Fuels* 2017, 1 (9), 1915–1920.

6. **L. F. Pan**; Y. H. Li; S. Yang; P. F. Liu; M. Q. Yu; H. G. Yang. Molybdenum Carbide Stabilized on Graphene with High Electrocatalytic Activity for Hydrogen Evolution Reaction. *Chem. Commun.* 2014, 50 (86), 13135–13137.

7. M. M. Tavakoli; D. Bi; **L. Pan**; A. Hagfeldt; S. M. Zakeeruddin; M. Grätzel. Adamantanes Enhance the Photovoltaic Performance and Operational Stability of Perovskite Solar Cells by Effective Mitigation of Interfacial Defect States. *Adv. Energy Mater.* 2018, 8 (19), 1800275.

8. M. Q. Yu; Y. H. Li; S. Yang; P. F. Liu; **L. F. Pan**; L. Zhang; H. G. Yang. Mn 3 O 4 Nano-Octahedrons on Ni Foam as an Efficient Three-Dimensional Oxygen Evolution Electrocatalyst. *J. Mater. Chem. A* 2015, 3 (27), 14101–14104.

9. H. B. Jiang; **L. F. Pan**; P. F. Liu; W. Q. Fang; H. G. Yang. Synthesis of Well-Defined Functional Crystals by High Temperature Gas-Phase Reactions. *Chinese Sci. Bull.* 2014, 59 (18), 2135–2143.

Google Scholar: https://scholar.google.com/citations?user=eoZHkUwAAAAJ&hl=en

Awards and Honors

2015-2019	EPFL Full Scholarship
2014	The National Scholarship
2014	Outstanding Student Awards
2012-2014	The First Prize Academic Scholarship, consecutive
	Individual Scholarship, The Second Prize Academic Scholarship, The Third Prize Academic Scholarship, Multiple times

Miscellaneous

- Oral presentation in MRS Fall Meeting and Exhibit, 2017, Boston, MA, U.S.A.: "Pushing the Boundaries of Cu_2O Photocathodes for Solar Water Splitting."

- Invited talk in International Symposium on Solar Energy Conversion & 2018 International Talents Sub-forum on Photo-electronics, 2018, Naikai University, China: "Advancing the performance of Cu_2O photocathodes for unassisted overall water splitting."

- Winter School NRG, 2018, Crans Montana, Switzerland.

- Summer School URPP LightChEC, 2015, Zurich, Switzerland.

- Swiss Snow Symposium 2019, Saas-Fee, Switzerland.

- Teaching assistant of Chemical thermodynamics for 3 years, CH-241, EPFL.

- Lecturer: Hagfeldt Ulf Anders.

- Supervisor of Master project: "Recycling of Dye-Sensitized Solar Cells", 2016, EPFL.

Language

English (proficient), Chinese (Native), French (A1, beginner)